University of California,
Irvine

Toward Computational Oncology: Nonlinear Simulation of Centimeter-Scale Tumor Growth in Complex, Heterogeneous Tissues

dissertation

submitted in partial satisfaction of the requirements
for the degree of

Doctor of Philosophy

in Mathematics

by

Paul Thomas Macklin

Dissertation Committee:
Professor John S. Lowengrub, Chair
Professor Natalia Komarova
Professor Hongkai Zhao

2007

The dissertation of Paul Thomas Macklin
is approved and is acceptable in quality and form for
publication on microfilm and in digital formats:

_____

_____

_____

Committee Chair

University of California at Irvine
2007

DEDICATION

to Angela Prazak (1927-2004) and all others who have fought cancer

Table of Contents

List of Figures

Page

List of Tables

Page

List of Symbols

$\mathbb{N}$	set of natural numbers $\{0, 1, 2, \cdots\}$
$\mathbb{Z}$	set of integers
$\mathbb{R}$	set of real numbers
$\partial\Omega$	boundary of the region Ω
$\|\|\mathbf{v}\|\|$	norm of the vector $\mathbf{v}$
∇	gradient operator
$\mathbf{n}$	outward (unit) normal vector
$\mathbf{s}$	positively-oriented (unit) tangent vector
κ	(mean) curvature
$\mathbf{a} \cdot \mathbf{b}$	dot product of $\mathbf{a}$ and $\mathbf{b}$
$[q(\mathbf{x}_\Sigma)]_\Sigma$	inside-to-outside jump in $q(\mathbf{x})$ at a point $\mathbf{x}_\Sigma$ on an interface Σ
$\chi_\Omega(\mathbf{x}) = \begin{cases} 1 & \mathbf{x} \in \Omega \\ 0 & \text{else} \end{cases}$	characteristic function
$H(x) = \begin{cases} 0 & x < 0 \\ 1 & x \geq 0 \end{cases}$	Heaviside function
$\mathcal{O}(\Delta x^n)$	"big-O" notation; a term on the order of Δx^n
$\frac{\partial f}{\partial \mathbf{a}}$	directional derivative of f in the direction of the unit vector $\mathbf{a}$.

Acknowledgements

First and foremost, I would like to thank my wife, Angela, for her patient understanding, love, and support through the years of weekend qualifier studies, marathon coding sessions, lengthy research trips to Scotland, and workshops. I wouldn't be here without her, and she's endured so much talk of cancer, level set methods, and finite differences that she truly deserves a Ph.D. herself! Angela, thank you for being not only my wife but also my greatest, truest friend. Thanks to you, we're finally done!

I would also like to thank my advisor, John Lowengrub, for his guidance and support, both at the University of Minnesota and here at UCI. I've learned a lot under him as a mathematician and a scientist, and a Ph.D. student could not possibly hope for a more dedicated and knowledgeable mentor. I'm pleased to have had the opportunity to travel to conferences and workshops with John over the past couple of years, and I'm grateful that he has not only been an advisor, but also a great advocate and a trusted friend. John, I hope that I will continue to develop as a scientist in a way that will make you proud!

I'm deeply grateful to have interacted with so many excellent mathematicians and scientists over the past few years. In particular, I enjoyed enlightening discussions of numerics with Hongkai Zhao and Steve Wise, as well as interesting conversations on cancer with Natalia Komarova and Vittorio Cristini. I treasure my collaboration with "Sandy" Anderson, Mark Chaplain, and Steven McDougall in Scotland. To my friends in Scotland: your modeling experience and wisdom have helped me grow as a biomathematician, and I'm grateful for the hospitality and friendship that you've extended to me over the past year.

I also wouldn't be here without my family and friends. My siblings, relatives, and in-laws have always been very supportive of my education, and I especially appreciate the thought-provoking conversations I've had with them over the years on work, research, and

family. I credit my parents for encouraging curiosity, creativity, and tinkering from as early as I can remember. Mom and Dad, I thank you for the countless opportunities that you provided for my educational, moral, and spiritual growth. I wouldn't be the person or scientist I am today without you!

Lastly, I'd like to thank the UCI Department of Mathematics for making Irvine such a great place to live and work. I wouldn't be here without the efforts of the faculty and the (past and present) departmental staff. In particular, I'd like to thank Jennifer Dugan, Donna McConnell, Darla Becker, Maria Graziano and all the others in the department who helped me navigate the whole Ph.D. process. I'm also grateful for the strong, vibrant, and supportive graduate student community here at UCI, particularly my friends Nick Alexander, Sunil Chetty, Timothy Choi, Phong Le, and Evelyn Manalo-Lunasin. Thanks for making UCI such a fun place to be!

This research was funded in part by a U.S. Department of Education GAANN (Graduate Assistance in Areas of National Need) fellowship, several UCI Department of Mathematics dissertation and research fellowships, and National Science Foundation (Division of Mathematical Sciences) grant support from John Lowengrub.

The materials in Chapter 2, 3, and 4 are copyrighted by Elsevier and are used with permission according to the journal author rights policy granted by Elsevier. This policy can be verified at http://www.elsevier.com/wps/find/authorshome.authors/copyright.

Part of the text of this dissertation is a reprint of material as it appears in Macklin and Lowengrub (2005), Macklin and Lowengrub (2006), and Macklin and Lowengrub (2007). The co-author listed in those publications directed and supervised research which forms the basis of this dissertation.

Curriculum Vitae

Paul Macklin

Office Address:
Department of Mathematics
MSTB 112
University of California at Irvine
Irvine, CA 92697-3875

Home Address:
available upon request

email: pmacklin@math.uci.edu
web: http://math.uci.edu/∼pmacklin

EDUCATION:

Sept. 2003 to June 2007	**Ph.D. in Computational and Applied Mathematics** University of California, Irvine Thesis Topic: Ghost fluid / level set methods and their application to computational oncology Advisor: Professor John Lowengrub
June 2000 to Sept. 2003	**M.S. in Industrial and Applied Mathematics** University of Minnesota, Twin Cities Thesis Topic: Nonlinear simulation of tumor growth and chemotherapy Advisor: Professor John Lowengrub
June 1999 to May 2000	Graduate study in applied mathematics University of Nebraska, Lincoln
Aug. 1995 to May 1999	**B.A. in Mathematics and German** University of Nebraska, Lincoln Minors: Physics and Economics Thesis Topic: Finite difference methods for contaminant transport in aquifers Advisors: Professor J. David Logan Professor Steven Cohn highest distinction (summa cum laude), honors program

RECENT EXPERIENCE:

Sept. 2003 to present	Graduate Teaching Assistant and Research Fellow Department of Mathematics University of California, Irvine
June 2000 to Sept. 2003	NSF Graduate Research Fellow Research and Teaching Assistant Department of Mathematics University of Minnesota, Twin Cities
June 2000 to Sept. 2001	Intern, fiber optics research group 3M, Saint Paul, MN
July 1999 to May 2000	NSF Graduate Research Fellow, Teaching Assistant Department of Mathematics and Statistics University of Nebraska, Lincoln
July 1998 to May 1999	Undergraduate Teaching Assistant Department of Mathematics and Statistics University of Nebraska, Lincoln

HONORS AND GRANTS:

2007 GAANN (Graduate Assistance in Areas of National Need) Fellowship
2007 University of California, Irvine Department of Mathematics Dissertation Fellowship
2006 University of California, Irvine Department of Mathematics Fellowship
2003 University of California, Irvine Department of Mathematics Research Fellowship
1999 NSF Graduate Research Fellowship
1999 Inducted Phi Beta Kappa
1998 Barry M. Goldwater Scholarship
1995 Regents Scholarship, University of Nebraska, Lincoln

PUBLICATIONS:

1. P. Macklin, *Nonlinear Simulation of Tumor Growth and Chemotherapy*, M.S. Thesis, University of Minnesota School of Mathematics (2003).

2. P. Macklin and J.S. Lowengrub, *Evolving interfaces via gradients of geometry-dependent interior Poisson problems: application to tumor growth*, J. Comput. Phys., 203 (1) (2005), pp. 191-220.

3. P. Macklin and J.S. Lowengrub, *An improved geometry-aware curvature discretization for level set methods: application to tumor growth*, J. Comput. Phys., 215 (2) (2006), pp. 392-401.

4. P. Macklin and J.S. Lowengrub, *Nonlinear simulation of the effect of microenvironment on tumor growth*, J. Theor. Biol., 245 (4) (2007), pp. 677-704.

5. H.B. Frieboes, J.S. Lowengrub, S. Wise, X. Zheng, P. Macklin, and V. Cristini, *Computer Simulation of Glioma Growth and Morphology*, NeuroImage, in press (2007).

6. P. Macklin, *Toward Computational Oncology: Nonlinear Simulation of Centimeter-Scale Tumor Growth in Complex, Heterogeneous Tissues*, Ph.D. Dissertation, University of California-Irvine Department of Mathematics (2007).

WORK IN PROGRESS AND IN REVIEW:

1. P. Macklin and J.S. Lowengrub, *A New Ghost Cell/Level Set Method for Moving Boundary Problems: Application to Tumor Growth*, J. Sci. Comput., in review.

2. P. Macklin, S.R. McDougall, A.R.A. Anderson, M.A.J. Chaplain, V. Cristini, and J.S. Lowengrub, *Nonlinear simulation of the effect of tumor growth on neovascular remodeling*, Bull. Math. Biol., in preparation.

3. J.S. Lowengrub and P. Macklin, *A Centimeter-Scale Nonlinear Model of Tumor Growth in Complex, Heterogeneous Tissues*, J. Math. Biol., in preparation.

4. P. Macklin, N.L. Komarova, and J.S. Lowengrub, *A Cellular Automata Study of the Effect of Neighbor Dynamics on Carcinogenesis*, in preparation.

RESEARCH INTERESTS:

continuum, cellular automata, agent, and hybrid modeling of tumor growth; healthy and pathological tissue modeling; tissue engineering; integrative biomathematical modeling; scientific visualization; mathematical biology; tumor-microenvironment interaction; multicomponent fluid flows; nonlinear simulation of free boundary problems; high performance computing

REFERENCES:

John Lowengrub (UC Irvine); Natalia Komarova (UC Irvine); Mark Chaplain (U. Dundee, Scotland)

SERVICE:

1. Developed and Maintained EasyBMP, an open source, cross-platform C++ bitmap (BMP) image library for industrial, educational, and academic use - http://easybmp.sourceforge.net (2005-present)

2. Developed and Maintained Easy BMP to AVI Movie Creator, an open source, cross-platform tool for converting images to movies, primarily for scientific visualization - http://easybmptoavi.sourceforge.net (2006-present)

3. Co-founded and Organized the UCI Mathematics Graduate Student Colloquium (MGSC) - http://math.uci.edu/mgsc/ (2006-2007)

INVITED TALKS:

1999 Workshop on Mathematical Methods in the Geosciences and Related Areas, University of Nebraska, Lincoln

2006 Mathematics Graduate Student Colloquium, University of California, Irvine

CONTRIBUTED AND OTHER TALKS:

1999 Second Annual Regional Workshop in Mathematics and Statistics, University of Nebraska, Lincoln

2005 The Modeling of Cancer Progression and Immunotherapy Workshop, American Institute of Mathematics (AIM), Palo Alto, CA

2007 Mathematical Modelling and Analysis of Cancer Invasion of Tissues Workshop, Dundee, Scotland

TECHNICAL AND OTHER SKILLS:

Programming and Software skills:

- C++ and OpenGL/GLUT, with emphasis on scientific and high-performance computing
- Cross-platform/cross-architecture software development
- Open source/collaborative software development
- 2D and 3D scientific visualization
- MATLAB, Maple, Mathematica, and other mathematics software
- GIMP, Inkscape, and other open source graphic editing software
- W3C standards-compliant HTML and CSS web authoring
- PHP webpage authoring

Other skills:

- Building and maintaining computers
- Wired and wireless networking and security
- Fluent spoken and written German
- Public speaking skills

Abstract of the Dissertation

Toward Computational Oncology: Nonlinear Simulation of Centimeter-Scale Tumor Growth in Complex, Heterogeneous Tissues

by

Paul Thomas Macklin

Doctor of Philosophy in Mathematics

University of California at Irvine, 2007

Professor John S. Lowengrub, Chair

In this dissertation, we present three increasingly sophisticated mathematical models of solid tumor growth and new numerical techniques for accurately and efficiently solving these models. In the first model, we simulate necrotic tumor growth into perfectly-vascularized, homogeneous tissue. We solve the model using a new level set/ghost fluid method that can produce accurate solutions on arbitrary domains, even when faced with challenging topological changes. This model provides a core framework for the development of more sophisticated models.

After a brief presentation of a new geometry-aware curvature discretization for level set methods, we focus on a second model where we now include nutrient perfusion and proliferative pressure dissipation in the tissue surrounding the tumor. Using this model, we conduct a thorough study of the impact of the tumor microenvironment on tumor growth. We find that three characteristic morphologies emerge that depend primarily upon the mi-

croenvironment: *invasive, fragmenting growth* into nutrient-poor tissue; *invasive, fingering growth* into nutrient-rich, biomechanically unresponsive tissue; and *compact/hollow growth* into nutrient-rich, biomechanically responsive tissue. We discuss the implications of this finding on anti-angiogenic and anti-invasive cancer therapies.

The third model treats tumor growth in complex, heterogeneous tissues using a nonlinear nutrient equation and a two-sided pressure equation with geometric jump boundary conditions. We solve the model using a new level set/ghost cell method that can accurately and efficiently solve nonlinear elliptic PDEs on large, complex domains, even with geometry-dependent jump boundary conditions. After testing the new technique, we simulate the growth of *glioblastoma* (an aggressive brain tumor) in a large, 1 cm square of brain tissue that includes heterogeneous nutrient delivery and varied biomechanical characteristics (white and gray matter, cerebrospinal fluid, and bone). We observe growth morphologies that are highly dependent upon the variable tissue characteristics–an effect observed in real tumor growth.

We close with a discussion of ongoing research, possible future extensions, the potential implications of our work, and the long-term goals of computational oncology. We outline some of the key mathematical, scientific, computational, and clinico-medical challenges that must be overcome before computational oncology can be accepted as a clinical tool for patient-tailored cancer therapy.

Chapter 1

Introduction to Cancer Biology

While cancer has been known even since early civilizations (Franks and Knowles, 2005), our scientific understanding of cancer has only progressed relatively recently with the development of modern investigational tools and techniques. In the late 18th century, Percivall Pott conducted a pioneering epidemiological study of the high incidence of cancer in chimney sweeps in the United Kingdom that established a positive link between chimney soot and scrotal cancer, marking the discovery of the first carcinogen (Pott, 1775; Dobson, 1972). Studies of families with high cancer rates (such as breast cancer) suggested that the risk for cancer could be inherited, and while the structure of DNA would remain unknown for several decades, it was postulated that cancer may be related to the function of genes. (e.g., see the discussion of the 19th century neurologist Pierre Paul Broca in Lynch et al. (1972)). In the early 20th century, it was discovered that cell lines infected with a virus developed cancer. (See the discussion in Farrell (2005) of the 1908 discovery of an infectious chicken leukemia, as well as the 1910 discovery a virus-induced avian sarcoma by Rous (1910).) Because viruses were known to inject genetic material into cells, this was further evidence that cancer may be a genetic disease. Later, as the structure of DNA was understood and genetic testing techniques were improved, specific cancer genes were isolated and the genetic role in cancer was confirmed. In the 1990s, the pace of discovery was hastened as the human genome project concluded and genomic mapping techniques improved by orders of magnitude. Never before has a greater wealth of information on the innermost workings of the cell been available, raising the possibilities of understanding cancer on a genetic and molecular level and developing rational drugs for treatment.

Nevertheless, cancer remains a great medical and societal problem, particularly as

the average human lifespan increases. Improved drugs and therapies, the result of the substantial biological understanding of cancer genetics, have improved the prognosis for cancer treatment and even cured specific cancers, but many other cancers remain difficult to treat, and inspired treatment ideas have sometimes only marginally improved patient survival. (e.g., see the discussion of two decades of glioblastoma multiforme treatments in Brandes (2005).) The greater the understanding of cancer and its interaction with the human body and its systems, the clearer it has become that cancer is a complex problem that cannot be solved without due consideration of the entire system.

In this dissertation, we shall develop mathematical and computational tools capable of examining the complex interaction between solid tumors and their host microenvironment and explore the impact that such tools could have on the development of improved, long-term treatment protocols.

1.1 Noncancerous Tissue and Carcinogenesis

Most simply stated, cancer occurs when defective genes cause cells to malfunction and interact with the body in an aberrant, proliferative manner. It is therefore natural to begin by examining the normal function of noncancerous cells and tissue, followed by an examination of how a breakdown of cellular machinery can lead to cancer.

1.1.1 The Structure and Function of Noncancerous Tissue

A *tissue* is a collection of interconnected cells that together perform a similar function. There are four main types of adult tissue: *epithelium* is tissue composed of sheets of specialized cells that perform a specific function; *connective tissue* consists of a combination of extracellular matrix (fibronectin, collagen fibers, etc.) and fibroblast cells that create the matrix; *muscle tissue* includes not only contractile tissue, but also blood, immune cells, cartilage, and bone; and *nervous tissue*, which makes up the bulk of the brain and the nervous system. The term *mesenchyme* is often used to refer to all supporting tissues collectively, including connective tissue, muscle, and bone. The epithelial cells that comprise the functional element of an organ are sometimes called the *parenchyme*.

Organs are made of one or more of these tissue types and have a standard structure: a layer of epithelium consisting of specialized cells (e.g., pancreatic islet cells) that perform the actual function of the organ, supported by a layer of connective tissue (often called

the *stroma*). The connective tissue is interlaced by blood vessels, nerves, and lymphatic vessels, and it may rest on an additional layer of muscle or bone, depending upon the organ. Collectively, the non-epithelial layers make up the mesenchyme of the organ. A thin, semi-permeable *basement layer* (also referred to as the *basal lamina*) separates the epithelium from the mesenchyme. See Figure 1.1.

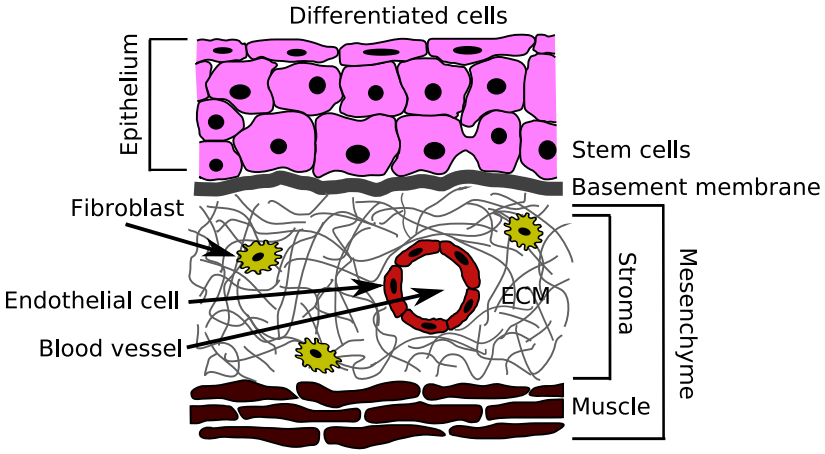

Figure 1.1: Typical mammalian tissue organization, including epithelium and mesenchyme.

To maintain this complex structure in *homeostasis*, the population of each cell type must be rigorously maintained, and so cellular proliferation and apoptosis (programmed cell death) are balanced. Whenever a differentiated cell dies, it must be replaced. A *somatic* (adult, non-germline) stem cell senses the loss of the cell and divides either symmetrically into two new stem cells or asymmetrically into a stem cell and a *progenitor cell*. The progenitor cell either further divides or terminally differentiates into the desired cell type, which must then migrate to the correct position and assume its function. This entire process is tightly regulated by a complex system of biochemical signals (growth factors) that are secreted and sensed by all the cells in the structure. The proper response of each cell to the signals it receives is governed by the activation of receptors on its surface, which then trigger the activation and/or deactivation of genes within the nucleus (*epigenetic* events, or changes to the gene expression). The activated genes then direct the production of proteins within the cell that regulate cell function as well as the cell cycle. There is a building body of evidence that the stromal cells play a great role in properly regulating the activity of stem cells and the differentiation of progenitor cells by creating and responding to growth

factors and other chemical signals (Lotem and Sachs, 2006; Nelson and Bissell, 2006; Zipori, 2006).

For further information on tissue and organ structure, please see Franks and Knowles (2005) and the references therein. The review by Blanpain and Fuchs (2006) gives an excellent overview of (epidermal) stem cells. The work by Zipori (2006) also includes a discussion of the origin of somatic stem cells and relates them to embryonic development. The review by Nelson and Bissell (2006) provides an interesting discussion on the role of signaling between cells and the microenvironment in determining and maintaining tissue architecture.

1.1.2 The Cell Cycle

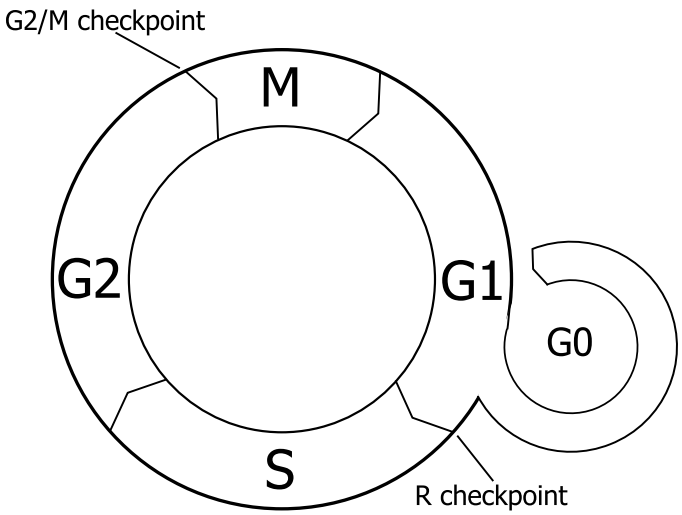

Figure 1.2: The cell cycle.

All dividing human cells proceed through the *cell cycle*, a highly regimented series of stages involving the growth and eventual division of the cell. In the first stage in the cell cycle, G1 (gap 1), the cell physically grows, proteins are synthesized, new organelles are constructed, and the cell prepares for DNA replication. In the following S (synthesis) phase, the DNA is copied, and in the G2 (gap 2) phase, final preparations are made within the cell nucleus for the division of the DNA. In the final M (mitosis) phase, the two copies of the DNA are separated into two nuclei (*mitosis*), and the cytoplasm and the organelles are divided into two daughter cells (*cytokinesis*). See Figure 1.2.

A cell's progress through the cell cycle is regulated by the production and balance of internal chemical signals, which can be divided into two classes: *cyclins* and *cyclin-dependent kinases* (CDKs). The balance of production of these chemicals controls the speed of progression through the cycle. Receptors on the cell's surface control the gene expression levels through complex signaling pathways. The gene expression pattern, in turn, determines which biochemicals (including cyclins and CDKs) are produced and in what balance, and thus the rate of progression of the cell cycle is determined through a complex interaction between the internal biomachinery of the cell and its surrounding neighbors (Clyde et al., 2006).

The stages in the cell cycle are divided by numerous checkpoints, each of which is designed to check for critical errors and/or malfunctions of the cell, provide opportunities to repair damage to the DNA, and control the pace of progression through the cycle. One major checkpoint is the R (restriction) checkpoint late in the G1 phase, where the cell either commits to division (and progresses to the S phase) or exits the cell cycle (Zetterberg et al., 1995; Blagosklonny and Pardee, 2002). The majority of human somatic cells reside in this "resting" or quiescent cycle, which is denoted G0. There are numerous checkpoints in the S and G2 phases to detect and repair DNA damage, the most of important of which governs the progression from G2 into the M phase. See Figure 1.2.

Because the checkpoints are responsible for controlling the progress of the cell toward eventual cell division, they are of critical importance to cancer. The R checkpoint is of particular significance: prior to reaching the checkpoint, environmental stimuli can push a cell into the quiescent G0 state; after the R checkpoint, the cell tends to be less responsive to extracellular signals, as it is irreversibly committed to division (Sherr, 1996). Indeed, some very important cancer genes, such as the *Rb* tumor suppressor gene, are directly tied to the function of the R checkpoint (Classon and Harlow, 2002). The remaining checkpoints are primarily relevant to cancer in that they can induce apoptosis if the DNA is sufficiently damaged, and the failure of a checkpoint can lead to increased genetic instability (Clyde et al., 2006).

1.1.3 Oncogenes and Tumor Suppressor Genes

Key to maintaining healthy adult tissues and organs is the correct receipt and interpretation of growth and inhibitory signals by each cell. Often, the cell receives both

growth-promoting and -inhibiting signals, and the final behavior of the cell is determined by the balance of the signals and the resulting gene expression pattern. Of all the genes contained in the genome, two types are particularly relevant to the regulation of cellular proliferation. *Oncogenes* respond to or create growth signals and promote the progression of the cell cycle and cell division. *Tumor suppressor genes* (TSGs) respond to inhibitory signals, retard or halt the cell cycle, ensure the proper repair of damaged genes, and may prompt the cell to self-destruct (*apoptose*) under certain circumstances. Cancer initiation, or *carcinogenesis*, starts with the malfunction of one or more of these genes (Hanahan and Weinberg, 2000).

Some genetic mutations in oncogenes can result in their *overexpression*. This can occur in a variety of ways. If errors occur during cell division (e.g., during the M phase), a daughter cell may mistakenly receive extra copies of an oncogene, an error that is known as *aneuploidy*. (For example, see Calcagno et al. (2006), Castro et al. (2006), and Fogarty et al. (2007).) An uncorrected single point mutation (e.g., during the S phase) can affect the function of an oncogene (Malumbres and Barbacis, 2001). Errors during cell division may create a mutant fusion gene, where the protein coding portion of an oncogene is mistakenly fused with the triggering portion of another, frequently expressed gene. As a result, signals originally intended for the frequently expressed gene are misrouted to the oncogene. (For an example of this phenomenon, see Küppers and Dalla-Favera (2001), which describes the activation of the *MYC* oncogene by translocation with an immunoglobulin gene.)

Likewise, genetic mutations in tumor suppressor genes can result in their *underexpression*. Damage to the protein coding portion of the gene can render it incapable of creating functional proteins; in some cases, a single point mutation can be disable a gene (Horowitz et al., 1989). During cell division, one of the daughter cells may fail to inherit one or both copies of a TSG. Because normal cells possess two copies of each gene, both copies must be damaged for a total loss of function of the gene. This is known as the Knudson two-hit model (Knudson, 1971, 2001), which was formulated when studying retinoblastoma in children and eventually led to the discovery of the *Rb* tumor suppressor gene by Friend et al. (1986). The mutation rate depends upon many factors, but because damage to any base pair of the gene could potentially disable it, the probability of damage to a TSG increases with the size of the gene. If the probability of losing one copy of a TSG due to a point mutation is p, then the probability of losing both copies is p^2, which is exceedingly small. However, *loss of heterozygosity* (LOH), in which two copies of the damaged TSG

are passed to a daughter cell, can result in a significantly higher probability of losing both copies (Nowak et al., 2002). Furthermore, more recent work suggests that the loss of just one TSG copy (*haplo-insufficiency*) can significantly impair the tumor suppressing activity of a TSG and increase the probability of completing a multi-step carcinogenesis pathway (Quon and Berns, 2001).

1.1.4 DNA Repair and the Role of Genetic Instability

To protect against uncontrolled cellular proliferation due to damaged tumor suppressor genes and oncogenes, normal cells possess numerous DNA repair pathways. If an error is detected during DNA replication, the process is halted until the error can be repaired. If an error is detected at any other time, the cell cycle is arrested until the error can be repaired, and if repair is impossible, apoptosis is triggered. Of particular significance is the G2/M checkpoint, which provides an opportunity for DNA repair prior to mitosis in the M phase. Tumor suppressor genes such as *BRCA1* play an important part in regulating the G2/M checkpoint (Yarden et al., 2002).

The genes responsible for DNA repair (generally TSGs) can be damaged, leaving a cell more vulnerable to further genetic damage. In these circumstances, the cell may experience *genetic instability*, where more frequent genetic mutations occur and are allowed to accumulate. The increased rate of genetic mutation increases the probability of damaging a tumor suppressor gene, creating a fusion oncogene, duplicating oncogenes, or creating mutations favorable to carcinogenesis. In fact, many advanced tumors demonstrate genetic instability, which indicates a potentially important role (Nowak et al., 2002).

1.1.5 Causes of Genetic Damage

Because the genome is encoded as a long sequence of nucleosides (DNA bases) fused to a sugar-phosphate backbone, it is susceptible to damage by altering the chemical bonds between the molecules or by altering the molecules themselves. Generally, this can occur by exposure to chemicals that react directly with either the nucleosides or the sugar-phosphate backbone of the DNA, or by encountering increased energy that reacts with the tissue to create reactive chemical species that interact with the DNA.

Chemicals that can directly or indirectly damage the DNA are known as *carcinogens*. For instance, when arsenic is metabolized, several reactive oxygen species (ROS) can result,

including peroxyl radical, superoxide radical, and hydroxl radical (Yu et al., 2006). These can lead to the formation of DNA *adducts*, where the radicals (or other mutagens) bind to either the sugar-phosphate backbone or the nucleotides. These DNA adducts can often twist and deform the DNA, thereby altering the sequence of the amino acid base pairs, sometimes in ways that cannot be repaired by the cell's DNA repair machinery. Benzopyrene, a mutagen in tobacco smoke, is also known to create DNA adducts (Sadikovic and Rodenhiser, 2006). Other chemical-induced DNA damage mechanisms include single strand breaks (SSBs), double strand breaks (DSBs), and DNA mismatch (mismatch between the nucleotides in a base pair), for instance. The topic of the specific types of DNA damage and repair is too extensive for review in this dissertation; the reader is encouraged to consult the review in Köberle et al. (2005).

Other DNA damage is not caused directly by chemicals encountered in the environment, but rather by excess energy that can either alter the chemical bonds or introduce reactive chemical species. Ultraviolet radiation in the 280-320 nm range (UVB) and 320-400 nm range (UVA) can damage the DNA in several ways. When the UV radiation reacts with biological molecules, it can create ROS that damage the DNA and other phospholipid structures in the cell. UV radiation can also interact directly with the DNA by exciting new bonds between adjacent base pairs, thereby distorting the structure of the DNA molecule. Both UVA and UVB radiation can create mutagenic bipyrimidine *photoproducts* by creating bonds between adjacent pyrimidine (thymine/T and cytosine/C) bases (Douki et al., 2003). When unrepaired, these lesions can lead to C to T and CC to TT mutations, as well as possible A insertion mutations. An excellent overview on the effects of UV radiation on the skin, including DNA damage, can be found in Matsumura and Ananthaswamy (2004).

The depth of penetration by UV radiation increases as the wavelength decreases: UVB radiation cannot penetrate past the epidermis (the upper layer skin), whereas UVA radiation from 340 to 400 nm affects the basal cell layer (on the boundary between the epidermis and the dermis), and UVA from 320 to 340 nm acts deeper in the dermis. (e.g., see Matsumura and Ananthaswamy (2004).) Other (ionizing) radiation of shorter wavelengths can penetrate and affect deeper cells, and due to the shorter wavelengths, impart more energy. Ionizing radiation of sufficient strength, such as X-ray radiation (0.01-10 nm wavelength), can interact with tissue anywhere in the body and damages the DNA in several ways. First, the energetic photons can damage the sugar-phosphate backbone to cause DSBs. Alternatively, photons can strike and damage the DNA base pairs, which can then bond with

neighboring base pairs and distort the DNA structure (e.g., form bipyrimidine products). Secondly, when the photons strike the DNA and cause initial damage, energetic electrons and reactive chemical species (such as ROSs) can be ejected, and these interact with nearby DNA base pairs to cause additional damage (Elshaikh et al., 2006; Gudkov and Komarova, 2003). It is not uncommon to find multiple DSBs within several base pairs' distance, or a combination of DSBs and adjacent base-pair bonds (Kiltie, 2005). As a result, the DNA damage is more complex and can be more difficult to repair than in UV and chemical carcinogenesis.

Pathogens can also damage the integrity of the genome. Because DNA viruses insert their own DNA into the host cell, cellular function is altered. Sometimes, the inserted genetic material can lead to the disabling of a TSG or the creation of an oncogene. For example, the human papilloma virus (HPV) inserts viral DNA sequences that inhibit TSG function. In particular, higher-risk HPV variants (e.g., HPV16) insert the viral *E6* oncogene, whose associated E6 protein binds and inactivates the pRb protein (Sdek et al., 2006). The viral *E7* oncogene creates the E7 protein that binds to the p53 protein. Both *p53* and *Rb* are important in regulating the R and G2/M checkpoints, arresting the cell cycle when DNA damage is detected, and committing the cell to apoptosis when necessary (Eguchi et al., 2007; Sdek et al., 2006). The loss of *Rb* function can also lead to gross chromosomal mutations, such as centrosome amplification and aneuploidy, and indicates chromosomal instability (Iovino et al., 2006).

Lastly, we note that some deficient genes may be inherited, rather than obtained through genetic damage. Some families may observe an increased incidence of particular types of cancer, and this generally is the result of inheriting one or more defective tumor suppressor genes. This yields a shortcut in the Knudson two-hit model, in that fewer genetic mutations are necessary for loss of function of a particular TSG. The specificity of familial cancer tendencies arises from the fact that different cells types each depend on specific TSGs for proper regulation of proliferation. For instance, inheriting a defective copy of the *Rb* gene increases the risk of retinoblastoma, and inherited defective copies of the *BRCA1* gene increase the risk of breast cancer (Miki et al., 1994).

1.1.6 Changes in Gene Expression

The gene expression pattern is important in maintaining the proper balance of pro- and anti-growth signaling within a cell as well as the status of the cell cycle. Recently, research has begun to examine the over- and underexpression of genes, rather than outright genetic damage, as a potential contributor to unchecked cellular proliferation. Because gene expression patterns are heritable, changes in the gene expression can potentially affect the malignant transformation of a cell (e.g., by disabling a tumor suppressor gene) in the same way as a genetic mutation (Jones and Baylin, 2002).

Several biochemical processes are used to control the level of gene expression within a cell. Of particular importance is DNA methylation, where methyl groups (CH_3) are attached to the DNA to prevent the activation and transcription of specific genes. During early embryonic development, the entire genome is demethylated in all the embryonic cells, thereby allowing the cells to differentiate according to their destined location and function (Reik and Walter, 2001). Thus, methylation plays a role in deactivating undesired genes in specialized cells and is crucial to proper function. Recent work has shown that many human cancers are globally hypomethylated (i.e., previously silenced genes have become transcriptionally active) with localized hypermethylation (e.g., deactivated tumor suppressor genes), suggesting an important role for methylation in carcinogenesis as well (Jones and Laird, 1999; Jones and Baylin, 2002; Lotem and Sachs, 2006). DNA hypomethylation may also lead to increased chromosomal instability, which can accelerate carcinogenesis through increased genetic mutation. Interestingly enough, methylation can also affect the susceptibility of cells to genetic damage; methylated cytosine (C) has a shifted absorption band into the UV range of sunlight, thereby increasing the risk of mutations that could result in skin cancers (Jones and Baylin, 2002).

As was mentioned in an earlier section, gene expression is also controlled by the level of activation of cell surface receptors by various signaling factors. Internal chemical levels can also affect gene expression patterns, regardless of surface signaling. In particular, all cells continuously create hypoxia-inducible factor (HIF) molecules (e.g., HIF-1α), which are ordinarily degraded in the presence of oxygen molecules. However, when a cell experiences hypoxia (a lack of oxygen), the HIF-1α molecules are no longer degraded and are allowed to carry out their function in activating certain "survival" genes in the cell, particularly those that decrease cell-cell and cell-ECM adhesion, increase motility, secrete angiogenic growth

factors, and allow for glycolysis (an inefficient metabolism attained by reacting glucose with glucose, rather than oxygen) (Harris, 2002; Zagorska and Dulak, 2004; Allen et al., 2006; Pouysségur et al., 2006).

Lastly, we note that the biochemistry of gene expression is very complicated and involves means other than DNA methylation. For an excellent review on epigenetics, please see Ducasse and Brown (2006).

1.1.7 When Everything Goes Wrong: Carcinogenesis

Carcinogenesis is a multistage process. Mutation and epigenetic events are exceedingly rare (on the order of 10^{-7} per cell division), but given enough time, one of these rare events will activate an oncogene or silence a tumor suppressor gene in one of the human body's approximately 10^{14} cells. If the cell survives and the mutation escapes its DNA repair mechanisms, it may eventually acquire another mutation. Over time, the cell (or its descendants) can acquire a sufficient number of genetic mutations to ignore growth-inhibiting signaling from its neighbors, bypass its internal controls and checkpoints, and form a colony (i.e., a tumor) of rapidly proliferating, aberrant cells. If the microenvironment is conducive, the colony will have a relative survival advantage over the surrounding, normal cells. This accumulation of sufficient genetic damage marks the beginning of cancer, and the rapid expansion of the mutated cells is known as *clonal expansion*. The dynamics of the spread of a mutation throughout a fixed tissue population is a rich topic of active research. An excellent discussion of the process can be found in Wodarz and Komarova (2005). Generally, the process takes tens of years to progress, but it can be accelerated by chronic exposure to carcinogens. If the mutated cells arose from the epithelium, the resulting cancer is referred to as a *carcinoma*, and if the tumor originated in stromal/mesenchymal cells, it is a *sarcoma*.

Ordinary, differentiated somatic cells are not immortal: they can only divide a limited number of times before they reach *senescence*, the point at which the cell is no longer allowed to divide, but instead either enters cell cycle arrest or commits apoptosis. Only stem cells have the capacity for unlimited division. Thus, for a differentiated somatic cell to mutate and give rise to a cancer, it must regain its capacity for unlimited division through additional mutations, i.e., become like a stem cell. There is a building body of evidence that cancer arises not from differentiated somatic cells, but rather from mutated somatic stem

cells (Beachy et al., 2004; Lotem and Sachs, 2006; Sharifi et al., 2006). In this scenario, cancerous stem cells divide into both cancerous stem and differentiated somatic cells, with the cancer stem cells making up a small percentage of the tumor cell population. At a tissue scale, both models yield the same phenomenon: a mass of rapidly proliferating cells.

1.2 Avascular Solid Tumor Growth

Once a tumor has established a foothold in its host tissue, it begins an early period of rapid growth as it becomes an *in situ* cancer. We now discuss the major aspects of this stage of cancer.

1.2.1 Interaction with the Microenvironment

As the nascent tumor grows in its host tissue, it interacts with the surrounding microenvironment in a variety of ways. It mechanically displaces and compresses the surrounding tissue, including membranes and the pre-existing vasculature. The tumor degrades and remodels the extracellular matrix (ECM), both biomechanically (e.g., by strain) and biochemically by the secretion of matrix degrading enzymes (MDEs) such as matrix metalloproteinases (MMPs) that degrade the ECM. The degradation of the ECM, in turn, can release ECM-associated growth factors that fuel further tumor growth (Sun and Zhang, 2006). The degradation of the ECM by the MDEs increases increases the ability of the tumor to push into the surrounding tissue, both by reducing the mechanical rigidity of the surrounding tissue and by creating extra space for the growing tumor (Hotary et al., 2003). The combination of proliferation-induced pressure and proteolytic degradation of the surrounding tissue results in *tissue invasion*: the invasion of sheets or fingers of tumor cells into the surrounding tissue along paths of least mechanical resistance. Interestingly, while proliferation-induced pressure has received little study in the reductionist, cell- and genetics-oriented approach to cancer research, it may have the greatest impact on invasion by carcinoma. (See the discussion by Hart (2005), for instance.)

Lastly, we note that there is recent evidence that the tumor induces epigenetic changes in the surrounding stroma that are conducive to continued tumor growth (Hu et al., 2005; Zipori, 2006). For instance, carcinomas may release signaling molecules (e.g., interleukin-1β, or IL-1β) that stimulate the overexpression of hepatocyte growth factor (HGF) in fibroblast cells in the stroma. The HGF, in turn, acts as a growth-promoting factor in the

tumor cells, decreases cell-cell adhesion, and increases the secretion of MMPs (Matsumoto and Nakamura, 2006). There is also evidence of tumor-induced epigenetic changes in the surrounding non-neoplastic epithelial cells (Ishii et al., 2007).

1.2.2 The Limiting Role of Nutrient Diffusion, Hypoxia, and Necrosis

In this early stage of cancer, the tumor has no vascular system of its own, and so it must rely upon the host tissue for the delivery of crucial nutrients (e.g., oxygen and glucose) and growth factors via diffusion. Nutrients diffuse from the surrounding vascularized tissue, enter the tumor, and are uptaken by proliferating tumor cells. Of particular importance is the diffusion of oxygen, which generally diffuses on the order of 100-200 μm into tissue before dropping to levels insufficient for cellular metabolism (Carmellet and Jain, 2000; Cristini et al., 2003; Fischer et al., 2005; Macklin and Lowengrub, 2005, 2007). When a tumor grows sufficiently large, on the order of 100-200 μm in radius, oxygen can no longer reach the center of the tumor, as outer proliferating cells uptake the oxygen for use in metabolic activity. Therefore, a *hypoxic* region forms in the center of the tumor. (See Figure 1.3.) At this stage, however, the rapid proliferation of cells on the tumor boundary continues to increase the overall volume and size of the tumor.

As the tumor continues to grow, the size of the hypoxic region increases, and oxygen levels continue to drop in the center. When oxygen levels have dropped to critically low levels, the hypoxic cells begin to die in a process known as *necrosis*. (See Figure 1.3). As opposed to apoptosis, necrosis is a relatively uncontrolled process. The contents of the cell, including the organelles and any biological chemicals and growth factors, are not disposed of properly by the cell, but instead are released into the microenvironment and slowly degraded over time. Water content and cellular material eventually escape through the interstitial spaces in the tumor, diffuse through the tissue, and are removed by macrophages (a particular kind of white blood cell). Through this process, the tumor begins to lose volume, and as the size of the necrotic core grows with the tumor, the rate of volume gain from proliferation eventually balances with the rate of volume loss from necrosis. This leads to a halt in the growth of the tumor at a characteristic size of 1-2 mm in diameter.

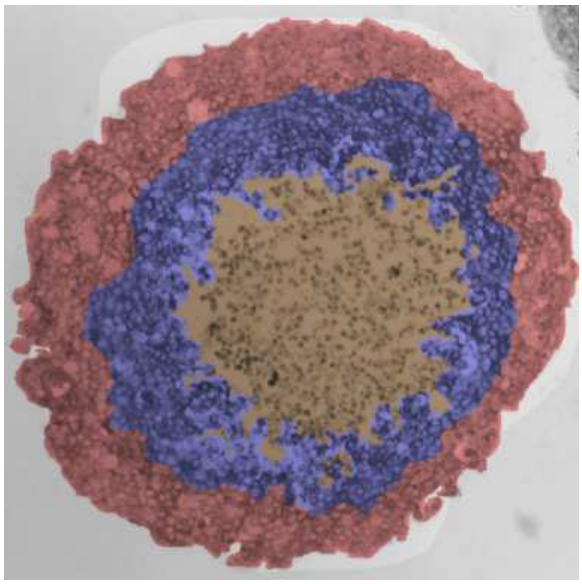

Figure 1.3: T47D tumor spheroid displaying the characteristic viable rim (red), hypoxic region (blue), and necrotic core (brown). Original image from Owen et al. (2004) and postprocessed and recolored by Paul Macklin to emphasize the regions.

1.3 Vascular Tumor Growth and Metastasis

The next stage in cancer development can be viewed as a response to the hypoxia and nutrient diffusional limits encountered during avascular growth. The ultimate result is *angiogenesis*, where the tumor induces endothelial cells (ECs) to form a new vasculature that directly supplies the tumor with the nutrients necessary for further expansion. Some of the same mechanisms responsible for angiogenesis play a role in *metastasis*, the spread of tumor cells to distant locations. We now discuss these aspects of advanced cancer development.

1.3.1 Angiogenesis

Hypoxia triggers a number of biological changes in human and animal cells. Hypoxia inducible-factors, such as HIF-1α, are created within cells regardless of the oxygen levels. Under normoxic conditions, HIF-1α is inactivated; under hypoxic conditions, HIF-1α accumulates in the cell and triggers numerous signaling pathways. In particular, genes that increase cellular motility are activated, and the hypoxic cell begins to secrete tumor angiogenic growth factors (TAFs) such as vascular endothelial growth factor (VEGF) (Zagorska

and Dulak, 2004; Kaur et al., 2005; Allen et al., 2006; Pouysségur et al., 2006). These TAFs diffuse outward from the hypoxic regions of the tumor and eventually reach nearby blood vessels. We note that in cancers with a mutated *VHL* tumor suppressor gene, HIFs may be overexpressed even in normoxic conditions (Rini and Small, 2005).

Blood vessels are composed of tightly connected squamous endothelial cells that are surrounded by a basement membrane as well as other supporting cells, including smooth muscle cells and pericytes (Loureiro and D'Amore, 2005). When the endothelial cells detect the TAF gradient emanating from the tumor, they begin to secrete matrix degrade enzymes that break down the basement membrane and the extracellular matrix (Ausprunk and Folkman, 1977). This allows the endothelial cells to migrate away from the blood vessel and toward the TAF source in the tumor. The original migrating endothelial cells are referred to as *sprout tips*; immediately behind the sprout tips, other endothelial cells divide, migrate, align, and form tubes of polarized endothelial cells surrounding a vascular lumen (Nakatsu et al., 2003). The vessels then link with other new vessels to form a network of loops in a process called *anastomosis*. It can take on the order of 10 to 21 days for new vessels to form and connect to the parent vessels (Gimbrone et al., 1974; Ausprunk and Folkman, 1977; Muthukkaruppan et al., 1982).

The end result is a *neovasculature* that provides the tumor with a direct supply of oxygen and other nutrients. The eventual configuration of the neovasculature is determined by the balance of pro- and anti-angiogenic growth factors, as well as by the mechanical pressures from the growing tumor and flow stresses within the nascent blood vessels (Lehoux and Tedgui, 1998; Taber, 1998; Quick et al., 2000; Godde and Kurz, 2001; Fisher et al., 2001). With this fresh supply of nutrients, the tumor can now begin a new stage of rapid growth into the surrounding tissue.

Angiogenesis is not unique to tumor growth, but is also a key part of wound healing, the female menstrual cycle, and embryonic development (Carmellet and Jain, 2000; Fischer et al., 2005). However, we note that tumor angiogenesis is pathological in nature, and the resulting vasculature is inefficient in a number of ways: the vessels are often "leaky" due to large gaps between endothelial cells; the newly formed vessels are not as stiff and rigid as mature vessels and may collapse when subjected to tissue stress (such as that created by rapidly growing tumors); the basement membrane that forms outside the vessels may not be fully formed; some of the newly formed vessel walls may be composed of a mosaic of tumor and endothelial cells; and the tumor neovascular network tends to be much more

tortuous than regular vascular networks (Folkman, 1995; Carmellet and Jain, 2000). This inefficiency may hinder drug delivery within tumors (Jain, 1990, 2001; Sinek et al., 2004), as well as lead to the development of new hypoxic regions within the tumor and additional sessions of angiogenesis.

1.3.2 Tissue Invasion and Metastasis

A particularly damaging aspect of advanced cancer is *metastasis*, the spread of tumor cells to form secondary tumors in distant locations. Metastasis occurs most commonly in breast, prostate, and lung cancers (Berenson et al., 2006), and it is estimated that over 90% of all deaths from solid tumors result from metastasis (Gupta and Massagu, 2006). In spite of the great clinical importance of metastasis, it is the most poorly understood aspect of cancer (Kaplan et al., 2006).

Metastasis is a complex phenomenon that involves several mechanisms that are closely related to tissue invasion. When coupled with genetic instability, intrinsic (e.g., senescence, telomere degradation) and extrinsic selective pressures (e.g., limited nutrients, the basement membrane, immune system attacks) lead to competition within heterogeneous tumor cell populations and the eventual selection for pro-metastatic genes (Gupta and Massagu, 2006). In particular, hypoxia creates a strong selective pressure, leading to increasing internal HIF-1α levels in the tumor cells and the expression of genes responsible for increased motility, glycolysis, reduced response to apoptotic pathways, and increased production of matrix degrading enzymes (Harris, 2002). The selective pressures also lead to increased expression of genes responsible for locomotion (Prall, 2007). As a result, tumor cells degrade the extracellular matrix and basement membranes, invade the stroma, and enter the vasculature, either individually, as small clumps of cells (emboli), or in cohort motion of sheets of cells linked by cell-cell adhesion (Nabeshima et al., 1995; Gupta and Massagu, 2006).

For sarcomas, which originate from mesenchymal cells that already reside in the stroma, this is accomplished by the proteolytic degradation of the ECM and the basement membrane surrounding the stromal capillaries, followed by direct entry into the capillaries. For carcinomas, which originate in epithelial cells that are separated from the stroma by a basement membrane, entry into the vasculature is often indirect via the lymphatic system (Elshimali and Grody, 2006). The mesenchymally-derived sarcoma cells move with built-in cellular machinery in a contractile, "amoeboid" manner: by first degrading the ECM on their lead-

ing edge, adhering to the ECM, and contracting, followed by rebuilding the ECM on the trailing edge (Vasko and Saji, 2007). Epithelial-derived carcinoma cells initially lack this locomotive ability, but genetic and epigenetic events can cause these tumor cells to regain these locomotive mechanisms; the process is often referred to as the epithelial-mesenchymal transition, or EMT (Prall, 2007; Vasko and Saji, 2007).

Once the metastatic tumor cells have reached the vasculature, they circulate in the blood. Initially, survival of the circulating tumor cells is inhibited by the immune system, which kills most of the individual cells; emboli consisting of 5 to 10 cells are more likely to escape attack by the immune system (Elshimali and Grody, 2006). We note that the role of the immune system is complex, is poorly understood, and may both promote and inhibit metastasis. Circulating tumor cells that do survive can eventually lodge in the capillary bed of distant organs; the most frequent destinations include the liver, lungs, and bones (Berenson et al., 2006).

However, without further tumor-host interaction, the destination microenvironment will not support the newly arrived metastatic tumor cells. Different types of tumor cells tend to metastasize to specific tissues, and the reasons for this are only now being elucidated in an emerging area of cancer research. This "seed and soil" idea, that only specific tissues are suitable to each tumor cell line, was first formulated by Stephen Paget in 1889 when studying breast cancer metastases (Paget, 1889; Dell, 1989; Mundy, 2002). The emerging theory is that tumors release cytokines, VEGF, and other chemical signals into the circulatory system that recruit progenitor and endothelial cells from the bone marrow and vasculature that assist in creating a *pre-metastatic niche*: a modified microenvironment in a distant host tissue that is suitable for metastasis by the tumor (Gupta and Massagu, 2006). In the process, the chemical signals cause epigenetic changes in the endothelial cells in capillary walls at the destination tissue, which then express additional adhesion molecules and secrete MMPs to degrade the basement membrane surrounding the capillaries (Hiratsuka et al., 2002; Elshimali and Grody, 2006; Kaplan et al., 2006). The increased expression of adhesion molecules on the inner surface of the capillary bed improves the ability of the metastatic tumor cells to arrest at the destination, and the degraded basement membrane assists in extravasation of the tumor cells from capillaries into the destination tissue.

Once the metastatic tumor cells successfully invade the destination tissue, they secrete growth factors that induce additional epigenetic changes in the new microenvironment. Growth in the new location is similar to the mechanisms of tissue invasion that were in-

troduced earlier, but with additional elements. Tumor-induced epigenetic changes in the stromal cells cause them to contribute to matrix remodeling and degradation, even as the tumor cells also secrete MMPs to degrade the matrix. Growth-promoting molecules that were previously sequestered in the ECM fuel further tumor growth (Elshimali and Grody, 2006). With ample room to grow and a favorable microenvironment, these tumor cells are able to develop into secondary tumors. Because the metastatic tumor cells have already been selected for their invasive phenotype, they are already capable of expressing pro-angiogenic growth factors to initiate angiogenesis and enter rapid, vascularized growth. The tissue specificity of this process is likely due to the combination and balance of cytokines and chemicals secreted by the tumors, which, in turn, depends upon the genetic and epigenetic makeup of the tumors (Slettenaar and Wilson, 2006). It is thought that only a small fraction of the cells in the primary tumor have the ability to recruit the proper progenitor and endothelial cells to build the pre-metastatic niche (Gupta and Massagu, 2006).

The scientific understanding of metastasis is advancing rapidly, and the reader is encouraged to read the reviews by Elshimali and Grody (2006), Gupta and Massagu (2006), Kaplan et al. (2006), and Palmieri et al. (2006). The reviews on bone metastases by Lipton (2004) and Berenson et al. (2006) provide well-written, concrete examples of the process, and they give an excellent overview of the state-of-the-art in metastasis research.

1.4 Mathematical Modeling Techniques

As we have seen, cancer spans a large range of problems, ranging in spatial scales from the biochemistry of DNA mutation (on the order of nanometers) to full tumor modeling on the centimeter scale. Consequently, a wide variety of modeling approaches are used to study these problems. We now discuss the most major approaches in use today. For further depth, see the reviews by Adam (1996), Bellomo et al. (2003), Araujo and McElwain (2004a), Byrne et al. (2006), Sanga et al. (2006), and Quaranta et al. (2005).

1.4.1 Cellular Automata and Agent-Based Models

Cellular automata (CA) models simulate uniformly spaced cells on a rectangular 2-D or 3-D grid, which are updated according to a set of biophysical rules. CA models are easy to implement, particularly due to the simple spatial arrangement and connection of the cells. As it is straightforward to translate biological processes (e.g., complex mutation

pathways) into new rules, CA methods have the benefit of being biologically-based. When combined with fields such as nutrient levels, CA models can be used to couple the cells to their environment. For some recent examples of CA-based modeling, see Kansal et al. (2000), Anderson (2005), and Mallett and de Pillis (2006).

Agent-based models are similar to CA models, with an important exception: the cells are no longer assumed to maintain a uniform, rectangular arrangement, allowing for the modeling of richer biomechanical couplings of cells and their environment. The cells are treated as distinct objects or agents and are allowed to move, divide, and die individually according to biologically-based rules. The agent interpretation of the cells makes modern object-oriented programming languages (e.g., C++ and Java) ideal for implementing these models.

Because both CA and agent-based models are based upon simple, easily implemented biological rules and can be made to incorporate complex biochemical machinery (e.g., cell receptor pathways), they are often preferred by biologists. CA models are well-suited to study mutation population dynamics and natural selection within tissues. Weaknesses of the CA approach include the uniform spacing assumption, and the difficulty of relating the cellular behavior to proliferation-induced biomechanical stress and pressure. In particular, the uniform spacing of the cells can make it difficult to model complex tissues and organs, where the various cell types have different arrangements within the tissue. (See Figure 1.1.)

Agent-based models are more ideal for situations of freely-wandering and nonuniformly arranged cells, such as angiogenesis, carcinogenesis, immune system attacks on tumor cells, and metastasis. The level of detail of the individual agents can be tailored to the simulation. Some agent-based models evolve the boundary shapes of the individual cells (e.g., see the cellular potts work by Mansury et al. (2002), Jiang et al. (2005), and Knewitz and Mombach (2006)), while others include models of the cell cycle (e.g., Zhang et al. (2007)) and gene expression and mutation patterns (Abbott et al., 2006). The flexibility of the level of detail, at times even down to the biochemical level, can make agent-based models easier to calibrate to biological data.

Both CA and agent-based models share some common weaknesses. Because the methods rely upon the discrete behavior of individual cells to determine emergent system properties, they can be difficult to analyze. Perhaps more importantly, the computational cost of the methods increases rapidly with the number of cells modeled, and in the case of agent-based models, with the complexity of each cellular object. This can make the models

difficult or impossible to implement without parallel computing when studying large systems. Nonetheless, some are making the attempt using cellular potts models, albeit on a very small scale (Alarcón et al., 2004).

1.4.2 ODE Methods

Ordinary differential equations (ODEs) have been used to model cancer for many years. (See the early work by Greenspan (1976) in modeling solid tumor growth.) ODE models are generally simpler to analyze and can provide early, useful results, particularly for liquid tumors (e.g., leukemia) where spatial dependencies are not as important. Unlike cellular automata and agent-based models, they are well suited to studying large cell populations. From a computational point of view, ODE models are the simplest and fastest to solve, allowing for extensive investigations of parameter spaces. However, the usefulness of ODE models is somewhat mitigated by the fact that they ignore spatial aspects of cancer that are of critical importance, such as inhomogeneous nutrient delivery, heterogeneous tissue structure, and angiogenesis. Furthermore, ODE models ignore stochastic effects (e.g., extinction) that may come into the play for small tumor cell populations. We note that some PDE models (see below) can be reduced to ODE models when considering special cases, such as spherical tumor growth.

ODE models are still being used with good success to model heterogeneous tumor population dynamics. For instance, Shuryak et al. (2006) recently used an ODE model to estimate the risk of leukemia due to radiotherapy. Piccoli and Castiglione (2006) recently used optimal control theory to analyze an ODE model of cancer vaccine dosing, while de Pillis et al. (2006) modeled combination chemotherapy/immunotherapy with a coupled system of ODEs.

1.4.3 PDE Models

Partial differential equation (PDE) models use systems of PDEs to simulate the spatiotemporal evolution of one or more key variables, such as oxygen, matrix degrading enzymes, and tumor angiogenic growth factors. Like ODE models, PDE methods are (computationally) well-suited to studying large cell populations and can be simpler to analyze than discrete models. The continuous nature of the PDEs makes them more ideal for incorporating larger-scale phenomena, such as tissue stress. However, because PDEs tend

to smooth regions, they can be poorly-suited to studying the motion of smaller groups of cells. Furthermore, because PDE models are generally phenomenological in nature, they can be more difficult to calibrate to biological data. We note that both linear and nonlinear PDE models (generally reaction-diffusion systems) are currently in widespread use in active research; we refer the reader to the introductory discussion in Chapter 4 for a discussion of past and present PDE cancer modeling efforts. This dissertation will focus on the use of PDE models to study tumor-microenvironment interactions with increasing complexity.

1.4.4 Stochastic Models

Stochastic models are often used to study carcinogenesis and population dynamics, particularly in the context of mutation pathways and natural selection. In this technique, cell birth, death, and mutation events are modeled as stochastic processes, either at a discrete level (see mutation modeling in CA and agent-based techniques) or as stochastic differential equations. Recent examples of stochastic modeling can be seen in an analysis of the two-hit model in colorectal cancer by Komarova and Wang (2004) and some novel investigations of optimal tissue design (with respect to preventing cancer) in Komarova (2005) and Komarova and Cheng (2006).

1.4.5 Hybrid Models

Sometimes, multiple techniques are combined to leverage their relative strengths and weaknesses. For example, Zheng et al. (2005), Frieboes et al. (2006a), and Macklin et al. (2007) combine cellular automata models of angiogenesis with PDE models of tumor growth to study tumor-induced angiogenesis. Another potential application is to use a PDE reaction-diffusion system to model tumor growth within a structure tissue, with the release of metastatic emboli modeled by agents. The immune system could also potentially be modeled individual agents interacting with a PDE-based model of tumor growth. Genetic instability within tumors could be modeled by coupling PDE models with cellular agents that are governed by stochastic differential equations. As future multiscale models of cancer emerge, hybrid techniques will likely be at the forefront of the effort.

1.5 Outline of the Dissertation and Summary of Advances

This dissertation is structured as a chronological ordering of papers that detail progress from 2003 to 2007 in modeling tumor growth in complex, heterogeneous tissues, along with the development of numerical techniques necessary for solving the formulated models. In Chapter 2, we present a level set model of tumor growth that we first studied in Macklin (2003) and Macklin and Lowengrub (2005). The level set model we describe is a reformulation of a model that was proposed by Cristini et al. (2003), and it was extended to include volume loss due to necrosis. The work in Chapter 2 forms the core upon which the rest of the dissertation builds and contains several advances. By reformulating the model in the level set context, we were able to simulate complex morphological changes in the tumor, including fragmentation and coalescence of fragments; earlier boundary integral work by Cristini et al. (2003) was unable to continue past such topological changes. By including the necrotic volume loss, we found that necrosis had a destabilizing effect on tumor morphology. The mathematical model we formulated and solved posed tumor growth as incompressible fluid flow in a porous medium (the extracellular matrix) and was challenging to solve numerically due to the curvature boundary conditions. To accurately solve the problem, we developed a new, higher-order ghost fluid method for solving (interior) linear elliptic problems on arbitrary domains. We also found that when two interfaces are in close contact, irregularity in the level set function contributes to inaccuracy in the standard normal vector and curvature discretizations, which can cause further inaccuracy in simulating the position of the tumor boundary. We solved this problem by introducing the first adaptive level set-based curvature and normal vector discretization. To improve efficiency and circumvent a prohibitive third-order ($\Delta t \sim \Delta x^3$) stability condition, we developed an accurate velocity extension technique based upon bilinear interpolation and a Gaussian filtration technique that eliminated numerical noise from the normal velocity. Our method tested second-order accurate, and there was excellent agreement between our results and the spectrally-accurate boundary integral results from Cristini et al. (2003). We used the new techniques to simulate long-time necrotic tumor growth and predicted the repeated encapsulation of non-cancerous tissue.

In Chapter 3, we present an improved adaptive curvature discretization for level set methods that we first introduced in Macklin and Lowengrub (2006). Our technique tested second-order accurate, even during complex morphological changes (such as the merger of

two fluid drops) where existing level set curvature discretizations failed. We briefly presented an extension of our tumor growth model to include interaction with the local microenvironment and used the new curvature discretization in long-time simulations of tumor growth into nutrient-poor, biomechanically responsive tissue. The results demonstrated repeated fragmentation of the tumor into multiple satellite tumors that invaded the surrounding tissue.

In Chapter 4, we conduct a detailed study of the impact of the microenvironment on tumor morphology using the numerical techniques from Chapters 2 and 3. We advanced the model to include nutrient diffusion and pressure dissipation in a small region surrounding the tumor (the microenvironment). The extended model included normal derivative jump boundary conditions of the form $[D\nabla\sigma \cdot \mathbf{n}] = 0$, which required extensions of our ghost fluid method. We presented a new discretization of this jump condition that was more stable than the original method presented by Liu et al. (2000). We presented the first detailed study of the impact of the microenvironment on tumor morphology, focusing in particular on the effects of nutrient availability (modeled by varying the external nutrient diffusivity) and the external tissue biomechanical responsiveness (modeled by the external cellular mobility). We found that while the tumor microphysical parameters (e.g., the nutrient uptake rate, sensitivity to necrosis, rate of degradation of the necrotic core) had a great impact on the quantitative aspects of the tumor progression, the microenvironment was the primary determinant of the tumor morphology. The tumor morphologies could be classified as according to three types: invasive, fragmenting growth into nutrient-poor tissue; invasive, fingering growth into nutrient-rich, biomechanically responsive tissue; and compact/hollow growth into nutrient-rich, biomechanically responsive tissue. These results helped to advance the mathematical modeling of tumor microenvironments at the macroscopic scale and provided new understanding of how the microenvironment might affect the response of a tumor to treatment, particularly anti-angiogenic therapy. Our results also suggested that anti-invasive adjuvant therapy could be effective when properly applied, particularly if it selectively increases tumor cell-cell and cell-matrix adhesion and does not alter non-cancerous cellular adhesion.

In Chapter 5, we present new numerical techniques that will be used in a new generation of tumor growth models. Our new ghost cell method includes the first ghost cell/ghost fluid discretization of the normal derivative jump boundary condition that does not numerically smear the jump in the tangential derivative jump, is easy to implement, and tests

better than 1.5-order accurate. By contrast, previous ghost fluid techniques by Liu et al. (2000) either fail to converge or are at best 0.3-order accurate, and other methods that properly treat the normal derivative jump boundary condition (e.g., the immersed interface method (LeVeque and Li, 1994) and the matched interface boundary method (Zhou et al., 2006; Zhou and Wei, 2006; Yu et al., 2007)) are much more complicated. We present a new iterative technique for solving nonlinear elliptic PDEs, along with a new approach to adaptivity that attains between a 10% and 50% reduction in computational time without the use of complex, adaptive meshes. We also present a new discrete approximation of the Heaviside function for level set methods that better preserves the local area of regions represented by level set functions and is both more accurate and computationally simpler than other Heaviside function approximations when applied to ghost fluid problems with jump boundary conditions. We apply the technique to Hele-Shaw-like flow in heterogeneous media and present a simulation of *glioblastoma* (an aggressive brain tumor) in a 1 cm square of brain tissue that includes heterogeneous nutrient delivery and varied biomechanical characteristics (white and gray matter, cerebrospinal fluid, and cranium), and we observe growth morphologies that are highly dependent upon variations in these tissue characteristics. The work in this chapter advances the state-of-the-art in level and ghost fluid methods and is a step toward modeling tumor growth in realistic tissues.

In Chapter 6, we discuss future extensions and applications of the mathematical model and numerical techniques that we developed in this dissertation, as well as potential clinical implications. We close by exploring the future of mathematical modeling of tumor growth in simulated human tissues and organs and outline several key modeling, scientific, computational, and clinico-medical advances necessary for ensuring the clinical relevance of mathematical oncology.

Chapter 2

Initial Tumor Growth Model

Note:

This chapter is based upon Macklin (2003) and Macklin and Lowengrub (2005), which can be accessed at http://dx.doi.org/10.1016/j.jcp.2004.08.010.

Chapter Abstract:

We develop an algorithm for the evolution of interfaces whose normal velocity is given by the normal derivative of a solution to an interior Poisson equation with curvature-dependent boundary conditions. We improve upon existing techniques and develop new finite difference, ghost fluid/level set methods to attain full second order accuracy for the first time in the context of a fully-coupled, nonlinear moving boundary problem with geometric boundary conditions (curvature). The algorithm is capable of describing complex morphologies, including pinchoff and merger of interfaces. Our new methods include a robust, high-order boundary condition-capturing Poisson solver tailored to the interior problem, improved discretizations of the normal vector and curvature, a new technique for extending variables beyond the zero level set, a new orthogonal velocity extension technique that is both faster and more accurate than traditional PDE-based approaches, and a new application of Gaussian filter technology ordinarily associated with image processing. While our discussion focuses on two-dimensional problems, the techniques presented can be readily extended to three dimensions. We apply our techniques to a model for tumor growth and present several 2D simulations. Our algorithm is validated by comparison to an exact solution, by resolution studies, and by comparison to the results of a spectrally accurate method boundary integral method (BIM). We go beyond morphologies that can be described by the BIM and present accurate simulations of complex, evolving tumor morphologies that demonstrate the repeated encapsulation of healthy tissue in the primary tumor domain– an effect seen in the growth of real tumors.

2.1 Introduction

The algorithms developed herein are motivated by our interest in modeling tumor growth and the morphological response of tumors to environmental stimuli and tissue inhomogeneity. Tumor growth is a fundamental scientific and societal problem. While much work has been done in the mathematics community on tumor modeling (e.g., see the recent review (Preziosi, 2003)), the state-of-the-art in modeling and numerical simulation lags behind the current understanding of the biophysical processes. The work presented in this paper is a step towards closing this gap and can be viewed as a building block towards a sophisticated virtual cancer simulator. In addition, the methods described in this paper have application beyond the tumor growth context and can be applied to general systems of coupled interior Poisson problems on a moving domain with geometric boundary conditions.

The tumor model we consider here was previously investigated by Cristini et al. (2003). This model is a reformulation of several classical models by Adam (1996), Byrne and Chaplain (1996b), Byrne and Chaplain (1996a), Chaplain (2000), Cristini et al. (2003), and McElwain and Morris (1978). A continuum-level description of tumor growth is used, and a sharp interface separates the tumor and healthy tissue. The tumor tissue is modeled as an incompressible fluid, and tissue elasticity is neglected. Cell-to-cell adhesive forces are modeled by a surface tension at the tumor-healthy tissue interface. The cell velocity is determined by Darcy's law, and growth occurs due to pressure gradients induced by mitosis (cell proliferation). A single nutrient (e.g., oxygen or glucose) is required for cell viability and mitosis. The nutrient diffuses through the tissue and is consumed by the tumor cells. This can limit the overall growth through the formation of a necrotic core (region of dead cells). Tumor cells die when the nutrient level drops below a critical level necessary for cell viability. This model is appropriate for characterizing solid tumors of sufficient size growing into soft tissue such as the brain. We note that discrete models such as cellular automata have been used to simulate tumor growth and are particularly applicable when the tumor boundary is fractal-like or diffuse (Kansal et al., 2000).

Currently, we do not model a number of important biophysical processes, including angiogenesis (the formation of new blood vessels), genetic mutations, different cell species, and more realistic tissue responses (e.g., viscoelastic). These effects can be included in our framework. In fact, there is very recent work by Zheng et al. (2005) that uses an adaptive level set method to simulate tumor necrosis, angiogenesis, and tissue invasion.

Genetic effects can be incorporated by including different cell species and by varying the biophysical parameters via a stochastic model. The different cell species can be included in this framework by introducing an interface for each species, which is straightforward in the level set approach taken in this paper.

In (Cristini et al., 2003), Cristini et al. presented the first nonlinear simulations of this continuum model of tumor growth using a spectrally-accurate boundary integral method. However, the boundary integral method does not allow for inhomogeneous microphysical parameters and is not well-suited to the complex morphological changes inherent in tumor evolution, including the pinchoff and coalescence of tumor tissue and the development and evolution of a necrotic core. The tumor model is a special case of a classical system of coupled interior Poisson and Poisson-like problems on a moving domain with geometric boundary conditions. The velocity of the domain boundary is determined from the normal derivatives of the solutions to the Poisson equations. Therefore, we sought to use a robust, second order accurate finite difference ghost fluid/level set method. The methods described in this paper are formulated for the classical system and thus can be applied beyond the tumor growth context.

Ghost fluid and level set methods have been applied with great success in a wide variety of physical applications (e.g. see the texts Sethian (1999) and Osher and Fedkiw (2002)). We first applied standard level set (Sethian, 1999; Osher and Sethian, 1988; Osher and Fedkiw, 2002), WENO (Jiang and Shu, 1996; Jiang and Peng, 2000), total variation diminishing Runge-Kutta (Gottlieb et al., 2001; Gottlieb and Shu, 1997), and ghost fluid methods (Glimm et al., 1981; Fedkiw et al., 1999; Liu et al., 2000; Gibou et al., 2003; Chen et al., 1997), as well as a standard PDE-based velocity extension (Zhao et al., 1996) to the tumor growth model. However, because the full moving boundary problem is sensitive to variations in the curvature, the speed can become noisy when even small perturbations in the level set function are present. For these equations, the dependence of the normal velocity upon the derivative of the curvature requires a severe third order CFL time step restriction (Cristini et al., 2003). Furthermore, we still obtained merely first-order to 1.6-order convergence, and the standard discretizations for the normal vector and curvature were highly inaccurate near merging interfaces.

To obtain full second order accuracy in space and time, we develop a new Poisson solver capable of capturing geometric boundary conditions on a complicated interface. We develop geometry-aware discretizations of the normal vectors and curvature that automati-

cally detect and cope with level set irregularity, particularly during morphological changes. We also develop new gradient and velocity extension techniques that take full advantage of the geometric information embedded in the level set function to obtain greater accuracy and faster computational speed than techniques currently in use. As a way to remove the high order time step constraint, Gaussian filtering is applied to remove small, high frequency perturbations before they pollute the numerical solution. This is computationally inexpensive, does not degrade the accuracy of the numerical solution, and allows a first order time step restriction.

Our Poisson solver, an extension of the ghost fluid method found in Liu et al. (2000), Gibou et al. (2003), and Gibou et al. (2002), retains all the qualities developed therein. In particular, we avoid the complication of solving on an irregular grid by solving on a simpler rectangular grid. The solution satisfies the boundary condition at the precise location of the interface, rather than at nearby nodes. The method is robust and allows a straightforward, dimension-by-dimension implementation, although a small consideration needs to be made for the interaction of spatial dimensions in one case. We present numerical evidence that strongly suggests our algorithm yields second order accuracy, even when applied to the full moving boundary problem with geometric boundary conditions (e.g., curvature). We note that Gibou and Fedkiw (2005) recently proposed an extension of the ghost fluid method that attains fourth-order accuracy on a fixed domain and third-order accuracy for the Stefan problem (on a moving boundary) without curvature-dependent boundary conditions (i.e. zero surface tension).

The outline of this paper is as follows. In Section 2, we formulate the classical system of interior Poisson-like problems on a moving boundary; our tumor growth model is a special case. Section 3 provides an outline of our general method. In Section 4, we describe our new interior Poisson solver, our gradient discretization and new gradient extension, our new velocity extension, our modifed normal vector and curvature discretizations, and our new application of Gaussian filter technology. In Section 5, we verify the second order convergence with geometric boundary conditions, compare our results to spectrally-accurate results in (Cristini et al., 2003), and investigate the effects of the velocity filtering, the new velocity extension technique, and our modifications to the normal vector and curvature algorithms. Lastly, in Section 6 we give numerical evidence for second order convergence in the presence of necrosis and present several simulations of tumor growth that showcase the robustness of the algorithm through complex morphological changes. This work is a

continuation of the techniques developed by Macklin (2003) in his M.S. thesis.

2.2 The Equations for the Interior Problem

2.2.1 Interior Equations

We wish to solve a system of Poisson-like problems in a moving domain $\Omega(t)$ whose boundary $\Sigma(t)$ evolves with a velocity that depends upon the gradients of these solutions. That is, we solve for a system of functions $p_1, p_2, \ldots, p_k$ on $\Omega \cup \Sigma$ that satisfy

$$\begin{cases} \nabla^2 p_i = f_i(p_1, p_2, \ldots, p_{i-1}, p_i, \mathbf{x}, t) & \text{in } \Omega \\ p_i = g_i(\kappa, \mathbf{x}, t) & \text{on } \Sigma \end{cases} \qquad 1 \le i \le k \tag{2.1}$$

and determine the outward normal velocity of the interface by

$$V\Big|_{\Sigma} = \sum_{i=1}^{k} \alpha_i (\nabla p_i \cdot \mathbf{n})\Big|_{\Sigma}, \tag{2.2}$$

where $\mathbf{n}$ is the unit normal vector on Σ oriented outward from Ω, and each ∇p_i is a one-sided "interior" gradient at Σ based on values on Σ and in Ω. In our formulation, each p_i depends upon p_{i-1}, p_{i-2}, ..., allowing for a partial decoupling of the system, but this restriction could be removed.

As in (Sethian, 1999; Osher and Sethian, 1988; Osher and Fedkiw, 2002; Peng et al., 1999), we capture the boundary Σ implicitly by introducing a level set function φ defined on a rectangular domain $\mathcal{D} \supset (\Omega \cup \Sigma)$ such that

$$\varphi(\mathbf{x}) \begin{cases} < 0 & \text{if } \mathbf{x} \in \Omega \\ = 0 & \text{if } \mathbf{x} \in \Sigma \\ > 0 & \text{else.} \end{cases} \tag{2.3}$$

In this framework, we call Ω the interior region, $\Omega_o = \mathcal{D} \backslash (\Sigma \cup \Omega)$ the exterior region, and Σ the interface between the regions. (Let us denote by $A \backslash B$ the set subtraction B from A.) To update the interface position Σ in time, we solve the additional Hamilton-Jacobi equation

$$\varphi_t + \widetilde{V} \, |\nabla \varphi| = 0 \tag{2.4}$$

throughout $\mathcal{D}$ (Sethian, 1999; Osher and Fedkiw, 2002; Peng et al., 1999). Here, $\widetilde{V}$ is an extension of V beyond the interface.

We further stipulate that φ is a signed distance function: $|\varphi(\mathbf{x})| = d(\mathbf{x}, \Sigma)$. We ensure this property by reinitializing φ at every time step (Sethian, 1999; Osher and Fedkiw, 2002; Sussman and Fatemi, 1999). From the level set function, we can readily compute geometric quantities:

$$\mathbf{n} = \frac{\nabla\varphi}{|\nabla\varphi|} \tag{2.5}$$

and

$$\kappa = \nabla \cdot \left(\frac{\nabla\varphi}{|\nabla\varphi|} \right). \tag{2.6}$$

2.2.2 Application: Tumor Growth

We will apply the techniques developed in this paper to a model of tumor growth, which is a reformulation of several classical models found in Adam (1996), Byrne and Chaplain (1996b), Byrne and Chaplain (1996a), Chaplain (2000), Cristini et al. (2003), and McElwain and Morris (1978). Let Ω denote a two-dimensional tumor mass, let Σ be its boundary, let Ω_N denote the necrotic core of Ω (note that $\Omega_N \subset \Omega$), and let us denote the boundary of Ω_N by Σ_N. As stated earlier, we enclose $\overline{\Omega} = \Omega \cup \Sigma$ in a larger rectangular domain $\mathcal{D}$, and we define $\Omega_o = \mathcal{D} \backslash \overline{\Omega}$.

Let c and p denote a nondimensionalized concentration and pressure, respectively. (See Byrne and Chaplain (1996b), Cristini et al. (2003), and Macklin (2003) for the model and nondimensionalization.) The dimensionless parameters include G which is related to the rate of mitosis (cell proliferation), and G_N measures the rate of volume loss due to necrosis (cell degradation) relative to the rate of mitosis. In addition, the parameter A measures the rate of apoptosis ("pre-programmed" cell death), and N is the value of c necessary for cell viability. Note that the necrotic core Ω_N is the region where $c < N$.

From Cristini et al. (2003), the concentration satisfies

$$\begin{cases} \nabla^2 c &= c \text{ in } \Omega \\ c|_\Sigma &= 1 \\ c &= 1 \text{ outside } \Sigma, \end{cases} \tag{2.7}$$

and the pressure satisfies

$$\begin{cases} \nabla^2 p &= \begin{cases} -G(c - A) & \text{in } \Omega \text{ if } c \geq N \\ GG_N & \text{in } \Omega \text{ if } c < N \end{cases} \\ p|_\Sigma &= \kappa \\ p &= 0 \text{ outside } \Sigma. \end{cases} \tag{2.8}$$

Note that the concentration is determined solely by the position of the interface Σ and can be solved independently of the pressure. This allows the necrotic core to be determined prior to the pressure solve by the region where $c - N$ is negative.

The outward normal velocity is given by Darcy's law

$$V|_\Sigma = -\mathbf{n} \cdot \nabla p, \tag{2.9}$$

where ∇p is the interior pressure gradient in the region $\overline{\Omega}$.

2.3 Numerical Solution: General Technique

We begin by enclosing the interface within a larger, rectangular computational domain $\mathcal{D} = [a, b] \times [c, d]$. (We will postpone our discussion of how large $[a, b] \times [c, d]$ is for a later part of this paper.) We then proceed via:

1. Initialize a level set function φ to represent the interface Σ while ensuring that there are sufficiently many computational node points between Σ and the computational boundary.

2. Check for proximity of the interface Σ to the computational boundary. If there is insufficient space between Σ and $\partial\mathcal{D}$, then extend x, y, and φ. Reinitialize φ.

3. Calculate the normal vector $\mathbf{n}$ and the curvature κ where required.

4. Solve the Poisson problems for $p_1, \ldots, p_k$.

5. Calculate the gradients ∇p_i inside and on Σ, and extend the components of the gradients beyond Σ into Ω_o.

6. Calculate the normal velocity V in a band about Σ according to (2.2). Extend the normal velocity orthogonally from the interface Σ, and filter high-frequency numerical noise from the extended speed.

7. Update φ according to (2.4).

8. Repeat (2)-(7) for each step of the time discretization.

2.4 Discretizations

2.4.1 Interior Poisson Solver

Our solution technique for the Poisson problem was first developed by Macklin (2003) and is an extension of the ghost fluid methods in Glimm et al. (1981), Fedkiw et al. (1999), and Liu et al. (2000) to higher-order accuracy. In this method, we solve a general interior problem for u (which can be either the nutrient concentration c or the pressure p) in a complex domain

$$\begin{cases} \nabla^2 u = f(u, \mathbf{x}) & \text{in } \Omega \\ u = g(\kappa, \mathbf{x}) & \text{on } \Sigma \end{cases} \tag{2.10}$$

by embedding the problem in the rectangular domain $\mathcal{D}$ and extending u as a constant γ into Ω_o. Thus, we solve the system

$$\begin{cases} \nabla^2 u = f(u, \mathbf{x}) & \text{in } \Omega \\ u = g(\kappa, \mathbf{x}) & \text{on } \Sigma \\ u = \gamma & \text{in } \Omega_o. \end{cases} \tag{2.11}$$

The solution u can be assumed to be smooth within Ω up to Σ. We assume that Σ is defined by means of a level set function φ as described before. Also, we assume that g is a function that can be evaluated at all node points near Σ.

Note that the equations governing the tumor nutrient concentration (2.7) and the

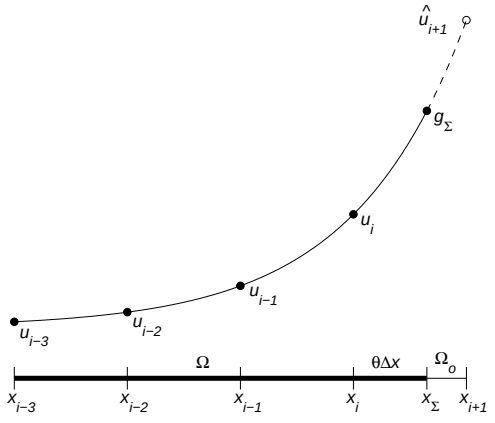

Figure 2.1: Ghost Fluid Method: Extrapolation to $\widehat{u}_{i+1}$.

pressure (2.11) can be written in the above form, where

$$u = c, \quad f(c, \mathbf{x}) = c, \quad g(\kappa, \mathbf{x}) = 1, \quad \gamma = 1 \tag{2.12}$$

and

$$u = p, \quad f(p, \mathbf{x}) = \begin{cases} -G\,(c - A) & \text{in } \Omega_P \\ G\,G_N & \text{in } \Omega_N \end{cases}, \quad g(\kappa, \mathbf{x}) = \kappa, \quad \gamma = 0, \tag{2.13}$$

respectively. Note that in the presence of necrosis, the pressure has a discontinuous second derivative at the boundary of the necrotic core.

The central idea of the discretization technique (Fedkiw et al., 1999; Liu et al., 2000) begins with the standard centered difference for u_{xx}: if $[x_{i-1}, x_{i+1}]$ lies entirely within Ω, then

$$u_{xx} = \frac{u_{i-1} - 2u_i + u_{i+1}}{\Delta x^2} + \mathcal{O}\left(\Delta x^2\right). \tag{2.14}$$

However, if the interface intersects $[x_{i-1}, x_{i+1}]$, then u is potentially discontinuous, and the finite difference approximation in (2.14) is inaccurate. Supposing that the interface occurs between x_i and x_{i+1}, u_{i+1} is replaced in (2.14) with $\widehat{u}_{i+1}$, a smooth extension of u from the inner domain to x_{i+1}. See Figure 2.1.

As stated above, the pressure has a discontinuous second derivative across the boundary of the necrotic core. If left untreated (as is done here) this limits the overall accuracy of the scheme to second order. A higher order accurate treatment can be achieved by applying a ghost fluid discretization at the boundary of the necrotic region as well as at the interface Σ.

In our approach, we make three principal approximations. We estimate the location of the interface between x_i and x_{i+1} by linear interpolation of φ; this is known as *subcell resolution* (Liu et al., 2000; Gibou et al., 2003, 2002). We approximate the value of the boundary condition at the interface by cubic interpolation of g near Σ. Lastly, we extrapolate $\widehat{u}_{i+1}$ from the boundary condition and multiple points within Ω using linear, quadratic, or cubic extrapolation.

Classification of Node Points

For points contained in Ω, the solver proceeds by constructing an approximation to $\nabla^2 u$ at each point (x_i, y_j) while considering which points of the 5-point stencil

$$\{(x_i, y_j), (x_i, y_{j\pm1}), (x_{i\pm1}, y_j)\}$$

are contained in Ω, in Ω_o, and on Σ. The level set formulation of the interface makes this classification a straightforward matter:

$$x_{i,j} \in \begin{cases} \Omega & \text{if} \quad \varphi_{i,j} < -\epsilon \\ \Sigma & \text{if} \quad |\varphi_{i,j}| \leq \epsilon \\ \Omega_o & \text{if} \quad \varphi_{i,j} > \epsilon, \end{cases} \tag{2.15}$$

where ϵ is introduced to account for finite machine precision. We take $\epsilon = 2\epsilon_{mach}$, where

$$\epsilon_{\text{mach}} = \max\{\epsilon > 0 : 1.0 + \epsilon = 1.0\} \tag{2.16}$$

in machine floating-point arithmetic. Note that because computer hardware can only represent finitely-many floating-point numbers, this set has a unique, nonzero maximum. On most modern, 32-bit machines, this number is typically $2^{-53} \approx 1.11\,\text{e-}16$.

Discretizing the Equation

We discretize (2.11) on the full rectangular domain although we are solving the interior problem. The rows corresponding to the trivially-solvable discretizations are included in the coefficient matrix because this preserves the row (or column) ordering of the coefficient matrix, yielding a banded matrix that can be stored efficiently in memory. We proceed by discretizing (2.11) at each node x_i according to the classification of x_i and its neighbors by (2.15).

The discretization on Σ and in Ω_o is trivial:

1. **Case:** $x_i \in \Omega_o$**:**
   By (2.11), $u_i = \gamma$. To improve the conditioning number of the coefficient matrix, we shall use
   $$\frac{-1}{\Delta x^2} u_i = \frac{-1}{\Delta x^2} \gamma. \tag{2.17}$$

2. **Case:** $x_i \in \Sigma$**:**
   In this case, $u_i = g(\kappa_i, x_i)$. Again, we set
   $$\frac{-1}{\Delta x^2} u_i = \frac{-1}{\Delta x^2} g(\kappa_i, x_i). \tag{2.18}$$
   to improve the conditioning number of the coefficient matrix.

When considering points in Ω, we must approximate $\nabla^2 u$. Let us first consider the discretization of u_{xx}. We shall then approximate $\nabla^2 u$ dimension-by-dimension, as the discretization of u_{yy} is identical except in one case where the two-dimensionality is important. We proceed by classifying the node points $\{(x_{i\pm1}), x_i\}$. Consider the following cases:

3. **Case:** $x_i \in \Omega$**:**

   (a) **Case:** $x_{i-1} \in \Omega$ **and** $x_{i+1} \in \Omega$**:**
   In this case, the entire stencil is contained in the inner region, so we can use the standard second order approximation to $u_{xx} = f$:

$$\frac{1}{\Delta x^2}\left(u_{i-1} - 2u_i + u_{i+1}\right) = f(u_i, x_i). \tag{2.19}$$

   (b) **Case:** $x_{i-1} \in \Omega$ **and** $x_{i+1} \in (\Sigma \cup \Omega_o)$**:**
   In this case, the interface is located between x_i and x_{i+1} on the right-hand side of the stencil. Let us denote this location by x_Σ. We denote

$$x_\Sigma = x_i + \theta\,\Delta x, \qquad 0 < \theta \leq 1, \tag{2.20}$$

   where θ is determined by interpolating the level set function φ. This provides us with the subcell resolution introduced earlier. Notice that if $\theta \to 0$, then $x_i \in \Sigma$, and we are in case 2.

   Next, let us define $\mathcal{S} = \{x_{i-1}, x_i, x_{i+1}, x_{i+2}\}$. We evaluate g at the points in $\mathcal{S}$ and the corresponding $\{\kappa_{i-1}, \kappa_i, \kappa_{i+1}, \kappa_{i+2}\}$, apply cubic interpolation, and evaluate the interpolation at x_Σ. Let us denote the value of the interpolation by g_Σ.

   We extend u from the interior region to x_{i+1} and obtain a "ghost value" $\widehat{u}_{i+1}$. We determine $\widehat{u}_{i+1}$ by extrapolating from the neighboring values of u contained in Ω, solving algebraically for $\widehat{u}_{i+1}$, and substituting the expression for $\widehat{u}_{i+1}$ in

$$\frac{1}{\Delta x^2}\left(u_{i-1} - 2u_i + \widehat{u}_{i+1}\right) = f(u_i, x_i). \tag{2.21}$$

   For completeness, we give linear, quadratic, and cubic extrapolations in Appendix 2.9. Similar extrapolations are also given in Gibou and Fedkiw (2005). We note that because all the points in our extrapolations are at least Δx apart, the case where $\theta \to 0$, if it should occur, poses no difficulty for our discretization.

(c) **Case:** $x_{i-1} \in (\Sigma \cup \Omega_o)$ **and** $x_{i+1} \in \Omega$**:**

In this case, the interface is located between x_{i-1} and x_i. The discretization is completely analogous to that in the previous case.

(d) **Case:** $x_{i-1} \in (\Sigma \cup \Omega_o)$ **and** $x_{i+1} \in (\Sigma \cup \Omega_o)$**:**

In this case, the interface intersects the stencil not once but twice; this requires more careful consideration as a series of subcases:

i. **Subcase:** $x_{i-1} \in \Sigma$ **and** $x_{i+1} \in \Sigma$**:**

We can construct an approximation to u_{xx} by

$$\frac{1}{\Delta x^2}\Big(g(\kappa_{i-1}, x_{i-1}) - 2u_i + g(\kappa_{i+1}, x_{i+1})\Big). \tag{2.22}$$

ii. **Subcase:** $x_{i-1} \in \Sigma$ **and** $x_{i+1} \in \Omega_o$**:**

In this subcase, we can proceed as in Case 3b with two minor modifications: we replace u_{i-1} by $g(\kappa_{i-1}, x_{i-1})$ in the extrapolation for $\widehat{u}_{i+1}$, and the extrapolation must be linear. (We do not allow for extrapolations using both u_i and g_Σ because such extrapolations become unstable as $\theta \to 0$.)

iii. **Subcase:** $x_{i-1} \in \Omega_o$ **and** $x_{i+1} \in \Sigma$**:**

This case is completely analogous to the previous subcase.

iv. **Subcase:** $x_{i-1} \in \Omega_o$ **and** $x_{i+1} \in \Omega_o$**:**

The interface occurs on both the right- and left-hand sides of the stencil, and there is insufficient data to extrapolate both $\widehat{u}_{i-1}$ and $\widehat{u}_{i+1}$. (We avoid extrapolations using both u_i and $u(x_i + \theta\Delta x)$, as these become unstable as $\theta \to 0$. Similarly, we avoid extrapolations using u_i and $u(x_{i-1} + \theta\Delta x)$, as these become unstable as $\theta \to 1$.) In this case, we take $u_{xx} = 0$ and consider the y-direction. If the same occurs so that we take $u_{yy} = 0$, we say that the discretization fails to resolve Σ around (x_i, y_j) and take the point to fall in Ω_o. Hence, we set

$$\frac{-1}{\Delta x^2}u_i = \frac{-1}{\Delta x^2}\gamma. \tag{2.23}$$

Notice that we cannot make such a distinction without considering the two-dimensionality of the problem. (See Figure 2.2.) We note that in Gibou et al. (2002) and Gibou and Fedkiw (2005) constant extrapolations are also allowed and so in those works it was unnecessary to consider the two-dimensionality.

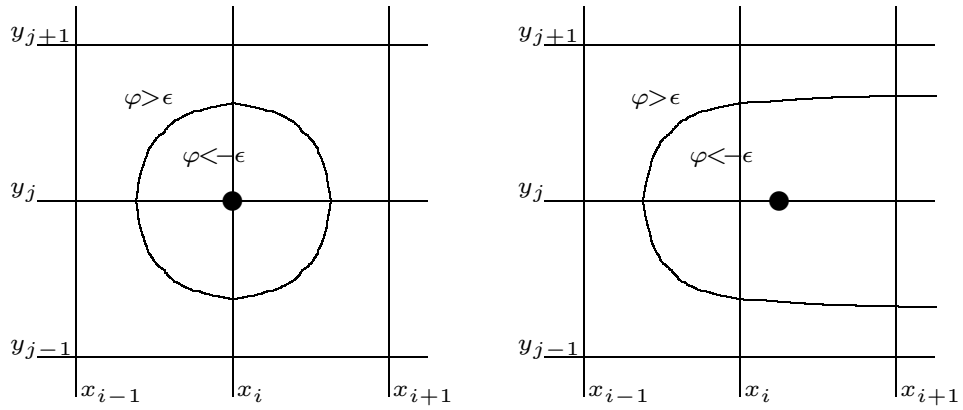

Figure 2.2: Impact of Two-Dimensionality on the Poisson Solver: In the left figure, the interface Σ is unresolved near (x_i, y_j). In the right figure, $u_{yy} = 0$ but the interface is still resolved.

When we use this technique with cubic extrapolation, which shall denote it by Poisson3. Likewise, quadratic and linear extrapolation for $\widehat{u}$ are Poisson2 and Poisson1, respectively. When using Poisson3, if there are not sufficiently many interior node points for cubic extrapolation to $\widehat{u}$, we use Poisson2 or Poisson1 in that instance. The same applies to Poisson2. In our work, we solved the resulting linear systems with the stabilized biconjugate gradient method (BiCG-Stab(2)) (Duff et al., 1998) with a compact banded matrix storage scheme (Press et al., 1992).

2.4.2 Gradients

The normal velocity in (2.2) requires ∇p_i on Σ for each i. For our method, we must also calculate the gradients in Ω. Let u be a function whose gradient we wish to calculate, and consider u_x. For interior points $x_i \in \overline{\Omega}$ where $\varphi \leq \epsilon$, we use the five-point stencil

$$u_x(x_i) = \frac{1}{12\Delta x}\Big(u_{i-2} - 8u_{i-1} + 8u_{i+1} - u_{i+2}\Big) + \mathcal{O}\left(\Delta x^4\right) \tag{2.24}$$

when $\{x_i, x_{i\pm1}, x_{i\pm2}\} \subset \overline{\Omega} = \Omega \cup \Sigma$; when only $\{x_i, x_{i\pm1}\} \subset \overline{\Omega}$, we use the standard second order centered difference. If one of $x_{i\pm1} \in \Omega_o$, we construct a polynomial interpolation of u in $\overline{\Omega}$ using two-to-four nearby points in Ω, differentiate the interpolation, and evaluate at x_i. In this way, we can calculate u_x to second order or better accuracy at all points in Ω and on Σ. We obtain the partial derivative u_y similarly.

2.4.3 Extensions

Since we solve the advection equation (2.4), we require an extended normal velocity in a band surrounding Σ. Because the Poisson solutions p_i only have meaningful gradients (in the context of the interior problem) on $\overline{\Omega}$, the first step of our extension procedure is to extend the individual components of the gradients ∇p_i beyond Σ into Ω_o. Once this is done, we can evaluate (2.2) at any point near Σ.

To help maintain the accuracy of the level set φ, we then use a velocity extension technique that satisfies the orthogonality criterion $\nabla V \cdot \mathbf{n} = 0$, which helps preserve the spacing of the level set contours. We note that our orthogonal extension is a new technique based upon bilinear interpolation.

Once we have orthogonally extended the velocity, we apply a Gaussian filter in a narrow band about the interface; this removes high frequency noise from the speed function that would otherwise perturb the interface and destabilize the calculation (See Section 2.4.4). Because the filter only smooths the speed closest to the interface, we must extend the smoothed velocity one final time. We found this approach works best among the various combinations of extension and filtering available.

Gradient Extension

As the gradient algorithm only defines the gradients where $\varphi \leq \epsilon$, we must extend to a band of nodes where $\varphi > \epsilon$. For stability, our technique must preserve information flow in an outward direction from the interface. The method we describe can be used to extend any scalar function f defined on Σ and in Ω, and we apply it to the components of the ∇p_i individually.

We extend f to a point $\mathbf{x} \in \Omega_o$ by one-dimensional, grid-aligned extrapolation from points where f has either been previously extended or was originally defined (e.g., in Ω). We choose the points used in the extrapolation according to whether the normal vector $\mathbf{n} = (n_1, n_2)$ at $\mathbf{x}$ is mostly horizontal ($|n_1| - |n_2| > \epsilon$ as at point $\mathbf{a}$ in Figure 2.3), mostly vertical ($|n_2| - |n_1| > \epsilon$ as at point $\mathbf{c}$ in Figure 2.3), or mostly diagonal ($||n_1| - |n_2|| \leq \epsilon$ as at point $\mathbf{b}$ in Figure 2.3). This allows the use of high-order extrapolation without the complexity of multidimensional extrapolation; in our work, we used cubic extrapolation. See Figure 2.3.

To preserve information flow in the outward direction from the interface, we tag the

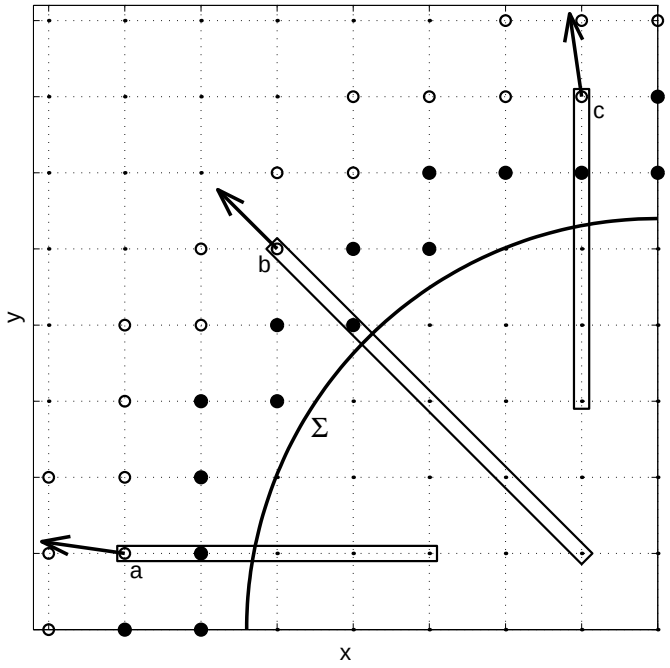

Figure 2.3: Gradient Extension: We extend a scalar function beyond $\Omega \cup \Sigma$ by one-dimensional, grid-aligned extrapolation. The points used in the extrapolation are chosen according to the direction of the normal vector. We preserve outward information flow by choosing the next point for extension according to the value of the level set function at the remaining points (open circles).

points requiring extension (larger circles in Figure 2.3), and among those points, we choose the point closest to Σ which has not yet been updated (open circles); notice that by the level set formulation, this point can be determined by choosing the remaining point with the smallest positive value of φ.

In our simulations, we applied this technique to each component of the ∇p_i within a band of width $5\Delta x$.

Identifying the Closest Point on the Interface.

Ordinarily, it can be an expensive operation to determine the closest point $\mathbf{x_1}$ on the interface Σ to a given point $\mathbf{x_0}$ (Adalsteinsson and Sethian, 1999; Sethian, 1999; Osher and Fedkiw, 2002). However, we can use the information afforded by the level set function φ to make this a simple, efficient operation; no search is required.

At any point $\mathbf{x_0}$, the outward normal vector $\mathbf{n}(\mathbf{x_0})$ points away from the interface, and

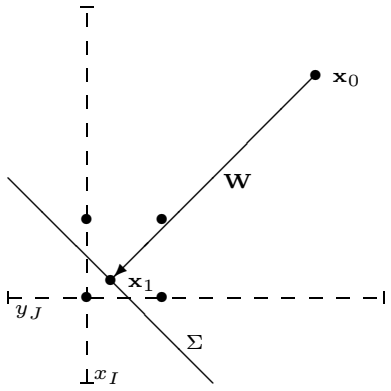

Figure 2.4: Finding the closest point on the interface. $\mathbf{W} = -\varphi(\mathbf{x_0})\mathbf{n}(\mathbf{x_0})$.

$|\varphi(\mathbf{x_0})|$ gives the distance to the interface. Therefore, the vector

$$\mathbf{W}(\mathbf{x_0}) = -|\varphi(\mathbf{x_0})|\,\mathbf{n}(\mathbf{x_0}) = -\varphi\mathbf{n} \tag{2.25}$$

points towards the closest point on Σ and has length equal to the distance from Σ. The point

$$\mathbf{x_1} = \mathbf{x_0} + \mathbf{W} \tag{2.26}$$

explicitly gives the closest point to $\mathbf{x_0}$ on Σ to second order. See Figure 2.4.

Orthogonal Velocity Extension

Once we have a velocity defined in a band about the interface Σ, we apply an extension routine to ensure that $\nabla\widetilde{V}\cdot\mathbf{n} = 0$. We developed an extension based on bilinear interpolation of the velocity near the interface that proved to be more accurate and less computationally expensive than PDE-based techniques (e.g., that given by Zhao et al. (1996)). The vector $\mathbf{W}$ defined in (2.25) suggests the new extension technique: if we wish to extend V to $\mathbf{x_0}$, we define $\mathbf{W}$ as in (2.25) and

$$\mathbf{x_1} = \mathbf{x_0} + \mathbf{W} \tag{2.27}$$

to be the closest point to $\mathbf{x_0}$ on the interface. Next, we locate (x_I, y_J) such that $\mathbf{x_1}$ is contained in the box $[x_I, x_{I+1}) \times [y_J, y_{J+1})$ and calculate $V(\mathbf{x_1})$ with bilinear interpolation of V at the corners of the box. See Figure 2.4. Lastly, we define $\widetilde{V}(\mathbf{x_0}) = V(\mathbf{x_1})$. Notice

that as $\widetilde{V}$ is constant along $\mathbf{W}$, which is parallel to $-\mathbf{n}$ at all extended points,

$$\frac{\partial \widetilde{V}}{\partial \mathbf{n}} \equiv 0. \tag{2.28}$$

This approach differs from the discrete, fast marching velocity extension given by Adalsteinsson and Sethian (1999) in several ways. First, the fast marching extension technique extends the velocity outward from the interface while simultaneously updating the level set function; ours uses an already-updated level set function to aid in the extension process. We use the level set function to readily locate the closest position on the interface, while the fast marching technique depends on explicitly reconstructing the zero level set as piecewise linear curves and considering multiple cases. Also, while the fast marching method depends upon solving a discretized PDE at every point of extension, ours depends upon a simpler interpolation of previously known values in a way similar to Malladi et al. (1995).

2.4.4 Velocity Filtering

Because the physical problem is sensitive to variations in the curvature, the speed can become noisy when even small perturbations in the level set function are present. In addition, grid effects such as mesh-induced anisotropies can act as sources of numerical perturbations. In the boundary integral context (Cristini et al., 2003), it was shown that for these equations, the normal velocity depends upon the derivative of the curvature (i.e., $V \sim \mathcal{H}(\kappa_s)$, where $\mathcal{H}$ is the Hilbert transform and s is arclength). It can be shown that such velocity fields damp high frequency perturbations δ_k at the rate $-|k|^3$, where k is the wave number. Thus, perturbations evolve according to $\delta_k \sim e^{-|k|^3 t}$ at large k. From this consideration, the high frequency perturbations in the speed and interface position should be damped away, provided a CFL restriction is satisfied. The CFL restriction for an explicit boundary integral method is $\Delta t \sim \Delta s^3$. An analysis of our ghost fluid/level set method reveals that this time step restriction also applies, with Δs replaced by Δx. This severe time step restriction can be overcome in a number of ways. For example, in Cristini et al. (2003), a non-stiff, time integration scheme using a discretization in which the leading order term (term with the largest number of spatial derivatives) is integrated explicitly. This effectively removes the third order constraint, leaving only a standard first order CFL time step restriction. The application of such an implicit time integration scheme in the level set context is not straightforward. We are currently working to develop such a scheme.

Another way to remove the high order time step constraint is to use numerical diffusion to remove small, high frequency perturbations before they pollute the numerical solution. This has the advantage that it is computationally inexpensive, and if done carefully, it does not degrade the accuracy of the numerical solution. We find that adapting a Gaussian filter from image processing applications (Gonzalez and Woods, 1992) to smooth the normal velocity within a prescribed band about the interface provides an efficient means of controlling the noise without affecting the accuracy. In addition, the Gaussian filtering removes grid anisotropies as a side benefit.

In one spatial dimension, a Gaussian filter is applied to a function f by

$$\widehat{f}_I = \frac{1}{\sigma\sqrt{2\pi}} \sum_i f_{I-i} \exp\left(-\frac{(i\ \Delta x)^2}{2\sigma^2}\right) \Delta x, \tag{2.29}$$

where σ is the standard deviation of the filter. Typically, $\sigma = M\Delta x$ for some integer M. For $|i\Delta x| \geq 3\sigma$, the exponential function in the convolution has a very small value (less than approximately .0111); consequently, we can truncate the sum above to

$$\widehat{f}_I = \frac{1}{S}\frac{1}{M\sqrt{2\pi}} \sum_{i=-3M}^{3M} f_{I-i} \exp\left(-\frac{1}{2}\left(\frac{i}{M}\right)^2\right), \tag{2.30}$$

where S is the value of the sum for $f \equiv 1$.

To smooth a two-dimensional data array, we use (2.30) first in the x-direction, and then again in the y-direction. In our calculations, we found that the necessary value of σ depends upon the spatial resolution but decreases with refinement. Because the filter requires that f be defined within a distance of 3σ, we only apply the filter to a narrow band around Σ. In our simulations, we used a narrow band of width $3\Delta x$. As will be shown later, this technique yields accurate results using only a first order CFL time step restriction.

2.4.5 Level Set Reinitialization and Advection

As in Sussman and Fatemi (1999), we reinitialize φ to be a signed distance function by solving

$$\varphi_\tau - \text{sign}(\varphi^0)\,(1 - |\nabla\varphi|) = 0, \tag{2.31}$$

where φ^0 is the level set function prior to reinitialization and τ is pseudo-time. We discretize the temporal derivative with the third-order total variation diminishing Runge-Kutta

Method (TVD-RK), and we approximate $\text{sign}(\varphi^0)\,|\nabla\varphi|$ with either the third-order or the fifth-order WENO scheme (Jiang and Shu, 1996; Jiang and Peng, 2000). We discretize the sign function according to

$$\text{sign}_\delta(\varphi) = 2\left(H_\delta(\varphi) - \frac{1}{2}\right), \tag{2.32}$$

where

$$H_\delta(\varphi) = \begin{cases} 0 & \text{if } \varphi < -\delta \\ \frac{1}{2}\left(1 + \frac{\varphi}{2\delta} + \frac{1}{\pi}\sin\left(\frac{\pi\varphi}{\delta}\right)\right) & \text{if } |\varphi| \le \delta \\ 1 & \text{if } \varphi > \delta, \end{cases} \tag{2.33}$$

and δ is a small number (Sussman et al., 1998). In our calculations, we took $\delta = \Delta x$.

In our numerical implementation of the level set equation (2.4), we discretize $V\,|\nabla\varphi|$ with the third-order or fifth-order WENO method. We approximate the temporal derivative with the third-order total variation diminishing Runge-Kuta (TVD-RK) method (Gottlieb et al., 2001; Gottlieb and Shu, 1997), and we use the CFL condition

$$\Delta t \le \frac{\Delta x}{4\max|V|}. \tag{2.34}$$

2.4.6 Normal Vectors and Curvature

The standard, second order discretization of the normal vector $\mathbf{n}$ uses centered differences for φ_x and φ_y and normalizes the result. For curvature, the standard second order method is to calculate each partial derivative in

$$\kappa = \nabla\cdot\frac{\nabla\varphi}{|\nabla\varphi|} = \frac{\varphi_{xx}\varphi_y^2 - 2\varphi_x\varphi_y\varphi_{xy} + \varphi_{yy}\varphi_x^2}{\left(\varphi_x^2+\varphi_y^2\right)^{\frac{3}{2}}} \tag{2.35}$$

using second order, centered differences. Note that this uses a 9-point stencil, and we discretize φ_{xy} as in Chen et al. (1997) by

$$\varphi_{xy}(x_i,y_j) \;\approx\; \frac{1}{4\Delta x\Delta y}\Big(\varphi_{i+1,j+1} - \varphi_{i-1,j+1} - \varphi_{i+1,j-1} + \varphi_{i-1,j-1}\Big). \tag{2.36}$$

However, there are cases where these normal vector and curvature discretizations are inaccurate. If two interfaces approach one another, a "ridge" forms between them where the derivatives of φ are discontinuous. Discretization across this ridge will cause large errors in the normal vector and curvature for an exact (i.e., unperturbed, error-free) level set. See Figure 2.5.

Because such ridges tend to introduce error into the surrounding level set function during reinitialization and advection level set operations, the standard discretizations of

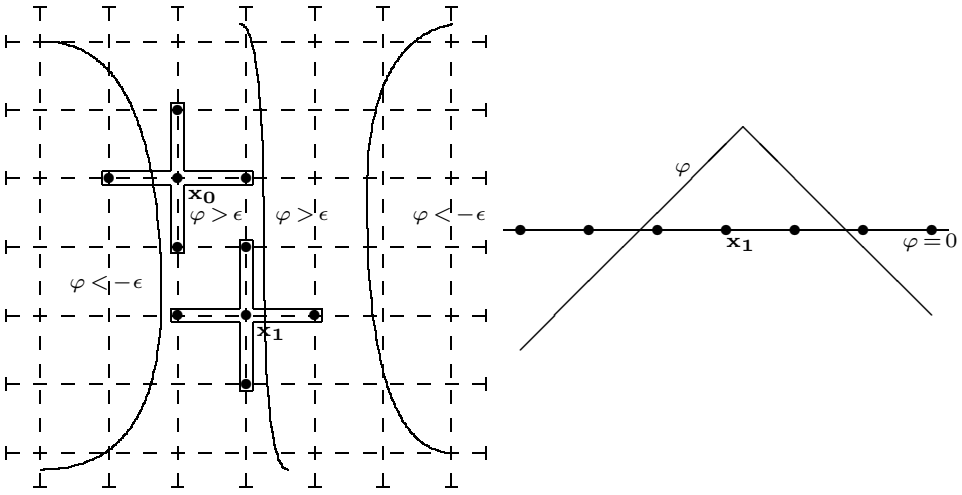

Figure 2.5: Effect of Level Set Irregularity on κ and $\mathbf{n}$: In the left figure, two interfaces are close together. The middle curve shows the points equidistant from both interfaces, and the level set function is irregular along this curve. The standard techniques for calculating κ and $\mathbf{n}$ work well at $\mathbf{x_0}$ (where the derivatives of φ are continuous), whereas they break down numerically at $\mathbf{x_1}$. The right figure shows a cross-section through $\mathbf{x_1}$ of the level set function; the "peak" in the middle is equidistant from the two interfaces and a point of irregularity in φ.

curvature and the normal vectors are also erratic in the nodes near the ridge. Because our extension techniques require that the normal vectors point away from the interface, and as the boundary conditions of the Poisson problems depend on the curvature, it is critical that we develop a technique to detect these situations and discretize accordingly. In our approach, we first detect these "ridges" and any other irregularities in the level set function, create a field of direction vectors near the ridges to assist in determining one-sided discretizations, and finally discretize the normal vectors and curvature.

Detecting "Ridges" in the Level Set

Recall that for a signed distance function φ, $|\nabla\varphi| \approx 1$. Thus, a simple technique to detect the points on and near a ridge is to compute $\mathbf{v} = \nabla\varphi$ using centered second order differences, and then to define a "normal quality function" $Q(\mathbf{v})$ according to

$$Q(\mathbf{v}) = |1 - |\mathbf{v}|| \,. \tag{2.37}$$

Table 2.1: Discretization of the x-component of $\mathbf{n}$ based on the direction vectors.

Case	Discretization of x-component of $\mathbf{n}$
$(\mathbf{D}_{i-1,j} \cdot \mathbf{D}_{i,j} > 0$ or $\lvert\mathbf{D}_{i-1,j}\rvert = 0)$ and $\mathbf{D}_{i+1,j} \cdot \mathbf{D}_{i,j} \leq 0$	use a left-based stencil for φ_x
$\mathbf{D}_{i-1,j} \cdot \mathbf{D}_{i,j} \leq 0$ and $(\mathbf{D}_{i+1,j} \cdot \mathbf{D}_{i,j} > 0$ or $\lvert\mathbf{D}_{i+1,j}\rvert = 0)$	use a right-based stencil for φ_x
$(\mathbf{D}_{i-1,j} \cdot \mathbf{D}_{i,j} > 0$ or $\lvert\mathbf{D}_{i-1,j}\rvert = 0)$ and $(\mathbf{D}_{i+1,j} \cdot \mathbf{D}_{i,j} > 0$ or $\lvert\mathbf{D}_{i+1,j}\rvert = 0)$	use centered difference for φ_x
$\mathbf{D}_{i-1,j} \cdot \mathbf{D}_{i,j} \leq 0$ and $\mathbf{D}_{i+1,j} \cdot \mathbf{D}_{i,j} \leq 0$	use centered difference for φ_x

We set $Q_{i,j} = Q(\nabla\varphi(x_i, y_j))$. If $Q_{i,j} \geq \eta$ for some fixed $0 < \eta < 1$, then the point (x_i, y_j) is on or near a ridge. In our testing, we found that $\eta = .1$ reliably detects the points on and near the ridges with few false positives.

Creating a Direction Vector Field

We next introduce a direction field $\mathbf{D}(x, y)$ to assist in determining whether two neighboring points are on the same side of a ridge. We require that $\mathbf{D}(x_i, y_j)$ points away from a ridge if $Q \geq \eta$ at (x_i, y_j) or any one of its eight neighbors in the Cartesian grid, in which case $\mathbf{D}(x_i, y_j)$ points towards one of the eight neighboring points. Otherwise, $\mathbf{D} = \mathbf{0}$. If $\mathbf{D} \neq 0$, we take it to be among the set

$$\mathcal{V} = \{(0,-1), (0,1), (-1,0), (-1,-1), (-1,1), (1,0), (1,-1), (1,1)\}. \tag{2.38}$$

For a function f at (x_i, y_j), we define the $\mathbf{D}$-difference of ∇f component-wise by:

$$\partial_x f = \begin{cases} \frac{f_{i,j} - f_{i-1,j}}{\Delta x} & \text{if } D_x = -1 \\ \frac{f_{i+1,j} - f_{i,j}}{\Delta x} & \text{if } D_x = 1 \\ \frac{f_{i+1,j} - f_{i-1,j}}{2\Delta x} & \text{if } D_x = 0, \end{cases} \tag{2.39}$$

where $(D_x, D_y) = \mathbf{D}(x_i, y_j)$; $\partial_y f$ is defined similarly.

We determine $\mathbf{D}$ component-wise according to the value of Q at (x_i, y_j) and its eight

neighbors. For the x-direction,

$$D_x = \begin{cases} -1 & \text{if } Q_{i-1,j} < \eta \text{ and } Q_{i+1,j} \geq \eta \\ 1 & \text{if } Q_{i-1,j} \geq \eta \text{ and } Q_{i+1,j} < \eta \\ 0 & \text{if } Q_{i-1,j} < \eta \text{ and } Q_{i,j} < \eta \text{ and } Q_{i+1,j} < \eta \\ 0 & \text{if } Q_{i-1,j} \geq \eta \text{ and } Q_{i,j} \geq \eta \text{ and } Q_{i+1,j} \geq \eta \\ \text{undetermined} & \text{otherwise.} \end{cases} \tag{2.40}$$

We determine D_y similarly. We shall denote $\mathbf{D}(x_i, y_j)$ by $\mathbf{D}_{i,j}$. If D_x or D_y is undetermined, then we set $\mathbf{D}'$ equal to the element in $\mathcal{V}$ most parallel to $\nabla\varphi$ (where we again use centered differences). We set $\mathbf{D}^1$ and $\mathbf{D}^2$ to be perpendicular to $\mathbf{D}'$, and we define $\mathbf{v}^1$ and $\mathbf{v}^2$ to be the $\mathbf{D}^1$- and $\mathbf{D}^2$-differences of $\nabla\varphi$, respectively. If $Q(\mathbf{v}^1) < Q(\mathbf{v}^2) + \mu$, then we choose $\mathbf{D}_{i,j} = \mathbf{D}^1$; otherwise, $\mathbf{D}_{i,j} = \mathbf{D}^2$. It is desirable to choose $\mu \neq 0$ to give the direction field $\mathbf{D}$ a small bias towards one side for points resting exactly on a ridge, as $Q(\mathbf{v}^1) \approx Q(\mathbf{v}^2)$ in such cases. In our testing, we found $\mu = \frac{1}{8}\eta$ works well.

Using these direction vectors, we can readily determine if two adjacent points are on the same side of a ridge or other level set irregularity. Consider, for example, $\mathbf{D}_{i-1,j}$ and $\mathbf{D}_{i,j}$. If the dot product $\mathbf{D}_{i-1,j} \cdot \mathbf{D}_{i,j} > 0$ or $\mathbf{D}_{i-1,j} = \mathbf{0}$, then we say that (x_{i-1}, y_j) and (x_i, y_j) are on the same side of any and all ridges and level set irregularities.

Discretizing the Normal Vector

To discretize $\mathbf{n}$ at (x_i, y_j), we discretize the x-component of $\mathbf{n}$ as in Table 2.1. If we use a left-based stencil, we use a stencil based of φ on

$$\Big\{(x_{i-4}, y_j), (x_{i-3}, y_j), (x_{i-2}, y_j), (x_{i-1}, y_j), (x_i, y_j)\Big\}. \tag{2.41}$$

Let K be the number of points adjacent to and left of (x_i, y_j) for which all the points are on the same side of all the ridges; that is, let

$$K = \max\{k : \mathbf{D}_{i-\ell,j} \cdot \mathbf{D}_{i,j} > 0 \text{ or } |\mathbf{D}_{i-\ell,j}| = 0 \text{ for all } 1 \leq \ell \leq k\}. \tag{2.42}$$

If $K > 5$, set $K = 5$. Then for the left stencil, we approximate φ_x using the K-point difference of φ at $\{(x_{i-\ell}, y_j)\}_{\ell=0}^{K}$. A right-based stencil for φ_x can be defined similarly, and the y-component is discretized analogously. The resulting vector is then normalized.

Discretizing the Curvature

Recall that the standard curvature discretization involves the nine points in the square $[x_{i-1}, x_{i+1}] \times [y_{j-1}, y_{j+1}]$. If each $Q_{k,\ell} < \eta$ for $i-1 \leq k \leq i+1$ and $j-1 \leq \ell \leq j+1$, we use the standard curvature discretization.

If any $Q \geq \eta$ for one of these nine points but $Q < \eta$ on

$$\mathcal{P} = (x_{i\pm1}, y_j) \cup (x_i, y_{j\pm1}) \cup (x_i, y_j), \tag{2.43}$$

then we use the alternate discretization of κ via

$$\kappa = \nabla \cdot \mathbf{n}, \tag{2.44}$$

where we use second order centered differences for $\partial_x n_x$ and $\partial_y n_y$.

If $Q \geq \eta$ on any point in $\mathcal{P}$, we have found that no one-sided difference can stably calculate κ. In such a case, we apply an extension of the previously-defined κ values in a manner similar to the components of the pressure gradient as described in Section 2.4.2. The only difference is that rather than fitting a higher-order (up to cubic) polynomial through the interpolated points and extrapolating, we fit a least-squares line through those data points. In our testing, we found that this gives much more stable results. Because the algorithm is one-sided, we apply it twice: once for the undefined curvature values outside Σ, and once for the undefined curvature values inside Σ.

2.4.7 The Narrow Band/Local Level Set Technique and the Size of the Computational Domain

Following Malladi et al. (1996) and Peng et al. (1999), we update φ within a distance R of the interface. Given an initialized level set function φ, the points which fall within that distance are

$$\{\mathbf{x} : |\varphi(\mathbf{x})| \leq R + \epsilon\} \tag{2.45}$$

for some small ϵ. This set is referred to as a "narrow band" about Σ, R is the width of the band, and the technique is known as the "narrow band" (or "local") level set method. The value of R is determined by the numerical implementation; we begin this determination by considering the smoothed normal velocity.

We require a smoothed normal velocity within three nodes of the interface. Thus, $R \geq 3\Delta x$. If σ is the standard deviation of the Gaussian filter, then the outermost of these

Table 2.2: Filtering parameter σ used for each spatial resolution.

Δx	σ
0.16	$2\Delta x = 0.32$
0.08	$3\Delta x = 0.24$
0.04	$4\Delta x = 0.16$

smoothed points requires that $\widetilde{V}$ be defined within a rectangle that extends 3σ in all four mesh directions. The farthest node point within this rectangle is at a distance of $3\sqrt{2}\sigma$, so $R \geq 3\Delta x + 3\sigma\sqrt{2}$.

To extend the velocity to the outermost of these points, we require a valid normal vector. As we obtain the normal vector with centered difference of φ, this requires one-to-two additional node points. Thus, $R \geq 3\Delta x + 3\sqrt{2}\sigma + 2\Delta x$. Lastly, we often multiply R by a safety factor because the interface tends to change position between intermediate steps of the TVD-RK method. In our calculations, we chose a safety factor of 1.25. Thus, our band size is

$$R = 1.25\Big(5\Delta x + 3\sqrt{2}\sigma\Big) = R = 1.25\Big(5 + 3M\sqrt{2}\Big)\Delta x, \tag{2.46}$$

where we have used $\sigma = M\Delta x$.

The size of the band for the narrow band level set method determines the size of the computational domain $\mathcal{D}$: it must be large enough to contain the contour $\{\mathbf{x} : \varphi(\mathbf{x}) \leq R + \epsilon\}$. We typically allow three-to-four additional nodes of buffer between the edge of the computational domain and this contour. Thus, whenever

$$|\varphi(\mathbf{x})| > R + 3\Delta x, \tag{2.47}$$

for any $\mathbf{x} \in \partial\mathcal{D}$, we must extend the computational domain. We therefore modify the width R of the narrow band to include this distance:

$$R = 1.25\Big(5\Delta x + 3\sqrt{2}\sigma + 3\Delta x\Big) = R = 1.25\Big(8 + 3M\sqrt{2}\Big)\Delta x. \tag{2.48}$$

2.5 Convergence and Testing Results

2.5.1 Convergence of the Full Method: Exact Circular Solution

We tested our algorithm on the full system (2.7)-(2.9) with $A = 0.5$, $G = 20$ and $N = 0$ (i.e. no necrosis). Note that G_N is not used in the absence of necrosis. The initial interface

Table 2.3: Full Convergence Results for WENO5, Poisson2, bilinear velocity extension.

time	$\Delta x = .16$	$\Delta x = .08$	$\Delta x = .04$	order
0.05	.005691	.001447	3.634e-4	1.98
0.10	.01111	.002765	7.424e-4	1.95
0.15	.01572	.003869	9.839e-4	2.00
0.20	.01963	.004942	.001259	1.98
0.25	.02405	.005774	.001467	2.02

Σ is a circle of radius 2.0 centered at the origin. According to Cristini et al. (2003), if $R(t)$ denotes the radius of Σ at time t, the exact solution of this problem is given by solving

$$R'(t) = -AG\frac{R}{2} + G\frac{I_1(R)}{I_0(R)} \quad , \quad R(0) = 2. \tag{2.49}$$

The level set function φ at time t is given by

$$\varphi(r,t) = r(x,y) - R(t), \tag{2.50}$$

where $r(x,y) = \sqrt{x^2+y^2}$.

To test the convergence, we measured the maximum absolute error at the common mesh points within the band $\mathcal{B} = \{(x,y) : |r(x,y) - R(t)| < 0.5\}$

$$\ell_\infty^{band}(\Delta x) = \max\Big\{|\varphi_{\Delta x}(x_i,y_j,t) - \varphi_{\text{actual}}(x_i,y_j,t)| \ : \ (x_i,y_j) \in \mathcal{B}\Big\} \tag{2.51}$$

at $t = 0.05$ to $t = 0.25$ in 0.05 increments. We tested with $\Delta x = \Delta y = 0.16$, $\Delta x = \Delta y = .08$, and $\Delta x = \Delta y = 0.04$. In all these calculations, we used linear interpolation of φ for the subcell resolution in the various Poisson solvers. We calculated curvature within a band of width $3\Delta x$ of Σ, we set $\eta = 0.1$ for the normal vector and curvature algorithms, and we chose σ large enough to maintain the expected circular symmetry and convergence at

Table 2.4: Full Convergence Results for WENO5, Poisson1, bilinear velocity extension.

time	$\Delta x = .16$	$\Delta x = .08$	$\Delta x = .04$	order
0.05	.01520	.004157	.001535	1.65
0.10	.02650	.008049	.002896	1.60
0.15	.03739	.01111	.004055	1.60
0.20	.04663	.01372	.005074	1.60
0.25	.05528	.01733	.006007	1.60

Table 2.5: Full Convergence Results for non-necrotic, complex morphology.

time	$\ell_\infty^{band}(\Delta x, 2\Delta x)$	$\ell_\infty^{band}(\Delta x, \frac{1}{2}\Delta x)$	order
0.05	0.005650	0.001333	2.08
0.10	0.009698	0.002453	1.98
0.15	0.01339	0.003473	1.97
0.20	0.01607	0.004014	2.00
0.25	0.1850	0.004878	1.92
0.50	0.03282	0.007068	2.22
0.70	0.03417	0.009704	1.82

every time step. The values of σ used are given in Table 2.2. Notice that σ decreases with refinement of the computational mesh, so there is no lower limit on the feature size that can be resolved by mesh refinement. All calculations used our new bilinear velocity extension technique.

We define the overall convergence rate at a given time t to be

$$\text{convergence rate} = \frac{\log\left(\frac{\ell_\infty^{band}(\Delta x=.16)}{\ell_\infty^{band}(\Delta x=.04)}\right)}{\log 4}. \tag{2.52}$$

We tested all combinations of WENO and Poisson orders and determined that WENO5 with Poisson2 is the best combination of algorithms to yield full second order accuracy. The convergence results for WENO5-Poisson2 are given in Table 2.3. Furthermore, we found that using Poisson1 yielded 1.6-order convergence with significantly larger errors. See Table 2.4 for a characteristic example with WENO5-Poisson1 and bilinear velocity extension. Similar results have been obtained for simulations including necrotic effects (see Section 2.6.1).

2.5.2 Convergence of the Full Method for Complex Morphology and Comparison to Boundary Integral Results

Consider the problem (2.7)-(2.9) with $A = 0.5$, $G = 20$ and $N = 0$ (i.e. no necrosis). We solve with $\Delta x = \Delta y = 0.08$, $\eta = 0.1$, WENO5, and Poisson2. The initial shape is given by

$$\Sigma(s) = (2 + .2\cos(2s), 2 + .2\sin(2s)), \qquad 0 \le s \le 2\pi. \tag{2.53}$$

There is no analytical solution for this case. Thus, to test convergence, we compare the solutions at different resolutions. This case has been investigated previously using boundary

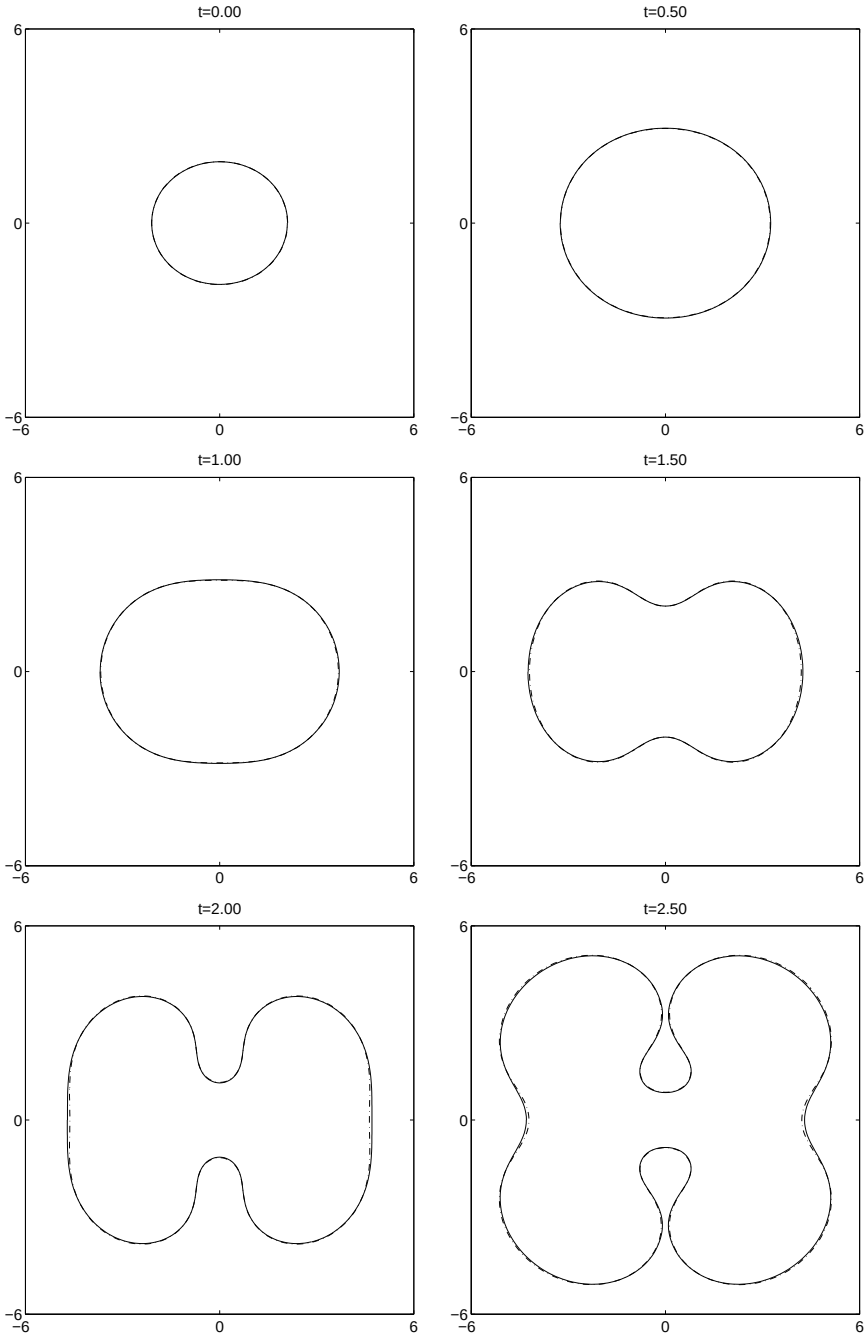

Figure 2.6: Comparison of computed solutions: We compare the WENO5-Poisson2 (dashed curves) and boundary integral (solid curves) solutions from t=0.0 to t=2.50 in 0.5 increments.

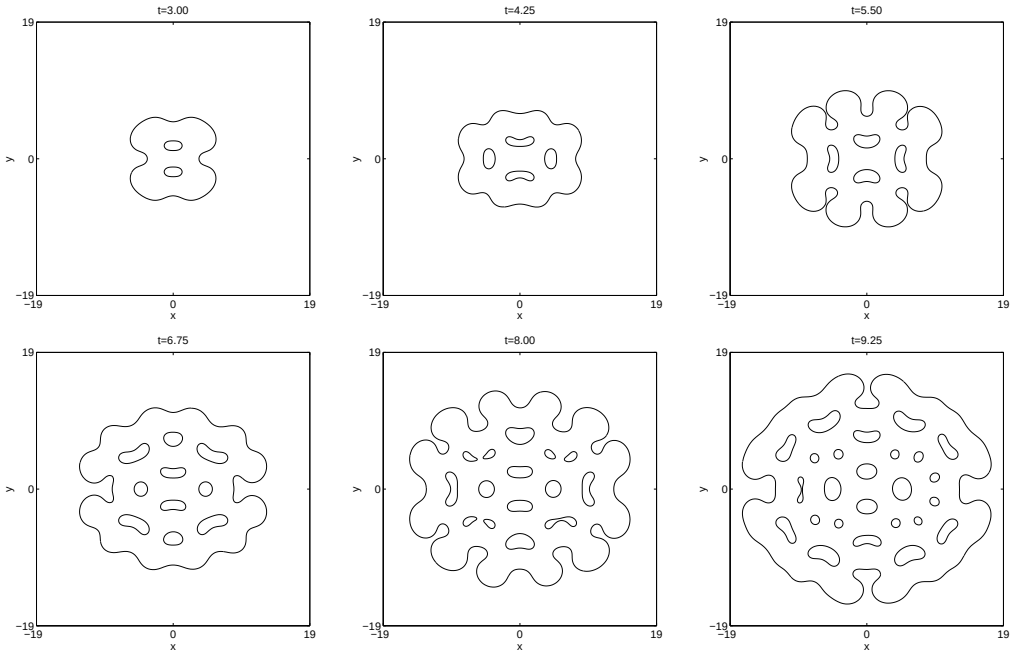

Figure 2.7: Comparison of computed solutions: We continue our WENO5-Poisson2 solution to additional times which the boundary integral method cannot compute. Note that the spatial scale is different than in Figure 2.6.

integral methods in Cristini et al. (2003); we also compare our results to these.

In Table 2.5, the differences between the solutions at different mesh refinements in maximum norm and the associated orders of convergence are shown at various times. The differences are defined by

$$\ell_\infty^{band}(\Delta x_1, \Delta x_2) = \max\Big\{ |\varphi_{\Delta x_1}(x_i, y_j, t) - \varphi_{\Delta x_2}(x_i, y_j, t)| \ : \ (x_i, y_j) \in \mathcal{B} \Big\}, \tag{2.54}$$

where the band $\mathcal{B}$ consists of the set of common mesh points within a distance of 0.5 of the

Table 2.6: Full Convergence Results for necrotic, complex morphology.

time	$\ell_\infty^{band}(\Delta x, 2\Delta x)$	$\ell_\infty^{band}\left(\Delta x, \frac{1}{2}\Delta x\right)$	order
0.05	0.004290	0.001153	1.89
0.10	0.006469	0.001612	2.00
0.15	0.006852	0.001820	1.91
0.20	0.009999	0.002754	1.86
0.25	0.01360	0.003528	1.95
0.30	0.01804	0.004908	1.88

interface. The order of convergence is given by

$$\text{convergence rate} = \frac{1}{\log 2} \log \left(\frac{\ell_\infty^{band}(\Delta x, 2\Delta x)}{\ell_\infty^{band}\left(\Delta x, \frac{1}{2}\Delta x\right)} \right). \tag{2.55}$$

The results in Table 2.5 clearly demonstrate that the overall solution is second order accurate.

Next, we compare our simulation to the boundary integral result from Cristini et al. (2003). Cristini et al. (2003) showed that this tumor undergoes a morphological instability, and the evolving interface was accurately simulated using a spectrally-accurate boundary integral method.

In Figure 2.6, we compare our results (dashed curves) to the spectrally-accurate results (solid curve) from Cristini et al. (2003). This is an especially difficult test due to the morphological instability which makes the solution very sensitive to numerical errors. There is excellent agreement between the results. Shortly after the final time ($t = 2.531$) shown in Figure 2.6, the boundary integral method breaks down as the tumor boundary self-intersects, resulting in the capture of healthy tissue within the tumor domain.

In Figure 2.7, we continue our solution. As the tumor grows, healthy tissue is captured by the tumor multiple times as morphological stability occurs. It is well-known that healthy tissue often mixes with tumor tissue, especially near the tumor/healthy tissue boundary (Maher et al., 2001). The collapse of tumors encapsulating healthy tissue has also been observed (S. Ramakrishnan, private communication). In our simple model, these features are reflected through the multiple tumor boundary reconnections.

2.5.3 Impact of Speed Filtering

We now demonstrate the necessity of speed filtering in maintaining a first order CFL time step restriction. We solve the same problem as in Section 2.5.2 with $\Delta x = \Delta y = 0.08$, $\eta = 0.1$, WENO5, Poisson2, and no speed filtering.

Without speed filtering, significant perturbations in the interface appear as early as $t = 0.02$, leading to large oscillations in the curvature because the coefficient of the curvature is order one in comparison to the other microphysical parameters. The large variations in curvature disturb the pressure solution and its gradient near the interface, which creates further feedback to disturb the interface. In Figure 2.8, we see that these disturbances quickly grow

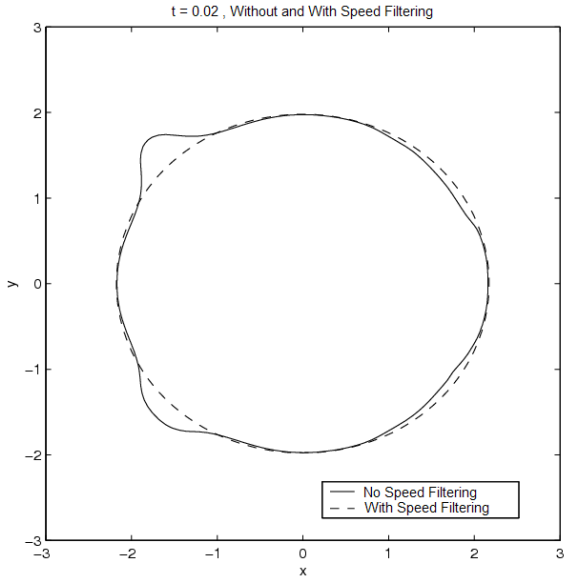

Figure 2.8: Effect of Filtering on Overall Stability and Accuracy: Initially small perturbations have grown to grossly distort the shape of the interface by $t = 0.02$. The dashed curve shows the solution at the same time with speed filtering.

to destabilize the entire simulation (solid curve). We show the same calculation with speed filtering for comparison (dashed curve).

2.5.4 Impact of the New Velocity Extension Technique

We tested the impact of the new bilinear velocity extension technique by solving the same problem as in Section 2.5.2 with either the bilinear velocity extension or the traditional PDE-based velocity extension, where one solves the PDE

$$\widetilde{V}_\tau + \text{sign}(\varphi)\, \mathbf{n} \cdot \nabla \widetilde{V} = 0 \tag{2.56}$$

to steady state. Here, $\widetilde{V}(\tau = 0)$ equals the unextended velocity (Zhao et al., 1996).

The results, shown in Figure 2.9 at $t = 2.50$, demonstrate that the bilinear velocity extension (dashed) gives results superior to those obtained with the PDE-based velocity extension (dash-dotted) when compared to the boundary integral results (solid) from Cristini et al. (2003).

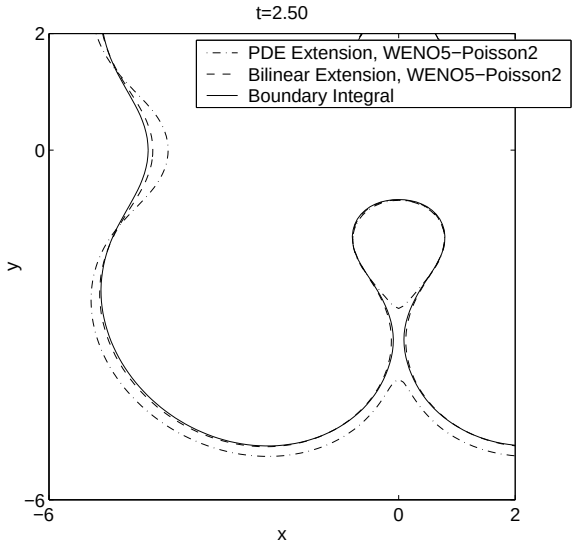

Figure 2.9: Comparison of the velocity extension techniques at $t = 2.50$ with Poisson2 and WENO5. The boundary integral solution is given by the solid curve.

2.5.5 Impact of the Curvature and Normal Vector Modifications

To study the impact of our modifications to the curvature and normal vector, we solved the system (2.7)-(2.9) again with the same setup as in Section 2.5.2. In Figure 2.10, we show the position of the interface at $t = 2.5$, 2.75, and 2.77 with both the standard (top) and modified (bottom) curvature and normal vector algorithms. Because our speed extension requires normal vectors that point away from the interface, we used the standard PDE-based extension (see Zhao et al. (1996)) for simulations with the standard curvature and normal vector routines. In the results that use the standard discretizations, an artificial "repulsive" effect can be seen that prevents approaching interfaces from merging until much later times when numerical error finally causes them to merge. In Figure 2.11, we plot the contours of the curvatures at $t = 2.5$ around the merging interfaces for both algorithms. As we can see, the modified curvature (right) is smooth, whereas the standard curvature (left) is oscillatory.

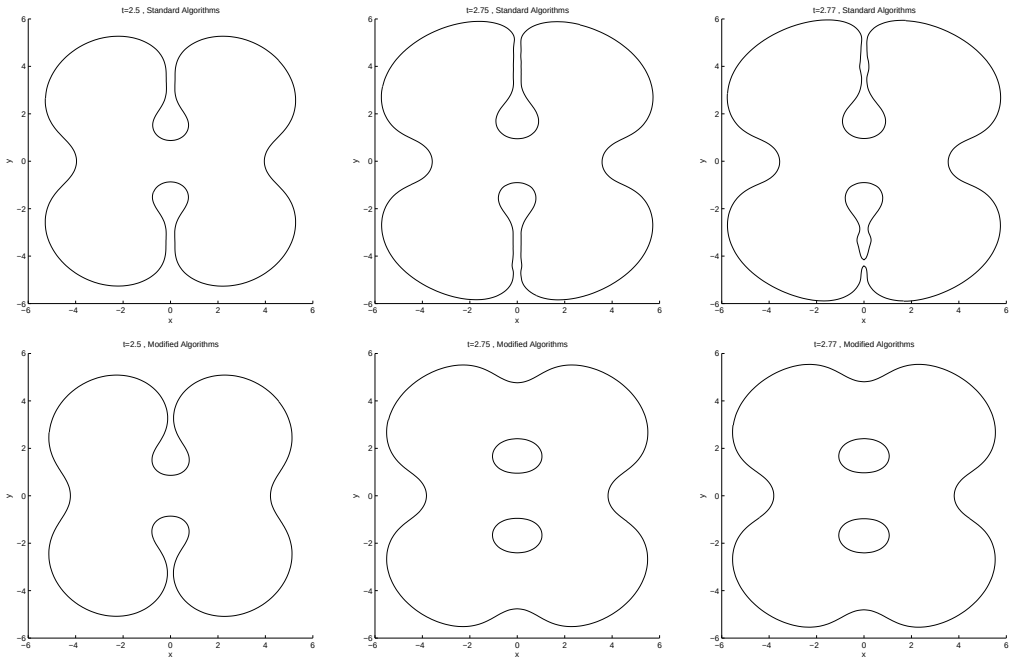

Figure 2.10: Effect of the Curvature and Normal Vector Modifications on a Tumor Growth Simulation: The plots show the solution to the problem in Section 2.5.3 at $t = 2.5$, $t = 2.75$, and $t = 2.77$. The top row shows the calculation using standard centered differences for κ and $\mathbf{n}$; the bottom row shows the same calculation with our modified algorithms.

2.6 Numerical Examples with Necrotic Effects

2.6.1 An Example with Symmetric Initial Data

To demonstrate the robustness of our technique, we next solve the system with necrosis. The initial interface is given by (2.53) as before. Here, $A = 0.0$ (i.e. no apoptosis), $G = 20.0$, $N = 0.35$, and $G_N = 1.0$. Again, we use $\Delta x = \Delta y = 0.08$, $\sigma = 3\Delta x = 0.24$, and $\eta = 0.1$. We use Poisson2 and WENO5 with our bilinear velocity extension method.

We begin by demonstrating the convergence of the overall numerical solution. As in Section 2.5.2, we determine the order by considering ratios of the differences in the numerical solutions at three spatial resolutions ($2\Delta x, \Delta x$, and $\frac{1}{2}\Delta x$). The results, given in Table 2.6, clearly demonstrate the second order accuracy of the overall method, indicating that necrosis (and the associated discontinuities in the second derivatives of the pressure) does not affect the result.

In Figure 2.12, the morphologies of the growing tumor are shown. In this figure, we see

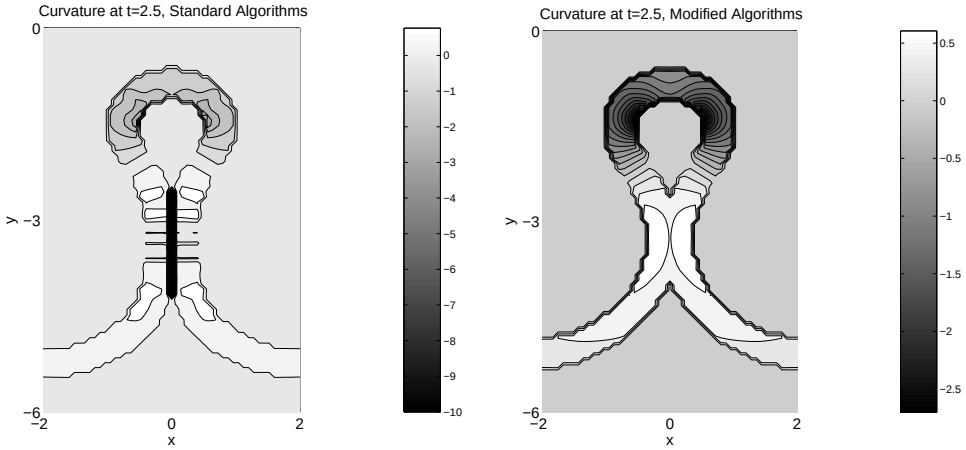

Figure 2.11: Effect of the Curvature and Normal Vector Modifications on a Tumor Growth Simulation: The left plot shows the curvature at $t = 2.5$ using the standard algorithms (The black regions are where $\kappa \sim -1e3$); the right plot shows the curvature using our modified algorithms at the same time.

that as the tumor grows, healthy tissue is captured as morphological instability occurs, just as in the non-necrotic case. (See Figures 2.6-2.7.) This capture of healthy tissue is repeated, leading to a complex, lattice-like structure. A necrotic core (indicated as a black region) first develops in the center of the tumor, splits, and also changes morphology multiple times.

In our implementation, $c = 1$ on the boundary of the captured regions. This mimics the vascularization of the tumor from a third spatial dimension, thereby providing an source of nutrient internal to the tumor. In addition, the velocity along the boundaries of the captured regions is determined from Darcy's law, where the pressure gradient is taken from the tumor side of the interface. This allows the captured regions to grow or shrink depending upon the local tumor pressure gradient. For example, if the normal velocity is negative, this mimics the pulling of healthy tissue from the third spatial dimension into the tumor interior. This expansion could also be interpreted as mimicking the compressibility of the healthy tissue. (In the future, we will modify these internal boundary conditions to be more realistic and allow nutrient to diffuse into the captured healthy tissue instead, and we will and prescribe limits on the volume change of the captured regions.)

Observe in Figure 2.12 that the necrotic core is roughly equidistant to the tumor/healthy tissue interfaces; the distance is the (diffusion) length that the nutrient molecules diffuse before they are consumed by cells. Beyond this diffusion distance, the levels of nutrient are

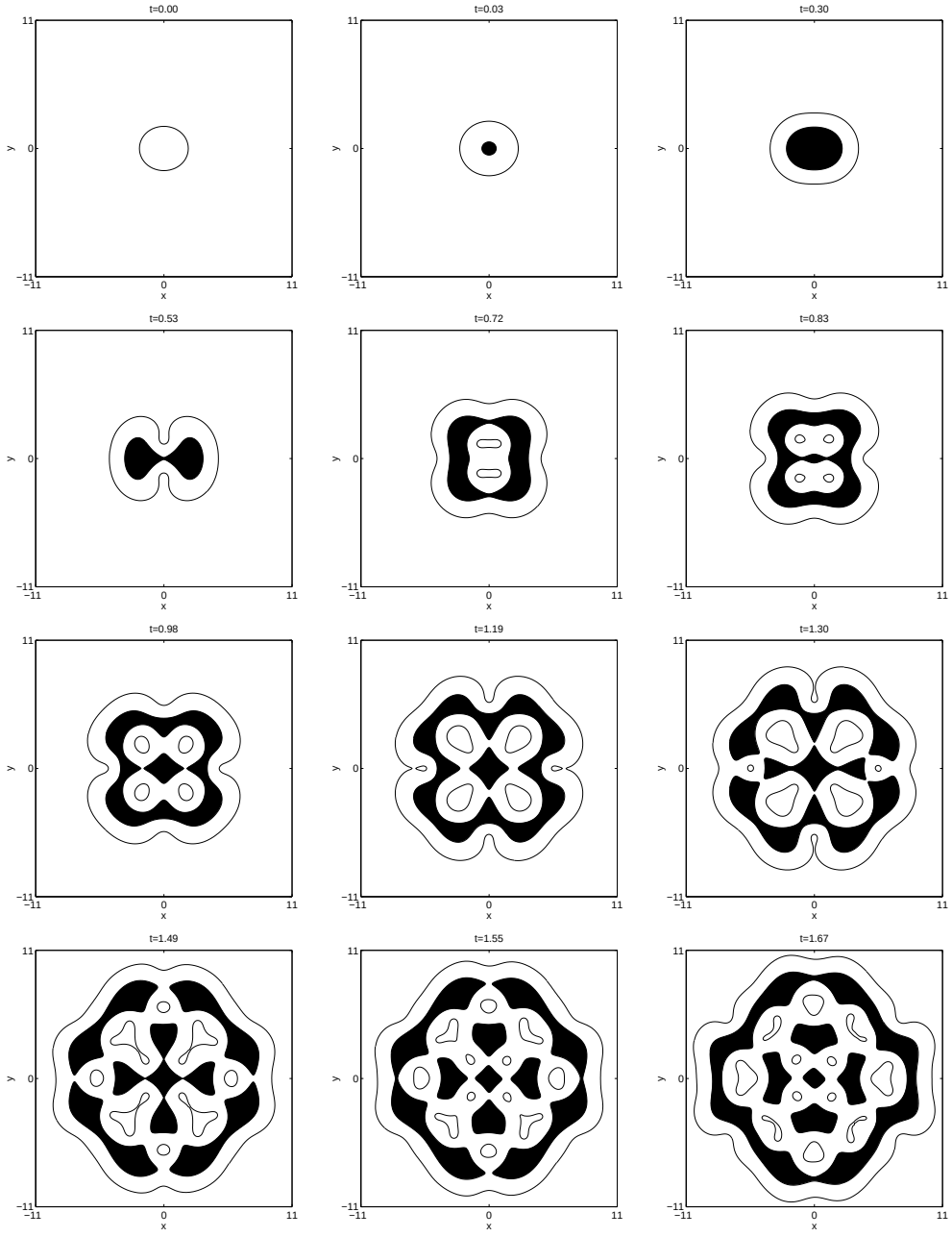

Figure 2.12: A simulation including necrotic effects. The necrotic regions are shown in black.

too low for cells to be viable.

Note that it would be very difficult to perform such a simulation with the boundary integral techniques used by Cristini et al. (2003) due to the frequent morphological changes

in both the tumor boundary and the necrotic core.

2.6.2 An Example with Asymmetric Initial Data

We give one final example with necrotic effects. We consider an asymmetric initial interface. We again solve (2.7)-(2.9) with the initial interface as given in Figure 2.13. Here, $A = 0.5$, $G = 20.0$, $N = 0.5$, and $G_N = 1.0$. As before, we use $\Delta x = \Delta y = 0.08$, $\sigma = 3\Delta x = 0.24$, and $\eta = 0.1$. We use Poisson2 and WENO5 with the bilinear velocity extension. We plot our solution in 1.00 time-unit increments in Figure 2.13. An evolution analogous to that seen in Figures 2.6-2.7 and Figure 2.12 is observed. Because the necrotic parameter is larger in this simulation, the lattice-like structure observed in Figures 2.7 and 2.12 is more pronounced. Notice that despite the initial asymmetry, the lattice structure attains a level of regularity in its pattern. In addition, growth occurs through a "bump-by-bump" mechanism, where the tumor expands by the growth of small bumps that invade the neighboring region. This growth mechanism has been recently observed by Frieboes et al. (2006b) in experiments on tumor spheroids. See Figure 2.14.

2.7 Conclusions and Future Work

In this paper, we developed a second order accurate ghost fluid/level set algorithm for the evolution of interfaces whose normal velocity is given by the normal derivatives of solutions to interior Poisson equations with curvature-dependent boundary conditions. The algorithm is capable of describing complex morphologies including pinchoff and merger of interfaces. In particular, we developed a new Poisson solver capable of capturing geometric boundary conditions on a complicated interface. We developed geometry-aware discretizations of the normal vectors and curvature that automatically detect and cope with level set irregularity, particularly during morphological changes. We also developed new gradient and velocity extension techniques that take full advantage of the geometric information embedded in the level set function to obtain greater accuracy and faster computational speed than techniques currently in use. To maintain stability, we applied Gaussian filter techniques often used in image processing to smooth the extended velocity while preserving the overall accuracy.

We validated the algorithm by simulating a model for tumor growth and comparing the numerical results to exact solutions and to spectrally accurate boundary integral results.

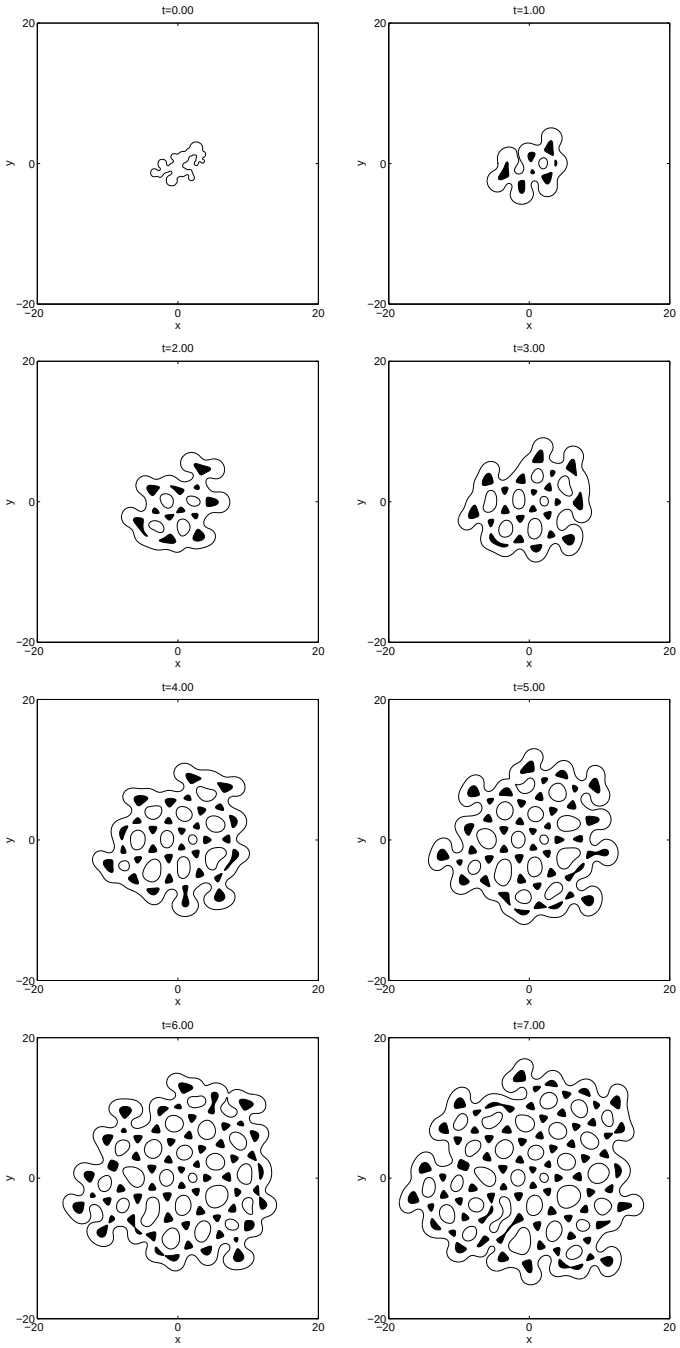

Figure 2.13: A simulation including necrotic effects with asymmetric initial data. The necrotic regions are shown in black.

We provided numerical evidence that our algorithm (i.e. WENO5 for the level set equation,

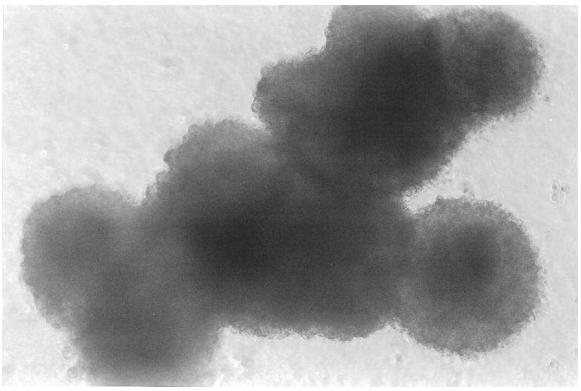

Figure 2.14: *In vitro* glioblastoma from Frieboes et al. (2006b) growing by the "bump-by-bump" mechanism.

Poisson2 for the interior Poisson equations, linear interpolation to determine the interface position, cubic interpolation for the curvature at the interface, bilinear velocity extension off the interface and Gaussian filtering for the normal velocity) indeed achieves full second order accuracy, even when the coefficient of the curvature is order one (with respect to the other microphysical parameters). This is the first such demonstration we are aware of in the context of a fully-coupled, nonlinear moving boundary problem with geometric boundary conditions (curvature).

We also went beyond the morphologies that can be described by the boundary integral method and presented accurate simulations of complex, evolving tumor morphologies that demonstrate the repeated encapsulation of healthy tissue in the primary tumor domain– an effect seen in the growth of real tumors.

In future work, we plan to continue developing and simplifying our new normal vector, curvature, and gradient extension routines. In addition, we will also develop implicit time integration schemes as an alternative means to remove the stiffness. We will apply and enhance the numerical techniques we have developed to study the biophysics of tumor growth. In a future work, we will consider more realistic microphysical parameters (i.e. A, G and G_N) by allowing spatial and temporal variability in order to study the morphological response of the tumors to chemotherapy, tissue inhomogeneity, and genetic mutations with the basic techniques developed here (Macklin and Lowengrub, 2007).

2.8 Acknowledgments

The authors gratefully thank Vittorio Cristini for discussions concerning this work. The authors also thank the Network and Academic Computing Services (NACS) at the University of California at Irvine (UCI) and the Minnesota Supercomputer Institute for generous computing resources. P. Macklin acknowledges support from the the National Science Foundation (Graduate Research Fellowship) as well as the Department of Mathematics and the Department of Biomedical Engineering at UCI. J. Lowengrub thanks the National Science Foundation (mathematics division) for partial support. We gratefully thank the mathematics and biomedical engineering departments for the use of computational resources funded by a National Science Foundation SCREMS grant and the Whitaker Foundation.

2.9 Extrapolations for the Poisson Solver

In Section 2.4.1, if Σ intersected $[x_{i-1}, x_{i+1}]$, we discretized u_{xx} at x_i by replacing u_{i+1} (or u_{i-1}) by an extrapolated value $\widehat{u}_{i+1}$ (or $\widehat{u}_{i-1}$). For completeness, we give the extrapolations for these cases here.

If $x_i < x_\Sigma \leq x_{i+1}$, then we extrapolate from interior and boundary data to replace $\widehat{u}_{i+1}$ in the discretization of u_{xx} at x_i. Some possible discretizations include:

1. **Cubic Extrapolation:** If $\{x_{i-3}, x_{i-2}, x_{i-1}\} \subset \Omega$ as described in (2.15), then we extrapolate $\widehat{u}_{i+1}$ from u_{i-3}, u_{i-2}, u_{i-1}, and u_Σ, where

$$u_\Sigma = u(x_\Sigma) = g(x_\Sigma) = g_\Sigma. \tag{2.57}$$

2. **Quadratic Extrapolation:** If $\{x_{i-2}, x_{i-1}\} \subset \Omega$, then we define $u_\Sigma = g_\Sigma$ as before, and we extrapolate $\widehat{u}_{i+1}$ from u_{i-2}, u_{i-1}, and u_Σ.

3. **Linear Extrapolation:** If $x_{i-1} \in \Omega$, then we define $u_\Sigma = g_\Sigma$ as before, and we define a linear extrapolation via

$$\widehat{u}_{i+1} = (1-\theta)(u_i - u_{i-1}) + g_\Sigma. \tag{2.58}$$

If $x_{i-1} \leq x_\Sigma < x_i$, then we extrapolate from interior and boundary data to replace $\widehat{u}_{i-1}$ in the discretization of u_{xx} at x_i. Some possible discretizations include:

1. **Cubic Extrapolation:** If $\{x_{i+3}, x_{i+2}, x_{i+1}\} \subset \Omega$, then we use cubic extrapolation from u_{i+3}, u_{i+2}, u_{i+1}, and u_Σ, where

$$u_\Sigma = u(x_\Sigma) = g(x_\Sigma) = g_\Sigma. \tag{2.59}$$

2. **Quadratic Extrapolation:** If $\{x_{i+2}, x_{i+1}\} \subset \Omega$, then we define $u_\Sigma = g_\Sigma$ as before, and we extrapolate $\widehat{u}_{i-1}$ from u_Σ, u_{i+1}, and u_{i+2}.

3. **Linear Extrapolation:** If $x_{i+1} \in \Omega$, then we define $u_\Sigma = g_\Sigma$ as before, and our linear extrapolation of $\widehat{u}_{i-1}$ is

$$\widehat{u}_{i-1} = g_\Sigma - \theta(u_{i+1} - u_i). \tag{2.60}$$

Chapter 3

Improved Numerical Techniques with Application to the Tumor Growth Model

Note:

This chapter is based upon Macklin and Lowengrub (2006), which can be accessed at http://dx.doi.org/10.1016/j.jcp.2005.11.016.

Chapter Abstract:

An advantage of using level set methods for moving boundary problems is that geometric quantities such as curvature can be readily calculated from the level set function. However, in topologically challenging cases (e.g., when two interfaces are in close contact), level set functions develop singularities that yield inaccurate curvatures when using traditional discretizations. In this note, we give an improved discretization of curvature for use near level set singularities. Where level set irregularities are detected, we use a local polynomial approximation of the interface to construct the level set function on a local subgrid, where we can accurately calculate the curvature using the standard 9-point discretization. We demonstrate that this new algorithm is capable of calculating the curvature accurately in a variety of situations where the traditional algorithm fails and provide numerical evidence that the method is second-order accurate. Examples are drawn from modified Hele-Shaw flows and models of solid tumor growth.

3.1 Introduction

Many important physical problems involve the motion of free boundaries or interfaces with velocities dependent upon curvature. For instance, in Hele-Shaw multiphase flows, tumor growth, and crystal growth, the motion of interfaces depends nonlocally upon the derivatives of curvature. Therefore, the stable and accurate computation of curvature is paramount when simulating such systems. This is particularly important in regions where interfaces are in near contact.

Level set methods have been used with good success to implicitly track moving interfaces and automatically detect topology changes in these problems (Osher and Fedkiw, 2001, 2002; Osher and Sethian, 1988; Sethian, 1999; Sethian and Smereka, 2003). However, level set functions develop discontinuities in their derivatives near regions of topological change, making the curvature discretization problematic. In Macklin (2003) and Macklin and Lowengrub (2005), it was demonstrated that if the curvature is computed without regard for the local geometry by using standard centered difference algorithms as proposed by Osher and Fedkiw (2002), Osher and Fedkiw (2001), Osher and Sethian (1988), Sethian (1999), and Sethian and Smereka (2003), then the curvature becomes oscillatory and inaccurate for interfaces in near contact. This may lead to sudden spikes in the curvature error. Refining the mesh near topology changes may delay the onset of these problems but cannot eliminate them. For example, we show a case in which mesh refinement delays the formation of spikes but actually increases the spike magnitude. In our example, this can lead to the blow-up of the solution when using a traditional curvature discretization. Furthermore, due to computational cost, mesh refinement cannot be continued indefinitely as the distance between interfaces approaches zero.

In Macklin (2003) and Macklin and Lowengrub (2005), a complicated curvature discretization was given that addressed the accurate approximation of curvature in complex 2D geometries in the context of a nonlinear model of tumor growth. In this paper, we introduce a simpler and more robust geometry-aware curvature discretization that can be extended to 3 dimensions. We calculate the curvature using standard level set methods when the level set function is sufficiently smooth. Otherwise, our method works by first constructing a properly-oriented (least squares, quadratic) polynomial approximation of the interface through a point. With this curve, we create a local level set function with which to compute the curvature by a standard discretization on a local subgrid.

In our work, we have found that using a local level set function is more robust in calculating the curvature than directly differentiating an interpolating spline (Macklin, 2003; Macklin and Lowengrub, 2005). Alternative methods of representing the curve (e.g., B-splines; see de Boor (1978), Li et al. (2005), and Segall and Sipics (2004)) can be used together with our method, but we find that quadratic least squares polynomial approximations are easy to implement and sufficient for second-order accuracy.

Our method calculates the curvature accurately in a variety of difficult topological situations (e.g., merging interfaces, drop fragmentation), as we demonstrate in examples of modified Hele-Shaw multiphase flow and *in vivo* tumor growth. In the Hele-Shaw example, we present numerical evidence of second-order convergence. Furthermore, we also demonstrate that in this example, the traditional curvature discretization fails in a way that is worsened by decreasing the mesh size. Our method is generally applicable to any level set model involving morphological changes or interfaces in near contact, e.g., multiphase flows (e.g., Sethian and Smereka (2003)), dendritic crystal growth (e.g., Gibou et al. (2003)), and image processing (e.g., Osher and Fedkiw (2002) and Sethian (1999)).

3.2 Overview

Traditional level set methods (e.g., Osher and Fedkiw (2002), Osher and Fedkiw (2001), Osher and Sethian (1988), Sethian (1999), and Sethian and Smereka (2003)) compute curvature as

$$\kappa = \nabla \cdot \left(\frac{\nabla \varphi}{|\nabla \varphi|} \right) = \frac{\varphi_{xx}\varphi_y^2 - 2\varphi_x\varphi_y\varphi_{xy} + \varphi_{yy}\varphi_x^2}{\left(\varphi_x^2 + \varphi_y^2\right)^{3/2}}, \tag{3.1}$$

where φ is an approximation of the signed distance function to the interface Γ. On a Cartesian grid, this divergence is generally calculated at node points by using a 9-point stencil with centered differences for all the partial derivatives.

Suppose we have a level set function φ defined on a Cartesian grid with mesh points given by $X \times Y = \{x_i\}_{i=1}^{M} \times \{y_j\}_{j=1}^{N}$ and we require the curvature $\kappa(x, y)$ at an interior point $(x, y) \in [x_i, x_{i+1}) \times [y_j, y_{j+1})$. If the level set function is sufficiently smooth to compute the curvature $\kappa(x_k, y_\ell)$ at each mesh point $(x_k, y_\ell) \in \{x_k\}_{k=i-1}^{i+2} \times \{y_\ell\}_{\ell=j-1}^{j+2}$, then we can accurately compute $\kappa(x, y)$ by calculating the curvature at these 16 mesh points (with the 9-point stencil) and using bicubic interpolation[1]. If the level set function is only

[1] In our testing, this gives a second-order accurate curvature (Macklin, 2003; Macklin and Lowengrub, 2005)

sufficiently smooth to compute the curvature $\kappa(x_k, y_\ell)$ at each of the four mesh points $(x_k, y_\ell) \in \{x_i, x_{i+1}\} \times \{y_j, y_{j+1}\}$, then we proceed with bilinear interpolation instead. It often occurs that the level set function is insufficiently smooth to allow even a bilinear interpolation. (See Section 3.3 for a measure of smoothness.) When two interfaces are in close contact (generally 5-7 nodes apart or less), the derivatives of φ become inaccurate and develop discontinuities in the region between the interfaces. Our method provides a means to deal with this situation accurately.

We first detect regions where the traditional curvature discretization fails. In these regions, we find a least squares quadratic, properly-oriented curve $\gamma(s)$ approximating the interface Γ near the point (x, y) where we desire the curvature. We have found that directly differentiating γ to obtain the curvature is not robust, as γ is sensitive to errors in the parameterization. Instead, we construct a local level set function $\widehat{\varphi}$ about (x, y) and use the standard 9-point stencil on a locally refined subgrid to discretize the curvature.

3.3 Detecting regions where the traditional curvature fails

In Macklin (2003) and Macklin and Lowengrub (2005), we found that if we defined a level set quality function by

$$Q(x, y) = |1 - |\nabla\varphi|| \tag{3.2}$$

and set a threshold η, then (x, y) is near a singularity of the level set function φ whenever $Q(x, y) \geq \eta$; we compute $\nabla\varphi$ using centered finite differences. In our testing, we found that using $\eta = 0.004$ reliably identified such regions without yielding false positives.

Suppose we wish to calculate the curvature at (x_i, y_j) using the standard 9-point discretization. If $Q(x, y) \geq \eta$ at any $(x, y) \in \{x_k\}_{k=i-1}^{i+1} \times \{x_\ell\}_{\ell=j-1}^{j+1}$, then the level set function is not smooth enough to accurately discretize the curvature at (x_i, y_j), and we use our geometry-aware algorithm instead.

3.4 Approximating the interface with proper orientation

Let (x, y) be contained in the mesh square $[x_i, x_{i+1}) \times [y_j, y_{j+1})$, with $\varphi(x, y) = 0$. We seek to construct an accurate approximation $\gamma(s) = (x(s), y(s))$, where s is arclength, of the interface Γ near (x, y) with proper orientation. Let $\mathbf{x_3} = (x_3, y_3) = (x, y)$, and let $s_3 = 0$ such that $\gamma(s_3 = 0) = \mathbf{x_3}$.

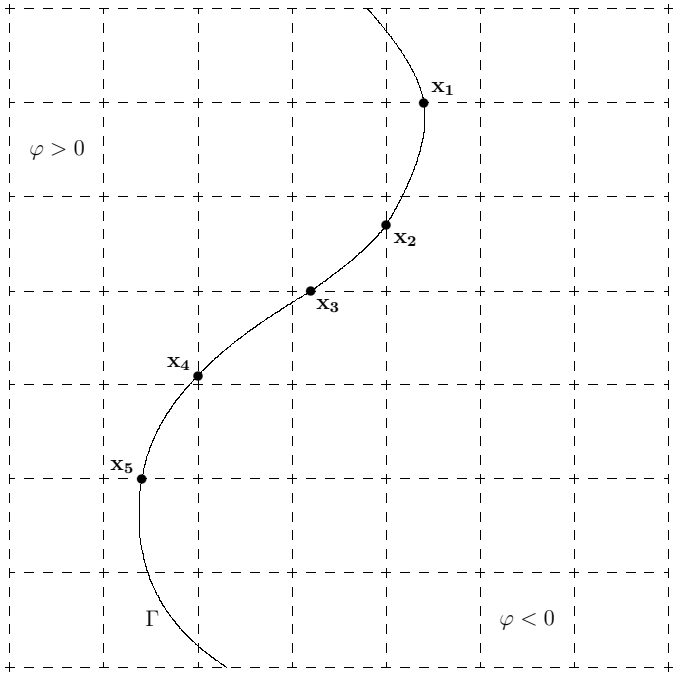

Figure 3.1: Finding points on Γ near $\mathbf{x_3}$.

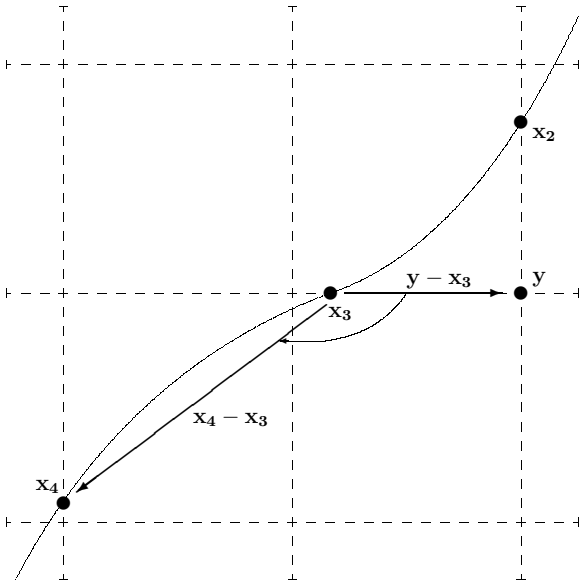

Figure 3.2: Determining the orientation of $(\mathbf{x_2}, \mathbf{x_3}, \mathbf{x_4})$: Notice that the z-component of $(\mathbf{y} - \mathbf{x_3}) \times (\mathbf{x_4} - \mathbf{x_3})$ is negative, so $\mathbf{y}$ is on the left side of the curve in this orientation.

We choose points $\mathbf{x_2} = (x_2, y_2)$ and $\mathbf{x_4} = (x_4, y_4)$ where the interface Γ intersects the mesh immediately surrounding $\mathbf{x_3}$. To improve the stability of the approximating curve we seek to construct, we choose these points to be at least $\frac{1}{10}\Delta x$ away from $\mathbf{x_3}$. Similarly, we choose a point $\mathbf{x_1} = (x_1, y_1)$ where the mesh surrounding $\mathbf{x_2}$ intersects Γ and is at least $\frac{1}{10}\Delta x$ from $\mathbf{x_2}$, and $\mathbf{x_5} = (x_5, y_5)$ is similarly chosen to be close to $\mathbf{x_4}$. See Figure 3.1.

We choose the ordering $(\mathbf{x_1}, \mathbf{x_2}, \mathbf{x_3}, \mathbf{x_4}, \mathbf{x_5})$ such that when traversing the curve in the direction of increasing arclength s, the region where $\varphi < 0$ is on the left side of the curve. The orientation of the curve can readily be determined by examining the cross product of $\mathbf{x_4} - \mathbf{x_3}$ and $\mathbf{y} - \mathbf{x_3}$, where $\mathbf{y}$ is a point off the curve. See Figure 3.2.

We choose arclengths s_1, s_2, s_4, and s_5 such that $\gamma(s_i) = \mathbf{x_i}$, for $1 \leq i \leq 5$. We then approximate these arclengths by using the linear distances between the points. That is, moving backward along the curve from $\mathbf{x_3} = \gamma(s_3)$, $s_3 = 0$, and $s_2 = -|\mathbf{x_3} - \mathbf{x_2}|$, $s_1 = s_2 - |\mathbf{x_2} - \mathbf{x_1}|$; moving forward, $s_4 = |\mathbf{x_4} - \mathbf{x_3}|$ and $s_5 = s_4 + |\mathbf{x_5} - \mathbf{x_4}|$.

Finally, let $x(s)$ and $y(s)$ be the least squares quadratic curves fitted to $\{(s_i, x_i)\}_{i=1}^5$ and $\{(s_i, y_i)\}_{i=1}^5$, respectively. We reset the constant coefficients such that $\gamma(0) = \mathbf{x_3} = (x, y)$. Notice that because $\gamma(s)$ is only used to construct the level set function on a local subgrid, it does not affect the position of the actual contour of the original level set function. Although we do not show it here, the resulting curve approximates Γ very well; this is reflected in our numerical tests in later sections.

3.5 Constructing a new local level set and computing the curvature

Lastly, we construct a local level set function near $\mathbf{x_3} = (x, y)$. For a fixed $\delta > 0$, let $\widehat{X} = \{x - \delta, x, x + \delta\}$ and $\widehat{Y} = \{y - \delta, y, y + \delta\}$, so that $\widehat{X} \times \widehat{Y}$ is a 3×3 grid centered at $\mathbf{x_3}$. See Figure 3.3. Let $\widehat{\varphi}$ be the local level set function on $\widehat{X} \times \widehat{Y}$. We can choose any desired mesh size $\delta \leq \Delta x$ and $\delta \leq \Delta y$.

For each point $\widehat{\mathbf{x}} = (\widehat{x}_i, \widehat{y}_j) \in \widehat{X} \times \widehat{Y}$, we set $\widehat{\varphi}_{i,j}$ equal to the signed distance between $\widehat{\mathbf{x}}$ and γ. (The sign is determined based upon whether $\widehat{\mathbf{x}}$ is on the left or right side of the curve.) The end result is a local construction of φ on a refined subgrid that avoids level set singularities. We compute the curvature $\kappa(x, y)$ using the standard centered differences for $\widehat{\varphi}_x$, $\widehat{\varphi}_{xx}$, $\widehat{\varphi}_{xy}$, $\widehat{\varphi}_{yy}$, and $\widehat{\varphi}_y$ on the subgrid $\widehat{X} \times \widehat{Y}$.

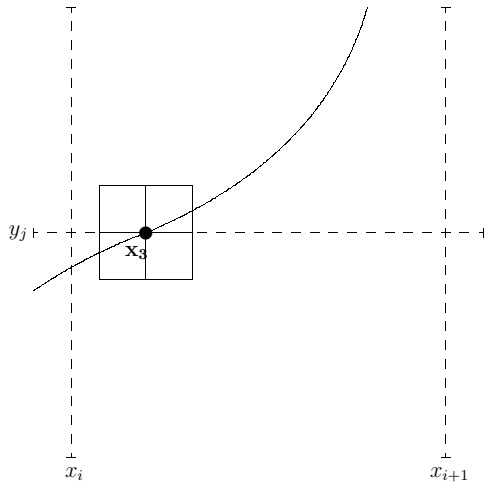

Figure 3.3: The local subgrid near $\mathbf{x_3}$, with $\delta = \frac{1}{8}\Delta x$. In our tests, we used $\delta = \frac{1}{1000}\Delta x$.

We tested with $\delta = \Delta x$, $\frac{1}{10}\Delta x$, $\frac{1}{100}\Delta x$, and $\frac{1}{1000}\Delta x$. In general, we found that all these values worked equally well when using a quadratic $\gamma(s)$. This is because the essential feature of our technique is that it removes the nearby second interface and locally rebuilds the level set function accordingly. However, smaller values tended to give more accurate results when two interfaces were in extremely close contact (less than one mesh point apart). In our remaining work, we chose $\delta = \frac{1}{1000}\Delta x$.

3.6 Numerical Examples

3.6.1 Two Drops Merging under Modified Hele-Shaw Flow

Let Γ be an interface describing the boundary of two circular drops of radius 1 centered at

$$(2.5\cos\theta, 2.5\sin\theta) \text{ and } (-2.5\cos\theta, -2.5\sin\theta), \tag{3.3}$$

respectively, where $\theta \in [0, 2\pi)$ is fixed. Let φ be a level set function for Γ, and let Γ evolve with normal velocity

$$V = 1 - \mathbf{n} \cdot [\nabla p] \qquad \text{if } \varphi(x) = 0, \tag{3.4}$$

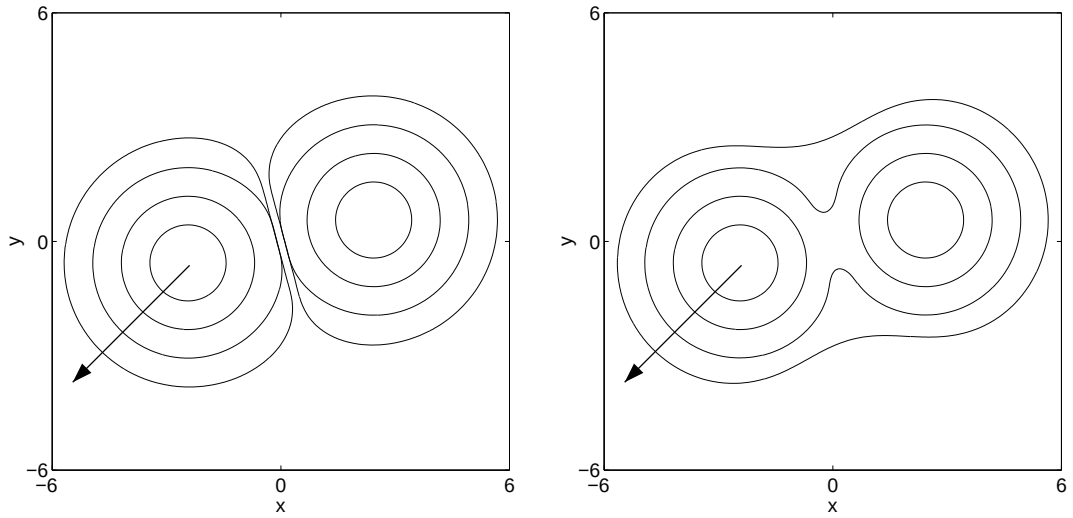

Figure 3.4: Comparison of methods for merging drops under modified Hele-Shaw flow at medium resolution. Left: Traditional curvature discretization. Right: Geometry-aware curvature discretization. Times shown: $t = 0.0$, 0.75, 1.5, 2.25.

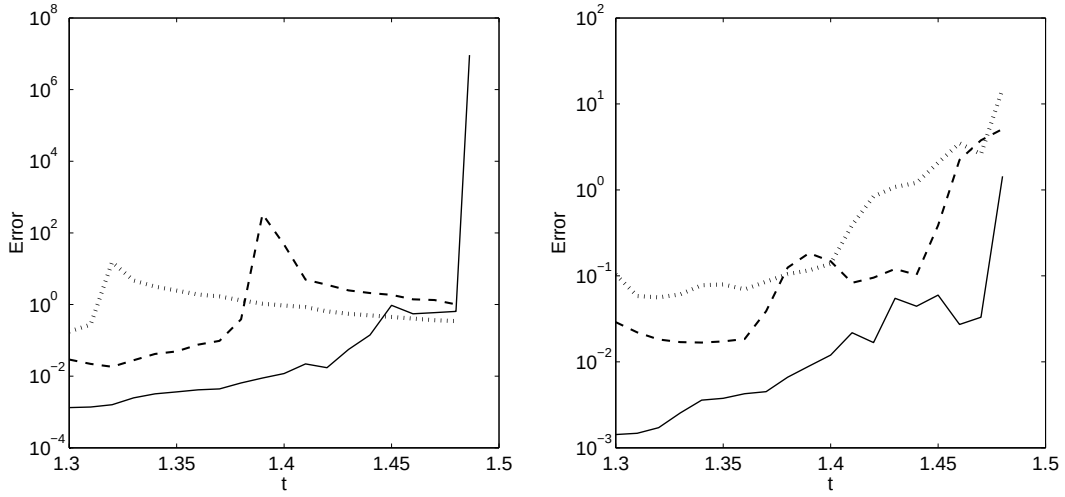

Figure 3.5: Maximum error in curvature before merging under modified Hele-Shaw flow. Left: Traditional curvature discretization. Right: Geometry-aware curvature discretization. Dotted ($\Delta x = 0.10$), dashed ($\Delta x = 0.05$), solid ($\Delta x = 0.025$).

where $[\nabla p]$ is the jump in the pressure gradient from the inside to the outside of the drops. The pressure p solves

$$\nabla^2 p = 0 \qquad \text{if} \qquad \varphi(x) < 0 \tag{3.5}$$

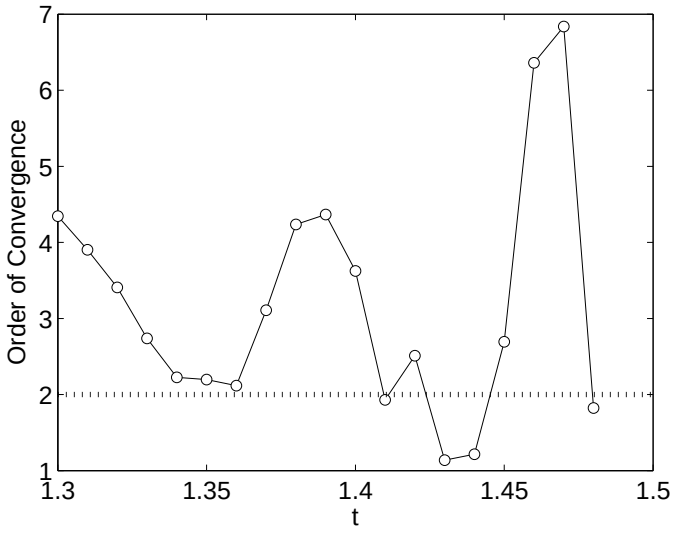

Figure 3.6: Order of convergence for the geometry-aware curvature for the modified Hele-Shaw problem.

$$[p] = \kappa \qquad \text{if} \qquad \varphi(x) = 0 \tag{3.6}$$

$$p = 0 \qquad \text{if} \qquad \varphi(x) > 0, \tag{3.7}$$

where (3.6) is the Laplace-Young boundary condition, and the surface tension (the coefficient of the curvature) is nondimensionalized to 1.

The level set function φ is updated via

$$\varphi_t + V_{ext} \left|\nabla \varphi\right| = 0, \tag{3.8}$$

where V_{ext} is an extension of V off of Γ.

Under these equations, both circles expand outward at a constant speed of 1 since $p \equiv \frac{1}{1+t}$ inside the drops and $p \equiv 0$ outside the drops. At $t = 1.5$, the drops merge and thus become noncircular. Consequently, at this time the curvature is no longer constant along the interface and instead takes large values near the intersection. The pressure p inside the drops is then no longer constant, steep pressure gradients emerge, and the Hele-Shaw-like term of the velocity dominates near the intersection of the circles.

To study the convergence behavior of our curvature technique, we solved this example with $\theta = 13^\circ$ on a computational domain of $[-6, 6] \times [-6, 6]$ with $\Delta x = \Delta y = 0.10$ (low resolution), $\Delta x = \Delta y = 0.05$ (medium resolution), and $\Delta x = \Delta y = 0.025$ (high resolution)

using the level set/ghost fluid method as described in Macklin and Lowengrub (2005). In Figure 3.4, we show the medium-resolution results ($\Delta x = 0.05$), where the interfaces are plotted every 0.75 time units from $t = 0$ to $t = 2.25$, and the arrows indicate the direction of growth. In the left plot, we show the results when using the traditional 9-point curvature discretization. The singular curvature between the merging interfaces creates steep and noisy false pressure gradients that prevent the merger of the drops. This behavior of the traditional algorithm is also seen in the low-resolution study ($\Delta x = 0.10$), and at high resolution ($\Delta x = 0.025$), the traditional curvature algorithm becomes so inaccurate that the simulation is unable to continue past $t = 1.486$. This is a non-trivial example where the traditional curvature discretization was inaccurate and led to incorrect simulation behavior, and decreasing Δx exacerbated the problem.

On the right side of Figure 3.4, we show the same simulation using our geometry-aware curvature discretization at medium resolution. (The high-resolution results are indistinguishable to graphical resolution.) Level set singularities between the merging interfaces are first detected at $t = 1.33$, and the discretization adapts accordingly. The drops merge at approximately $t = 1.48$, very close to the exact time of $t = 1.50$. Immediately after the merger, sharp cusps form in the interface that are smoothed out due to surface tension. This demonstrates that our geometry-aware curvature routine is robust and accurate even in situations involving interfaces with high curvature. Our curvature algorithm also performs well at low and high resolutions: the drops merge at $t = 1.47$ for the low-resolution study and at $t = 1.49$ for the high-resolution study, and the drops coalesce in a Hele-Shaw-dominated manner thereafter.

In Figure 3.5, we examine the maximum curvature error for the two curvature discretizations. In the left plot, we show the maximum curvature error for the traditional curvature discretization. At low resolution (dotted curve), the error for the traditional discretization has a spike at $t = 1.32$. Afterwards, the interface flattens out in the near-contact regions, the drops fail to merge, and the simulation tends to the wrong solution. Because the drops flatten rather than merge, the computed curvature is bounded away from the correct value; consequently, the error curve levels off after this initial spike. At medium resolution (dashed curve), the occurrence of this error spike is delayed until $t = 1.39$, but the magnitude of the spike increases; after the spike, the medium resolution study behaves similarly to the low-resolution study. At high resolution (solid curve), the appearance of the error spike is further delayed until $t = 1.486$, but its magnitude grows to $\sim 10^7$. Refining the

computational mesh delays the occurrence but exacerbates the magnitude of the problems inherent in the traditional curvature discretization; at high resolution, the error spike is so severe that the simulation is unable to continue.

In the right plot in Figure 3.5, we show the maximum curvature error for our geometry-aware discretization. The dotted curve gives the error at low resolution, the dashed curve the medium-resolution error, and the solid curve corresponds to high resolution. Overall, each mesh refinement improves the accuracy of our geometry-aware curvature discretization, and our geometry-aware method never experiences the large error spikes that characterize the traditional discretization. In the last several time steps, the interfaces are in very close contact (under two mesh lengths), making the conditions for accurately calculating the curvature very difficult. Even for these times, mesh refinement improves the accuracy.

In Figure 3.6, we show the order of convergence of our geometry-aware discretization:

$$\frac{\log\left(\frac{\text{max error}_{\Delta x=0.025}}{\text{max error}_{\Delta x=0.050}}\right)}{\log\left(\frac{0.025}{0.050}\right)}. \tag{3.9}$$

Note that we obtain second-order convergence or better for almost all times. The medium-resolution study first detects level set irregularity at $t = 1.33$, and the high-resolution study detects irregularity starting at $t = 1.44$; after our algorithm detects level set irregularity, it begins to use our geometry-aware discretization. Thus, between $t = 1.33$ and $t = 1.43$, the medium-resolution study uses the geometry-aware discretization between the merging interfaces while the high-resolution study continues to use the traditional 9-point stencil. In this time interval, the interfaces approach one another, the traditional curvature discretization loses accuracy for the high-resolution study, and the order of convergence steadily falls. After $t = 1.43$, the high-resolution simulation begins to use our geometry-aware discretization, and the order of convergence is restored to second-order or better until $t = 1.48$, at which time the drops begin to merge.

In the next section, we present examples that demonstrate the behavior of our adaptive curvature algorithm in the context of solid tumor growth. We shall see that the traditional curvature discretization again becomes inaccurate, leading to incorrect predictions on the behavior of the tumor growth models. Thus, the shortcomings of the traditional curvature discretization negatively impact the scientific investigation of tumor growth.

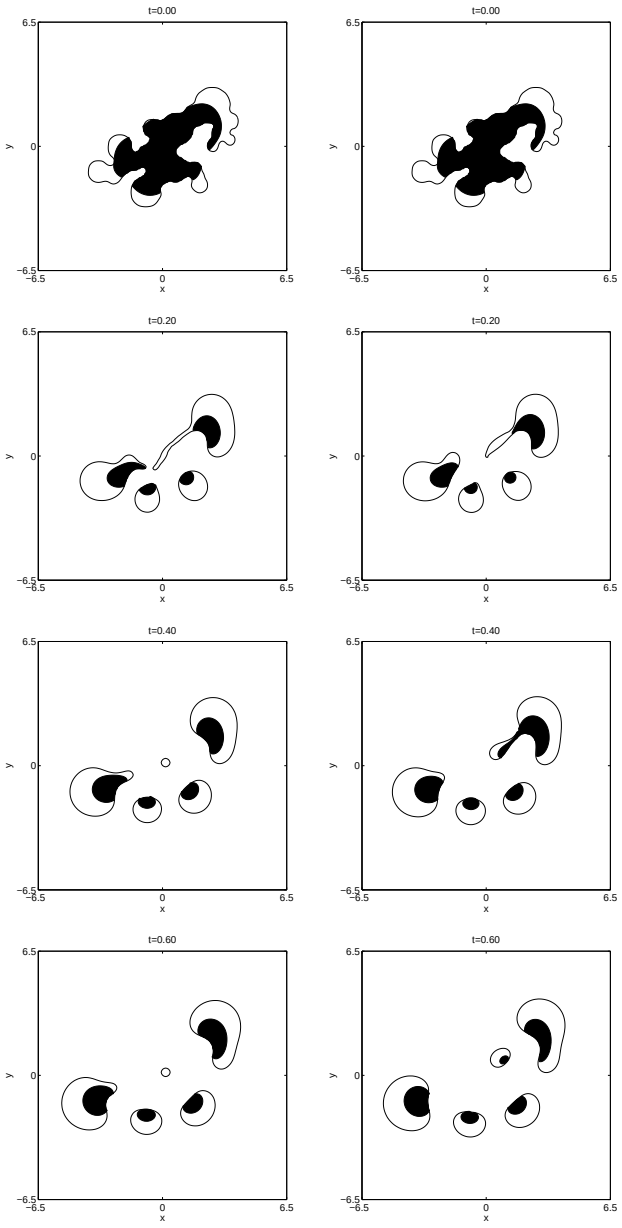

Figure 3.7: Comparison of methods for necrotic *in vivo* tumor growth. The left column uses the traditional curvature discretization; the right column uses our new geometry-aware discretization. Time increases from top to bottom in 0.2 increments from $t = 0.0$ to $t = 0.6$. The dark regions indicate necrotic regions where the tumor cells are dying due to lack of nutrient.

3.6.2 Necrotic *In Vivo* Tumor Growth

Let φ be a level set function whose zero level set denotes the boundary Γ of an avascular tumor growing into a surrounding, non-cancerous tissue. This models the early stage

of *in vivo* growth before angiogenesis occurs. Let $R = \max\{\text{dist}(\mathbf{x}, 0) : \mathbf{x} \in \Gamma\}$, and let $D_R = \{\mathbf{x} : |\mathbf{x}| \leq R + 1\}$ be a region containing the tumor and the non-cancerous tissue immediately surrounding the tumor where there is no blood vasculature. Outside D_R, the healthy tissue is assumed to have a pre-existing network of blood vessels.

Let c denote the nondimensionalized nutrient concentration within the tumor and the surrounding tissue. Outside D_R, the blood vasculature delivers sufficient nutrient that c is constant. Within D_R, the nutrient diffuses and is consumed as it enters the tumor interior. Where the nutrient level drops below a threshold value N, the tumor cells become necrotic, start to die, and are broken down by enzymes. The proliferating tumor cells generate an internal (oncotic) pressure p that pushes the tumor boundary outward with normal velocity V via Darcy's law. The enzymatic breakdown of necrotic tumor tissue is modeled by a local decrease in the pressure that slows growth. Cell-to-cell adhesive forces are modeled by a curvature boundary condition on Γ. The non-cancerous tissue in D_R is assumed to be close enough to the tumor to be affected by the pressure changes within the tumor, and the pressure is assumed to be constant outside of D_R. Accordingly, the nutrient concentration c satisfies

$$\nabla^2 c = c \qquad \text{if } \varphi(\mathbf{x}) < 0 \tag{3.10}$$

$$[c] = 0 \qquad \text{if } \varphi(\mathbf{x}) = 0 \tag{3.11}$$

$$D\nabla^2 c = 0 \qquad \text{if } \varphi(\mathbf{x}) > 0 \text{ and } \mathbf{x} \in D_R \tag{3.12}$$

$$[c] = 0 \qquad \text{if } \mathbf{x} \in \partial D_R \tag{3.13}$$

$$c = 1 \qquad \text{if } \mathbf{x} \notin D_R, \tag{3.14}$$

the oncotic pressure p is governed by

$$\nabla^2 p = G \cdot G_N \qquad \text{if } \varphi(\mathbf{x}) < 0 \text{ and } c < N \tag{3.15}$$

$$\nabla^2 p = -Gc \qquad \text{if } \varphi(\mathbf{x}) < 0 \text{ and } c \geq N \tag{3.16}$$

$$[p] = \kappa \qquad \text{if } \varphi(\mathbf{x}) = 0 \tag{3.17}$$

$$\mu\nabla^2 p = 0 \qquad \text{if } \varphi(\mathbf{x}) > 0 \text{ and } \mathbf{x} \in D_R \tag{3.18}$$

$$[p] = 0 \qquad \text{if } \mathbf{x} \in \partial D_R \tag{3.19}$$

$$p = 0 \qquad \text{if } \mathbf{x} \notin D_R, \tag{3.20}$$

and the normal velocity of the tumor boundary is given by Darcy's law:

$$V = -\mathbf{n} \cdot \nabla p \qquad \text{if } \varphi(\mathbf{x}) = 0. \tag{3.21}$$

Here, ∇p is computed on the interior side of the tumor, G is a parameter that relates to the relative proliferation rate of the tumor cells, G_N is a parameter that governs the rate of tumor cell breakdown in necrotic regions, D is the nutrient diffusivity in healthy tissue, and μ is the cellular mobility in healthy tissue. This tumor growth model is an extension of current models given in Cristini et al. (2003), Macklin (2003), Macklin and Lowengrub (2005), and Zheng et al. (2005) and will be further investigated in a future work (Macklin and Lowengrub, 2007).

In Figure 3.7, we solve this system with a random initial shape, $\Delta x = \Delta y = 0.08$, $G = 20.0$, $G_N = 1.0$, and $N = 0.35$. In the left column, we solve using the traditional curvature discretization, and in the right column, we use our new geometry-aware discretization. Time increases from top to bottom in 0.2 increments from $t = 0$ to $t = 0.6$. In the simulations, widespread fragmentation of the tumor occurs, and the remaining small tumor nodules move away from one another. The fragmentation is due to the combined effects of the diffusing nutrient concentration, selective proliferation in the high-nutrient regions (the nutrient is highest on ∂D_R), and the variable pressure outside the tumor. This will be explored at length in a forthcoming paper (Macklin and Lowengrub, 2007).

Notice that significant tumor fragmentation occurs for both curvature discretizations, but the discretizations yield significantly different results on the times of fragmentation; the shape, size, and location of fragments; and whether or not the fragments contain necrotic regions. This is important in the study of malignant tumors, where the fragmentation of tumor masses may lead to the development of metastases. Furthermore, the location and quantity of necrotic tumor cells has a great impact on the development of blood vessels in tumors (angiogenesis) (Zheng et al., 2005), and so the failures of the traditional curvature discretization may lead to erroneous predictions of the morphology and the subsequent vascular development of a tumor.

3.7 Conclusions

We have developed an improved geometry-aware discretization of curvature for use near level set singularities. In our method, we first detect regions where the traditional curvature discretization fails. Then, we find a least squares, oriented quadratic polynomial approximation of the interface centered at the point where we desire the curvature. A local level set function is constructed, and a standard 9-point stencil is used on a local subgrid

to discretize the curvature.

We have demonstrated that for complex geometries (e.g., interfaces in near contact), the traditional curvature discretization produced results that were not improved by mesh refinement, whereas our geometry-aware algorithm was second-order accurate and robust. Examples were given for modified Hele-Shaw flow and *in vitro* tumor growth. In the tumor growth example, it was demonstrated that an accurate and robust curvature discretization is critical for the accurate modeling of the biophysical properties of evolving tumors. Our method is generally applicable to any level set model involving morphological changes or interfaces in near contact, e.g., multiphase flows, dendritic crystal growth, and image processing.

Lastly, we note that the geometry-aware curvature discretization developed here can be extended to three dimensions by finding an approximating surface

$$\gamma(s_1, s_2) = (x(s_1, s_2), y(s_1, s_2), z(s_1, s_2))$$

and constructing a $3 \times 3 \times 3$ local level set function. We also note that this method could be used to improve the accuracy of normal vector discretizations near level set singularities; this is currently under study.

3.8 Acknowledgments

The authors gratefully thank Vittorio Cristini and Steven Wise for enlightening discussions concerning this work. The authors also thank the Network and Academic Computing Services (NACS) at the University of California at Irvine (UCI) and the departments of mathematics and biomedical engineering at UCI for generous computing resources. We thank the National Science Foundation (mathematics division) for partial support.

Chapter 4

A Numerical Study of the Effect of Microenvironment on Tumor Growth

Note:

This chapter is based upon Macklin and Lowengrub (2007). To access the original paper, please visit http://dx.doi.org/10.1016/j.jtbi.2006.12.004.

Chapter Abstract:

In this paper, we present and investigate a model for solid tumor growth that incorporates features of the tumor microenvironment. Using analysis and nonlinear numerical simulations, we explore the effects of the interaction between the genetic characteristics of the tumor and the tumor microenvironment on the resulting tumor progression and morphology. We find that the range of morphological responses can be placed in three categories that depend primarily upon the tumor microenvironment: tissue invasion via fragmentation due to a hypoxic microenvironment; fingering, invasive growth into nutrient-rich, biomechanically unresponsive tissue; and compact growth into nutrient-rich, biomechanically responsive tissue. We find that the qualitative behavior of the tumor morphologies is similar across a broad range of parameters that govern the tumor genetic characteristics. Our findings demonstrate the importance of the impact of microenvironment on tumor growth and morphology and have important implications for cancer therapy. In particular, if a treatment impairs nutrient transport in the external tissue (e.g., by anti-angiogenic therapy), increased tumor fragmentation may result, and therapy-induced changes to the biomechanical properties of the tumor or the microenvironment (e.g., anti-invasion therapy) may push the tumor in or out of the invasive fingering regime.

4.1 Introduction

Cancer is a fundamental scientific and societal problem, and in the past few decades, vast resources have been expended in an effort to understand the root causes of cancer, to elucidate the intricacies of cancer progression, and to develop effective prevention and treatment strategies. In this paper, we present and investigate a model for solid tumor growth that incorporates features of the tumor microenvironment. Using analysis and nonlinear numerical simulations, we explore the effects of the interaction between the genetic characteristics of the tumor and the tumor microenvironment on the resulting tumor progression and morphology. Implications for cancer therapies are discussed.

Cancer is marked by several increasingly aggressive stages of development. The first stage, *carcinogenesis*, is believed to be characterized by a sequence of genetic mutations that promote growth (i.e., acquisition of oncogenes), circumvent apoptosis (i.e., inactivation or loss of tumor suppressor genes), or hinder DNA repair processes, thereby increasing the probability of acquiring oncogenes or inactivating tumor suppressor genes. (e.g. see Hanahan and Weinberg (2000) and Lehmann (2001).) In the second stage of development, *avascular growth* occurs as the cancer cells proliferate and form an *in situ* cancer. The local production of matrix-degrading enzymes and subsequent degradation of the extracellular matrix (ECM) may also play a role in providing room for the tumor to expand into the surrounding tissue. (See Hotary et al. (2003) and the discussion throughout Anderson (2005).) Since the tumor lacks a vasculature, nutrients (e.g., glucose and oxygen) are received only by diffusion through the surrounding tissue. As the tumor grows, less nutrient reaches the center of the tumor. Interior cells become hypoxic, begin to die (*necrose*), and are broken down by enzymes. As cell death in the tumor interior balances with cell proliferation on the boundary, a spherical tumor may reach a diffusion-limited size, usually on the order of 2-4 mm. However, if the tumor boundary acquires an irregular shape, additional nutrient becomes available to the tumor interior due to the increased surface area to volume ratio, and continued growth may result. Indeed, there are now a number of *in vitro* studies in which complex growth morphologies have been observed. (e.g. see Bredel-Geissler et al. (1992), Mueller-Kleiser (1997), Hedlund et al. (1999), Enmon Jr. et al. (2001), and Frieboes et al. (2006b).)

The next stage of tumor growth, *angiogenesis*, is characterized by the development of a tumor-induced neovasculature that grows from the main circulatory system toward the

tumor in response to the imbalance of pro-angiogenic growth factors that are released by hypoxic cells in the tumor (e.g., vascular endothelial cell growth factor, or VEGF) relative to anti-angiogenic growth factors (e.g., angiostatin) present in the tumor microenvironment (Carmellet and Jain, 2000). In the final stage of tumor progression, *vascular growth*, the tumor is supplied with nutrients from the newly-developed, although typically inefficient vasculature (Jain, 1990; Haroon et al., 1999; Hashizume et al., 2000). Additional mutations and epigenetic events may occur that lead to increased cellular motility and greater production of matrix degrading enzymes that degrade the ECM. This can lead to *invasion*, where either individual or collections of cancerous cells protrude and/or separate from the tumor and migrate through the surrounding tissue, or *metastasis*, where the invading tumor cells (or cell collections) enter the blood vasculature and/or lymphatic system and travel to distant locations.

The tumor microenvironment plays a crucial role in these processes. (e.g., see Höckel et al. (1996), Enam et al. (1998), Schmeichel et al. (1998), Sansone et al. (2002), and Pennacchietti et al. (2003).) For example, hypoxic microenvironments lead to the upregulation of HIF-1 target genes in both tumor cells and endothelial cells, including those responsible for the secretion of angiogenic growth factors and matrix degrading enzymes, metabolic changes such as increased glycolysis, and decreased cell-cell and cell-matrix adhesion (Kaur et al., 2005; Erler et al., 2006; Pouysségur et al., 2006). These conditions are associated with increased tumor invasiveness (Kaur et al., 2005; Erler et al., 2006; Pouysségur et al., 2006) and poor patient outcome (Höckel et al., 1996). However, the effects of the interaction between intra- and extratumoral processes on tumor progression and morphology are not well understood. Mathematical modeling has the potential to provide insight into these interactions though systematic studies of fundamental constituent processes.

Over the past ten years, the interest in the mathematical modeling and numerical simulation of cancer has increased dramatically. (See the reviews by Adam (1996), Bellomo et al. (2003), and Araujo and McElwain (2004a), Byrne et al. (2006), Sanga et al. (2006), and Quaranta et al. (2005).) A variety of modeling strategies is now available, each of which is well-suited to investigate one or more aspect of cancer. Cellular automata and agent-based modeling, where individual cells are simulated and updated based upon a set of biophysical rules, are particularly useful for studying carcinogenesis, natural selection, genetic instability, and interactions of individual cells with each other and the microenvironment. Because these methods are based on a series of rules for each cell, it is straightforward

to translate biological processes (e.g., complex mutation pathways) into model rules. On the other hand, these models can be difficult to study analytically, and the computational cost increases rapidly with the number of cells modeled. Because a 1 mm tumor spheroid has over 500,000 cells, these methods can quickly become unwieldy when studying tumors of any significant size. For some examples of cellular automata modeling, see Anderson (2005), Alarcón et al. (2003), and Mallett and de Pillis (2006), and see Mansury et al. (2002) and Abbott et al. (2006) for examples of agent-based modeling.

In larger-scale systems where the cancer cell population is on the order of 1,000,000 or more, continuum methods provide a good modeling alternative. Early work (e.g. Greenspan (1976), Byrne and Chaplain (1996b), Byrne and Chaplain (1996a)) used ordinary differential equations (ODEs) to model cancer as a homogeneous population, as well as partial differential equation (PDE) models restricted to spherical geometries. Linear and weakly nonlinear analyses have been performed to assess the stability of spherical tumors to asymmetric perturbations (e.g., Chaplain et al. (2001), Byrne and Matthews (2002), Cristini et al. (2003), and Li et al. (2006), and discussed in the reviews by Araujo and McElwain (2004a) and Byrne et al. (2006)) as a means to characterize the degree of aggression. Various interactions of the tumor with the microenvironment, such as stress-induced limitations of tumor growth, have also been studied in this context (e.g., Jones et al. (2000), Ambrosi and Mollica (2002, 2004), Roose et al. (2003), Araujo and McElwain (2004b, 2005), and Ambrosi and Guana (2006)). Most of the previous modeling has considered single-phase tumors. More recently, multiphase mixture models have been developed to provide a more detailed account of tumor heterogeneity. (e.g., see the work by Ambrosi and Preziosi (2002), Byrne and Preziosi (2003), and Chaplain et al. (2006).)

Very recently, nonlinear modeling has been performed to study the effects of shape instabilities on avascular, angiogenic, and vascular solid tumor growth. Cristini, Lowengrub, and Nie used boundary integral methods and performed the first fully nonlinear simulations of a continuum model of tumor growth in the avascular and vascularized growth stages with arbitrary boundaries (Cristini et al., 2003). This work investigated the nonlinear regime of shape instabilities and predicted the encapsulation of external, non-cancerous tissue by morphologically unstable tumors. Interestingly, shape instabilities were found to occur only in the diffusion-dominated, avascular regime of growth. The effect of the extratumoral microenvironment was not considered.

Zheng et al. (2005) extended this model to include angiogenesis and an extratumoral

microenvironment by developing and coupling a new level set implementation with a hybrid continuous-discrete angiogenesis model originally developed by Anderson and Chaplain (1998). Zheng et al. investigated the nonlinear coupling between growth and angiogenesis. As in Cristini et al. (2003), it was found that low-nutrient (e.g. hypoxic) conditions may lead to instability. Zheng et al. did not fully investigate the interaction between the growth progression and the tumor microenvironment, but their work served as a building block for recent studies of the effect of chemotherapy on tumor growth by Sinek et al. (2004) and for studies of morphological instability and invasion by Cristini et al. (2005) and Frieboes et al. (2006b). Hogea et al. (2006) have also begun investigating tumor growth and angiogenesis using a level set method coupled with a continuous model of angiogenesis. In addition, Frieboes et al. (2006a) and Wise et al. (2006) have recently developed a diffuse interface implementation of solid tumor growth to study the evolution of multiple tumor cell species during progression.

In Macklin (2003) and Macklin and Lowengrub (2005, 2006), we also considered a level set-based extension of the tumor growth model that was previously investigated by Cristini et al. (2003) (described above). In these works, we developed new, highly-accurate numerical techniques to solve the resulting system of partial differential equations in a moving domain. These numerical methods are more accurate than those used by Zheng et al. (2005) and Hogea et al. (2006). Using these methods, we modeled tumor growth under a variety of conditions and investigated the role of necrosis in destabilizing the tumor morphology. We demonstrated that non-homogeneous nutrient diffusion inside the tumor leads to heterogeneous growth patterns that, when interacting with cell-cell adhesion, cause sustained morphological instability during tumor growth, as well as the repeated encapsulation of noncancerous tissue by the growing tumor.

In this paper, we extend the tumor growth models considered by Cristini, Lowengrub, Nie, Macklin, Zheng, and others (for example, Cristini et al. (2003), Macklin and Lowengrub (2005), and Zheng et al. (2005), all of which reformulated several classical models (Greenspan, 1976; McElwain and Morris, 1978; Adam, 1996; Byrne and Chaplain, 1996b,a; Chaplain, 2000)) to include more detailed effects of the microenvironment by allowing variability in nutrient availability and the response to proliferation-induced mechanical pressure (which models hydrostatic stress) in the tissue surrounding the tumor. In our model, the region surrounding the tumor aggregates the effects of ECM and noncancerous cells, which we characterize by two nondimensional parameters that govern the diffusional and biome-

chanical properties of the tissue. Fluids are assumed to move freely through the interstitium and ECM, and so such effects are currently neglected. The external nutrient and pressure variations, in turn, affect the evolution of the tumor in our model. Due to the computational cost of three-dimensional simulations, we shall focus our attention on two-dimensional tumor growth, although the model we develop applies equally well in three dimensions. In Cristini et al. (2003), it was found that the baseline model predicts similar morphological behavior for two-dimensional and three-dimensional tumor growth. This has been borne out by recent three-dimensional simulations by Li et al. (2006). We note that two-dimensional tumor growth may be well-suited to studying cancers that spread over large areas but are relatively thin, such as melanoma.

Using our model, we shall conduct a systematic investigation of the effect of the microenvironment on tumor growth over a broad range of biophysical parameters. In the process, we shall characterize the behavior predicted by the model and discuss the implications for cancer treatment. We note that by matching the results to known morphologies, one may infer the range of validity of the model and obtain estimates of parameter values; we discuss this at the end of this paper. These simulations are difficult and require the development of accurate numerical techniques, which we present in this paper.

We find that the range of morphological responses can be placed in three categories that depend primarily upon the tumor microenvironment. In nutrient-poor microenvironments, tumors tend to break into small fragments and invade the surrounding tissue, regardless of the mechanical properties of the surrounding tissue. When placed in nutrient-rich tissue, the tumor morphology depends upon the biomechanical characteristics of the tissue. Tumors growing into mechanically unresponsive tissue develop buds that grow into long, invasive fingers. Tumors growing into softer, mechanically responsive tissue develop buds that do not grow, but rather connect with neighboring buds to capture external ECM. The overall morphology remains compact, with a large central abscess containing encapsulated ECM, fluid, and cellular debris similar to a necrotic core. We found that the qualitative behavior of the tumor morphologies was similar across a broad range of parameters that govern the tumor genetic characteristics. Our findings demonstrate the importance of the impact of microenvironment on tumor growth and morphology, and this has implications for cancer therapy: the impact of a therapy on the microenvironment may either positively or negatively impact the outcome of the treatment. A treatment that impairs nutrient delivery in the host tissue (e.g., using anti-angiogenic drugs) may increase tumor fragmen-

tation, whereas a treatment that normalizies nutrient delivery may reduce or prevent tumor fragmentation. Therapies that affect the biomechanical responsiveness of the tumor or surrounding host tissue (e.g., anti-invasion therapy that alters cell-cell or cell-matrix adhesion) may either cause or prevent invasive fingering.

Using our model, we also investigate the internal structure of the tumors, including the volume fractions of the necrotic and viable portions of the tumor. We find that even during growth, the internal structure tends to stabilize due to apparent local equilibration of the tumors as characteristic feature sizes and shapes emerge. We also find that whereas the tumor morphology depends primarily upon the microenvironment, the internal structure is most strongly influenced by the genetic characteristics of the tumor, including resistence to necrosis, the rate at which the necrotic core is degraded, and the apoptosis rate. These results are not at all obvious from the examination of the model and underlying hypotheses alone. By hypothesis, the microenvironment, tumor genetics, and tumor morphology are all nonlinearly coupled. The tumor genetics determine biophysical properties like growth rates, which, in turn, are mediated by microenvironmental factors such as available nutrient supply. One would then expect that the tumor genetics have a greater impact on tumor morphology, and indeed, Cristini et al. (2003) found that the tumor genetics completely determine the morphological behavior when the microenvironment is not taken into account. While the important role of the microenvironment is consistent with experiments in the literature, the observed dominance of the microenvironment in determining the morphology is intriguing. Likewise, the weak dependence of the internal tumor structure on the microenvironment and morphology is difficult to predict *a priori*. The model can be analyzed to make this prediction for tumor spheroids, but such an analysis ignores variation in tumor morphology and does not lead to obvious conclusions for the general case, where the morphology (and presumably volume) of the necrotic core depends upon the morphology of the tumor boundary.

We note that while our model captures the basic features of tumor growth, it does not currently incorporate the effects of elastic and residual stress, ECM degradation, signaling by promoters and inhibitors, angiogenesis, and competition between tumor subpopulations. These effects represent model refinements that can readily be added to our current modeling framework. We shall discuss our plans to address these and other refinements in the closing remarks in Section 4.5.

The contents of this paper are as follows: in Section 4.2, we describe the tumor growth

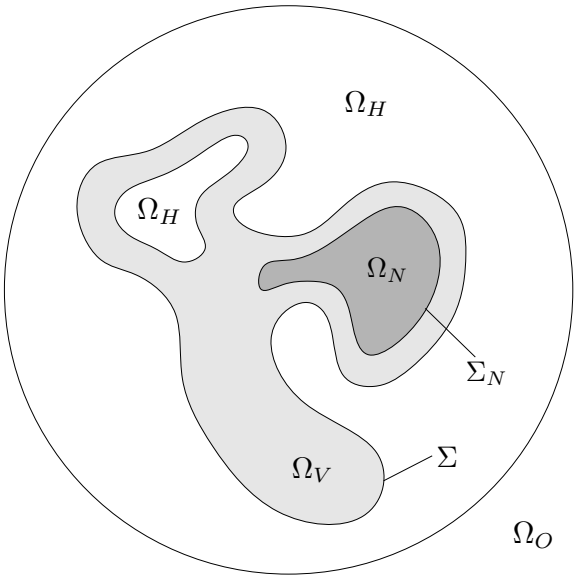

Figure 4.1: Diagram of the regions in and near a growing tumor: the tumor Ω is comprised of viable (proliferating and quiescent) cells in Ω_V and necrotic cells in Ω_N. The noncancerous tissue surrounding tissue surrounding the tumor, denoted by Ω_H, is affected by the growing tumor, and portions of Ω_H may be encapsulated by the growing tumor. Lastly, the noncancerous tissue Ω_O is not affected by the growing tumor.

and microenvironment models, nondimensionalize the resulting systems, and present an analysis of the internal structure of tumor spheroids that will be helpful in understanding non-spherical growth. In Section 4.3 and Appendix 4.7, we give the important features of our level set/ghost fluid method and extend our technique to solve the Poisson-like equations on the full domain. In Section 4.3.2, we present a convergence study to demonstrate the accuracy of our technique. In Section 4.4, we present the results of a parameter study of tumor growth in a variety of microenvironments, categorize the characteristic tumor morphologies, investigate the causal link between microenvironment and tumor morphology, and analyze the link between the internal tumor structure and the tumor genetic parameters. In Section 4.5 and throughout the text, we discuss the clinical implications of the behavior predicted by our model. In Section 4.5, we also summarize our work, address known deficiencies in the model, and discuss ongoing modeling refinements.

4.2 Governing Equations

We study and extend a model for solid tumor growth that applies equally well in two and three dimensions (Cristini et al., 2003; Macklin, 2003; Macklin and Lowengrub, 2005; Zheng et al., 2005), which is a reformulation of several classical models (Greenspan, 1976; McElwain and Morris, 1978; Adam, 1996; Byrne and Chaplain, 1996b,a; Chaplain, 2000). We model an avascular tumor occupying a volume $\Omega(t)$ with boundary $\partial\Omega$, which we denote by Σ. The tumor is composed of a viable region Ω_V where nutrient (e.g., oxygen and glucose) levels are sufficient for tumor cell viability and a necrotic region Ω_N where tumor cells die due to low nutrient levels and are broken down by enzymes. Note that $\Omega = \Omega_V \cup \Omega_N$.

The growing tumor also interacts with the surrounding microenvironment in the host tissue; we denote this region by Ω_H. The region Ω_H contains extracellular matrix (ECM) and a mixture of noncancerous cells, fluid, and cellular debris. As observed in Cristini et al. (2003), Macklin (2003), and Macklin and Lowengrub (2005), the growing tumor may encapsulate regions of Ω_H, and so these regions may lack living noncancerous cells. (See Figure 4.1.) Hereafter, we shall refer to Ω_H as noncancerous tissue, although our model applies equally well to the case in which Ω_H contains only ECM, fluid, and cellular debris.

4.2.1 Nutrient Transport

We describe the net effect of nutrients and growth-promoting and inhibiting factors with a single nutrient c. In the viable region of the tumor Ω_V, the nutrient diffuses and is uptaken by proliferating cells. Letting $\widetilde{D} = \widetilde{D}(\mathbf{x}, t)$ denote the nutrient diffusivity, and defining λ_V to be the nutrient uptake rate by proliferating tumor cells, then the nutrient is governed by the reaction-diffusion equation

$$\frac{\partial c}{\partial t} = \nabla \cdot \left(\widetilde{D} \nabla c \right) - \lambda_V c, \qquad \mathbf{x} \in \Omega_V. \tag{4.1}$$

Taking λ_V to be constant, note that the total nutrient uptake $\lambda_V c$ decreases with c. This models the fall in metabolic and mitotic behavior (i.e., quiescence) as the tumor cells become hypoxic. In future work, we shall explicitly model the quiescent tumor cell population, as these cells are particularly important when considering the efficacy of therapy (Konopleva et al., 2002; Ravandi and Estrov, 2006).

In the necrotic region Ω_N, there is little or no nutrient uptake, as there are few proliferating cells. However, necrosing cells release their intracellular contents, which are both

cytotoxic/growth-inhibiting (Freyer, 1988; Festjens et al., 2006) and oxygen-reactive (e.g., necrotic tissue rapidly reacts with reintroduced oxygen to form reactive oxygen species that react with and damage biological molecules (Kloner and Jennings, 2001; Galaris et al., 2006)). Recalling that the general nutrient c models the net effect of nutrients and growth-promoting and inhibiting factors, we can model these effects with a nutrient decay rate λ_D. Thus,

$$\frac{\partial c}{\partial t} = \nabla \cdot \left(\widetilde{D} \nabla c \right) - \lambda_D c, \qquad \mathbf{x} \in \Omega_N. \tag{4.2}$$

We assume that tumor cells uptake nutrient at a greater rate than noncancerous cells, and so nutrient uptake is negligible in Ω_H (Vaupel et al., 1989; Garber, 2004; Esteban and Maxwell, 2005; Arvind et al., 2005). Furthermore, we assume that there is little cellular debris in Ω_H and thereby no nutrient decay in that region. Therefore,

$$\frac{\partial c}{\partial t} = \nabla \cdot \left(\widetilde{D} \nabla c \right), \qquad \mathbf{x} \in \Omega_H. \tag{4.3}$$

Summarizing, the nutrient satisfies

$$\frac{\partial c}{\partial t} = \nabla \cdot \left(\widetilde{D} \nabla c \right) - \lambda(\mathbf{x}, t) c, \qquad \mathbf{x} \in \Omega \cup \Omega_H \tag{4.4}$$

where

$$\lambda(\mathbf{x}, t) = \begin{cases} 0 & \mathbf{x} \in \Omega_H \\ \lambda_V & \mathbf{x} \in \Omega_V \\ \lambda_D & \mathbf{x} \in \Omega_N. \end{cases} \tag{4.5}$$

Because nutrient diffusion, uptake, and decay all occur much more quickly than tumor growth, the quasi-steady assumption applies and $\partial c / \partial t \approx 0$.

The tumor cells become necrotic when the nutrient falls below a critical value c_N for cellular viability. Therefore, the viable and necrotic regions can be identified by the nutrient concentration:

$$\begin{aligned} \Omega_V &= \{\mathbf{x} \in \Omega : c \geq c_N\} \\ \Omega_N &= \{\mathbf{x} \in \Omega : c < c_N\}. \end{aligned} \tag{4.6}$$

By equation (4.6), the morphology and location of Ω_N depends upon c, i.e., $\Omega_N = \Omega_N(c)$. Because λ varies within the tumor based upon the position of the necrotic core $\Omega_N(c)$, we see that $\lambda = \lambda(\mathbf{x}, t, c)$, which makes the nutrient equation nonlinear. However, we can linearize the problem by setting $\lambda_D = \lambda_V$, i.e., $\lambda \equiv \lambda_V$ throughout the tumor. This

modeling convenience allows us to solve for the nutrient concentration using linear solvers. In test simulations with nonlinear solvers that we are currently developing (not shown), we have found that this assumption does not significantly affect the qualitative features of the necrotic core morphology and the overall tumor progression.

We assume that the nutrient and nutrient flux are continuous across the tumor boundary Σ:

$$[c] = 0 \qquad \mathbf{x} \in \Sigma \tag{4.7}$$

$$\left[\widetilde{D}\nabla c \cdot \mathbf{n}\right] = 0 \qquad \mathbf{x} \in \Sigma, \tag{4.8}$$

where $\mathbf{n}$ is the outward unit normal vector.

Here, for any quantity $q(\mathbf{x})$ and any $\mathbf{x} \in \Sigma$, we define

$$\begin{aligned} [q(\mathbf{x})] &= q(\mathbf{x})\Big|_{\Omega} - q(\mathbf{x})\Big|_{\Omega_H} \\ &= \lim_{\Omega \ni \mathbf{y} \to \mathbf{x}} q(\mathbf{y}) - \lim_{\Omega_H \ni \mathbf{y} \to \mathbf{x}} q(\mathbf{y}) \end{aligned} \tag{4.9}$$

to be the jump in q across the boundary Σ.

Nutrient delivery by the blood vasculature and uptake by noncancerous cells are assumed to be in balance outside of $\Omega \cup \Omega_H$. Therefore, we take

$$c \equiv c_\infty \qquad \mathbf{x} \in \partial(\Omega \cup \Omega_H) \tag{4.10}$$

on the far-field boundary.

In this paper, we shall consider the special case of avascular growth in piecewise homogeneous tissue and assume $\widetilde{D} \equiv D_H$ in Ω_H and $\widetilde{D} \equiv D_T$ in Ω, where D_H and D_T are (generally different) constants.

4.2.2 Cellular Velocity Field

The cells and ECM in the host tissue Ω_H and the viable tumor region Ω_V are affected by a variety of forces, each of which contributes to the cellular velocity field $\mathbf{u}$. The proliferating tumor cells in Ω_V generate an internal (oncotic) mechanical pressure (hydrostatic stress) that also exerts force on the surrounding noncancerous tissue in Ω_H. Tumor and noncancerous cells and the ECM can respond to pressure variations by overcoming cell-cell and cell-ECM adhesion and moving within the scaffolding of collagen and fibroblast cells (i.e., ECM) that provides structure to the host tissue. The ECM in Ω_H can deform in

response to the pressure. Following previous work, we assume constant cell density and model cellular motion within the ECM as incompressible fluid flow in a porous medium. The response of the cells and the ECM to the pressure is governed by Darcy's law

$$\mathbf{u} = -\widetilde{\mu}\nabla P \qquad \mathbf{x} \in \Omega_V \cup \Omega_H, \tag{4.11}$$

where the cellular mobility $\widetilde{\mu} = \widetilde{\mu}(\mathbf{x})$ measures the overall ability of tissue to respond to the pressure. We note that $\widetilde{\mu}$ also measures the permeability of the tissue to tumor cells. See Ambrosi and Preziosi (2002) and Byrne and Preziosi (2003) for further motivation of this approach from a mixture modeling point of view.

When tumor cells are in a state of hypoxia, cellular pathways that increase cell migration may become activated (Höckel et al., 1996; Kaur et al., 2005; Lester et al., 2005; Erler et al., 2006; Pouysségur et al., 2006). This may be modeled by increasing the mobility $\widetilde{\mu}$ as the nutrient level decreases or as a tactic response to nutrient gradients (Friedl and Wolf, 2003). In this paper, we shall focus upon the effects of proliferative pressure only; the effects of increased cellular motility in response to hypoxia will be considered in a future work (Macklin et al., 2007).

The outward normal velocity V of the tumor boundary Σ is given by

$$V = \mathbf{u} \cdot \mathbf{n} = -\widetilde{\mu}\nabla P \cdot \mathbf{n}, \tag{4.12}$$

where $\mathbf{n}$ is the outward unit normal vector along Σ. We assume that the normal velocity is continuous across the tumor boundary Σ, i.e., voids do not form between the tumor and host tissue.

4.2.3 Proliferation, Apoptosis, and Necrosis

In the viable region Ω_V, proliferation increases the number of tumor cells and thus the volume occupied by the viable region. Apoptosis decreases the total volume of Ω_V at a constant rate λ_A. We assume that cell birth and death are in balance in Ω_H, and so there is no change in the volume in that region. (Note that if there are no cells in Ω_H, then there is no cell birth or death, and the assumption still holds.) In fact, unvascularized tumors are often hypoxic, leading to glycolysis in the tumor and acidosis (a reduced pH level) in the surrounding healthy tissue (Gatenby and Gawlinski, 1996, 2003). Noncancerous cells cannot survive in this condition, leading to an imbalance in cell birth and death that results

in a relative survival advantage for tumor cells and a potential volume loss in Ω_H when cells are present. This effect will be considered in a future work.

Putting this together as in Cristini et al. (2003), the change in volume is

$$\nabla \cdot \mathbf{u} = \begin{cases} 0 & \mathbf{x} \in \Omega_H \\ bc - \lambda_A & \mathbf{x} \in \Omega_V. \end{cases} \tag{4.13}$$

Here, b is a constant related to the tumor cell mitosis rate.

Throughout the necrotic core Ω_N, the enzymatic breakdown of necrotic tumor cells is assumed to decrease the tumor volume at a constant rate λ_N. This volume loss can be imposed via a nonlocal boundary condition on the boundary Σ_N of the necrotic core:

$$\begin{aligned} \int_{\Sigma_N} \mathbf{u} \cdot \mathbf{n} \, ds &= -\int_{\Sigma_N} (\widetilde{\mu} \nabla P \cdot \mathbf{n}) \, ds \\ &= -\lambda_N \left| \Omega_N \right|, \end{aligned} \tag{4.14}$$

where $\mathbf{u} \cdot \mathbf{n}$ is the limit from inside Ω_V, and $|\Omega_N|$ denotes the area of Ω_N.

As a computational convenience, we can achieve the correct volume loss by continuously extending the velocity $\mathbf{u}$ into Ω_N. Instead of using (4.14), we define

$$\nabla \cdot \mathbf{u} = -\lambda_N, \qquad \mathbf{x} \in \Omega_N. \tag{4.15}$$

We assume that voids do not form between the viable and necrotic regions. Therefore, we choose our extension such that the normal velocity is continuous across the necrotic boundary, i.e., $[\mathbf{u} \cdot \mathbf{n}] = 0$ across Σ_N. We note that because Σ_N is determined by the nutrient level, it is not a material boundary and is not advected by the velocity field $\mathbf{u}$; the extension of the velocity field is used solely to yield the correct volume change in the tumor necrotic core.

One way to attain this is to extend the pressure continuously into the necrotic core as well, by taking

$$\begin{aligned} \mathbf{u} &= -\widetilde{\mu} \nabla P \qquad && \mathbf{x} \in \Omega_N \\ [P] &= 0 && \mathbf{x} \in \Sigma_N \\ [-\widetilde{\mu} \nabla P \cdot \mathbf{n}] &= 0 && \mathbf{x} \in \Sigma_N. \end{aligned} \tag{4.16}$$

We note that the jump condition $[P] = 0$ across Σ_N models low cellular adhesion and is consistent with the increased cellular mobilty observed in hypoxic cells (Brizel et al., 1996;

Cairns et al., 2001; Höckel and Vaupel, 2001; Postovit et al., 2002; Rofstad et al., 2002; Pouysségur et al., 2006). We close this section by noting that (4.16) automatically satisfies $[\mathbf{u} \cdot \mathbf{n}] = 0$ on Σ_N.

4.2.4 Mechanical Pressure

We can obtain an equation for the mechanical pressure in $\Omega \cup \Omega_H$ by combining (4.11) and (4.13) and by noting the pressure extension in (4.16):

$$-\nabla \cdot (\widetilde{\mu} \nabla P) = \begin{cases} 0 & \mathbf{x} \in \Omega_H \\ bc - \lambda_A & \mathbf{x} \in \Omega_V \\ -\lambda_N & \mathbf{x} \in \Omega_N. \end{cases} \tag{4.17}$$

By the continuity of the normal velocity across the tumor boundary, by Darcy's law (4.11) there is no jump in the normal derivative $\widetilde{\mu} \nabla P \cdot \mathbf{n}$ across Σ. Following Cristini et al. (2003) and others, we model cell-cell adhesion forces in the tumor by introducing a Laplace-Young surface tension boundary condition. Therefore,

$$[P] = \gamma \kappa \qquad \mathbf{x} \in \Sigma \tag{4.18}$$

$$0 = [\mathbf{u} \cdot \mathbf{n}] = -[\widetilde{\mu} \nabla P \cdot \mathbf{n}] \qquad \mathbf{x} \in \Sigma, \tag{4.19}$$

where κ is the mean curvature and γ is a constant cell-cell adhesion parameter.

Cellular proliferation and death are in balance outside of $\Omega \cup \Omega_H$. Therefore,

$$P \equiv P_\infty \qquad \mathbf{x} \in \partial(\Omega \cup \Omega_H). \tag{4.20}$$

on the far-field boundary.

In this paper, we shall consider the special case of avascular growth in piecewise homogeneous tissue and take $\widetilde{\mu} \equiv \mu_H$ in Ω_H and $\widetilde{\mu} \equiv \mu_T$ in Ω, where μ_H and μ_T are constants that are generally not equal. Note that because $\widetilde{\mu}$ is constant within the tumor (and across Σ_N), the pressure boundary conditions across Σ_N in (4.16) are automatically satisfied for any C^1 smooth solution P.

4.2.5 Nondimensionalization

Following Cristini et al. (2003), Macklin (2003), Macklin and Lowengrub (2005), and Zheng et al. (2005), we first note that the nutrient concentration equation reveals intrinsic

diffusional length (L) and relaxation time (λ_R^{-1}) scales:

$$L = \sqrt{\frac{D_T}{\lambda_V}} \quad \text{and} \quad \lambda_R = \frac{\mu_T \gamma}{L^3}, \tag{4.21}$$

Note that $L \approx 200$ μm (Cristini et al., 2003; Macklin, 2003; Macklin and Lowengrub, 2005). We nondimensionalize the nutrient and pressure by

$$\sigma = \frac{c}{c_\infty} \quad \text{and} \quad p = \frac{L}{\gamma}(P - P_\infty). \tag{4.22}$$

As in Zheng et al. (2005), we define the dimensionless numbers

$$G = \frac{\lambda_M}{\lambda_R} = \frac{bc_\infty}{\lambda_R}, \quad G_N = \frac{\lambda_N}{\lambda_M}, \quad A = \frac{\lambda_A}{\lambda_M}, \quad \text{and} \quad N = \frac{c_N}{c_\infty}, \tag{4.23}$$

where $\lambda_M = bc_\infty$ gives an intrinsic mitosis rate. The nondimensional parameter G gives the mitosis rate relative to the rate of relaxation due to cell-cell adhesion in the tumor and is a measure of tumor aggressiveness. G_N and A measure the rates of enzymatic degradation of the necrotic core and apoptosis relative to the mitosis rate, respectively. N is the threshold nutrient level for cell viability.

Using these scales, the nondimensionalized nutrient concentration we solve for satisfies

$$\begin{cases} D\nabla^2\sigma = 0 & \mathbf{x} \in \Omega_H \\ \nabla^2\sigma = \sigma & \mathbf{x} \in \Omega \\ [\sigma] = 0 & \mathbf{x} \in \Sigma \\ D\nabla\sigma\Big|_\Omega \cdot \mathbf{n} = \nabla\sigma\Big|_{\Omega_H} \cdot \mathbf{n} & \mathbf{x} \in \Sigma \\ \sigma \equiv 1 & \mathbf{x} \in \partial(\Omega \cup \Omega_H). \end{cases} \tag{4.24}$$

Here, $D = D_H/D_T$ provides a measure of the nutrient richness of the tumor microenvironment relative to the tumor.

The nondimensionalized pressure solves

$$\begin{cases} \mu\nabla^2 p = 0 & \mathbf{x} \in \Omega_H \\ -\nabla^2 p = G(\sigma - A) & \mathbf{x} \in \Omega_V \\ -\nabla^2 p = -GG_N & \mathbf{x} \in \Omega_N \\ [p] = \kappa & \mathbf{x} \in \Sigma \\ \mu\nabla p\Big|_\Omega \cdot \mathbf{n} = \nabla p\Big|_{\Omega_H} \cdot \mathbf{n} & \mathbf{x} \in \Sigma \\ p \equiv 0 & \mathbf{x} \in \partial(\Omega \cup \Omega_H). \end{cases} \tag{4.25}$$

Here, $\mu = \mu_H/\mu_T$ is a measure of the relative ability of the external tissue to (biomechanically) respond to the pressure, compared to the biomechanical response of the tumor. Using this definition of μ, the nondimensional normal velocity that we use to update the tumor boundary position is given by

$$V = -\mu \nabla p\Big|_{\Omega_H} \cdot \mathbf{n} = -\nabla p\Big|_{\Omega} \cdot \mathbf{n}. \tag{4.26}$$

In this paper, we model $\Omega \cup \Omega_H$ to be everything inside of the ball

$$B(\mathbf{x}_{\text{cent}}, R+1), \tag{4.27}$$

where

$$R = \sup\{|\mathbf{x} - \mathbf{x}_{\text{cent}}| : \mathbf{x} \in \Omega\} \tag{4.28}$$

is the largest distance from the center of mass $\mathbf{x}_{\text{cent}}$ of the tumor. Notice that this ball contains the tumor Ω and all noncancerous tissue that is within the diffusional distance from the tumor. See Figure 4.1. Lastly, we note that the viable and necrotic regions of the tumor are given by

$$\Omega_V = \{\mathbf{x} \in \Omega : \sigma(\mathbf{x}) \geq N\} \tag{4.29}$$

$$\Omega_N = \{\mathbf{x} \in \Omega : \sigma(\mathbf{x}) < N\}. \tag{4.30}$$

4.2.6 Analysis of Volume Fractions for Tumor Spheroids

Following Byrne and Chaplain (1996b) and Cristini et al. (2003), we obtain and analyze the steady-state, two-dimensional circular solution of the full tumor system; the analysis for three-dimensional growth is similar. The results of the analysis will be instructive when we interpret our nonlinear simulation results for more complex geometries.

We shall solve for the exact nutrient concentration, pressure, and tumor boundary velocity. Using the exact tumor boundary velocity, we can find the equilibrium radii of the tumor (R_∞) and the necrotic core ($R_{N,\infty}$) and calculate the (two-dimensional) necrotic volume fraction:

$$\frac{\text{Volume}_{\text{necrotic}}}{\text{Volume}_{\text{tumor}}} = \left(\frac{R_{N,\infty}}{R_\infty}\right)^2. \tag{4.31}$$

We seek to understand the sensitivity of the necrotic volume fraction to D, μ, A, G, G_N, and N.

For simplicity of analysis, we first assume that $D \gg 1$ and examine the effects of D later in this section. If $R = R(t)$ is the radius of the tumor at time t, then $\sigma \approx 1$ in the region $R < r \leq R + 1$, and the nutrient concentration $\sigma(r, t)$ is given by

$$\sigma(r,t) = \begin{cases} \frac{I_0(r)}{I_0(R)} & 0 \leq r \leq R \\ 1 & R < r \leq R+1, \end{cases} \tag{4.32}$$

where $I_0(x)$ is the 0^{th} modified Bessel function of the first kind.

Once the nutrient concentration profile is known, we can define

$$R_N(t) = \{r : \sigma(r) = N\} = I_0^{-1}\left(N\, I_0(R)\right) \tag{4.33}$$

to be the radius of the necrotic core at time t. Notice that R_N is completely determined by R and N.

The cellular velocity is given by

$$\mathbf{u} = -\begin{cases} p'(r)\,\mathbf{r} & 0 \leq r \leq R(t) \\ \mu p'(r)\,\mathbf{r} & R(t) < r \leq R(t)+1, \end{cases} \tag{4.34}$$

where $\mathbf{r}$ is the outward unit vector. By the continuity of the cellular velocity across $R(t)$, the velocity of the tumor boundary $R'(t)$ is

$$R'(t) = -\lim_{r \uparrow R(t)} p'(R(t)) = -\mu \lim_{r \downarrow R(t)} p'(R(t)). \tag{4.35}$$

When the tumor has reached its equilibrium radius R_∞,

$$0 = \lim_{r \uparrow R_\infty} p'(R_\infty) = \mu \lim_{r \downarrow R_\infty} p'(R_\infty). \tag{4.36}$$

Because $p(R_\infty + 1) = 0$, we see that $p \equiv 0$ on $R_\infty < r \leq R_\infty + 1$ when the tumor has reached its steady size, and

$$0 = \mu \lim_{r \downarrow R_\infty} p'(R_\infty). \tag{4.37}$$

Therefore, μ has no impact on the equilibrium radii R_∞ and $R_{N,\infty}$, and hence the equilibrium necrotic tumor volume fraction. For simplicity of analysis, we shall now assume $\mu \gg 1$, in which case the exact solution of the pressure is

$$p(r) = \begin{cases} d_1 + \frac{1}{4} G G_N r^2 & 0 \leq r \leq R_N \\ d_2 + d_3 \ln r - G\frac{I_0(r)}{I_0(R)} + \frac{1}{4} A G r^2 & R_N < r \leq R \\ 0 & R < r \leq R+1, \end{cases} \tag{4.38}$$

where d_1, d_2, and d_3 are chosen to satisfy the continuity and boundary conditions:

$$d_1 + \frac{1}{4}GG_N R_N^2 = d_3 + d_4 \ln R_N - G\frac{I_0(R_N)}{I_0(R)} + \frac{1}{4}AGR_N^2 \tag{4.39}$$

$$\frac{1}{2}GG_N R_N = \frac{d_4}{R_N} - G\frac{I_1(R_N)}{I_0(R)} + \frac{1}{2}AGR_N \tag{4.40}$$

$$d_3 + \ln R - G + \frac{1}{4}AGR^2 = \frac{1}{R}. \tag{4.41}$$

Notice that we can explicitly solve for d_4 and find the boundary velocity:

$$\begin{aligned} R'(t) &= -p'(R) \\ &= -G\left(\frac{1}{2}\frac{R_N^2}{R}(G_N - A) + \frac{I_1(R_N)}{RI_0(R)} - \frac{I_1(R)}{I_0(R)} + \frac{1}{2}AR\right). \end{aligned} \tag{4.42}$$

To find the equilibrium radius R_∞, we set (4.42) equal to zero. Notice that G scales out, and so R_∞ (and thereby the equilibrium necrotic volume fraction) depends only upon A, G_N, N, and $R_{N,\infty}$, which itself depends only upon R_∞ and N. Therefore, for large D, the necrotic volume fraction is a function of A, G_N, and N, and independent of G and μ. In fact, we have found that this trend holds for any fixed value of D, and the necrotic volume fraction is independent of D for values greater than approximately 10. For example, if $G = 20$, $G_N = 1$, $A = 0$, and $N = 0.35$, then the necrotic volume fraction increases rapidly from 26.4% ($D = 0.25$) to 35.8% ($D = 10$), increases more slowly to approximately 36.3% ($D = 20$), and then quickly approaches a limiting value of approximately 36.9% as D increases further.

By solving (4.32) and (4.42), one can examine the evolution of the necrotic volume fraction as a tumor spheroid approaches its equilibrium size. We have found that the relative rate of change of the necrotic volume fraction is approximately equal to the relative rate of change in the spheroid radius. (e.g., if the radius is increasing at 0.1% per time, then the necrotic volume fraction is increasing at a similar rate.) Thus, a steady necrotic volume fraction indicates that a tumor spheroid has reached a steady state.

As we shall verify numerically, it turns out that even during growth, the viable and necrotic volume fractions of nonspherical tumors tend toward constant values that depend primarily upon A, D, G_N, and N. This indicates the emergence of characteristic feature sizes within the tumor and suggests local equilibration. In large part, the emergent local configuration is determined by the thickness of the viable rim and the size of the necrotic core. The viable rim size is determined by how well nutrients penetrate the tumor (D),

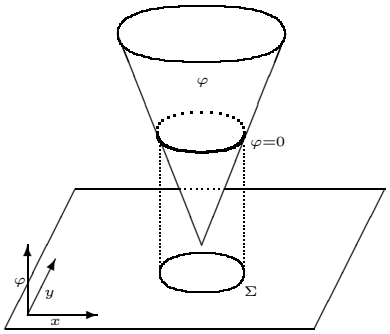

Figure 4.2: Representing an ellipse Σ as the zero contour of a level set function φ.

the amount of apoptosis (A), and the threshold nutrient level for necrosis (N). The size of the necrotic core is determined by how quickly necrotic tumor cells are broken down and removed (G_N). This is in contrast with the spherical tumor case, where the volume fractions only stabilize when the tumor reaches its (global) equilibrium radius.

We note that because a spheroid has minimum surface area to volume ratio, it provides a growing tumor with the least access to nutrient and therefore the largest necrotic volume fraction. Therefore, for non-spheroids, we expect smaller necrotic volume fractions. In fact, it is the attempt of growing tumors to improve access to nutrient that often drives morphological instability.

4.3 Numerical Method

We adapt and apply the numerical techniques we recently described in Macklin (2003) and Macklin and Lowengrub (2005, 2006). Because we anticipate frequent tumor morphology changes (e.g., the tumor breaks into fragments, or tumor fragments merge), we use the level set method: we introduce an auxilliary "level set" signed distance function φ satisfying $\varphi < 0$ inside Ω, $\varphi > 0$ outside Ω, and $\varphi = 0$ on the tumor boundary Σ. See Figure 4.2. For more information on the level set method and its application to fluid mechanics, please see Osher and Sethian (1988), Sussman et al. (1994), Malladi et al. (1995, 1996), Adalsteinsson and Sethian (1999), Sethian (1999), Osher and Fedkiw (2001, 2002), and Sethian and Smereka (2003).

At every fixed simulation time, our method consists of the following steps:

1. Solve for the nutrient with Equation (4.24). Note that this determines the updated position of the necrotic core boundary Σ_N.

2. Solve for the pressure with Equation (4.25).

3. Update the position of the boundary Σ by evolving the level set function φ with the normal velocity V in Equation (4.26).

4. Maintain φ as a distance function.

4.3.1 Solution of the Tumor System

We solve for all quantities on a regular Cartesian mesh that is dynamically resized to contain the growing tumor Ω and the noncancerous tissue Ω_H. Both the nutrient and pressure equations take the form

$$\alpha \nabla^2 u = f_1(\mathbf{x}, t) + f_2(\mathbf{x}, t) u \qquad \text{in} \quad \Omega \text{ and } \Omega_H \tag{4.43}$$

$$[u] = g(\mathbf{x}, t) \qquad \text{on} \quad \Sigma \tag{4.44}$$

$$[\alpha \nabla u \cdot \mathbf{n}] = 0 \qquad \text{on} \quad \Sigma \tag{4.45}$$

$$u \equiv u_O \qquad \text{on} \quad \partial(\Omega \cup \Omega_H) \tag{4.46}$$

where u is either σ or p,

$$\alpha = \begin{cases} \alpha_T & \text{in} \quad \Omega \\ \alpha_H & \text{in} \quad \Omega_H, \end{cases} \tag{4.47}$$

and α_T and α_H are positive constants. We solve with a second-order accurate extension to the ghost fluid/level set method that we developed in Macklin and Lowengrub (2005). Please see Appendix 4.7 for new enhancements we have made to the method to satisfy $[\alpha \nabla u \cdot \mathbf{n}] = 0$ on the boundary Σ.

The pressure boundary condition requires an accurate curvature discretization. In Macklin (2003) and Macklin and Lowengrub (2005), we found that standard curvature discretizations are inaccurate and unstable near singularities that result from morphological change. In all our numerical simulations, we use a second-order accurate curvature discretization (in two dimensions) that we developed in Macklin and Lowengrub (2006) to overcome these problems.

We update the position of the interface Σ by solving the PDE

$$\frac{\partial \varphi}{\partial t} + \widetilde{V} \left| \nabla \varphi \right| = 0, \tag{4.48}$$

where $\widetilde{V}(\mathbf{x}, t)$ is an extension of V off of the tumor boundary Σ such that $\widetilde{V} \equiv V$ on Σ. We construct $\widetilde{V}$ using the bilinear extrapolation we developed in Macklin and Lowengrub (2005). As described in Macklin (2003) and Macklin and Lowengrub (2005), we filter the high-frequency variations from $\widetilde{V}$ to attain second-order accuarcy without a third-order CFL condition.

Lastly, we keep φ as a distance function ($|\nabla \varphi| \sim 1$) by solving the PDE

$$\varphi_\tau - \text{sign}(\varphi^0) \left(1 - |\nabla \varphi| \right) = 0 \tag{4.49}$$

to steady-state, where τ is pseudo-time and φ^0 is the level set function prior to reinitialization (Osher and Sethian, 1988; Malladi et al., 1995, 1996; Adalsteinsson and Sethian, 1999; Sethian, 1999; Osher and Fedkiw, 2001, 2002; Sethian and Smereka, 2003). We solve the PDE's in (4.48) and (4.49) with the third-order total variation-diminishing Runge-Kutta method (Gottlieb and Shu, 1997; Gottlieb et al., 2001) and the fifth-order WENO method (Jiang and Shu, 1996; Jiang and Peng, 2000).

4.3.2 Convergence of the Numerical Method

To evaluate the convergence of our extended numerical method, we simulated two-dimensional tumor growth with $D = 100$, $\mu = 50$, $G = 20$, $G_N = 1$, $N = 0.35$, and $A = 0$, and with a complex initial shape. (See the first frame of Figure 4.5.) We simulated up to time $t = 0.15$ at three spatial resolutions: $\Delta x \in \{0.04, 0.08, 0.16\}$.

In Figure 4.3 we plot the resulting tumor morphology at low resolution ($\Delta x = 0.16$; upper left plot), medium resolution ($\Delta x = 0.08$; upper right plot), and high resolution ($\Delta x = 0.04$; lower left plot). In all three plots, the dark region denotes the necrotic core Ω_N where $\sigma \leq N$. In the lower right plot of Figure 4.3, we compare the position of the tumor boundary for all three resolutions: the dotted curve is for $\Delta x = 0.16$, the dashed curve shows $\Delta x = 0.08$, and the solid curve gives $\Delta x = 0.04$. As we can see, there are considerable differences in the positions of the necrotic core and tumor boundary between the low- and medium-resolution plots, but far fewer differences between the medium- and high-resolution plots; this is indicative of fast convergence. In this and all plots hereafter,

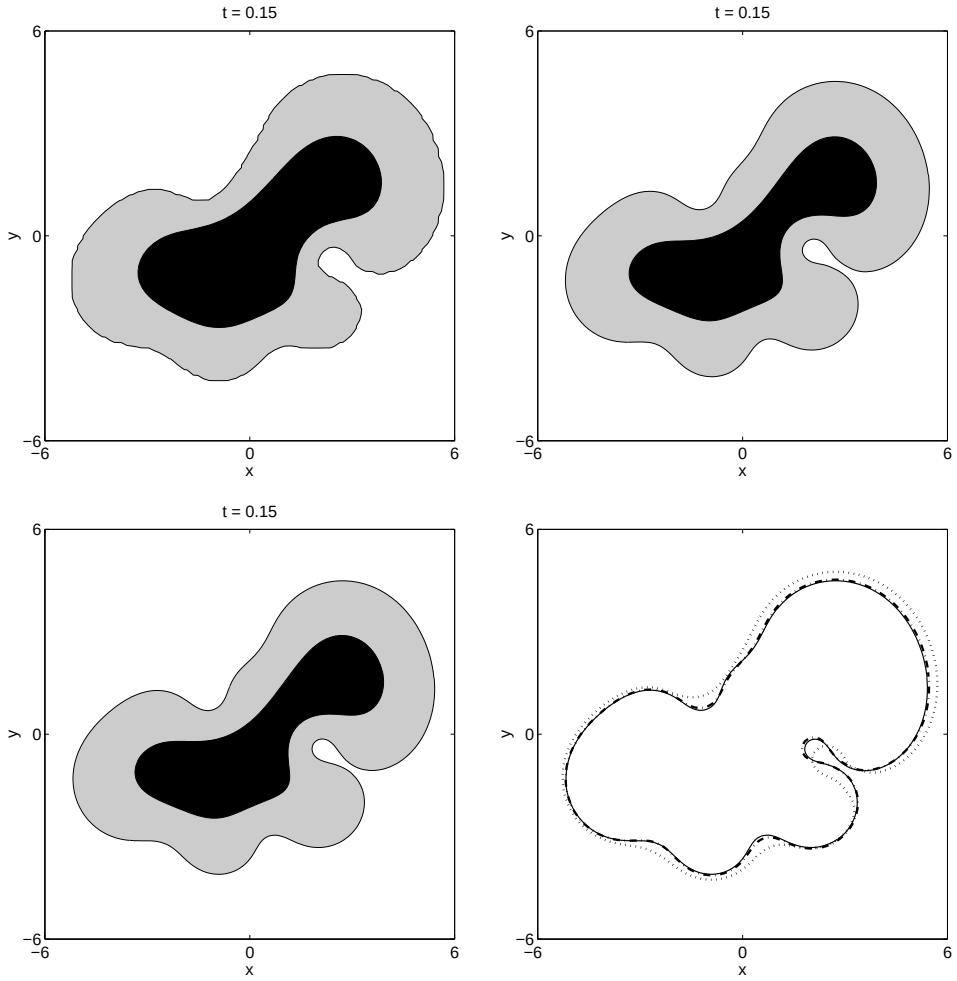

Figure 4.3: Numerical Convergence: Tumor morphology at $t = 0.15$ at low resolution (upper left), medium resolution (upper right), and high resolution (lower left). The dark region denotes the necrotic core Ω_N where $\sigma \leq N = 0.35$, and the gray regions show the viable region Ω_V. In the lower right plot, we compare the position of the tumor boundary at low resolution (dotted curve), medium resolution (dashed curve), and high resolution (solid curve).

white regions correspond to Ω_H, which consists of the ECM, noncancerous cells, and any other material outside of the tumor. Black regions denote the necrotic core Ω_N, and gray regions show the viable portion Ω_V of the tumor.

Defining the order of convergence (of the interface position) similarly to Macklin and Lowengrub (2005) (but measuring error over the entire computational domain, rather than in a band near the tumor boundary), the order of convergence for this example was 2.22,

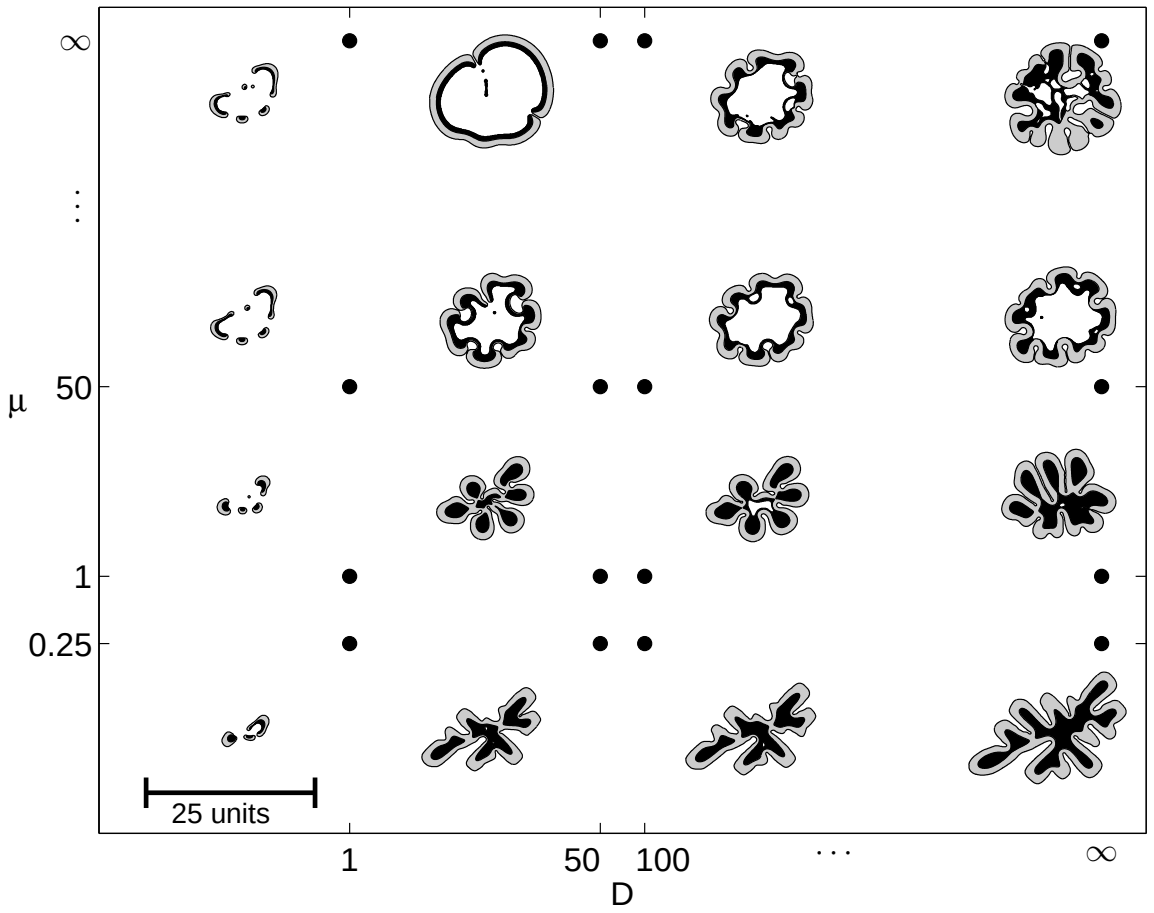

Figure 4.4: Tumor morphological response to the microenvironment. The external tissue nutrient diffusivity D increases from left to right, and the external tissue mobility μ increases from bottom to top. Three major morphologies are observed: fragmenting growth (left), invasive fingering (lower right), and compact/hollow (upper right). All tumors are plotted to the same scale, where the indicated length is $25L \approx 0.5$ cm.

thereby demonstrating that our numerical method is capable of accurately simulating tumor growth, even when faced with complex morphologies.

4.4 Numerical Results

We now investigate the effects of the tumor microenvironment on the morphology and growth patterns of two-dimensional, avascular tumors growing into piecewise homogeneous tissues. In all simulations, we set the apoptosis parameter $A = 0$ because the tumors are as-

sumed to ignore inhibitory signals for self-destruction (apoptosis). We numerically compute the solutions using a computational mesh with $\Delta x = \Delta y = 0.08$. All tumors are simulated to a scaled nondimensional time of $T = G\,t = \lambda_M t' = 20$, where t' is dimensional time. (The dimensional time is given by $t' = T/\lambda_M$.) Because $\lambda_M^{-1} \sim 1$ day, this nondimensional time allows us to compare tumors of varying simulated genotypes at fixed physical times. (e.g., $T = 20 \approx 20$ days.)

We shall characterize the effects of the modeled tumor microenvironment on growth by presenting a morphology diagram. (Figure 4.4.) We simulate growth over a wide range of microenvironmental parameters (D and μ) with $G = 20$, $G_N = 1$, and $N = 0.35$, each with identical initial shape as in the first frame of Figure 4.5. Recall that D and μ characterize the relative nutrient diffusivity and biomechanical responsiveness of the exterior tissue, G measures the tumor aggressiveness (proliferation compared to cellular adhesion), G_N characterizes the rate of degradation of the necrotic core, and N is the threshold nutrient level for tumor cell viability.

Later in this paper, we shall consider the effect of G, G_N, and N. We let $D \in \{1, 50, 100, \infty\}$ and $\mu \in \{0.25, 1, 50, \infty\}$. When $D = \infty$, we set $\sigma \equiv 1$ in non-encapsulated regions of Ω_H and only solve the Poisson equation for σ in Ω and the encapsulated portions of Ω_H (with diffusion constant 1). Likewise, when $\mu = \infty$, we set $p \equiv 0$ in non-encapsulated regions of Ω_H and only solve the Poisson equation for p in Ω and the encapsulated portions of Ω_H (with mobility 1). In Figure 4.4, we plot the shape of each tumor at time $T = 20.0$. In all figures, the black regions denote Ω_N where the tumor is necrotic, the gray regions show the viable tumor region Ω_V, and the white regions correspond to Ω_H, which consists of the ECM, noncancerous cells, and any other material outside of the tumor.

On the horizontal axis, we vary the nutrient diffusivity of the surrounding tissue; as D increases from left to right, the simulated microenvironment varies from nutrient-poor to nutrient-rich. On the vertical axis, we vary the mobility of the surrounding material; as μ increases from bottom to top, the microenvironment ranges from low-mobility to high-mobility. The greater the mobility μ, the greater the ability of the external, non-cancerous tissue to respond to the pressure generated by the growing tumor, and tumor cells are more able to penetrate the tissue.

We observe three distinct tumor morphologies through this broad range of simulated tissue types. In the nutrient-poor regime on the left side of the diagram, tumors demonstrate

fragmenting growth, characterized by the repeated breakup of the tumor in response to the low nutrient level. The nutrient-rich, low-mobility regime in the bottom right of the morphology diagram is characterized by *fingering growth*, where buds develop on the tumor boundary that invade the surrounding tissue, forming long, invasive fingers. The nutrient-rich, high-mobility regime in the top right of the diagram demonstrates *compact/hollow growth*, where the tumors tend to grow into spheroids and typically form abscesses filled with noncancerous tissue and fluid, similar to a necrotic core. As we shall discuss further in Section 4.5, these morphologies are similar to those observed experimentally *in vitro* by Frieboes et al. (2006b). See Figure 4.18.

We have found that the tumor morphologies in the morphology diagram in Figure 4.4 are qualitatively similar when recomputed with different genetic characteristics (modeled by A, G, G_N, and N), although, as we demonstrate in Section 4.4.2, large changes in the genetic parameter values can shift the morphology from one type to another. Therefore, a tumor's morphology depends primarily upon the characteristics of the microenvironment. We shall demonstrate this by investigating the three major tumor morphologies in the following sections.

To better characterize the morphological characteristics of a tumor, we define

$$\mathcal{S} = \frac{(\text{Perimeter})^2}{4\pi \text{ Area}} \qquad \text{(shape parameter)} \tag{4.50}$$

$$\mathcal{LS} = \frac{2 \text{ Area}}{\text{Perimeter}} \qquad \text{(length scale).} \tag{4.51}$$

The shape parameter $\mathcal{S}$ is a measure of how noncircular a tumor fragment is. Note that $\mathcal{S} \geq 1$, and $\mathcal{S}$ increases as a tumor fragment is deformed away from a circle. The length scale $\mathcal{LS}$ is a measure of the smallest dimension of a tumor fragment. For example, for a rectangular fragment with width W and length L, $\mathcal{LS} = LW/(L+W)$, and $\mathcal{LS} \sim W$ if $W \ll L$. To describe tumors comprised of multiple fragments, we calculate $\mathcal{S}$ and $\mathcal{LS}$ for each individual fragment and aggregate the results with a fragment volume-weighted average.

4.4.1 Fragmenting Growth into Nutrient-Poor Microenvironments

In Figure 4.5, we show the evolution of a tumor growing into a high-mobility, nutrient-poor tissue, where $D = 1$ and $\mu = \infty$. Here, $G = 20$, $G_N = 1$, $N = 0.35$, and $A = 0$. Due to the low nutrient diffusivity D, the nutrient level lies below N in much of the tumor

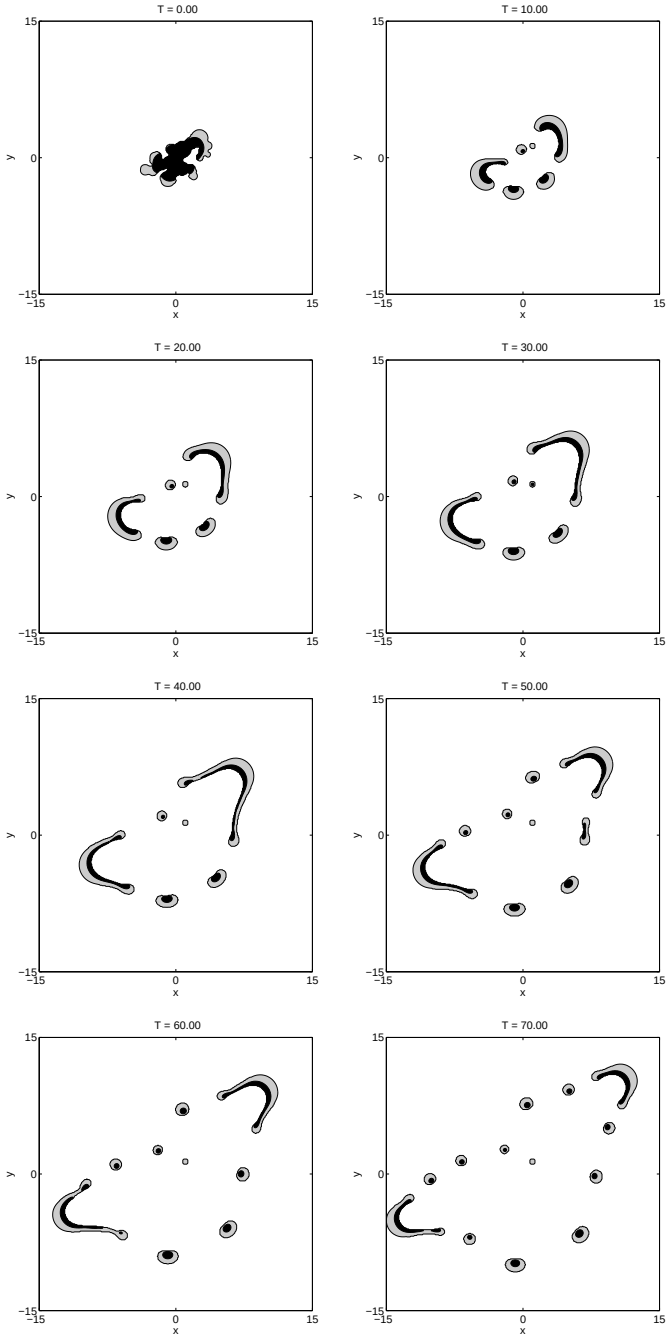

Figure 4.5: Long time simulation of fragmenting growth into nutrient-poor ($D = 1$), high-mobility ($\mu = \infty$) tissue. Plots are in $T = 10.0$ increments, $G = 20$, $G_N = 1$, $N = 0.35$, and $A = 0$.

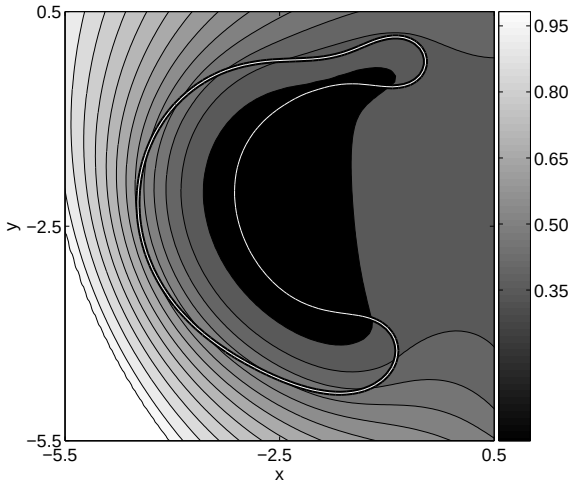

Figure 4.6: Contours of the nutrient concentration near a tumor fragment from the previous figure at $T = 20.0$. The black regions denote nutrient-starved regions where $\sigma < N$. Notice the large variation in nutrient level from the left side of the fragment to the right.

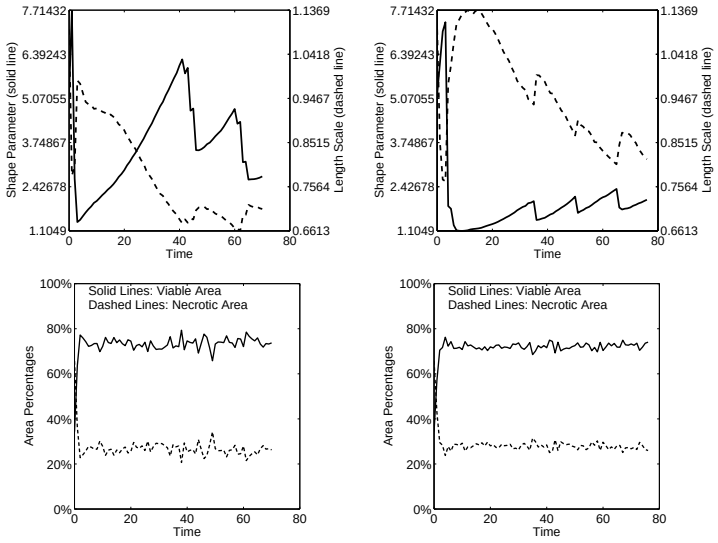

Figure 4.7: **Top Row:** Evolution of the shape parameter $\mathcal{S}$ (solid curves) and length scale $\mathcal{LS}$ (dashed curves) for fragmenting tumor growth into nutrient-poor tissue. The left plot is for growth into high-mobility tissue ($D = 1$, $\mu = \infty$), and the right plot is for growth into low-mobility tissue ($D = 1$, $\mu = 1$). **Bottom Row:** Evolution of the viable and necrotic volume fractions for the high-mobility case ($\mu = \infty$; left plot) and low-mobility case ($\mu = 1$; right plot).

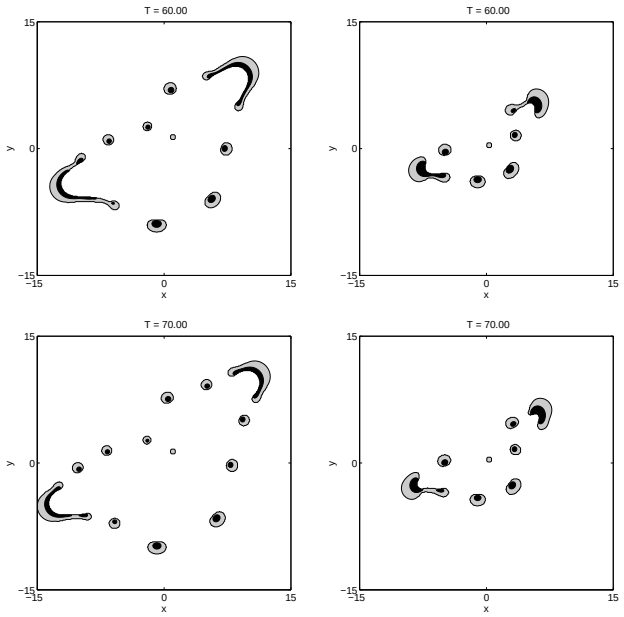

Figure 4.8: Comparison of fragmenting tumor growth into high-mobility tissue ($\mu = \infty$, left plots) and low-mobility tissue ($\mu = 1$, right plots) at $T = 60.0$ and $T = 70.0$.

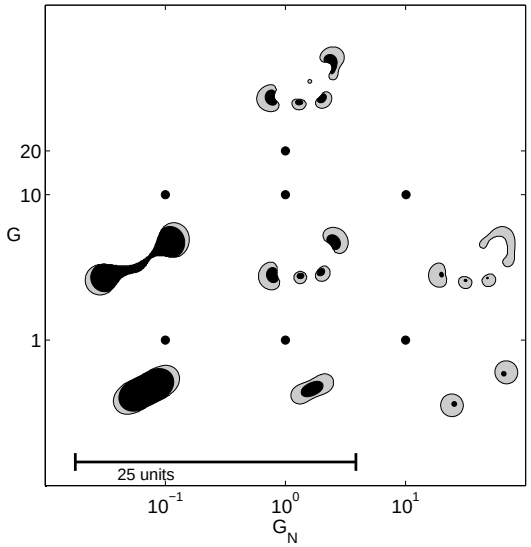

Figure 4.9: Parameter study in G and G_N for fragmenting tumor growth into nutrient-poor, low-mobility tissue ($D = 1$, $\mu = 1$). The tumor aggressiveness parameter G increases from bottom to top, and the necrotic degradation parameter G_N increases from left to right.

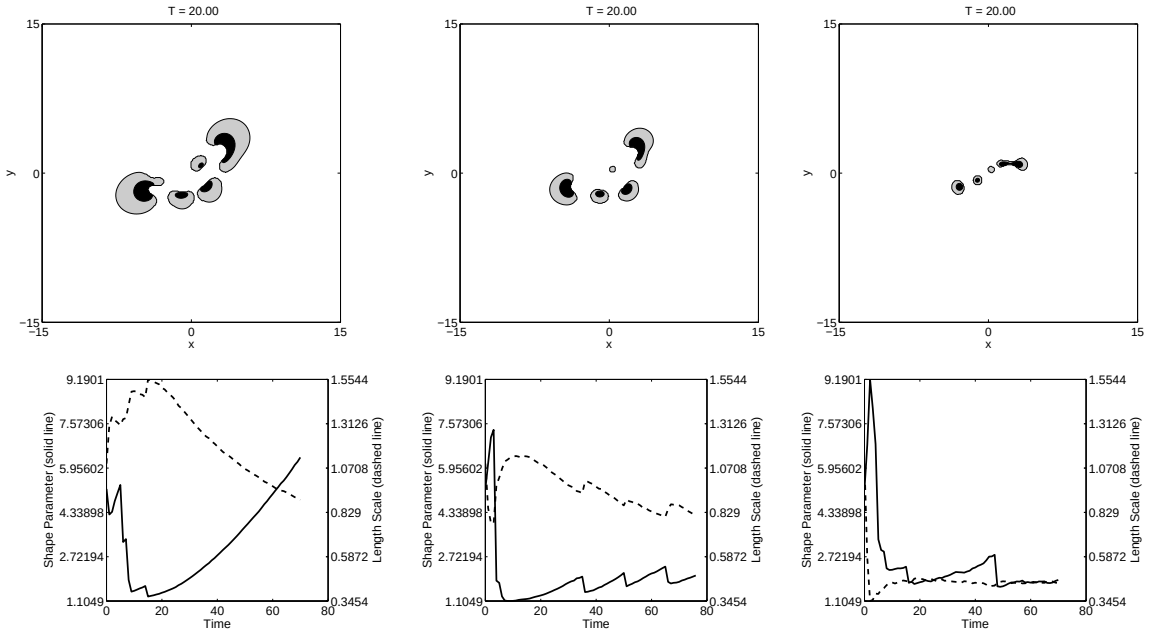

Figure 4.10: The effect of N on fragmenting tumor growth into nutrient-poor, low-mobility tissue ($D = 1$, $\mu = 1$): From left to right: $N = 0.175$, $N = 0.350$, and $N = 0.700$. The top row gives the morphology at $T = 20.0$, and the bottom row plots the shape parameter $\mathcal{S}$ (solid curves) and length scale $\mathcal{LS}$ (dashed curves). $G = 20$, $G_N = 1$, and $A = 0$ for all three simulations.

microenvironment. Accordingly, a large portion of the tumor becomes necrotic and is broken down by enzymes, leading to early fragmentation. (See $T = 10.0$ in Figure 4.5.)

In each tumor fragment, cell proliferation is faster on the outer side (toward the outer boundary of Ω_H) where the nutrient level is highest. (See Figure 4.6 to see the nutrient concentration near a typical tumor fragment.) On the opposite side of each fragment, the nutrient level is lowest, leading to slow proliferation and necrosis. The net result is preferential growth of the tumor fragment away from the nutrient-depleted center of the computational domain. In the nutrient-poor microenvironment, it is advantageous for the fragments to elongate, thereby increasing the surface area of the fragments and allowing better access to nutrient. (See $T = 20.0$ and $T = 30.0$ in Figure 4.5.) Eventually, when a tumor fragment grows sufficiently long, necrosis causes the fragment to break into multiple satellite fragments which are temporarily stabilized by cellular adhesion, and the process repeats. (See $T = 50.0$, $T = 60.0$, and $T = 70.0$ in Figure 4.5.)

We can gain a more detailed understanding of this repeating elongation-fragmentation

cycle by examining the evolution of $\mathcal{S}$ and $\mathcal{LS}$ in the top left plot in Figure 4.7. Initially, the shape parameter $\mathcal{S}$ (solid line) is large but drops rapidly as cell-cell adhesion pulls cells together and shrinks high-frequency perturbations in the tumor boundary. Thereafter, the shape parameter steadily rises as the tumor fragments elongate and become increasingly noncircular. At the same time, the length scale (dashed line) decreases because the width of the fragments decreases as they elongate. Whenever a fragment becomes sufficiently noncircular, the shape parameter $\mathcal{S}$ peaks, and decay of the necrotic core breaks the fragment into multiple smaller pieces. After the break, the cell-cell adhesion causes the new fragments to coalesce into spheroids, resulting in a rapid drop in $\mathcal{S}$ and an increase in the length scale $\mathcal{LS}$. Consequently, $\mathcal{S}$ reaches a peak when $\mathcal{LS}$ reaches a local minimum, and vice versa. As the trend repeats, $\mathcal{S}$ and $\mathcal{LS}$ trace out a "sawtooth" pattern in Figure 4.7 that is characteristic of fragmenting tumor growth. In fact, the formation of smaller fragments at more frequent time intervals can be observed as smaller sawteeth superimposed on the overall pattern.

The repeated elongation-fragmentation cycle is observed in tumor growth into lower-mobility, nutrient-poor regions as well. In Figure 4.8, we compare the tumor morphology at $T = 60.0$ and $T = 70.0$ for a high-mobility tissue (left plot: $\mu = \infty$) and a lower-mobility tissue (right plot: $\mu = 1$); repeated fragmentation is observed in both cases. When growing into a lower-mobility region, however, it is more difficult for the tumor to deform into highly-elongated fragments. Instead, the individual fragments grow into larger spheroids before deforming and breaking into new fragments. All these trends can be observed in the evolution of the shape parameter $\mathcal{S}$ (solid curve) and $\mathcal{LS}$ (dashed curve) on the top right plot of Figure 4.7. The characteristic "sawtooth" pattern can still be seen in the shape parameter and length scale. However, the oscillations in the shape parameter are much smaller, which reflects the difficulty in forming large deformations when growing into low-mobility tissue. The lack of smaller, superimposed sawteeth indicates fewer topology changes and more localized growth, which is seen in the smaller number of tumor fragments in Figure 4.8. Because the tumor fragments grow to form larger spheroids before deforming and fragmenting, the length scale also tends toward higher values in the low-mobility tissue case.

When examining the internal structure of tumors growing in nutrient-poor ($D = 1$) tissues, we find that the high-mobility ($\mu = \infty$; lower left plot in Figure 4.7) and low-mobility ($\mu = 1$; lower right plot in Figure 4.7) tissue cases are quite similar. The viable and necrotic volume fractions rapidly approach limiting values that are nearly identical for both tumors,

at approximately 70% viable area and 30% necrotic area. The similarity of the limiting values is consistent with our analysis in Section 4.2.6, where we found that the necrotic volume fraction does not depend upon the tissue cellular mobility μ for steady-state tumor spheroids. Unlike the case of circular growth where the volume fractions only stabilize once a (global) steady-state has been achieved, the necrotic volume fraction here stabilizes even during growth because the tumor features apparently reach local equilibrium between cell proliferation and necrosis. Interestingly, the necrotic volume fraction is quite similar to that predicted for spheroids with $D = 1$ (see Section 4.2.6), albeit somewhat lower, which indicates that the deformation of the larger tumor fragments marginally increases access to nutrient.

Tumors growing into nutrient-poor microenvironments demonstrate repeated fragmentation through a wide range of mitosis rates (governed by the parameter G) and necrotic tissue degradation rates (G_N). In Figure 4.9, we show the tumor morphology at time $T = 20.0$ for a variety of values of G and G_N and $\mu = D = 1$. Tumor fragmentation is observed in almost all cases, particularly for fast-proliferating, aggressive tumors with higher values of G. An increased aggressiveness (G) increases the rate of tumor fragmentation. Similarly, increasing the rate of necrotic tissue degradation (G_N) tends to destabilize the tumor, also leading to an increased rate of fragmentation. However, this effect is highly nonlinear: if G_N is large relative to G, then proliferation, necrosis, and cellular adhesion can balance to maintain spheroids and prevent further tumor fragmentation. This can be seen in the $G = 1$, $G_N = 10$ case in Figure 4.9: the tumor splits into two spheroids that reach a steady size while preferentially growing outward toward higher nutrient levels. We note that for sufficiently low levels of tumor aggressiveness (e.g., $G = 0.10$), tumor instability decreases until the steady-state configuration is tumor spheroids, as predicted in Cristini et al. (2003) for non-necrotic tumors. (Results not shown.)

As was predicted in Section 4.2.6 in the case of tumor spheroids, we found that the volume fractions of viable and necrotic tissue were largely independent of the tumor aggressiveness parameter G and the microenvironmental characteristics (D and μ) and were primarily functions of N and G_N. For $N = 0.35$ and $G_N = 0.10$, necrotic tumor cells were degraded very slowly; consequently, the majority of the tumor (approximately 80%) was composed of necrotic tissue and 20% by viable cells. Fixing $N = 0.35$ and increasing G_N, the volume fraction occupied by necrotic tumor tissue steadily decreased, at approximately 30% for $G_N = 1$ and 5% for $G_N = 10$.

In the cases where the tumors have not fragmented by $T = 20.0$, moderate-to-significant deformation still occurs, and fragmentation is likely at a later time. The occurrence of repeated tumor fragmentation over a broad range of G and G_N demonstrates that in the nutrient-poor regime, tumor morphology is largely determined by the characteristics of the surrounding microenvironment, while the genetic characteristics of the tumor (G, G_N, A, and N) determine the size and rate of evolution of the tumor. In addition, increasing the apoptosis rate A to positive values results in similar morphological behavior, only with more rapid tumor fragmentation and a greater number of fragments. (Results not shown.)

We examined the impact of N on the morphology of tumor growth in the nutrient-poor regime, and the results for $N \in \{0.175, 0.350, 0.700\}$ are given in Figure 4.10, where $D = \mu = G_N = 1$ and $G = 20$. For all three values of N, the tumor demonstrated repeated fragmentation (top row of Figure 4.10), and therefore all demonstrated the characteristic sawtooth pattern in $\mathcal{S}$ and $\mathcal{LS}$. (Bottom row of Figure 4.10.) As N increases, the volume fraction of the tumor undergoing necrosis increases from approximately 20% ($N = 0.175$) to roughly 30% ($N = 0.350$) to nearly 40% ($N = 0.700$), leading to a decrease in the overall size and spread of the tumor fragments (top row of Figure 4.10).

The finding that tumor morphology in the nutrient-poor regime depends primarily upon the tumor microenvironment (μ and D) and not the tumor's genetic characteristics (N, G_N, and G) has important implications for cancer treatment. In anti-angiogenic therapy, drugs (e.g., Avastin) are supplied to prevent the neovascularization of the growing tumor and the surrounding tissue. As we have seen, the resulting nutrient-poor microenvironment may cause the tumors to fragment and invade nearby tissues, particularly for growth in higher-mobility tissues. This can negate the positive effects of antiangiogenic therapy and may lead to recurrence and metastasis. This result is consistent with the findings of Cristini et al. (2005), who suggested that combining antiangiogenic therapy with adhesion therapy may counteract the negative problems associated with tumor fragmentation in the nutrient-poor regime.

4.4.2 Invasive, Fingering Growth

In Figure 4.11, we show the evolution of a tumor growing into a low-mobility, nutrient-rich tissue, where $D = 50$ and $\mu = 1$. As in the previous section, $G = 20$ $G_N = 1$, and $N = 0.35$. Because nutrient readily diffuses through the surrounding tissue Ω_H, the

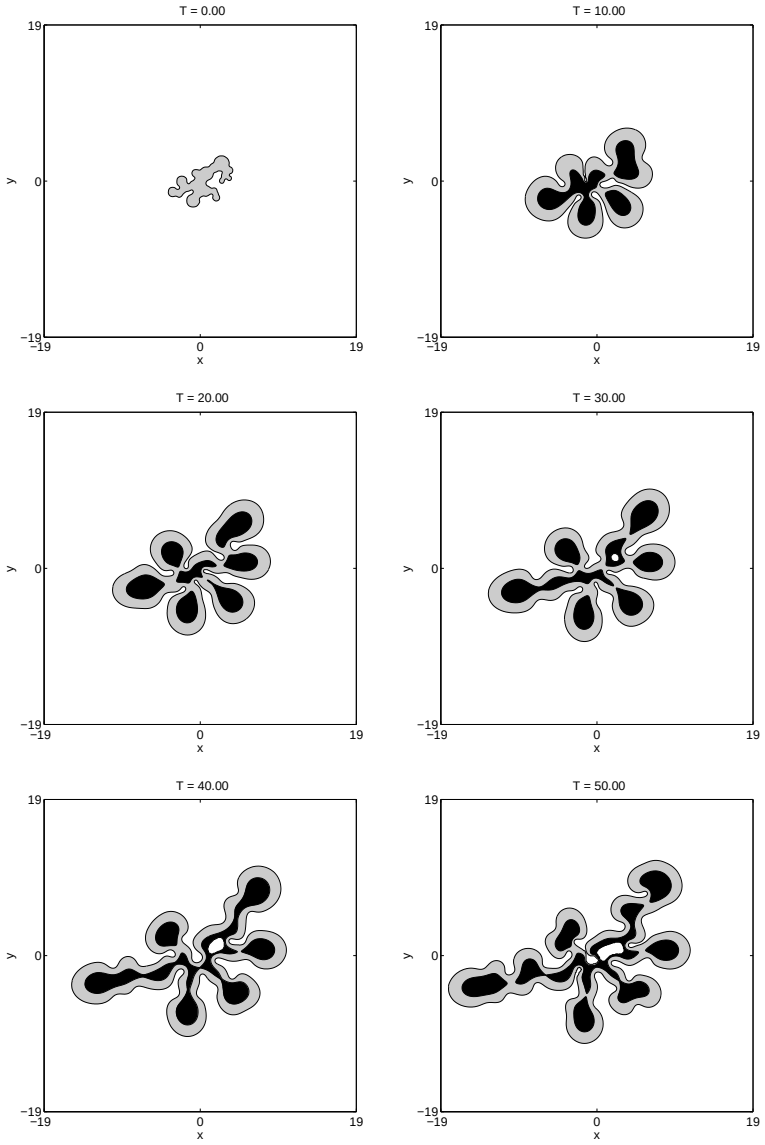

Figure 4.11: Long time simulation of invasive, fingering growth into nutrient-rich ($D = 50$), low-mobility ($\mu = 1$) tissue. Plots are in $T = 10.0$ increments, $G = 20$, $G_N = 1$, $N = 0.35$, and $A = 0$.

tumor is initially non-necrotic, allowing for unchecked growth and the development of buds on the tumor periphery that protrude into the surrounding tissue. (See time $T = 10$ in Figure 4.11.) Due to the cell-cell adhesion (modeled by the pressure jump in (4.18)), the proliferation-induced mechanical pressure is greatest surrounding any protusions of the tumor into the healthy tissue and approximately zero near flatter regions of the tumor

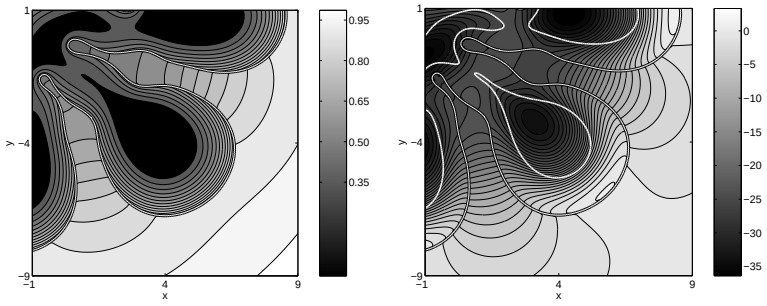

Figure 4.12: Contours of the nutrient concentration (left) and pressure (right) between growing fingers from the previous simulation at time $T = 20.0$. In the nutrient figure, the black region denotes where $\sigma < N$, and in the pressure figure, the boundary of the necrotic core is given by the white curve. Notice that the pressure gradient is primarily parallel to the fingers.

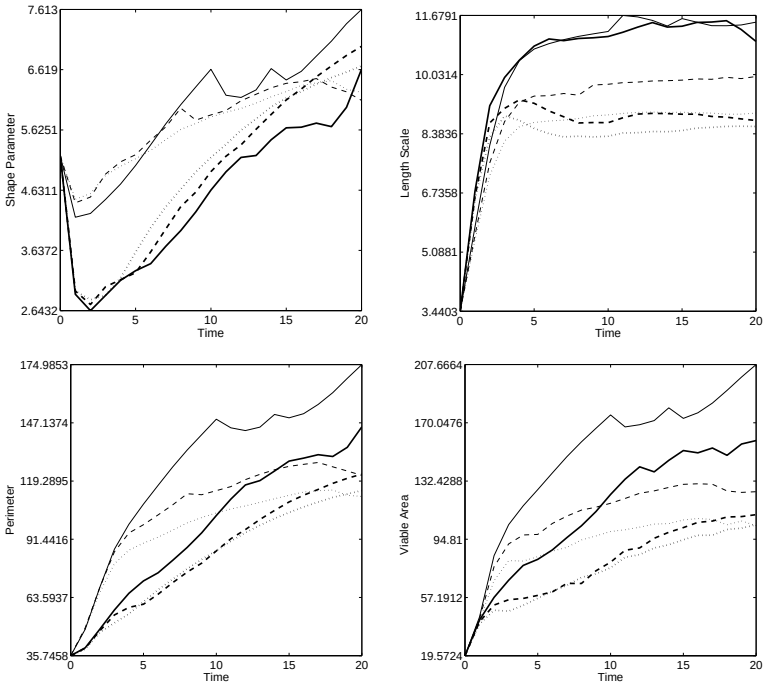

Figure 4.13: Evolution of the shape parameter $\mathcal{S}$ (top left), length scale $\mathcal{LS}$ (top right), perimeter (bottom left), and viable tumor area (bottom right) for invasive, fingering growth into nutrient-rich, low-mobility tissue (thin curves: $\mu = 0.25$, thick curves: $\mu = 1$). In all plots, dotted lines are for $D = 50$, dashed lines are $D = 100$, and solid lines are $D = \infty$.

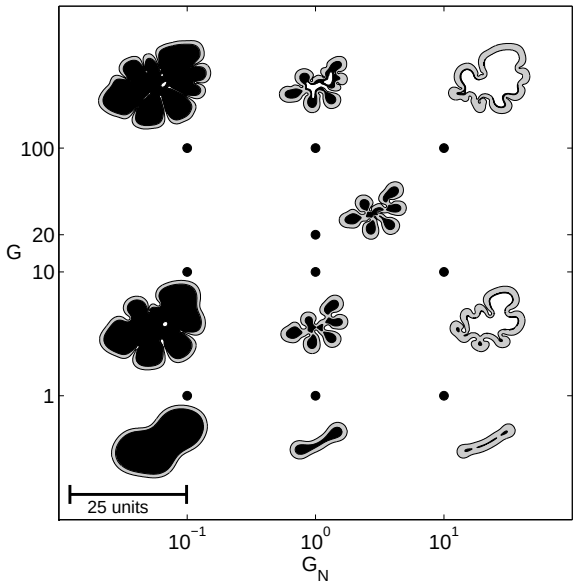

Figure 4.14: Parameter study in G and G_N for invasive, fingering tumor growth into nutrient-rich, low-mobility tissue ($D = 50$, $\mu = 1$). The tumor aggressiveness parameter G increases from bottom to top, and the necrotic degradation parameter G_N increases from left to right.

boundary. Because the cellular motility μ is low in the noncancerous tissue, the individual cells and the extracellular matrix cannot move to equilibrate the pressure. As a result, the cellular velocity field is mostly parallel to the buds, in spite of adequate nutrient levels between the growing buds. (See the left plot of Figure 4.12 for the nutrient concentration between two growing buds, and the right plot for the corresponding pressure field.) This makes it difficult for buds to merge, leading to the formation of long, invasive fingers. (See $T = 30.0$ to $T = 50.0$ in Figure 4.11.) The net effect is highly-invasive growth into the surrounding tissue. (See $T = 50.0$ in Figure 4.11.)

Within the nutrient-rich, low-mobility tissue regime, we examined two levels of tissue mobility ($\mu \in \{0.25, 1\}$) and three nutrient diffusivities ($D \in \{50, 100, \infty\}$), for a total of six combination of mobility and nutrient diffusivity. In the top left plot in Figure 4.13, we show the evolution of the shape parameter $\mathcal{S}$ for these six simulations. We found that the shape parameter depended primarily upon the tissue mobility: the three lower-mobility tissue examples ($\mu = 0.25$, thin dotted, dashed, and solid curves) had an overall higher shape parameter than the higher-mobility tissue ($\mu = 1$, thick dotted, dashed, and solid

curves), which reflects a higher degree of deformation. This trend is indeed observed in the morphologies along the $\mu = 0.25$ row of Figure 4.4. This is because the lower the tissue mobility, the more difficult it is for cells in the healthy tissue to overcome the cell-cell and cell-ECM adhesion and move to equilibrate pressure variations, and the more difficult it is for the ECM to deform in response to the pressure, allowing for the formation of sharper corners and greater shape instabilities.

This trend is also reflected in the tumor perimeters in the lower left plot of Figure 4.13: overall, the larger deformation in the lower-mobility tissue simulations leads to overall larger perimeters in the low-mobility tissue cases (thin curves) than in the higher-mobility tissue cases (thicker curves). As a result of the increased surface area, the low-mobility tissue tumors had greater access to nutrient. This leads to a surprising result: the increased morphological instability from growing into lower-mobility tissues improves access to nutrient and leads to larger tumors, as can be seen in the lower right plot in Figure 4.13; for each fixed nutrient diffusivity, the volume of the viable area of each tumor was larger for the lower-mobility tissue simulation ($\mu = 0.25$) than for the corresponding higher-mobility tissue example ($\mu = 1$). For all examples, the shape parameter steadily rose as a function of time, which reflects the increasing shape instability as the tumors invade the surrounding tissue; this is characteristic of invasive, fingering growth. This has implications for therapies that target cell-cell and cell-ECM adhesiveness: if the therapy decreases the mobility in the surrounding microenvironment (by increasing the cell-cell or cell-ECM adhesiveness or rendering the ECM more rigid), then invasive, fingering growth into the surrounding tissue is likely. Likewise, any treatment that decreases the permeability of the host tissue to tumor cells may lead to an increase in tumor invasiveness.

In the upper right plot of Figure 4.13, we see that the length scale $\mathcal{LS}$ is most strongly dependent upon the nutrient diffusivity D, and largely independent of the tissue mobility μ. As the nutrient diffusivity increases, nutrient is better able to diffuse between the growing fingers, allowing the nutrient to penetrate farther into the fingers. This allows the tumor to support thicker fingers, which can be seen in the increased length scale parameter $\mathcal{LS}$ for higher values of D. In all cases, the length scale tended toward a roughly fixed value, which demonstrates that each tissue can support a specific finger thickness.

As was predicted in Section 4.2.6 for tumor spheroids and observed in the fragmenting growth regime, the volume ratios of the tumor were nearly independent of the tumor microenvironment. We examined the viable and necrotic volume fractions for growing tumors

with $\mu \in \{0.25, 1\}$ and $D \in \{50, 100, \infty\}$. In all cases, the volume fractions quickly stabilized, with the viable rim comprising approximately 65% of the tumors and the remaining 35% being made up of necrotic cells. This necrotic volume fraction is slightly less than that predicted for tumor spheroids with $D = 50$ (approximately 37% for spheroids), which again reflects the fact that the tumor's morphological response to the microenvironment increases its access to nutrient.

In Figure 4.14, we examine the effect of the tumor aggressiveness parameter G and the necrotic degradation parameter G_N on the invasive, fingering morphology. We fix $D = 50$, $\mu = 1$, $N = 0.35$, and take $0.1 \leq G_N \leq 10.0$ and $1 \leq G \leq 100$. For lower tumor aggressiveness values ($G = 1$) and $G_N \geq 1$, the fingering effect was significantly reduced, resulting in more stable, tubular-shaped tumors, an effect that has been observed in experiments (Frieboes et al., 2006b). These structures form because tumor cell proliferation (the numerator of G) and cell-cell adhesion (the denominator of G) are roughly in balance when $G = 1$. The competition between proliferation and adhesion smooths but does not completely prevent shape instabilities, which may continue to grow. For sufficiently large values of G, the invasive fingering morphology was observed in all simulated tumors. For lower values of G_N (left column in Figure 4.14), the low rate of degradation of the necrotic tumor tissue leads to the formation of very wide fingers; this morphology may be better described as a collection of spheroids. As G_N is increased, the necrotic core is degraded more quickly, leading to a decreased finger thickness, less stable morphology, and more aggressive tissue invasion. As G_N is increased toward $G_N = 10$ (right column in Figure 4.14), the finger thickness is decreased to the point where the tumor periodically breaks into fragments and then reconnects, leading to the encapsulation of noncancerous tissue (white enclosed regions). This morphology, which we refer to as compact/hollow, is characterized by the presence of a large abscess containing a mixture of necrotic cells, fluid, noncancerous ECM, and cellular debris, much like a necrotic core. A long-time simulation of a tumor with the compact/hollow morphology can be seen in Figure 4.15 with a different value of μ; this morphology will be examined in greater detail in the following section. The effect of G_N on growth is seen to be non-monotonic: increasing G_N at first limits the size of the tumor by decreasing the thickness of the invasive fingers and limiting the overall spread of the tumor, but after a certain point, instability breaks the tumor and allows greater spread through the surrounding noncancerous tissue. For example, for $G = 10$, the total viable area at time $T = 20$ drops from 103.3404 when $G_N = 0.10$ to 93.3156 for $G_N = 1.0$, then

increases to 133.7360 for $G_N = 10$.

Lastly, we studied the effect of N on the invasive fingering growth regime by simulating with $N \in \{0.175, 0.350, 0.700\}$, $G = 20$, $G_N = 1$, $D = 1$, and $\mu = 1$. As in the fragmenting case, we found that varying N changes the tumor evolution quantitatively but not qualitatively. As N increases, the thickness of the viable rim and the overall spread of the tumor decrease, and the necrotic volume fraction increases ($N = 0.175$: approximately 25%; $N = 0.35$: nearly 35%; $N = 0.70$: over 40%.).

4.4.3 Compact, Hollow Growth

In Figure 4.15, we show the evolution of a tumor growing into a high-mobility ($\mu = 50$), nutrient-rich ($D = 100$) tissue, where $G = 20$, $N = 0.35$, and $G_N = 1$. In the beginning ($T = 0.0$ to $T = 5.0$ in Figure 4.15), growth is very similar to the invasive, fingering case. Because the noncancerous tissue is nutrient-rich, the tumor only develops a necrotic core after an initial period of growth, after which shape instabilities (buds) appear. However, because the noncancerous tissue has a greater mobility μ, the cells and extracellular matrix in the surrounding noncancerous tissue are more free to move and relieve the pressure caused by the growing tumor. Consequently, the buds on the outer edge of the tumor do not invade the surrounding tissue, but instead flatten and periodically merge, encapsulating healthy tissue in the process ($T = 10.0$ to $T = 20.0$ in Figure 4.15), a process that has been previously observed in boundary integral simulations of tumor growth (Cristini et al., 2003). In the meantime, necrotic tissue on the inside boundary of the tumor continues to degrade, leading to the formation of a large abscess in the tumor core filled with a mixture of noncancerous tissue and cellular debris ($T = 15.0$ and $T = 20.0$ in Figure 4.15). We expect that in reality, any noncancerous cells contained in the abscess may also undergo necrosis, and due to the presence of matrix degrading enzymes in the tumor, encapsulated ECM should be degraded. This suggests an evolution similar to those seen for smaller values of G. We shall further investigate these effects in a future work.

Within the nutrient-rich, high-mobility regime, we examined two levels of mobility ($\mu \in \{50, \infty\}$) and three nutrient diffusivities ($D \in \{50, 100, \infty\}$). In all plots, $G = 20$, $G_N = 1$, $N = 0.35$, and $A = 0$, thin curves denote lower-mobility ($\mu = 50$) simulations, and thick curves give higher-mobility ($\mu = \infty$) simulations. In all plots, the dotted lines are for $D = 50$, the dashed lines are $D = 100$, and the solid lines correspond to $D = \infty$.

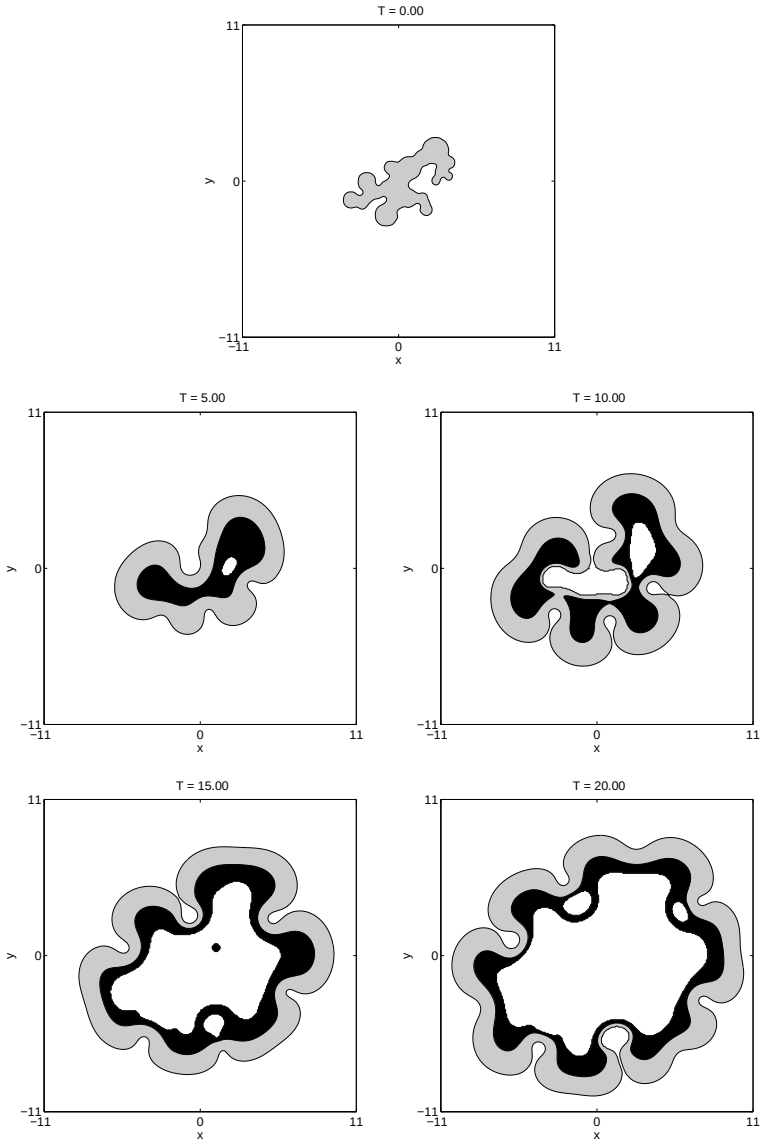

Figure 4.15: Long time simulation of compact tumor growth into nutrient-rich, high-mobility tissue ($D = 100$, $\mu = 50$). Plots are in $T = 10.0$ increments, with $G = 20$, $G_N = 1$, $N = 0.35$, and $A = 0.0$.

In the top left plot of Figure 4.16, we plot the evolution of the shape parameter $\mathcal{S}$ for all these simulations. In all cases, the shape parameter increased in an eratic manner, which is indicative of frequent increases in morphological complexity. This is a reflection of the frequent formation and merger of buds, and of the encapsulation of noncancerous tissue by the growing tumor seen in Figure 4.15, and the behavior is similar for all simulations

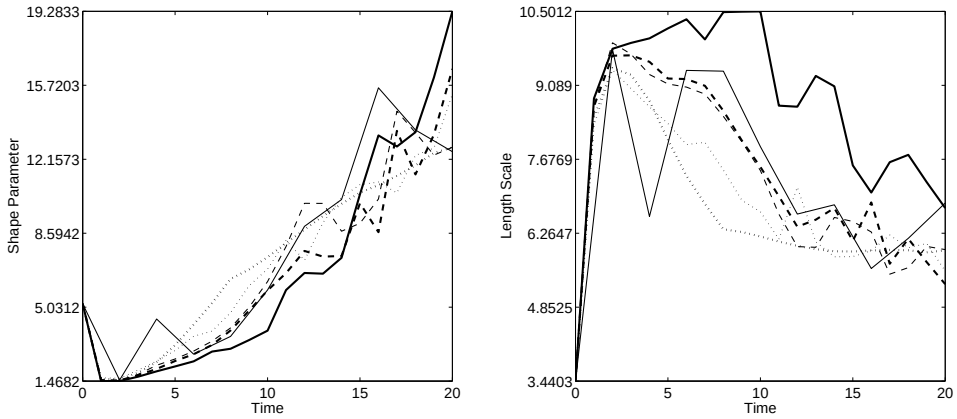

Figure 4.16: Evolution of the shape parameter $\mathcal{S}$ (left) and length scale $\mathcal{LS}$ (right) for compact growth into nutrient-rich, high-mobility tissue (thin curves: $\mu = 50$, thick curves: $\mu = \infty$). In all plots, dotted curves are for $D = 50$, dashed curves designate $D = 100$, and solid curves give $D = \infty$.

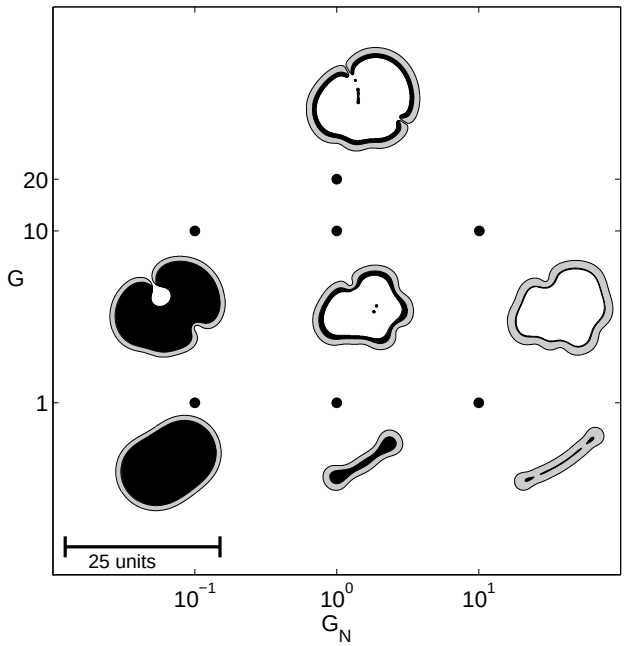

Figure 4.17: Parameter study in G and G_N for compact tumor growth into nutrient-rich, high-mobility tissue ($D = 50$, $\mu = \infty$). The tumor aggressiveness parameter G increases from bottom to top, and the necrotic degradation parameter G_N increases from left to right.

except for the $D = 50$, $\mu = \infty$ case. In that case, the encapsulation of tissue is much less frequent, and the behavior is similar to fragmenting growth: the tumor breaks into two halves, each of which resembles the elongated fragments observed in fragmenting growth. (See the uppermost tumor in Figure 4.17 for a closer view of this morphology.) For all six simulations, the values of $\mathcal{S}$ are generally higher than for the other growth regimes. This is because the tumor consists of two concentric boundaries like a ring: a complex, outer boundary with many shape instabilities, and a necrotic inner boundary. Accordingly, the compact/hollow tumors have a much greater ratio of perimeter to area. The length scale $\mathcal{LS}$, shown in the top-right plot of Figure 4.16, generally decreases for all simulations, with signs of tending toward a limiting value. This is because as the tumors grow, a characteristic rim thickness emerges, but the frequent encapsulation of noncancerous tissue causes the length scale to fluctuate in time.

We examined the viable and necrotic volume fractions for each of these simulations. As was the case with fragmenting and fingering growth, the percentages were nearly identical (approximately $65\% - 75\%$ viable and $30\% - 35\%$ necrotic) for all cases throughout most of the simulation time. The necrotic volume fraction was substantially less than the approximate 37% predicted for tumor spheroids with $D \geq 10$, and also generally less than that observed for invasive, fingering tumors with equal values of D. This is because the buds on the tumor periphery increase access to nutrient, are small enough to have very little necrotic tissue, and thereby reduce the necrotic volume fraction.

In Figure 4.17, we examine the effect of the tumor aggressiveness G and the necrotic degradation rate G_N on the compact tumor morphology. In all these simulations, we fix $D = 50$, $\mu = \infty$, and $N = 0.35$. For lower values of G (bottom of the plot), the tumors remain in compact morphologies that fail to encapsulate noncancerous tissue, although shape instabilities may occur at long times. When $G = 1$, cell proliferation (numerator of G) and adhesion (denominator of G) are roughly in balance, which shrinks but does not completely prevent shape instabilities. For larger values of G (upper portion of the plot), the cell proliferation rate outstrips cell-cell adhesion, resulting in folds in the outer tumor surface that encapsulate noncancerous tissue. For fixed values of G, we see that increasing the necrotic tissue degradation rate parameter G_N shrinks the necrotic volume fraction of the tumors. In the cases where noncancerous tissue has been encapsulated ($G > 1$), increasing G_N increases the size of the central tumor abscess.

Lastly, as in the fragmenting and fingering cases, we found that varying N changes the

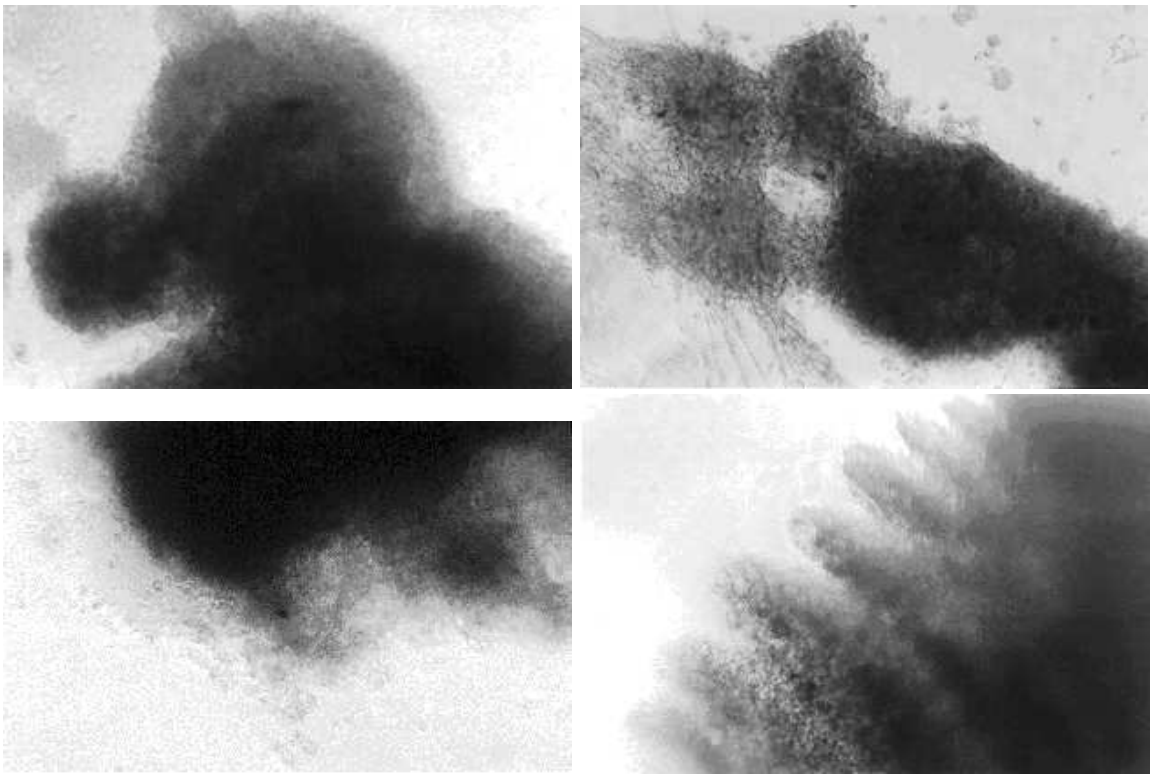

Figure 4.18: *in vitro* experimental evidence from the study by Frieboes et al. (2006b) of predicted tumor morphologies. **Lower left:** low glucose, 1% FBS. **Lower right:** high glucose, 1% FBS. **Upper left:** low glucose, 10% FBS. **Upper right:** high glucose, 10% FBS.

tumor evolution quantitatively but not qualitatively. As N increases, the thickness of the viable rim decreases, the necrotic volume fraction increases, and morphological instability also increases.

4.5 Discussion and Future Work

In this work, we have extended previous models of tumor growth and developed a framework to investigate the interaction between avascular solid tumors and their microenvironments during growth. In particular, we model the perfusion of nutrient through the tumor and the surounding microenvironment, the build-up of pressure in the tissue from the proliferation of cancerous cells, cell-cell and cell-ECM adhesion, and the loss of tumor volume due to necrosis.

Following previous models of solid tumor growth (Greenspan, 1976; McElwain and Morris, 1978; Adam, 1996; Byrne and Chaplain, 1996b,a; Chaplain, 2000), the genetic characteristics of the tumors are modeled by a small number of nondimensional parameters. One parameter, G, measures the tumor aggressiveness. A second parameter A measures the susceptibility of tumor cells to apoptosis, a third parameter N gives the critical nutrient level for tumor cell necrosis, and a fourth parameter G_N measures the enzymatic breakdown of necrotic tumor cells.

The biophysical characteristics of the microenvironment are modeled by a parameter D that measures the nutrient diffusivity of the host tissue relative to the diffusivity in the tumor, and a mobility parameter μ. The parameter D can be used to model normoxia (high D) or hypoxia (low D) in the microenvironment. The parameter μ models the combined effects of adhesion (both cell-cell and cell-ECM) and the capacity of the ECM to deform in response to pressure induced by tumor cell proliferation. The proliferative (oncotic) pressure serves as a simple model of tissue stress.

Using this framework, we investigated the effect of the microenvironment on tumor growth with a variety of genetic parameter combinations. In almost all cases, we found that the qualitative features of tumor morphologies are primarily determined by the microenvironmental parameters (D and μ). The parameters that characterize the tumor genetics (G, G_N, N, and A) generally affect quantitative aspects of the tumor progression, such as the size, the amount of invasion into the host tissue, the rate of growth, and the degree of morphological instability.

We found that the internal structure of the tumors (i.e., the necrotic and viable volume fractions of the tumors) depends primarily upon D, G_N, and N, and very little upon μ and G. Furthermore, we found that these volume fractions tend toward constant values even during growth, which indicates the emergence of characteristic feature sizes within the growing tumors and suggests a local equilibrium is attained. This is in contrast to the case of tumor spheroids, whose volume fractions only stabilize once a global steady state is established.

We observed three distinct morphologies: fragmenting, invasive/fingering, and compact/hollow growth. If the microenvironment is nutrient-poor (low D), tumors tend to break into small fragments and spread throughout the microenvironment, regardless of the cellular mobility μ. Within this nutrient-poor growth regime, decreasing the microenvironmental mobility μ (by increasing the noncancerous cell-cell and cell-ECM adhesion or

increasing the rigidity of the ECM) decreases the extent of the fragmentation and slows invasion into the surrounding tissue, but does not completely prevent the hypoxia-induced morphological instability. We note that unstable tumor morphologies in the nutrient-poor regime have also been observed by Anderson (2005) and Cristini et al. (2005).

The invasive, fingering morphology was found in cases of growth into nutrient-rich, low-mobility microenvironments. We found that increasing nutrient perfusion does not prevent this invasive morphology, and the lower the microenvironmental mobility μ, the greater the degree of morphological instability and invasiveness. Tumors growing into nutrient-rich, high-mobility tissues develop compact/hollow morphologies. A hallmark of this growth regime is the formation and merger of buds on the tumor periphery, which leads to the encapsulation of noncancerous regions Ω_H and the formation of a large abscess (a mixture of noncancerous cells, ECM, fluid, and cellular debris) in the tumor interior. Qualitatively, the interior abscess is similar to a necrotic core.

Within each of these three growth regimes, we investigated the effects of the genetic parameters G, G_N, and N. We found that lowering G, which corresponds to decreasing the tumor proliferation rate and/or increasing the tumor cell-cell adhesiveness, can stabilize growth, an effect that is already known. On the other hand, increasing G_N, which corresponds to an increased rate of degradation of the necrotic regions, tends to destabilize growth. Increasing N leads to smaller tumors.

Our results have important implications for therapy. Since decreasing the nutrient levels in the microenvironment tends to increase tumor fragmentation and invasion into the surrounding tissue, caution must be exercised when considering anti-angiogenic therapies. If this therapy is aimed at destroying the neovasculature as much as possible, this could lead to the adverse effect of inducing morphological instability that may lead to additional tumor fragmentation and invasion. Indeed, a number of experimental studies have now shown that anti-angiogenic therapies may increase the tendency of tumors to fragment and invade surrounding host tissue. (e.g., Sakamoto (1987), Rubinstein et al. (2000), DeJaeger et al. (2001), Rofstad and Halso (2002), Seftor et al. (2002), Lamszus et al. (2003), and Bello et al. (2004).) Conversely, we found that increasing the nutrient levels in the microenvironment leads to greater morphological stability and increased compactness of the tumor, thereby rendering the tumors more resectable. Consequently, our results support the contention of Cristini et al. (2005) that treatments that seek to normalize the tumor vasculature (by selectively "pruning" weak blood vessels with targeted anti-angiogenic therapy) may sta-

bilize the tumor morphology by providing the tumor with increased access to nutrient. Since such treatments may also increase the accessibility of the tumors to chemotherapeutic agents (Jain, 2001; Sinek et al., 2004), our results provide additional support for the use of targeted anti-angiogenic therapy as an adjuvant therapy to chemotherapy and resection. This is currently under investigation.

Our findings may have particular significance for breast cancer treatment when considered alongside other known effects of hypoxia. In our simulations, hypoxia, such as that caused by anti-angiogenic therapy, increases tumor morphological instability and invasiveness. In recent findings by Erler et al. (2006), it was shown that hypoxia upregulates lysl oxidase (LOX), which, in turn, is associated with estrogen receptor (ER)-negative breast cancer cells. This is of clinical importance, because ER-negative breast cancers are unsuited to hormone-based therapies and generally have worse prognosis (Chi et al., 2006). Therefore, when indiscriminant anti-angiogenic therapy is applied to breast cancer, it may lead to the fragmentation of the tumor into smaller, more invasive tumors which are resistant to further treatment.

As was pointed out by Cristini et al. (2005), another approach to therapy is to use anti-invasive drugs such as Met inhibitors (Boccaccio et al., 1998; Bardelli et al., 1999; Morotti et al., 2002) or hepatocyte growth factor antagonists (Date et al., 1998; Michieli et al., 1999) in addition to anti-angiogenic therapies. Such therapies affect the cell-cell and cell-ECM adhesive properties of the tumor. A recent experimental study on mouse models of malignant glioma shows that fragmentation can be prevented, and the elimination of tumor satellites may be achieved by a combined anti-angiogenic and anti-invasive therapy (Bello et al., 2004). In the nutrient-poor growth regime, increasing the cell-cell and cell-ECM adhesion of the microenvironment (i.e., reducing μ) can help to limit the rate of tumor fragmentation and the extent of tissue invasion. Decreasing the permeability of the microenvironmental ECM to tumor cells by other means such as making the extra-tumor ECM more dense, stiffer, and less able to support tumor cell movement could also attain this effect.

Interestingly, the *opposite* approach is warranted in the nutrient-rich growth regime. In this regime, increasing μ in the extra-tumor ECM decreases the extent of invasive fingering. Thus, in a nutrient-rich tissue, an approach to therapy is to increase the permeability of the microenvironment Ω_H to tumor cells. This can be accomplished by decreasing the cell-cell and cell-ECM adhesion in the microenvironment Ω_H (while leaving tumor cells unaffected),

or equivalently, by increasing the tumor cell-cell and cell-ECM adhesion. We note that this effect may also be attained by decreasing the stiffness or density of the surrounding ECM. Such subtleties highlight the importance of considering tumor-microenvironment interactions when planning therapies that affect the adhesive and mechanical properties of the tumor, the surrounding tissue, or both.

It is important to ask whether the morphologies predicted here in our study occur during real tumor growth. In fact, by characterizing the range of behavior in the tumor growth model and comparing to experiments, we may predict physically relevant parameter ranges. For example, in our studies, we have taken the aggressiveness parameter $G \geq 1$. In simulations not presented, we have found that taking $G < 1.0$ with apoptosis $A = 0.0$ may result in stable, circular tumor morphologies during avascular growth. We note that in recent work, Frieboes et al. (2006b) predicted a lower value of G for morphologic instability ($0.6 \leq G \leq 0.9$ for marginal stability, and $G > 0.9$ for very unstable behavior) based upon an approximation of a similar theoretical model of spheroid growth that accounted only for apoptosis and not necrosis. This analysis overpredicts instability.

Interestingly, all of the morphologies found in this work have been seen in an *in vitro* tumor growth study performed as part of a joint experimental/computational investigation of tumor growth by Frieboes et al. (2006b). In that study, tumor spheroids were placed in a solution containing various levels of glucose and fetal bovine serum (FBS). The levels of glucose and FBS were both found to affect the tumor progression and morphology. When the glucose level was low, the *in vitro* tumors shed cells and fragmented. The degree to which this occurred depended upon the level of FBS. When the FBS level was low, growth was slow and a limited amount of tumor fragmentation was observed. See the lower left plot of Figure 4.18 for a characteristic image. When the level of FBS was high, the growth was faster, the tumors developed bulbous protrusions, and many fragments were formed. See the upper left plot of Figure 4.18. When the glucose level was high and the FBS level was low, invasive fingers developed, and fragmentation was limited. See the lower right plot of Figure 4.18. When the levels of glucose and FBS were both high, the tumors had roughly spherical shapes with bulbous protrusions on the surface. The tumors shed cells that strongly connected with each other, creating networks. See the upper right plot in Figure 4.18. Very interestingly, if FBS can be correlated with the permeability of the ECM to tumor cells (in this case, the ECM is created by the tumor cells themselves), then this behavior correlates very well with our predictions using the parameters D and μ (high

glucose and FBS levels correspond to large D and μ, respectively). This will be a subject of future study.

Now that the general capabilities of the basic model have been demonstrated, we are working to extend the realism of our simulator by modeling additional biophysical effects, including more detailed modeling of the internal structure of the tumors and the surrounding tissue. In collaboration with A.R.A. Anderson, M.A.J. Chaplain, V. Cristini, and S.R. McDougall, we are fully coupling our tumor growth model with the DATIA (dynamic adaptive tumour-induced angiogenesis) model of McDougall et al. (2006). With our improved models, we plan to further investigate the dynamics of tumor growth, the complex interplay between the microenvironment and the tumor, and possibilties for improved therapies. With an improved model in hand, we hope to calibrate it to specific cancers, allowing for specific predictions that can be verified in a laboratory setting. Our ultimate goal is the development of efficient, effective, and eventually individualized treatment regimens.

4.6 Acknowledgements

We thank the National Science Foundation Division of Mathematical Sciences and the UCI Department of Mathematics for their financial support. We thank Vittorio Cristini and Hermann Frieboes at the UCI Department of Biomedical Engineering for valuable discussions and for their generosity in providing unpublished experimental data from their 2006 study in Frieboes et al. (2006b). We thank Alexander "Sandy" Anderson and Mark Chaplain at the University of Dundee and Steven McDougall at Heriot Watt University for valuable discussions. We thank the reviewers for their comments, which helped improve the presentation of this paper.

4.7 Improvements to the Ghost Fluid Method

We now describe a second-order accurate extension of the ghost fluid method (Fedkiw et al., 1999; Liu et al., 2000; Gibou et al., 2002, 2003; Gibou and Fedkiw, 2005) to solve the Poisson-like system

$$\alpha \nabla^2 u = f_1(\mathbf{x}, t) + f_2(\mathbf{x}, t) u \qquad \text{in} \quad \Omega \text{ and } \Omega_H \tag{4.52}$$

$$[u] = g(\mathbf{x}, t) \qquad \text{on} \quad \Sigma \tag{4.53}$$

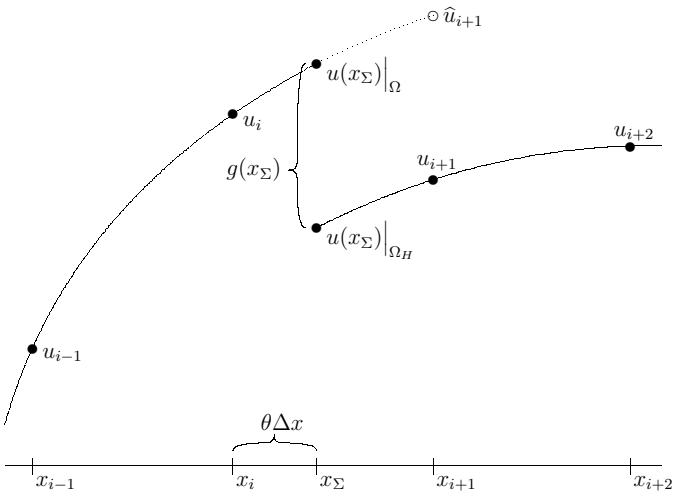

Figure 4.19: Discretizing $\alpha\nabla^2 u$ across the interface at x_Σ by a ghost fluid extension to $\widehat{u}_{i+1}$. Care must be taken to enforce the jump boundary conditions $[u] = g$ and $[\alpha\nabla u \cdot \mathbf{n}] = 0$.

$$[\alpha\nabla u \cdot \mathbf{n}] = 0 \qquad \text{on} \qquad \Sigma \tag{4.54}$$

$$u \equiv u_O \qquad \text{on} \qquad \partial(\Omega \cup \Omega_H) \tag{4.55}$$

on arbitrary domains embedded in a rectangular domain Ω_{comp}, where

$$\alpha = \begin{cases} \alpha_T & \text{in } \Omega \\ \alpha_H & \text{in } \Omega_H, \end{cases} \tag{4.56}$$

and α_T and α_H are positive constants.

In Macklin and Lowengrub (2005), we developed a second-order accurate extension of the ghost fluid method to solve this system in the case where $\Omega_H = \emptyset$ and $[\alpha\nabla u \cdot \mathbf{n}]$ is not specified on the boundary Σ. We now extend the method to solve the present system.

We discretize each partial derivative of $\alpha\nabla^2 u$ separately, and so we can focus our attention on the discretization of αu_{xx} at a node point $x_i \in \Omega$. If $x_{i-1} = x_i - \Delta x$ and $x_{i+1} = x_i + \Delta x$ are both contained in Ω, then we discretize $\alpha_T u_{xx}$ with the standard second-order stencil:

$$\alpha_T u_{xx} = \alpha_T \frac{u(x_{i-1}) - 2u(x_i) + u(x_{i+1})}{\Delta x^2} + \mathcal{O}(\Delta x^2). \tag{4.57}$$

However, if $x_{i+1} \in \Omega_H$, then the boundary must separate x_i and x_{i+1} at some point $x_\Sigma = x_i + \theta\Delta x$, where $0 < \theta < 1$. In this scenario, we must modify our stencil by first

extending the solution in Ω to a "ghost fluid point" $\widehat{u}(x_{i+1})$ in Ω_H; we replace $u(x_{i+1})$ by $\widehat{u}(x_{i+1})$ in the discretization of $\alpha_T u_{xx}$ in (4.57). See Figure 4.19. We proceed by a quadratic extrapolation of u from $u(x_{i-2})$, $u(x_{i-1})$, and $u(x_\Sigma)\Big|_\Omega = \lim_{x \uparrow x_\Sigma} u(x)$ to $\widehat{u}(x_{i+1})$.

We discretize (4.53) by

$$u(x_\Sigma)\Big|_\Omega = u(x_\Sigma)\Big|_{\Omega_H} + g(x_\Sigma, t), \tag{4.58}$$

where the jump notation is as defined in (4.9). If g is a function that is only defined at mesh points, then we evaluate $g(x_\Sigma, t)$ by cubic interpolation of $g(x_{i-1}, t)$, $g(x_i, t)$, $g(x_{i+1}, t)$, and $g(x_{i+2}, t)$.

We discretize (4.54) by

$$\alpha_T \frac{u(x_\Sigma)\Big|_\Omega - u(x_{i-1})}{(1+\theta)\Delta x} = \alpha_H \frac{u(x_{i+2}) - u(x_\Sigma)\Big|_{\Omega_H}}{(2-\theta)\Delta x}. \tag{4.59}$$

This discretization is similar to the discretization of Liu et al. (2000), although we use different points in the discretization for improved numerical stability. We note that this discretization approximates the jump condition $[\alpha \nabla u \cdot \mathbf{n}]$ as $[\alpha u_x] = 0$ and $[\alpha u_y] = 0$ when discretizing the x- and y-derivatives. (In three dimensions, $[\alpha u_z] = 0$ as well.) This is equivalent to assuming that the interface cuts the stencil at a right angle. Wherever this assumption is inaccurate, any tangential jump in $\alpha \nabla u$ is partially smeared out numerically. This limitation is characteristic of all current ghost fluid methods and is a trade-off for the dimension-by-dimension simplicity of the discretization. We are currently investigating solutions to this problem.

By combining (4.58) and (4.59), we can completely eliminate $u(x_\Sigma)\Big|_\Omega$ and $u(x_\Sigma)\Big|_{\Omega_H}$ from the discretization of $\alpha_T u_{xx}$. This allows the discretization of the entire Poisson system to be written in the form of a linear system $L\mathbf{u} = \mathbf{b}$, which can be solved by standard linear solvers. In our work, we used the stabilized biconjugate gradient method BiCG-Stab(2). (van der Vorst, 1992; Sleijpen et al., 1994; Duff et al., 1998) The case where $x_{i-1} \notin \Omega$ is handled analogously, and the discretization of $\alpha_H u_{xx}$ is similar. We discretize the far-field boundary condition (4.55) as in Macklin and Lowengrub (2005), where we define $\Omega_O = \Omega_{\text{comp}} \backslash \overline{(\Omega \cup \Omega_H)}$ to be the far field tissue and set

$$\frac{1}{\Delta x^2} u(x_i) = \frac{1}{\Delta x^2} u_O, \qquad \mathbf{x} \in \Omega_O. \tag{4.60}$$

This dimension-by-dimension discretization allows the use of the same method in both 2D and 3D problems, transforms the difficult problem of solving a diffusional problem on an

arbitrary domain to the simpler problem of diffusion on a rectangle, and is easy to extend to greater accuracy.

In our testing, we found this method to be second-order accurate. (See Section 4.3.2 for convergence testing results.) We are investigating the numerical smearing of tangential jumps in $\alpha \nabla u$, but our technique is currently the state-of-the art in solving Poisson-like systems on arbitrary evolving domains when using the ghost fluid approach. An alternative approach for overcoming the tangential smearing problem is the immersed interface method, which requires the use of local coordinates (based on the normal and tangential directions of the interface) to modify the discretization (LeVeque and Li, 1994).

Chapter 5

New Numerical Techniques for the Study of Tumor Growth in Large, Heterogeneous Tissues

Chapter Abstract:

In this paper, we present a ghost cell/level set method for the evolution of interfaces whose normal velocity depend upon the solutions of linear and nonlinear quasi-steady reaction-diffusion equations with curvature-dependent boundary conditions. Our technique includes a ghost cell method that accurately discretizes normal derivative jump boundary conditions without smearing jumps in the tangential derivative; a new iterative method for solving linear and nonlinear quasi-steady reaction-diffusion equations; an adaptive discretization to compute the curvature and normal vectors; and a new discrete approximation to the Heaviside function. We present numerical examples that demonstrate better than 1.5-order convergence for problems where traditional ghost cell methods either fail to converge or attain at best sub-linear accuracy. We apply our techniques to a model of tumor growth in complex, heterogeneous tissues that consists of a nonlinear nutrient equation and a pressure equation with geometry-dependent jump boundary conditions. We simulate the growth of *glioblastoma* (an aggressive brain tumor) into a large, 1 cm square of brain tissue that includes heterogeneous nutrient delivery and varied biomechanical characteristics (white and gray matter, cerebrospinal fluid, and bone), and we observe growth morphologies that are highly dependent upon the variations of the tissue characteristics–an effect observed in real tumor growth.

5.1 Introduction

The algorithms we develop in this paper are motivated by our interest in modeling tumor growth in complex, heterogeneous tissues. Cancer is a fundamental scientific and societal problem, and in the past several decades, intensive research has been focused on understanding the complexity of cancer progression, developing new therapies, and formulating optimal treatment protocols. While much work has been done in the mathematical community on tumor modeling (e.g., see the reviews by Adam (1996), Bellomo et al. (2003), Araujo and McElwain (2004a), Byrne et al. (2006), Sanga et al. (2006), and Quaranta et al. (2005)), to date there has been little work in modeling tumor growth in realistic, heterogeneous tissues on large spatial scales. The methods we present this paper will provide the foundation for a biologically-detailed millimeter-to-centimeter-scale model of tumor growth in heterogeneous tissues with realistic features (e.g., mechanically soft and hard regions, bone, and inhomogeneous nutrient delivery) (Macklin et al., 2007; Frieboes et al., 2007; Lowengrub and Macklin, 2007; Macklin, 2007). However, the methods described in this paper have applications beyond the tumor growth context and can be applied to general systems of linear and nonlinear quasi-steady reaction-diffusion problems on moving, heterogeneous domains.

In previous work (Macklin, 2003; Macklin and Lowengrub, 2005, 2006, 2007), we investigated simpler models of tumor growth using a level set/ghost fluid method that we developed in Macklin (2003) and Macklin and Lowengrub (2005); our technique tested second-order accurate when applied to interior problems, including the tumor growth model. (Hereafter, we refer to ghost fluid methods as ghost cell methods to emphasize that they have applications beyond fluid mechanics.) In Macklin and Lowengrub (2006), we improved the accuracy and robustness of level set-based curvature calculations in cases where two interfaces are in close contact, and we extended our approach to the two-sided problem in Macklin and Lowengrub (2007). However, this work still smeared any jumps in the tangential derivative across the interface, assumed homogeneous tumor microenvironments (with piecewise constant biophysical parameters) and was not capable of simulating growth into complex tissue structures. We note that Zheng et al. (2005) and Hogea et al. (2006) have also used level set methods to study tumor growth and angiogenesis, but this work also assumed homogeneous tissues and used lower-order accurate level set methods. Frieboes et al. (2006a, 2007) and Wise et al. (2006) have begun studying 3D tumor growth using a diffuse interface

approach, while others have begun studying the tumor problem using multiphase mixture models (e.g., see Ambrosi and Preziosi (2002), Byrne and Preziosi (2003), and Chaplain et al. (2006)). Still others use discrete models, such as cellular automata and agents (e.g., see Abbott et al. (2006), Anderson et al. (2006), and Byrne et al. (2006) for some recent examples).

In this paper, we present a ghost cell/level set method for the evolution of interfaces whose normal velocity depend upon the solutions of linear and nonlinear quasi-steady reaction-diffusion equations with curvature-dependent boundary conditions. We introduce a new normal derivative jump discretization for the ghost cell method that accurately discretizes the jump without numerically smearing any tangential derivative jump. In this approach, the normal jump is written as a combination of two grid-aligned jumps that are easier to compute. This addresses a longstanding problem with the ghost cell method, and in numerical testing, our extended ghost cell method achieves better than 1.5-order accuracy in cases where the traditional normal derivative jump stencil either fails to coverge or attains sub-first-order accuracy, regardless of mesh refinement. We also present a new adaptive normal vector calculation that allows us to robustly calculate appropriate normal vectors even in the presence of multiple, non-convex regions; we use this new adaptive normal vector discretization in our improved ghost cell method.

To solve nonlinear quasi-steady reaction-diffusion equations on large domains, we develop a nonlinear adaptive Gauss-Seidel-type iterative method (NAGSI) that can solve both linear and nonlinear problems using a localized update on a regular Cartesian mesh and is fully compatible with ghost cell extrapolations. NAGSI is an adaptive solution method that uses a dynamic selection criterion to focus computational effort without the need for a complex adaptive mesh. We find that NAGSI is second-order accurate when used to solve a variety of linear and nonlinear problems, and its adaptivity achieves between a 10% and 50% reduction in computational time.

We apply these techniques to nonlinear moving boundary problems where the velocity of the boundary depends upon the gradients of linear and nonlinear quasi-steady reaction-diffusion equations. When testing on a modified Hele-Shaw flow problem, our overall method demonstrates second-order accuracy. In the Hele-Shaw type problem, we simulate a growing drop of incompressible fluid in a medium with heterogeneous permeability; the drop grows preferentially in the regions of highest permeability. We also apply the techniques developed in this paper to model the growth of *glioblastoma* (an aggressive brain tumor) in a large

(1 cm $\times$ 1 cm), heterogeneous section of brain tissue, including white and gray matter with differing biomechanical properties, cerebrospinal fluid, and bone. The numerical advances presented in this paper enabled us to solve this complex problem in a short period of time (under 24 hours of computation) while observing new behavior, such as preferential growth of the tumor in regions of reduced biomechancial resistance.

The outline of this paper is as follows. In Section 5.2, we introduce the general system of quasi-steady, linear and nonlinear reaction-diffusion equations that we solve on moving domains. In Section 5.3, we discuss the level set method, present our techniques for robustly and accurately calculating geometric quantities (i.e., curvature and normal vectors), introduce the ghost cell method, present our new normal derivative jump discretization that preserves the tangential derivative jump, and introduce our nonlinear adaptive Gauss-Seidel-type iterative (NAGSI) scheme for solving linear and nonlinear quasi-steady reaction-diffusion equations. We close Section 5.3 by combining these techniques to solve the general system presented in Section 5.2. In Section 5.4, we test the numerical convergence of our new ghost cell method using the new normal derivative jump discretization and the NAGSI solver, as well as our overall technique. In Section 5.5, we present examples derived from Hele-Shaw flow in a heterogeneous material and tumor growth in a complex, heterogeneous simulated tissue. We discuss our results and future work in Section 5.6.

5.2 The Equations for the Quasi-Steady Reaction-Diffusion System

We wish to solve systems of (potentially nonlinear) quasi-steady reaction-diffusion equations on a domain $\mathcal{D}$ that is divided into two subdomains $\Omega(t)$ and $\Omega^c(t)$ by a moving interface $\Sigma(t)$. See Figure 5.1. The interface $\Sigma(t)$ evolves with a velocity that depends upon the gradients of these solutions. That is, we solve for a system of functions $p_1, p_2, \ldots, p_k$ on $\mathcal{D}$ that satisfy equations of the form

$$\begin{aligned} 0 &= \nabla \cdot (D_i(\mathbf{x}, t, p_i)\nabla p_i) + f_{R,i}(\mathbf{x}, t, p_1, \cdots, p_i)\, p_i \\ &\quad + f_{S,i}(\mathbf{x}, t, p_1, \cdots, p_i) \end{aligned} \tag{5.1}$$

on $\mathcal{D}\backslash\Sigma$, coupled with jump boundary conditions

$$[p_i] = g_i \tag{5.2}$$

$$[D_i \nabla p_i \cdot \mathbf{n}] = h_i \tag{5.3}$$

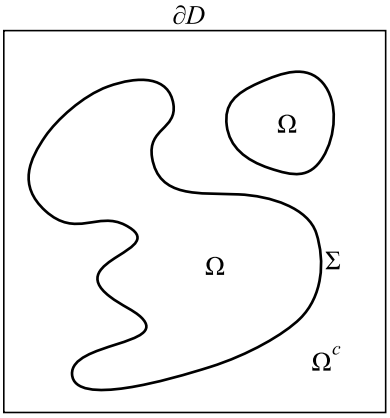

Figure 5.1: Regions for the general nonlinear quasi-steady reaction-diffusion moving boundary system.

on Σ and either Dirichlet, Neumann, or extrapolation (extrapolated from the interior of the domain) boundary conditions on $\partial\mathcal{D}$. Here, $\mathbf{n}$ is the outward unit normal vector (pointing into Ω^c), and we define a jump in a quantity q at a point $\mathbf{x}_\Sigma \in \Sigma$ by

$$\begin{aligned}[q(\mathbf{x})] &= q_{\text{in}} - q_{\text{out}} \\ &= \lim_{\Omega \ni \mathbf{x} \to \mathbf{x}_\Sigma} q(\mathbf{x}) - \lim_{\Omega^c \ni \mathbf{x} \to \mathbf{x}_\Sigma} q(\mathbf{x}). \end{aligned} \tag{5.4}$$

In the case where $g_i = 0$ and $h_i = 0$, this reduces to a regular (linear or nonlinear) diffusion problem throughout the domain $\mathcal{D}$.

The interfacial outward normal velocity V is given by

$$V = \sum_{i=1}^{k} \alpha_i \nabla p_i \cdot \mathbf{n}. \tag{5.5}$$

5.3 Numerical Solution Techniques

Before discussing our solution technique for the overall system, we introduce the key methods that will be required. Our overall technique is centered around a level set/ghost cell method which we first developed for a tumor growth problem in Macklin (2003), Macklin and Lowengrub (2005), Macklin and Lowengrub (2006), and Macklin and Lowengrub (2007). For completeness, we shall describe the overall approach, with a focus on new improvements in the method.

5.3.1 Narrow Band/Local Level Set Method

Level set methods were first developed by Osher and Sethian (1988) and have been used to study the evolution of moving surfaces that experience frequent topology changes (e.g., merger of regions and fragmentation), particularly in the contexts of fluid mechanics and computer graphics. (See the books by Sethian (1999) and Osher and Fedkiw (2002) and the references by Osher and Sethian (1988), Osher and Fedkiw (2001), and Sethian and Smereka (2003).) In the level set method, the location of a region Ω is captured implicitly by introducing an auxilliary signed distance function φ that satisfies

$$\begin{cases} \varphi(\mathbf{x}) < 0 & \mathbf{x} \in \Omega \\ \varphi(\mathbf{x}) = 0 & \mathbf{x} \in \Sigma = \partial\Omega \\ \varphi(\mathbf{x}) > 0 & \mathbf{x} \in \Omega^c \\ |\nabla\varphi(\mathbf{x})| \equiv 1. \end{cases} \tag{5.6}$$

In the level set approach, instead of explicitly tracking the position of interface Σ and manually handling topology changes, the level set function is updated by solving a PDE, which automatically accounts for the interface motion and all topology changes. If V is the outward normal velocity of the interface, then we update the position of the interface implicitly via

$$\varphi_t + \widetilde{V}\,|\nabla\varphi| = 0, \tag{5.7}$$

where $\widetilde{V}$ is an extension of V off of the interface. The extension $\widetilde{V}$ is often obtained using a Hamilton-Jacobi PDE. (e.g., see Zhao et al. (1996) and Adalsteinsson and Sethian (1999).) The fast marching method developed by Adalsteinsson and Sethian (1999) constructs an extension $\widetilde{V}$ while simultaneously reinitializing the level set function using an ordered sequence of discrete operations, but is only first-order accurate. In Macklin and Lowengrub (2005) we developed a bilinear extension technique that is both faster and more accurate than the traditional, PDE-based approach.

Solving (5.7) can introduce numerical error into the level set function that perturbs it away from being a distance function, even for special choices of $\widetilde{V}$ that are constant in the normal direction from the interface (Adalsteinsson and Sethian, 1999; Sethian, 1999) and thereby preserve distance functions. This is compensated for by reinitializing the level set function at regular intervals by solving

$$\varphi_\tau = \text{sign}(\varphi^0)\,(1 - |\nabla\varphi|) \tag{5.8}$$

to steady state (Peng et al., 1999; Sussman and Fatemi, 1999). Here, τ is pseudo-time, and φ^0 is the original level set function prior to the reinitialization.

We discretize the spatial operator $|\nabla\varphi|$ in (5.7) and (5.8) using the fifth-order weighted essentially non-oscillatory (WENO) method (Jiang and Shu, 1996; Jiang and Peng, 2000), and we discretize pseudo-time in (5.8) using the third-order total variation-diminishing Runge-Kutta method (TVD-RK) from Gottlieb and Shu (1997) and Gottlieb et al. (2001). Due to the computational cost and the complexity of our tumor system, we currently discretize time in (5.7) using a forward Euler algorithm and a small step size. We discretize the sign function as in Sussman and Fatemi (1999).

Lastly, because the primary purpose of a level set function is to track the position of the interface Σ over time, its accuracy is most important on and near the interface. To find the best compromise between accuracy and computational efficiency, we seek to update φ only as much as is necessary to accurately advect the interface. This can be done using the narrow band/local level set technique (Malladi et al., 1996; Peng et al., 1999). Given an initialized level set function φ, only the points that fall within a fixed distance of the interface are updated during level set operations (e.g., velocity extensions and level set reinitialization). In the level set context, the narrow band can be identified by

$$\{\mathbf{x} : |\varphi(\mathbf{x})| \leq R\}, \tag{5.9}$$

where $R > 0$ is a fixed constant that is chosen to suit the problem. In our work with the tumor problem, we use $R = 20\Delta x$. In some cases, we shall use a *semi*band $\{\mathbf{x} : \varphi(\mathbf{x}) \leq R\}$.

5.3.2 Calculating Geometric Quantities

One of the advantages of the level set method is that the level function encodes all the geometric information. In particular, the outward-facing normal vector $\mathbf{n}$ is given by

$$\mathbf{n} = \frac{\nabla\varphi}{|\nabla\varphi|}, \tag{5.10}$$

and the mean curvature can be computed via

$$\kappa = \nabla \cdot \mathbf{n} = \nabla \cdot \left(\frac{\nabla\varphi}{|\nabla\varphi|} \right). \tag{5.11}$$

As we noted and used in Macklin and Lowengrub (2005) and Macklin and Lowengrub (2006), the level set function can also be used to estimate the closest point $\mathbf{x}_\Sigma = (x_\Sigma, y_\Sigma)$ on the

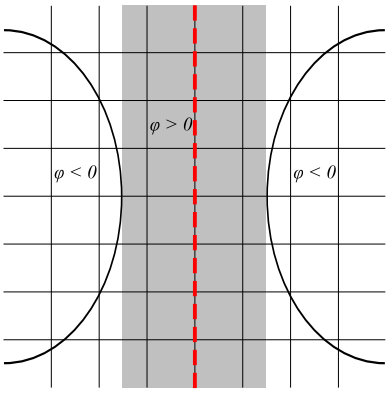

Figure 5.2: Two interfaces in close contact: Points along the central dashed line are equidistant from both interfaces, resulting in discontinuities in the level set derivatives. The level set function φ tends to be an inaccurate approximation of a distance function and irregular in the adjacent gray areas.

interface to a given point $\mathbf{x} = (x, y)$ by

$$\mathbf{x}_\Sigma = \mathbf{x} - \varphi(\mathbf{x})\mathbf{n}(\mathbf{x}). \tag{5.12}$$

These geometric quantities can readily be calculated at computational grid points using standard centered differences. If a geometric quantity (e.g., curvature) is desired at a non-grid point $\mathbf{x}'$, then we calculate the geometric quantity at nearby node points and interpolate to find the desired quantity at $\mathbf{x}'$ (Macklin, 2003; Macklin and Lowengrub, 2005, 2006). In our work, we have generally used bicubic interpolation (or cubic interpolation when $\mathbf{x}'$ lies on a grid edge but not on a computational grid point).

However, as we demonstrated in Macklin (2003) and Macklin and Lowengrub (2005), the level set function can develop discontinuities in its derivatives in regions that are equidistant from multiple portions of the interface. Furthermore, advecting and reinitializing the level set function tends to introduce error into the regions near these irregularities. This can lead to difficulty when computing normal vectors and curvature when two interfaces are in close contact, introducing inaccuracy into the geometric quantities. See Figure 5.2.

In Macklin and Lowengrub (2006), we introduced a new, geometry-aware curvature discretization to automatically detect and accurately deal with this scenario. To calculate the curvature κ at a point $\mathbf{x}_\Sigma = (x_\Sigma, y_\Sigma)$ on the interface, recall that we need to compute and interpolate the curvature $\kappa_{i,j}$ at nearby computational node points. Using the level set

quality function

$$Q(\mathbf{x}) = |1 - |\nabla\varphi(\mathbf{x})|| \tag{5.13}$$

that we first defined in Macklin (2003) and Macklin and Lowengrub (2005), we detected level set irregularity whenever $Q \geq \eta$ for some threshold $\eta > 0$. (In our work, we have generally used $\eta \sim 0.001$.) To calculate the curvature $\kappa_{i,j}$ at a computational node point (x_i, y_j), we evaluated Q at each of the nine grid points in $\{(x_{i+k}, j_{j+\ell}) : -1 \leq k, \ell \leq 1\}$. If $Q < \eta$ at each of these points, then the level set function was deemed sufficiently smooth to calculate the curvature $\kappa_{i,j}$ using the standard 9-point curvature stencil

$$\begin{cases} \varphi_x \approx \frac{\varphi_{i+1,j} - \varphi_{i-1,j}}{2\Delta x} & \varphi_y \approx \frac{\varphi_{i,j+1} - \varphi_{i,j-1}}{2\Delta y} \\ \varphi_{xx} \approx \frac{\varphi_{i-1,j} - 2\varphi_{i,j} + \varphi_{i+1,j}}{\Delta x^2} & \varphi_{yy} \approx \frac{\varphi_{i,j-1} - 2\varphi_{i,j} + \varphi_{i,j+1}}{\Delta y^2} \\ \varphi_{xy} \approx \frac{\varphi_{i+1,j+1} - \varphi_{i-1,j+1} - \varphi_{i+1,j-1} + \varphi_{i-1,j-1}}{4\Delta x \Delta y} & \\ \kappa_{i,j} \approx \frac{\varphi_{xx}\varphi_y^2 - 2\varphi_x\varphi_y\varphi_{xy} + \varphi_{yy}\varphi_x^2}{\left(\varphi_x^2 + \varphi_y^2\right)^{\frac{3}{2}}}, & \end{cases} \tag{5.14}$$

which is second order accurate where the level set function is smooth (Macklin, 2003; Macklin and Lowengrub, 2005). If we could calculate the curvature $\kappa_{i,j}$ at enough nearby points to compute a bicubic or bilinear interpolation at $\mathbf{x}_\Sigma$, then we used that interpolated curvature value.

If $Q > \eta$ at one of the points on the stencil, we constructed a positively-oriented local approximation of the interface $\gamma(s) = (x(s), y(s))$ by finding five points $\{\mathbf{x}_k = (x_k, y_k)\}_{k=-2}^{2}$ with $\mathbf{x}_0 = \mathbf{x}_\Sigma$ on the interface and calculating a quadratic least squares polynomial fit. After adjusting γ to ensure that $\gamma(0) = \mathbf{x}_\Sigma$, we then used γ to construct a local level set function that effectively removed the influence of the nearby irregularity, which we could then discretize using the standard 9-point stencil. In our numerical testing, this geometry-aware, adaptive curvature discretization was second order accurate, even during periods of topological change such as the merger of drops in modified Hele-Shaw flow (Macklin and Lowengrub, 2006). In more recent testing, we have found that so long as γ is a least squares quadratic or cubic polynomial fit and not a direct interpolation of the five points $\mathbf{x}_k$ on the interface, it can be differentiated directly to compute the curvature.

We now extend this technique to calculate normal vectors. Suppose we desire the normal vector at a computational node point (x_i, y_j). If the level set is sufficiently smooth at the four points of $\{(x_{i-1}, y_j), (x_i, y_{j-1}), (x_{i+1}, y_j), (x_i, y_{j+1})\}$ (i.e., $Q < \eta$ at those points),

then we use the standard normal vector discretization

$$\begin{cases} \varphi_x \approx \frac{\varphi_{i+1,j}-\varphi_{i-1,j}}{2\Delta x} \\ \varphi_y \approx \frac{\varphi_{i,j+1}-\varphi_{i,j-1}}{2\Delta y} \\ \mathbf{n} \approx \frac{1}{\sqrt{\varphi_x^2+\varphi_y^2+\epsilon}} \left(\varphi_x, \varphi_y\right), \end{cases} \tag{5.15}$$

where ϵ is a small positive number used to avoid division by zero; we use $\epsilon \sim 10^{-16}$ in our work.

Otherwise, we identify the closest point on the interface $\mathbf{x}_\Sigma$ by (5.12), construct the approximating curve $\gamma(s) = (x(s), y(s))$ through $\mathbf{x}_\Sigma$ as in the adaptive curvature algorithm, and directly differentiate the curve to determine the unit tangent and outward normal vectors:

$$\mathbf{s} = \frac{\gamma'(0)}{||\gamma'(0)||} = \frac{1}{\sqrt{(x'(0))^2 + (y'(0))^2}} \Big(x'(0)\ ,\ y'(0) \Big) \tag{5.16}$$

$$\mathbf{n} = \frac{1}{\sqrt{(x'(0))^2 + (y'(0))^2}} \Big(y'(0)\ ,\ -x'(0) \Big). \tag{5.17}$$

We have found that both quadratic and cubic least squares polynomial fits are sufficiently smooth for this direct differentiation of the normal and tangent vectors.

5.3.3 The Ghost Cell Method

We wish to solve quasi-steady reaction-diffusion problems of the form

$$\begin{cases} 0 = \nabla \cdot (D(\mathbf{x}) \nabla p) + f_R(\mathbf{x}) p + f_S(\mathbf{x}) & \mathbf{x} \in \Omega \cup \Omega^c \\ [p] = g & \mathbf{x} \in \Sigma \\ [D \nabla p \cdot \mathbf{n}] = h & \mathbf{x} \in \Sigma, \end{cases} \tag{5.18}$$

coupled with standard (e.g., Dirichlet, Neumann, or extrapolation) boundary conditions on $\partial\mathcal{D}$.

Standard finite differences cannot be applied across the interface due to the jump boundary conditions across Σ. The ghost cell method was developed to deal with this issue when solving elliptic problems by creating "ghost" computational points and using those ghost points in standard finite difference discretizations (Glimm et al., 1981; Fedkiw et al., 1999; Liu et al., 2000; Gibou et al., 2002, 2003). In Macklin (2003) and Macklin and Lowengrub (2005), we extended the ghost cell method to attain second-order accuracy on interior problems (i.e., p is constant in Ω^c) with boundary conditions that depend upon

the geometry (e.g., curvature) and without a jump condition on the normal derivative. A similar extension to the ghost cell method was presented in Gibou and Fedkiw (2005) to solve Laplace's equation without geometric boundary conditions and yielded fourth-order convergence on fixed domains and third-order convergence on moving boundaries. In Macklin and Lowengrub (2007), we extended our approach to solve systems like (5.18) in the case where $h = 0$ and D was constant in Ω and Ω^c (with different constants). We applied the method to model avascular tumor growth in Macklin and Lowengrub (2007) and verified second-order accuracy for our overall solutions, although our method numerically smeared jumps in the tangential derivative. In the following section, we present our new ghost cell scheme, which includes a new technique for discretizing the normal derivative jump condition without smearing the tangential derivative jump.

Alternative approaches for overcoming the tangential smearing problem include the immersed interface method (IIM) (LeVeque and Li, 1994) and the matched interface boundary (MIB) method (Zhou et al., 2006; Zhou and Wei, 2006; Yu et al., 2007). The IIM requires the use of local coordinates (based on the normal and tangential directions of the interface) to properly discretize the normal derivative jump. The MIB method is a high-order generalization of the IIM and the ghost cell method that constructs elaborate extensions of the solution to several ficticious points on both sides of the interface; the extensions are designed to explicitly satisfy $[p]$, $[\partial p/\partial \mathbf{s}]$, and $[D\partial p/\partial \mathbf{n}]$ simultaneously. The ghost cell method has several advantages over these alternatives. Because the method is applied in a dimension-by-dimension manner, it is simple to implement and can be trivially extended to higher dimensions. Its accuracy can easily be improved by using higher-order extrapolations on each side of the interface. Like the MIB method, our new ghost cell method satisfies the normal derivative jump boundary condition without smearing the tangential derivative jump, but it retains the dimension-by-dimension aspect of the ghost cell method and does not require the explicit treatment of the tangential derivative jump. It is also much simpler to implement and can be incorporated into existing ghost cell frameworks.

Ghost Cell Extrapolations for the Diffusional Term

Suppose we wish to discretize the x-derivative of $\nabla \cdot (D(\mathbf{x})\nabla p)$ at a computational node point $\mathbf{x} = (x_i, y_j)$, and assume that D is C^1 with respect to $\mathbf{x}$ throughout Ω and Ω^c. (The diffusion constant may be discontinuous across the interface Σ; this case is treated below.)

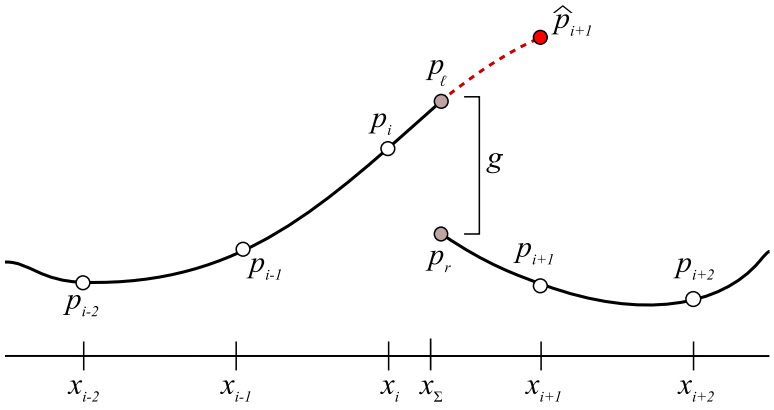

Figure 5.3: A typical ghost cell extrapolation $\widehat{p}_{i+1}$. Particular care must be taken to satisfy $[p] = g$ and $[D\nabla p \cdot \mathbf{n}] = h$ without numerically smearing any tangential derivative jump $[\nabla p \cdot \mathbf{s}]$.

If (x_{i-1}, y_j), (x_i, y_j), and (x_{i+1}, y_j) are all in the same region, i.e.,

$$\varphi_{i-1,j} \le 0, \qquad \varphi_{i,j} \le 0, \text{ and} \qquad \varphi_{i+1,j} \le 0, \tag{5.19}$$

or

$$\varphi_{i-1,j} > 0, \qquad \varphi_{i,j} > 0, \text{ and} \qquad \varphi_{i+1,j} > 0, \tag{5.20}$$

then we can use the standard second-order discretization

$$\begin{aligned} \partial_x \left(D(x) p_x \right) &\approx \frac{1}{\Delta x^2} \left(D_x^- p_{i-1,j} - \left(D_x^- + D_x^+ \right) p_{i,j} + D_x^+ p_{i+1,j} \right) \\ D_x^- &= D\left(x_i - \frac{1}{2}\Delta x, y_j \right) \\ D_x^+ &= D\left(x_i + \frac{1}{2}\Delta x, y_j \right). \end{aligned} \tag{5.21}$$

Suppose, however, that (x_i, y_j) and (x_{i+1}, y_j) are not in the same region. Assume without loss of generality that $(x_i, y_j) \in \Omega$ and $(x_{i+1}, y_j) \in \Omega^c$; the case where $(x_i, y_j) \in \Omega^c$ and $(x_{i+1}, y_j) \in \Omega$ is treated similarly. Then the interface Σ must separate (x_i, y_j) and (x_{i+1}, y_j) at some point

$$\mathbf{x}_\Sigma = (x_\Sigma, y_j) = (x_i + \theta \Delta x, y_j), \tag{5.22}$$

where $0 < \theta \le 1$. In this scenario, we must modify our computational stencil by extending the solution in Ω to a "ghost cell point" $\widehat{p}_{i+1,j}$ in the other region; we replace $p_{i+1,j}$ in (5.21) with the extrapolation $\widehat{p}_{i+1,j}$. See Figure 5.3. If (x_{i-2}, y_j) and (x_{i-1}, y_j) are both in Ω, then

we obtain $\widehat{p}_{i+1,j}$ as a quadratic extrapolation of p from $p_{i-2,j}$, $p_{i-1,j}$, and u_ℓ:

$$\widehat{p}_{i+1,j} = \frac{2(1-\theta)}{2+\theta} p_{i-2} - \frac{3(1-\theta)}{1+\theta} p_{i-1} + \frac{6}{(1+\theta)(2+\theta)} p_\ell. \tag{5.23}$$

If $(x_{i-1}, y_j) \in \Omega$ but $(x_{i-2}, y_j) \notin \Omega$, then we obtain $\widehat{p}_{i+1,j}$ by linear extrapolation from $p_{i-1,j}$ and p_ℓ:

$$\widehat{p}_{i+1,j} = \frac{-(1-\theta)}{1+\theta} p_{i-1,j} + \frac{2}{1+\theta} p_\ell. \tag{5.24}$$

If $(x_{i-1}, y_j) \notin \Omega$, then we use the constant extrapolation $\widehat{p}_{i+1,j} = p_\ell$. Note that in all cases, we require p_ℓ. In the ghost cell approach, p_ℓ is determined by the jump boundary conditions. We shall return to this point in the next section.

If D is continuous across the interface Σ, then D_x^+ may be used in the ghost cell approximation without modification. If D is discontinuous across Σ, then we replace it with an extension $\widehat{D}_x^+$ in a manner analogous to $\widehat{p}_{i+1,j}$. Suppose that D is defined at computational node points. If (x_{i-2}, y_j) and (x_{i-1}, y_j) are both in Ω, then we use quadratic extrapolation:

$$\widehat{D}_x^+ = \frac{3}{8} D_{i-2,j} - \frac{5}{4} D_{i-1,j} + \frac{15}{8} D_{i,j}. \tag{5.25}$$

If $(x_{i-1}, y_j) \in \Omega$ but $(x_{i-2}, y_j) \notin \Omega$, then we use linear extrapolation from $D_{i-1,j}$ and $D_{i,j}$:

$$\widehat{D}_x^+ = -\frac{1}{2} D_{i-1,j} + \frac{3}{2} D_{i,j}. \tag{5.26}$$

If $(x_{i-1}, y_j) \notin \Omega$, then we use constant extrapolation $\widehat{D}_x^+ = D_{i,j}$.

The case where we require a ghost cell extrapolation $\widehat{p}_{i-1,j}$ is completely analogous, and the y-derivative is discretized in exactly the same manner. To apply the method to a 3-D problem, we need only repeat the process separately for the z-derivative term $\partial_z \left(D(\mathbf{x}) p_z \right)$.

Determining p_ℓ from the Jump Boundary Conditions

As we have seen, the ghost cell extrapolations require p_ℓ. At the same time, the jump boundary conditions have not yet been applied to the scheme. By introducing the jump boundary conditions into the ghost cell extrapolation, we can simultaneously satisfy the jump conditions while eliminating p_ℓ from the extrapolation, instead expressing the discretization solely in terms of computational node points.

First, we discretize the jump boundary condition by

$$p_\ell - p_r = -\text{sign}(\varphi_{i,j}) g(\mathbf{x}_\Sigma). \tag{5.27}$$

The $-\text{sign}(\varphi_{i,j})$ term ensures that the jump condition has been applied in the proper direction from region Ω to region Ω^c.

This introduces an additional, non-grid point p_r into our calculation. However, by considering the normal derivative jump condition, we shall have two equations for p_ℓ and p_r, allowing us to completely eliminate them from the extrapolation. The proper discretization of the normal derivative jump $[D\nabla p \cdot \mathbf{n}]$ across the interface has been an open problem since the introduction of the ghost cell method for the Poisson problem (Fedkiw et al., 1999; Liu et al., 2000; Gibou et al., 2002). Suppose that we wish to discretize $[D\nabla p \cdot \mathbf{n}]$ at the point $\mathbf{x}_\Sigma = (x_\Sigma, y_j) = (x_i + \theta\Delta x, y_j)$ from the preceding discussion. In Liu et al. (2000), the normal derivative jump was discretized as

$$\begin{aligned}[D\nabla p \cdot \mathbf{n}] &= \left(D\frac{\partial p}{\partial \mathbf{n}}\right)_\ell - \left(D\frac{\partial p}{\partial \mathbf{n}}\right)_r \\ &\approx D_\ell \frac{p_\ell - p_{i,j}}{\theta\Delta x} - D_r \frac{p_{i+1,j} - p_r}{(1-\theta)\Delta x},\end{aligned} \tag{5.28}$$

where

$$\begin{aligned} D_r = \lim_{\zeta \downarrow x+\theta\Delta x} D(\zeta, y_j), \qquad D_\ell = \lim_{\zeta \uparrow x+\theta\Delta x} D(\zeta, y_j), \\ p_r = \lim_{\zeta \downarrow x+\theta\Delta x} p(\zeta, y_j), \qquad \text{and} \qquad p_\ell = \lim_{\zeta \uparrow x+\theta\Delta x} p(\zeta, y_j). \end{aligned} \tag{5.29}$$

Notice that this is equivalent to assuming that the normal vector cuts the computational mesh at a right angle (i.e., $\mathbf{n} = (1, 0)$), potentially leading to numerical smearing of any jump in the tangential derivative. Furthermore, if $\theta \sim 0$ or $\theta \sim 1$, then the discretization can be unstable due to the uneven spacing of the stencil points. See the left frame in Figure 5.4. In numerical testing in Liu et al. (2000), this stencil was less than first-order accurate due to the low order of the discretization (first-order left and right differences of the derivative), coupled with the numerical smearing of the tangential derivatives.

In Macklin and Lowengrub (2007), we introduced a new discretization for the normal derivative jump in the case where $[D\nabla p \cdot \mathbf{n}] = 0$:

$$[D\nabla p \cdot \mathbf{n}] \approx D_\ell \frac{p_\ell - p_{i-1,j}}{(1+\theta)\Delta x} - D_r \frac{p_{i+2,j} - p_r}{(2-\theta)\Delta x}. \tag{5.30}$$

This discretization guarantees that all three stencil points (x_{i-1}, y_j), (x_Σ, y_j), and (x_{i+1}, y_j) are at least Δx apart and consequently solves the stability problem. However, the discretization still numerically smears any jump in the tangential derivative because it approximates the normal vector as $\mathbf{n} = (1, 0)$. See the right frame in Figure 5.4.

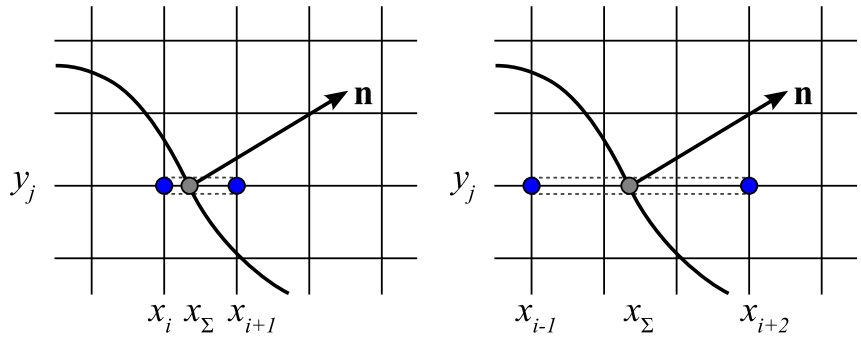

Figure 5.4: **Left:** The traditional, unstable stencil for $[D\nabla p \cdot \mathbf{n}]$ from Liu et al. (2000). **Right:** Our stablized extension of this stencil from Macklin and Lowengrub (2007).

We now introduce a new normal derivative jump discretization that eliminates the numerical smearing of the jump in the tangential derivative. Let $\mathbf{n} = (n_x, n_y)$, and suppose that $n_x \cdot n_y \geq 0$, i.e., the normal vector faces up and right or down and left. Assuming no additional nearby interfaces (so that all right and left points are contained within the same regions), we begin by defining

$$\begin{aligned} \mathbf{u}_r &= (x_{i+2} - x_\Sigma, 0) && = ((2-\theta)\Delta x, 0)\,, \\ \mathbf{v}_r &= (x_{i+1} - x_\Sigma, y_{j+1} - y_j) && = ((1-\theta)\Delta x, \Delta y)\,, \\ \mathbf{u}_\ell &= (x_{i-1} - x_\Sigma, 0) && = (-(1+\theta)\Delta x, 0)\,, \text{ and} \\ \mathbf{v}_\ell &= (x_i - x_\Sigma, y_{j-1} - y_j) && = (-\theta\Delta x, -\Delta y)\,. \end{aligned} \tag{5.31}$$

See the left frame in Figure 5.5.

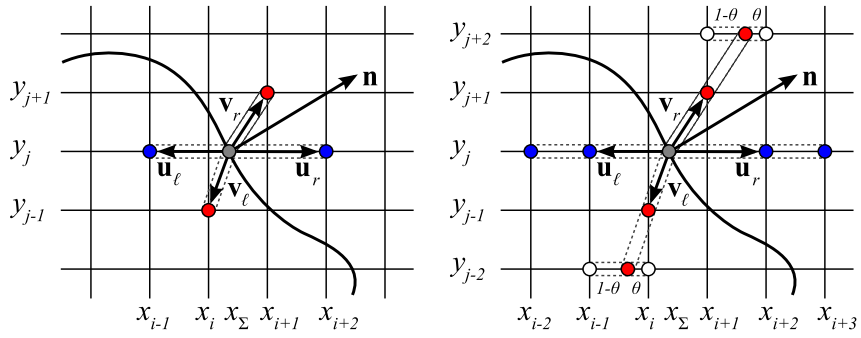

Figure 5.5: Our new first-order (**left**) and higher-order (**right**) computational stencils for the normal derivative jump $[D\nabla p \cdot \mathbf{n}]$.

Because $\mathbf{u}_r$ and $\mathbf{v}_r$ are linearly independent, they form a basis for $\mathbb{R}^2$, and we can write

$$\mathbf{n} = a_r \mathbf{u}_r + b_r \mathbf{v}_r, \tag{5.32}$$

where a_r and b_r are obtained by solving the linear system

$$\begin{aligned} (\mathbf{u}_r \cdot \mathbf{u}_r)\, a_r + (\mathbf{v}_r \cdot \mathbf{u}_r)\, b_r &= (\mathbf{n} \cdot \mathbf{u}_r) \\ (\mathbf{u}_r \cdot \mathbf{v}_r)\, a_r + (\mathbf{v}_r \cdot \mathbf{v}_r)\, b_r &= (\mathbf{n} \cdot \mathbf{v}_r)\,. \end{aligned} \tag{5.33}$$

Using this, we can express $(\partial p/\partial \mathbf{n})_r$ as a combination of grid ($\mathbf{u}_r$) and off-grid ($\mathbf{v}_r$) directional derivatives:

$$\begin{aligned} \left(\frac{\partial p}{\partial \mathbf{n}}\right)_r &= (\nabla p)_r \cdot \mathbf{n} \\ &= a_r \,(\nabla p)_r \cdot \mathbf{u}_r + b_r \,(\nabla p)_r \cdot \mathbf{v}_r \\ &= a_r \,||\mathbf{u}_r||\,(\nabla p)_r \cdot \frac{\mathbf{u}_r}{||\mathbf{u}_r||} + b_r \,||\mathbf{v}_r||\,(\nabla p)_r \cdot \frac{\mathbf{v}_r}{||\mathbf{v}_r||} \\ &= a_r \,||\mathbf{u}_r|| \left(\frac{\partial p}{\partial \left(\mathbf{u}_r/\,||\mathbf{u}_r||\right)}\right)_r + b_r \,||\mathbf{v}_r|| \left(\frac{\partial p}{\partial \left(\mathbf{v}_r/\,||\mathbf{v}_r||\right)}\right)_r, \end{aligned} \tag{5.34}$$

where

$$||\mathbf{u}_r|| = (2-\theta)\Delta x, \qquad ||\mathbf{v}_r|| = \sqrt{(1-\theta)^2 \Delta x^2 + \Delta y^2}. \tag{5.35}$$

Using one-sided, first-order differences, we obtain the approximation

$$\begin{aligned} \left(\frac{\partial p}{\partial \mathbf{n}}\right)_r &\approx a_r \,||\mathbf{u}_r||\, \frac{(p_{i+2,j} - p_r)}{||\mathbf{u}_r||} + b_r \,||\mathbf{v}_r||\, \frac{(p_{i+1,j+1} - p_r)}{||\mathbf{v}_r||} \\ &= a_r \,(p_{i+2,j} - p_r) + b_r \,(p_{i+1,j+1} - p_r)\,. \end{aligned} \tag{5.36}$$

Similarly, $\mathbf{u}_\ell$ and $\mathbf{v}_\ell$ form a basis for $\mathbb{R}^2$, and we can express

$$\mathbf{n} = a_\ell \mathbf{u}_\ell + b_\ell \mathbf{v}_\ell, \tag{5.37}$$

rewrite the normal derivative as

$$\left(\frac{\partial p}{\partial \mathbf{n}}\right)_\ell = a_\ell \,||\mathbf{u}_\ell|| \left(\frac{\partial p}{\partial \left(\mathbf{u}_\ell/\,||\mathbf{u}_\ell||\right)}\right)_\ell + b_\ell \,||\mathbf{u}_\ell|| \left(\frac{\partial p}{\partial \left(\mathbf{v}_\ell/\,||\mathbf{v}_\ell||\right)}\right)_\ell, \tag{5.38}$$

and approximate it (to first-order) as

$$\left(\frac{\partial p}{\partial \mathbf{n}}\right)_\ell \approx a_\ell \,(p_{i-1,j} - p_\ell) + b_\ell \,(p_{i,j-1} - p_\ell)\,. \tag{5.39}$$

By combining (5.36) and (5.39), we obtain a new discretization of $[D\nabla p \cdot \mathbf{n}] = h$:

$$\begin{aligned}[D\nabla p \cdot \mathbf{n}] &\approx D_\ell\Big(a_\ell\,(p_{i-1,j} - p_\ell) + b_\ell\,(p_{i,j-1} - p_\ell)\Big) \\ &\quad -D_r\Big(a_r\,(p_{i+2,j} - p_r) + b_r\,(p_{i+1,j+1} - p_r)\Big) \\ &= -\text{sign}(\varphi_{i,j})h(\mathbf{x}_\Sigma). \end{aligned} \tag{5.40}$$

When we combine this with the jump condition in (5.27), p_ℓ and p_r are completely determined. In practice, we implement this new discretization in the following way:

1. We construct 2×2 linear systems for a_r and b_r and and a_ℓ and b_ℓ and solve them exactly using the standard inversion for 2×2 systems.

2. We construct a 2×2 linear system for p_r and p_ℓ using the jump condition for $p_\ell - p_r$ and the normal derivative jump discretization in (5.40). We solve this linear system for p_ℓ and p_r using the standard 2×2 inversion and use p_ℓ in the ghost cell discretization.

The case where $n_x \cdot n_y < 0$ is similar: we replace $p_{i+1,j+1}$ by $p_{i+1,j-1}$ in $\mathbf{v}_r$, and we replace $p_{i,j-1}$ by $p_{i,j+1}$ in $\mathbf{v}_r$. All other calculations are identical. The case of discretizing $[D\nabla p \cdot \mathbf{n}]$ at a point $(x_i - \theta\Delta x, y_j)$ is completely analogous, and the discretization in the y-direction is identical. In the 3-D case, we would proceed similarly by defining third basis vectors such as

$$\begin{aligned}\mathbf{w}_r = (x_{i+1} - x_\Sigma, 0, z_{k+1} - z_k) &= \Big((1-\theta)\Delta x, 0, \Delta z\Big), \\ \mathbf{w}_\ell = (x_i - x_\Sigma, 0, z_{k-1} - z_k) &= \Big(-\theta\Delta x, 0, -\Delta z\Big). \end{aligned} \tag{5.41}$$

This method has several advantages. In the spirit of the ghost cell method, the new stencil can be expressed entirely in terms of computational grid points and the jump interface location. Furthermore, the discretization can be applied in a dimension-by-dimension manner, just as in existing ghost cell methods. The implementation is simple and can be readily substituted into existing code in place of previous normal discretizations. Because the stencil discretizes $D\partial p/\partial \mathbf{n}$ in the true direction of the normal vector, it should result in more accurate numerical solutions with less numerical smearing of the tangential derivative jump. (Indeed, we shall verify that our method is first-order accurate, even in situations where the discretization by Liu et al. (2000) fails to converge; the discretization we present in the next section attains above-1.5-order accuracy.) Lastly, we note that if $\mathbf{n} = (1, 0)$ or $\mathbf{n} = (-1, 0)$, then the normal derivative jump discretization in (5.40) simplifies to (5.30). This further illustrates the point that earlier discretizations of the normal derivative jump were equivalent to assuming that the interface cuts the computational grid at a right angle.

Higher-Order Approximations of $[D\nabla p \cdot \mathbf{n}]$

By using additional stencil points (with the same definitions of $\mathbf{u}_\ell$, $\mathbf{u}_r$, $\mathbf{v}_\ell$, and $\mathbf{v}_r$), we can improve the accuracy of the normal derivative jump discretization. If (x_{i+1}, y_j), (x_{i+2}, y_j), and (x_{i+3}, y_j) are all in the same region, we can replace the grid-aligned partial derivative in (5.34) with the second-order approximation

$$\begin{aligned}\left(\frac{\partial p}{\partial\left(\mathbf{u}_r/\left|\left|\mathbf{u}_r\right|\right|\right)}\right)_r \approx\ & \frac{-(5+2\theta)}{(2-\theta)(3-\theta)\Delta x}p_r + \frac{(3-\theta)}{(2-\theta)\Delta x}p_{i+2,j} \\ & -\frac{(2-\theta)}{(3-\theta)\Delta x}p_{i+3,j}. \end{aligned} \tag{5.42}$$

See the right frame of Figure 5.5.

Similarly, if (x_i, y_j), (x_{i-1}, y_j), and (x_{i-2}, y_j) are all in the same region, then we can replace the grid-aligned partial derivative in (5.38) with the second-order approximation

$$\begin{aligned}\left(\frac{\partial p}{\partial\left(\mathbf{u}_\ell/\left|\left|\mathbf{u}_\ell\right|\right|\right)}\right)_\ell \approx\ & -\frac{(1+\theta)}{(2+\theta)\Delta x}p_{i-2,j} + \frac{(2+\theta)}{(1+\theta)\Delta x}p_{i-1,j} \\ & -\frac{(3+2\theta)}{(1+\theta)(2+\theta)\Delta x}p_\ell. \end{aligned} \tag{5.43}$$

Because $\mathbf{v}_\ell$ and $\mathbf{v}_r$ generally do not intersect the computational mesh at grid points, interpolation of nearby grid points is required to improve the accuracy of the off-grid directional derivatives in (5.34) and (5.38).

If (x_{i+1}, y_j), (x_{i+1}, y_{j+1}), (x_{i+1}, y_{j+2}), and (x_{i+2}, y_{j+2}) are all in the same region, then we can replace the off-grid directional derivative in (5.34) by the higher-order approximation

$$\begin{aligned}\left(\frac{\partial p}{\partial\left(\mathbf{v}_r/\left|\left|\mathbf{v}_r\right|\right|\right)}\right)_r \approx\ & -\frac{3}{2\left|\left|\mathbf{v}_r\right|\right|}p_r + \frac{2}{\left|\left|\mathbf{v}_r\right|\right|}p_{i+1,j+1} \\ & -\frac{1}{2\left|\left|\mathbf{v}_r\right|\right|}[\theta p_{i+1,j+2} + (1-\theta)p_{i+2,j+2}], \end{aligned} \tag{5.44}$$

where the bracketed term is a linear interpolation to obtain a point along the path of $\mathbf{v}_r$. See the right frame of Figure 5.5.

Similarly, if (x_i, y_j), (x_i, y_{j-1}), (x_i, y_{j-2}), and (x_{i-1}, y_{j-2}) are all in the same region, then we can improve our approximation of the off-grid derivative in (5.38) with

$$\begin{aligned}\left(\frac{\partial p}{\partial\left(\mathbf{v}_\ell/\left|\left|\mathbf{v}_\ell\right|\right|\right)}\right)_\ell \approx\ & -\frac{3}{2\left|\left|\mathbf{v}_\ell\right|\right|}p_\ell + \frac{2}{\left|\left|\mathbf{v}_\ell\right|\right|}p_{i,j-1} \\ & -\frac{1}{2\left|\left|\mathbf{v}_\ell\right|\right|}[(1-\theta)p_{i,j-2} + \theta p_{i-1,j-2}]. \end{aligned} \tag{5.45}$$

Putting all this together, the higher-order discretization of $[D\nabla p \cdot \mathbf{n}] = h$ is given by

$$\begin{aligned}
[D\nabla p \cdot \mathbf{n}] \;\approx\;& D_\ell a_\ell\Big(-\frac{(1+\theta)^2}{(2+\theta)}p_{i-2,j} + (2+\theta)p_{i-1,j} - \frac{(3+2\theta)}{(2+\theta)}p_\ell\Big) \\
&+D_\ell b_\ell\Big(-\frac{3}{2}p_\ell + 2p_{i,j-1} - \frac{1}{2}\Big[(1-\theta)p_{i,j-2} + \theta p_{i-1,j-2}\Big]\Big) \\
&-D_r a_r\Big(\frac{-(5+2\theta)}{(3-\theta)}p_r + (3-\theta)p_{i+2,j} - \frac{(2-\theta)^2}{(3-\theta)}p_{i+3,j}\Big) \\
&-D_r b_r\Big(-\frac{3}{2}p_r + 2p_{i+1,j+1} - \frac{1}{2}\Big[\theta p_{i+,j+2} + (1-\theta)p_{i+2,j+2}\Big]\Big) \\
=\;& -\mathrm{sign}(\varphi_{i,j})h\left(\mathbf{x}_\Sigma\right). \qquad (5.46)
\end{aligned}$$

In principle, all these partial differences can be made more accurate still by using additional node points. In particular, one could use quadratic or cubic interpolations in the off-grid directional derivative differences.

5.3.4 NAGSI: a Nonlinear Adaptive Gauss-Seidel type Iterative method for solving Nonlinear Quasi-Steady Reaction-Diffusion Equations

We now develop a fully-nonlinear, adaptive method to solve the nonlinear reaction-diffusion equation

$$0 = \nabla \cdot \left(D\left(\mathbf{x}, p\right)\nabla p\right) + f_R\left(\mathbf{x}, p\right)p + f_S\left(\mathbf{x}, p\right), \qquad \mathbf{x} \in \mathcal{D}, \qquad (5.47)$$

where $\mathcal{D}$ is a rectangular domain in $\mathbb{R}^n$ and standard boundary conditions (e.g., Neumann, Dirichlet, or extrapolation) have been assigned. Here, f_R and f_S are the reaction and source terms, respectively. Without loss of generality, we assume that $f_R \leq 0$; if this condition is not satisfied, then the positive part of $f_R\, p$ can be rewritten as part of the source term f_S. The diffusivity D is assumed to be smooth and strictly positive. For simplicity, we shall consider the 2-D case where $\mathcal{D} = [a, b] \times [c, d]$; the n-D case is completely analogous.

To solve (5.47), we solve the related equation

$$\frac{\partial p}{\partial \tau} = \nabla \cdot \left(D\left(\mathbf{x}, p\right)\nabla p\right) + f_R\left(\mathbf{x}, p\right)p + f_S\left(\mathbf{x}, p\right) \qquad (5.48)$$

to steady state, where τ is pseudo-time. For numerical stability, we begin by implicitly discretizing pseudo-time with a backwards Euler difference, lagging the dependence of D, f_R, and f_S on p, and applying the standard second-order centered difference to the diffusional term:

$$\frac{p_{i,j}^{n+1} - p_{i,j}^{n}}{\Delta\tau} \;=\; \frac{1}{\Delta x^2}\Big(D_x^- p_{i-1,j}^{n+1} - \left(D_x^- + D_x^+\right)p_{i,j}^{n+1} + D_x^+ p_{i+1,j}^{n+1}\Big)$$

$$
\begin{aligned}
&+\frac{1}{\Delta y^2}\left(D_y^- p_{i,j-1}^{n+1} - \left(D_y^- + D_y^+\right) p_{i,j}^{n+1} + D_y^+ p_{i,j+1}^{n+1}\right) \\
&+f_R\left(x_i, p_i^n\right) p_i^{n+1} + f_S\left(x_i, p_i^n\right) + \mathcal{O}\left(\Delta\tau + \Delta x^2 + \Delta y^2\right), \\
D_x^- &= D\left(x_i - \frac{1}{2}\Delta x, y_j, \frac{1}{2}\left(p_{i-1,j}^n + p_{i,j}^n\right)\right), \\
D_x^+ &= D\left(x_i + \frac{1}{2}\Delta x, y_j \frac{1}{2}\left(p_{i,j}^n + p_{i+1,j}^n\right)\right), \\
D_y^- &= D\left(x_i, y_j - \frac{1}{2}\Delta y, \frac{1}{2}\left(p_{i,j-1}^n + p_{i,j}^n\right)\right), \\
D_y^+ &= D\left(x_i, y_j + \frac{1}{2}\Delta y, \frac{1}{2}\left(p_{i,j}^n + p_{i,j+1}^n\right)\right).
\end{aligned} \tag{5.49}
$$

Here, $p_{i,j}^n = p\left(x_i, y_j, \tau_n\right)$, $x_i = a + i\Delta x$, $y_j = c + j\Delta y$, $\tau_n = n\Delta\tau$, and Δx, Δy and $\Delta\tau$ are spatial and pseudo-temporal discretization step sizes, respectively.

This system has the form

$$
A\left(\mathbf{x}, \mathbf{p}^n\right)\mathbf{p}^{n+1} = \mathbf{b}\left(\mathbf{x}, \mathbf{p}^n\right) \tag{5.50}
$$

which can be solved to steady state by constructing the operator $A\left(\mathbf{x}, \mathbf{p}^n\right)$ and right-hand side $\mathbf{b}\left(\mathbf{x}, \mathbf{p}^n\right)$ and solving the linear system in (5.50) with an iterative method (e.g., BiCG-Stab(ℓ) from Sleijpen et al. (1994)) at every pseudo-time step until the system reaches steady state. However, constructing these operators may be computationally expensive, making the method disadvantageous. Furthermore, after some initial large change throughout the computational domain, the solution may only be rapidly changing on a small subset of the domain. In such a case, the majority of the computational cost of constructing and solving a new linear system at every pseudo-timestep will be unnecessary.

By changing the points used in the discretization of $\nabla\cdot(D\nabla p)$, we can make the scheme semi-implicit. Assuming that we sweep through grid points with increasing i and j:

$$
\begin{aligned}
\frac{p_{i,j}^{n+1} - p_{i,j}^n}{\Delta\tau} &= \frac{1}{\Delta x^2}\left(D_x^- p_{i-1,j}^{n+1} - \left(D_x^- + D_x^+\right) p_{i,j}^{n+1} + D_x^+ p_{i+1,j}^n\right) \\
&+\frac{1}{\Delta y^2}\left(D_y^- p_{i,j-1}^{n+1} - \left(D_y^- + D_y^+\right) p_{i,j}^{n+1} + D_y^+ p_{i,j+1}^n\right) \\
&+f_R\left(x_i, p_i^n\right) p_i^{n+1} + f_S\left(x_i, p_i^n\right) + \mathcal{O}\left(\Delta\tau + \Delta x^2 + \Delta y^2\right), \\
D_x^- &= D\left(x_i - \frac{1}{2}\Delta x, y_j, \frac{1}{2}\left(p_{i-1,j}^{n+1} + p_{i,j}^n\right)\right), \\
D_x^+ &= D\left(x_i + \frac{1}{2}\Delta x, y_j \frac{1}{2}\left(p_{i,j}^n + p_{i+1,j}^n\right)\right), \\
D_y^- &= D\left(x_i, y_j - \frac{1}{2}\Delta y, \frac{1}{2}\left(p_{i,j-1}^{n+1} + p_{i,j}^n\right)\right),
\end{aligned}
$$

$$D_y^+ = D\left(x_i, y_j + \frac{1}{2}\Delta y, \frac{1}{2}\left(p_{i,j}^n + p_{i,j+1}^n\right)\right), \tag{5.51}$$

which we can solve algebraically for $p_{i,j}^{n+1}$ based upon known quantities:

$$p_{i,j}^{n+1} = \frac{\frac{p_{i,j}^n}{\Delta\tau} + \frac{D_x^+ p_{i+1,j}^n + D_x^- p_{i-1,j}^{n+1}}{\Delta x^2} + \frac{D_y^+ p_{i,j+1}^n + D_y^- p_{i,j-1}^{n+1}}{\Delta y^2} + f_S\left(x_i, y_j, p_{i,j}^n\right)}{\frac{1}{\Delta\tau} + \frac{D_x^- + D_x^+}{\Delta x^2} + \frac{D_y^- + D_y^+}{\Delta y^2} - f_R\left(x_i, y_j, p_{i,j}^n\right)}. \tag{5.52}$$

Using this, we now introduce a 2-D scheme:

Step 1: Discretize the domain $[a, b] \times [c, d]$ by

$$a = x_0, \cdots, x_i = a + i\Delta x, \cdots, x_m = a + m\Delta x = b \tag{5.53}$$

$$c = y_0, \cdots, y_j = c + j\Delta y, \cdots, y_n = c + n\Delta y = d. \tag{5.54}$$

Step 2: Store an initial guess in the 2-D array $\mathbf{p} = \{p_{i,j}\}$.

Step 3: Update the boundary points $\{p_{0,j}, p_{m,j}\}_{j=0}^n$ and $\{p_{i,0}, p_{i,n}\}_{i=0}^m$ according to the boundary conditions.

Step 4: Choose a tolerance ϵ, and set $r > \epsilon$.

Step 5: While $r > \epsilon$:

Part a: For $1 \leq i < m$ and $1 \leq j < n$:

i: Set $r = 0$.

ii: Calculate $p_{i,j}^{n+1}$ based upon Equation 5.52.

iii: If $r_{i,j} = \left|p_{i,j}^{n+1} - p_{i,j}^n\right| > r$, set $r = r_{i,j}$.

iv: Overwrite $p_{i,j}$ with the newly calculated $p_{i,j}^{n+1}$.

The resulting scheme, which overwrites previous values $p_{i,j}^n$ with updated values $p_{i,j}^{n+1}$ while sweeping through the domain, is a nonlinear Gauss-Seidel-like iterative (GSI) method. To prevent biases (e.g., asymmetry) from the update order, we alternate sweeping directions: up and right (increasing i and j), then up and left (decreasing i, increasing j), then down and left (decreasing i and j), and then down and right (increasing i and decreasing j). By overwriting the current values in the $\{p_{i,j}\}$ data structure with newly-calculated values, the proper indexing of the pseudo-time index in the discretization of $\nabla \cdot (D\nabla p)$ is automatic.

There are numerous advantages to this technique. First and foremost, there is no need to invert a large linear system at every iteration. Second, because the scheme makes use of updated information while sweeping through the domain (unlike Jacobi-like iterations), the effects of lagging D, f_R, and f_S (with respect to pseudo-time) are reduced. Because (5.52) updates the solution based upon *local* operations (i.e., it only requires information on nearby computational nodes), it is parallelizable and simple to implement, particularly on shared-memory architectures. Lastly, we note that this technique is fully compatible with the ghost cell method of enforcing jump boundary conditions on irregular domains by replacing the appropriate point in the stencil with a ghost cell extrapolation. (e.g., replace $p^n_{i+1,j}$ with $\widehat{p}^n_{i+1.j}$.)

We note that Gauss-Seidel-like iterative methods have been used to solve nonlinear problems in the past, generally in the context of nonlinear optimization. (e.g., see Hallett et al. (1996) and Chatterjee and Chong (1997).) The idea of adapting linear iterative methods to solving nonlinear problems is not new. (e.g., see Vrahatis et al. (2003).) However, most of those techniques use complicated, block structures, which in themselves require iterative solutions and are not as well-suited to adaptivity.

Adaptivity

The local nature of our GSI technique allows for a new approach to adaptivity using a regular Cartesian mesh. On any sweep through the solution domain, as the solution converges, the numerical solution tends to change most on a small fraction of the computational nodes. Therefore, we can select computational nodes where the numerical solution is changing most rapidly and use (5.52) to update only those nodes. The modified, nonlinear adaptive GSI technique (NAGSI) is as follows:

Step 1: Discretize the domain $[a, b] \times [c, d]$ by

$$a = x_0, \cdots, x_i = a + i\Delta x, \cdots, x_m = a + m\Delta x = b \tag{5.55}$$

$$c = y_0, \cdots, y_j = c + j\Delta y, \cdots, y_n = c + n\Delta y = d. \tag{5.56}$$

Step 2: Store an initial guess in the 2-D array $\mathbf{p} = \{p_{i,j}\}$.

Step 3: Update the boundary points $\{p_{0,j}, p_{m,j}\}_{j=0}^{n}$ and $\{p_{i,0}, p_{i,n}\}_{i=0}^{m}$ according to the boundary conditions.

Step 4: Choose a tolerance ϵ, and set $r > \epsilon$.

Step 5: While $r > \epsilon$:

Part a: For $1 \leq i < m$ and $1 \leq j < n$:

i: Set $r = 0$.

ii: Calculate $p_{i,j}^{n+1}$ based upon (5.52).

iii: If $r_{i,j} = \left| p_{i,j}^{n+1} - p_{i,j}^{n} \right| > r$, set $r = r_{i,j}$.

iv: Overwrite $p_{i,j}$ with the newly calculated $p_{i,j}^{n+1}$.

Part b: Set a threshold $\eta < r$. In our work, we have used $\eta = \frac{1}{4}r$.

Part c: Sweep through the domain again (with a different sweep direction), this time creating a list $\mathcal{L} = \{(i_k, j_k)\}_{k=1}^{N}$ of nodes where $r_{i,j} > \eta$.

Part d: Repeat M times:

i: For $1 \leq k \leq N$, update p_{i_k,j_k} according to Equation 5.52.

The scheme is illustrated schematically in Figure 5.6.

In our work, we use $M = 2$; in testing, we have found that additional iterations through the selected nodes $\mathcal{L}$ resulted in little change in the approximate solution. This is because $\mathcal{L}$ behaves as a small, irregular subdomain of $\mathcal{D}$ with fixed boundary conditions (i.e., the remaining computational nodes), and so an elliptic equation can approach a steady state on the subdomain quickly. However, the optimal choice of M may depend upon the problem under study and could potentially be dynamically chosen; we are currently investigating these approaches.

While the method does need to sweep through the entire computational domain for some of the iterations, its adaptivity is based upon the same philosophy of traditional adaptive mesh techniques of focusing computational effort adaptively where it is most needed, leading to accelerated convergence when compared to non-adaptive, fixed grid methods. In testing on level set problems with large solution gradients, we have found that the adaptivity decreases the computational time of NAGSI by 10% to 50% (results not shown). Furthermore, the strategy for choosing the list $\mathcal{L}$ of flagged points can be tailored to the computational problem. (e.g., in level set methods, one might choose $\mathcal{L}$ to include a narrow band about the zero level set.) Because the method requires little extra effort to implement, it can conceivably be used to improve performance in existing computational frameworks

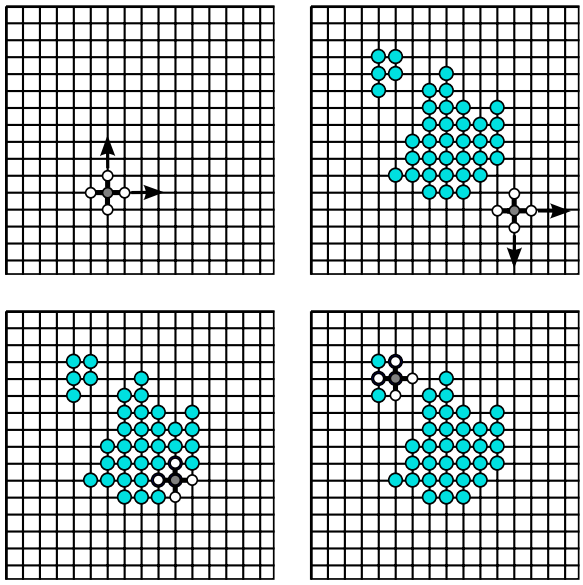

Figure 5.6: Overview of the NAGSI adaptivity: **upper left:** We sweep through the entire domain and update all points. We then set a threshold η not exceeding the residual. **upper right:** We sweep through the entire domain again (using a different sweep pattern) and flag all points where the change exceeded the threshold η. **lower left and right:** We sweep through and update the flagged points only, for one or more times.

with a minimum of reprogramming. Lastly, we note that while we have focused our adaptivity approach on improving performance on fixed, regular grids, we believe it is possible to apply a similar philosophy to irregular grids by choosing local discretizations that can be applied to selected mesh points for improved performance.

5.3.5 Solving the Overall System

We solve the overall model from Section 5.2 using a level set/ghost cell method that uses the methods we just introduced. At every fixed time t, our method consists of the following steps:

Step 1: Maintain φ as a distance function, and pre-compute any required geometrical quantities, such as normal vectors and curvature. Use the geometry-aware discretization discussed in Section 5.3.2.

Step 2: Solve the quasi-steady reaction-diffusion problems for each p_i using NAGSI. (See Section 5.3.4.) In the event that jump boundary conditions $[p_i]$ and $[D_i \nabla p_i \cdot \mathbf{n}]$ are

prescribed, use the ghost cell extrapolations described in Section 5.3.3.

Step 3: Calculate and extend the normal velocity V:

Part a: Calculate ∇p_i for each i in the narrow band $\{\mathbf{x} : |\varphi(\mathbf{x})| \leq R\}$ using second-order centered differences if all points in the stencil are in the same region (all inside Ω or all outside Ω). Otherwise, use high-order, one-sided Taylor expansions. In our work, we use five-point stencils when possible, and degrade to lower-order one-sided stencils as necessary.

Part b: Use our bilinear velocity extension from Macklin and Lowengrub (2005) to create a normal extension $\widetilde{V}$ of $V = \sum \alpha_i \nabla p_i \cdot \mathbf{n}$.

Part c: Problems with geometric boundary conditions (e.g., those that depend upon the curvature κ) require that $\Delta t \sim \Delta x^3$ to maintain stability. To avoid this prohibitive time step restriction, apply the Gaussian filtering technique we developed in Macklin (2003) and Macklin and Lowengrub (2005) to the extended velocity $\widetilde{V}$, which removes high-frequency noise from the velocity. Note that if the jump boundary conditions of the p_i do not require the curvature, then this filtering may not be required.

Part d: Use our bilinear velocity extension from Macklin and Lowengrub (2005) to extend the filtered velocity.

Part e: Calculate the CFL condition $\Delta t = \frac{\Delta x}{2\max(\widetilde{V})}$.

Step 4: Construct $\widetilde{V}\,|\nabla\varphi|$ using fifth-order WENO. Use this to advect the interface Σ.

Step 5: (*Optional*) If using a higher-order Runge-Kutta approximation, repeat steps (2)-(4) for each part of the Runge-Kutta scheme.

5.4 Convergence of the Numerical Techniques

We now present convergence results for the newly developed numerical techniques and the overall scheme. For a given norm $||\cdot||$, we define two orders of convergence. If p_h is a numerical solution computed on a computational grid with mesh length h, and if the exact

Traditional Stencil		New Stencil (1st order)		New Stencil (Higher order)	
Δx	ℓ_∞ error	Δx	ℓ_∞ error	Δx	ℓ_∞ error
0.16	0.168897	0.16	0.00295862	0.16	0.00331730
0.08	0.170776	0.08	5.11947e-4	0.08	5.73877e-4
0.04	0.168131	0.04	9.22828e-5	0.04	8.18444e-5
order	0.00751	order	2.50	order	2.67

Table 5.1: Comparison of the $[D\nabla p \cdot \mathbf{n}]$ stencil for the traditional (**left**), first-order new (**middle**), and higher-order new (**right**) methods on Example 1.

solution p is known, then we define

$$\text{order of convergence} = \frac{\log\left(\frac{||p_{h_1} - p||}{||p_{h_2} - p||}\right)}{\log\left(\frac{h_1}{h_2}\right)} \tag{5.57}$$

where the norm is computed at the computational node points, and $h_2 < h_1$ are two different mesh lengths.

If the exact solution is unknown, then we solve on meshes with mesh lengths $h_1 = h$, $h_2 = \frac{1}{2}h$, and $h_3 = \frac{1}{4}h$, and we compute the order of convergence via

$$\text{order of convergence} = \frac{\log\left(\frac{||p_h - p_{h_2}||}{||p_{h_2} - p_{h_3}||}\right)}{\log(2)}, \tag{5.58}$$

where each norm is computed on the common grid points. In our work, we use the discrete maximum ℓ_∞ norm for all convergence testing.

5.4.1 Convergence of the Ghost Cell Method with the New $[D\nabla p \cdot \mathbf{n}]$ stencils and NAGSI

Example 1: An Example with Large Tangential and Normal Jumps:

To test the convergence and impact of our new normal derivative jump discretization, we studied the following problem

$$\nabla^2 p = 0 \quad \text{if } |\mathbf{x}| < 1 \tag{5.59}$$

$$\nabla^2 p = 0 \quad \text{if } |\mathbf{x}| > 1 \tag{5.60}$$

$$[p] = x + y \quad \text{if } |\mathbf{x}| = 1 \tag{5.61}$$

$$[\nabla p \cdot \mathbf{n}] = x + y \qquad \text{if } |\mathbf{x}| = 1 \tag{5.62}$$

$$u = 0 \qquad \text{if } \mathbf{x} \in \partial\left([-2,2] \times [-2,2]\right), \tag{5.63}$$

whose solution is

$$p(x,y) = \begin{cases} x + y & \text{if } |\mathbf{x}| \leq 1 \\ 0 & \text{else.} \end{cases} \tag{5.64}$$

Note that the solution in (5.64) has a nonzero jump in tangential derivative:

$$[\nabla p \cdot \mathbf{s}] = (1,1) \cdot (y, -x) = y - x, \tag{5.65}$$

where $\mathbf{s}$ is the positively-oriented tangent vector along boundary of the circle.

We solved this system with mesh sizes $\Delta x \in \{0.16, 0.08, 0.04\}$, using our new NAGSI solver along with the ghost cell extrapolations described above, using both the traditional, grid-aligned normal derivative stencil from Liu et al. (2000) and the new normal derivative jump stencils. The traditional stencil from Liu et al. (2000) (as stabilized in Macklin and Lowengrub (2007)) failed to converge (left part of Table 5.1), with visible distortions in the solution (blue squares in Figure 5.7.) In contrast, when we recomputed the solution using our new normal derivative jump stencils, we obtained 2.50- and 2.67-order convergence for our first-order and higher-order stencils, respectively (middle and right parts of Table 5.1, respectively). Thus, we see that preserving the accuracy in the tangential derivative jump can have a substantial impact on the overall accuracy of the solution and is necessary for convergence in this example.

Example 2: An Example with a Large Tangential Jump and no Normal Jump:

We solved the same system as in the previous example, but with

$$[\nabla p \cdot \mathbf{n}] = 0 \quad \text{if } |\mathbf{x}| = 1. \tag{5.66}$$

In this example, the traditional stencil converged, but only to order 0.319 (top part of Table 5.2). In contrast, our first-order method attained 1.11-order accuracy (lower left part of Table 5.2), and our higher-order method achieved 1.53-order convergence (lower right part of Table 5.2).

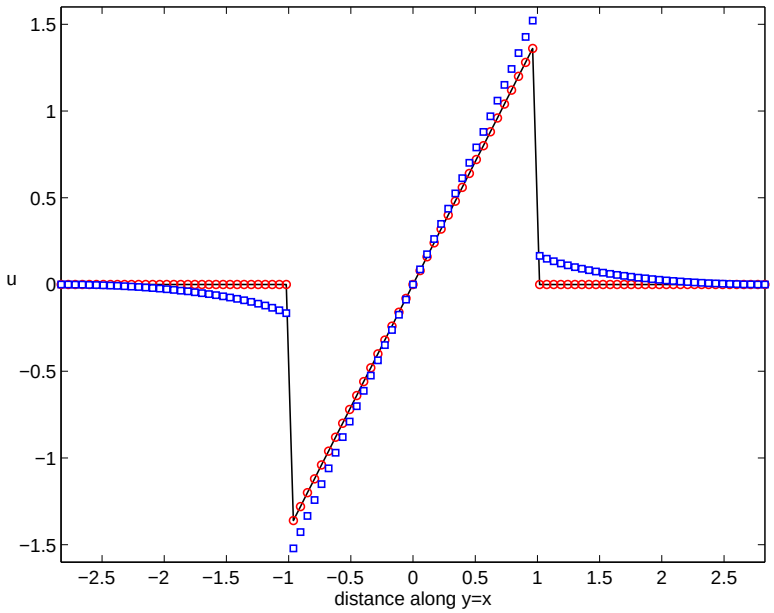

Figure 5.7: Comparison of solutions along the line $y = x$ using the traditional (blue squares) and new (red circles) $[D\nabla p \cdot \mathbf{n}]$ stencils using $\Delta x = 0.04$. The exact solution is given by the solid black line.

difference	ℓ_∞ norm
$p_{0.16} - p_{0.08}$	0.0282768
$p_{0.08} - p_{0.04}$	0.0226730
order	0.319

difference	ℓ_∞ norm
$p_{0.16} - p_{0.08}$	0.0201711
$p_{0.08} - p_{0.04}$	0.00936549
order	1.11

difference	ℓ_∞ norm
$p_{0.16} - p_{0.08}$	0.00655476
$p_{0.08} - p_{0.04}$	0.00226471
order	1.53

Table 5.2: Comparison of the $[D\nabla p \cdot \mathbf{n}]$ stencil for the traditional (**top**) and new first-order (**bottom left**) and higher-order (**bottom right**) methods on Example 2.

Traditional Stencil		New (1st Order) Stencil		New (Higher Order) Stencil	
Δx	ℓ_∞ error	Δx	ℓ_∞ error	Δx	ℓ_∞ error
0.16	0.647074	0.16	0.244280	0.16	0.0401866
0.08	0.540950	0.08	0.101704	0.08	0.00830349
0.04	0.458996	0.04	0.0492541	0.04	0.00312614
order	0.248	order	1.16	order	1.84

Table 5.3: Comparison of the $[D\nabla p \cdot \mathbf{n}]$ stencil for the traditional (**left**) and new first-order (**middle**) and higher-order (**right**) methods on Example 3.

Example 3: An Example with Large Normal Jumps and Zero Tangential Jumps:

To further investigate the accuracy of our new normal jump stencil, we studied the following problem:

$$\nabla^2 p = -4 \quad \text{if } |\mathbf{x}| < 1 \tag{5.67}$$

$$\nabla^2 p = 0 \quad \text{if } |\mathbf{x}| > 1 \tag{5.68}$$

$$[p] = 0 \quad \text{if } |\mathbf{x}| = 1 \tag{5.69}$$

$$[\nabla p \cdot \mathbf{n}] = -2 \quad \text{if } |\mathbf{x}| = 1 \tag{5.70}$$

$$p = 0 \quad \text{if } \mathbf{x} \in \partial\left([-2,2] \times [-2,2]\right), \tag{5.71}$$

whose solution is

$$p(x,y) = \begin{cases} 1 - x^2 - y^2 & \text{if } |\mathbf{x}| \le 1 \\ 0 & \text{else.} \end{cases} \tag{5.72}$$

Due to the jump boundary condition, this problem is sensitive to the discretization of the discontinuous source term: error in the numerical integral of the source term inside $|\mathbf{x}| \le 1$ will vertically shift the quadratic (interior) part of the solution, and due to the coupling of the interior and exterior normal derivatives, error in the source term will lead to error in the exterior region as well. We treat the discontinuous source term by solving

$$0 = \nabla^2 p + 4\, H(-\varphi), \qquad \mathbf{x} \in [-2,2] \times [-2,2], \tag{5.73}$$

and we discretize H with a numerical Heaviside function $\widetilde{H}$. See Section 5.8 for further discussion on the choice of $\widetilde{H}$.

Notice that this solution has no jump in the tangential derivative. Nonetheless, the traditional normal jump stencil (again, as stabilized in Macklin and Lowengrub (2007)) yields sub-first-order convergence (left part of Table 5.3), whereas our new stencil is first-order accurate (middle part of Table 5.3), and the higher-order method is 1.84-order accurate. Thus, we can see that the failure of the traditional $[D\nabla p \cdot \mathbf{n}]$ stencil to properly separate the normal and tangential jumps degrades the accuracy of the entire solution, even in the absence of a tangential derivative jump.

5.4.2 Convergence of the Overall Method

We examined the convergence of the overall method by studying a drop moving under Hele-Shaw-type flow in a heterogeneous medium. Let Σ be the boundary of a circle of radius 1 centered at $\left(5\sqrt{2}, 5\sqrt{2}\right)$.

We represent Σ as the zero contour of a level set function φ on the computational domain $\mathcal{D} = [0, 10] \times [0, 10]$ containing both $\Omega = \{\mathbf{x} \in \mathcal{D} : \varphi(\mathbf{x}) < 0\}$ and its complement $\Omega^c = \{\mathbf{x} \in \mathcal{D} : \varphi(\mathbf{x}) > 0\}$.

The drop has normal velocity

$$V = -\mu \nabla P \cdot \mathbf{n} \quad \text{if } \mathbf{x} \in \Sigma, \tag{5.74}$$

which we implement in the level set context as

$$\varphi_t + \widetilde{V} \left|\nabla \varphi\right| = 0, \tag{5.75}$$

where $\widetilde{V}$ is the normal extension of the velocity off of Σ that we described in Macklin and Lowengrub (2005).

The pressure P satisfies

$$\begin{aligned}
0 &= \nabla \cdot (\mu \nabla P) + H(-\varphi) \quad \text{if } \mathbf{x} \in \Omega \cup \Omega^c && (5.76)\\
[P] &= \kappa \quad \text{if } \mathbf{x} \in \Sigma && (5.77)\\
[\mu \nabla P \cdot \mathbf{n}] &= 0 \quad \text{if } \mathbf{x} \in \Sigma && (5.78)\\
& && (5.79)
\end{aligned}$$

with

$$\begin{aligned}
\mu &= \eta + (1 - \eta) e^{-1.5\left(\sqrt{x^2+y^2} - 5\sqrt{2}\right)^8} \quad \text{if } \mathbf{x} \in \mathcal{D} && (5.80)\\
\eta &= 0.0001, && (5.81)
\end{aligned}$$

t	$\|\|\varphi_{0.2} - \varphi_{0.1}\|\|_\infty$	$\|\|\varphi_{0.1} - \varphi_{0.05}\|\|_\infty$	order
0.1	0.0504799	0.0184189	1.45
0.2	0.0946371	0.0179485	2.40
0.3	0.0665503	0.0396410	0.747
0.4	0.130442	0.0342100	1.93
0.5	0.231275	0.0335707	2.78
average order of convergence			1.86

Table 5.4: Convergence of the Overall Method

and with boundary conditions

$$P \equiv 0 \quad \text{on } \partial D. \tag{5.82}$$

See Figure 5.8 for a plot of the permeability μ. Note that this models the growth of a drop of incompressible fluid in a heterogeneous domain, where fluid is added at a constant rate throughout the drop domain via the Heaviside source term $H(-\varphi)$.

We chose three spatial resolutions: $\Delta x = \Delta y = 0.20$ (low resolution), $\Delta x, \Delta y = 0.10$ (medium resolution), and $\Delta x = \Delta y = 0.05$ (high resolution). We used the discrete numerical Heaviside function that we describe in Section 5.8. We used a simple, first-order forward Euler time discretization with CFL condition

$$\Delta t \leq \max\left(\frac{\Delta x}{2\max|V|}, 0.05\right). \tag{5.83}$$

and fifth-order WENO for $V|\nabla\varphi|$. As in Macklin (2003) and Macklin and Lowengrub (2005), we used Gaussian filtering to attain a first-order CFL stability condition while maintaining accuracy. In these simulations, we used a smoothing parameter (standard deviation) of $\sigma = 2\Delta x = 0.40$ for low resolution, $\sigma = 3\Delta x = 0.30$ for medium resolution, and $\sigma = 4\Delta x = 0.15$ for high resolution.

We calculated the order of convergence (of the level set function φ) at times $t \in \{0.10, 0.20, 0.30, 0.40, 0.50\}$ according to (5.58). Due to the small time step, the time error is small and is consequently dominated by the spatial error. The average order of convergence was 1.86. See Table 5.4. We shall discuss the behavior of the solution in Section 5.1.

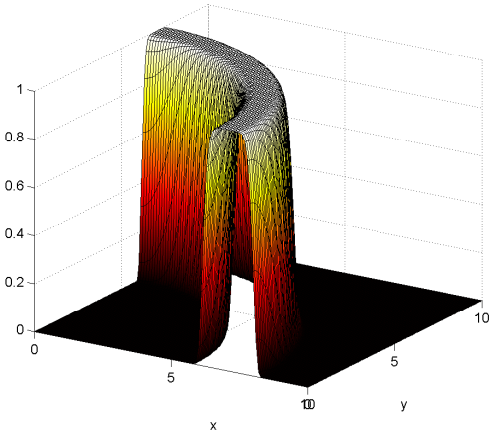

Figure 5.8: Permeability μ for the convergence example.

5.5 Numerical Examples

5.5.1 Hele-Shaw-type Flow in Heterogeneous Media

We solved the Hele-Shaw-type problem from the overall convergence study with $\Delta x = \Delta y = 0.10$, $\mathcal{D} = [0, 10] \times [0, 10]$, and the permeability μ shown in Figure 5.8 until $t = 1.8$. The solution is plotted in 0.20 time increments in Figure 5.9. As volume is added to the drop Ω (via the Heaviside source term in the pressure equation), pressure builds inside the drop that pushes the boundary Σ outward and causes the region Ω to grow. Because the permeability μ varies between 0.0001 and 1 throughout the domain, the drop grows preferentially inside the region where $\mu \sim 1$. See Figure 5.9. Because volume is added at a constant rate throughout the drop, the rate of growth is proportional to the volume of the drop; this can be observed as an increasing distance between solution curves.

5.5.2 Tumor Growth in Heterogeneous Tissues

We now demonstrate our technique by applying it to a nonlinear tumor growth problem. Let φ be a level set function whose zero contour denotes the boundary Σ of an avascular tumor $\Omega = \Omega(\mathbf{x}, t)$ growing into a surrounding, non-cancerous tissue $\Omega^c = \Omega^c(\mathbf{x}, t)$. This models the early stage of *in vivo* growth before the onset of angiogenesis. We take our computational domain $\mathcal{D}$ to be a rectangular region that fully contains Ω and Ω^c; note that

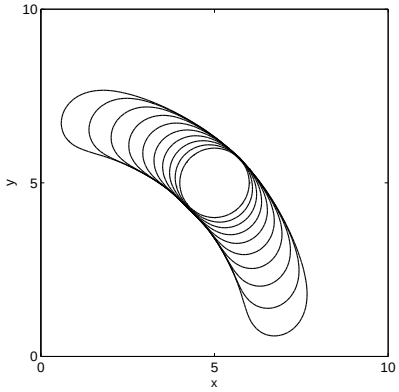

Figure 5.9: Outward growth of the medium-resolution ($\Delta x = \Delta y = 0.10$) solution in $t = 0.20$ increments for the convergence example.

$\mathcal{D} = \Omega \cup \Omega^c$.

Let c denote the non-dimensionalized nutrient concentration within the computational domain, scaled by the far-field nutrient value in well-vascularized, non-pathological tissue. We scale space by the oxygen diffusional length scale $L \approx 200$ μm. Outside the tumor, the blood vasculature (with density B) delivers nutrient, which diffuses into the tumor and is consumed by proliferating cells. As the tumor grows, less nutrient reaches the interior, until it drops to a level c_H where tumor cells become hypoxic. The hypoxic tumor cells become quiescent and consume less nutrient. If the tumor continues to grow and the interior nutrient level drops further below a critical threshold c_N, the tumor cells begin to die (necrose). When cells necrose, they release their cellular contents, which are both oxygen-reactive (e.g., see Kloner and Jennings (2001) and Galaris et al. (2006)) and growth-inhibiting. These processes can be modeled as

$$0 = \nabla \cdot (D\nabla c) - \lambda^c(\mathbf{x}, c)c + \lambda^c_{bulk}(1-c)B(\mathbf{x})H(\varphi) \quad \text{if } \mathbf{x} \in \Omega \tag{5.84}$$

$$\nabla c \cdot \mathbf{n} = 0 \quad \text{if } \mathbf{x} \in \partial\mathcal{D}, \tag{5.85}$$

where B is the pre-existing blood vessel density, λ^c_{bulk} is the nutrient delivery rate in the pre-existing blood vasculature, D is the nutrient diffusivity, and $\lambda^c(\mathbf{x}, c)$ is chosen to combine the rates of nutrient uptake (in the viable and hypoxic portion of the tumor) and decay (in the necrotic portion of the tumor); we assume no nutrient uptake in the non-cancerous tissue Ω^c. Normalized by the nutrient uptake rate in the viable region, the uptake and

decay function is modeled by

$$\lambda^c(\mathbf{x}, c) = \begin{cases} 0 & \text{if } \mathbf{x} \in \Omega^c \\ 1 & \text{if } \mathbf{x} \in \Omega \text{ and } 1 \geq c > c_H \\ q(c) & \text{if } \mathbf{x} \in \Omega \text{ and } c_H \geq c > c_N \\ \lambda_N^c & \text{if } \mathbf{x} \in \Omega \text{ and } c_N \geq c. \end{cases} \tag{5.86}$$

Here, λ_N^c is the rate of nutrient decay in the necrotic core, and $q(c)$ is a polynomial that smoothly connects regions and is chosen to satisfy

$$\begin{aligned} q(c_H) &= 1 \\ q'(c_H) &= 0 \\ q\left(\frac{c_H + c_N}{2}\right) &= \lambda_H^c \qquad (5.87) \\ q(c_N) &= \lambda_N^c \\ q'(c_N) &= 0, \qquad (5.88) \end{aligned}$$

where λ_H^c is the rate of nutrient uptake by hypoxic cells. In our numerical example, we shall take $c_H = 0.3$, $c_N = 0.2$, $\lambda_H^c = 0.5$, and $\lambda_N^c = 0.25$. In this case,

$$q(c) = -20000c^4 + 18500c^3 - 6275c^2 + 930c - 50.75. \tag{5.89}$$

Notice that this makes our nutrient equation nonlinear.

We model the tumor as an incompressible fluid growing in a porous medium, and so the local rate of change in tumor volume is given by $\nabla \cdot \mathbf{u}$, where $\mathbf{u}$ is the cellular velocity field. Proliferating tumor cells in the viable rim of the tumor generate an internal biomechanical pressure p that increases the tumor volume (at a rate proportional to the nutrient level c) and pushes the tumor boundary outward with normal velocity V via Darcy's law ($\mathbf{u} = -\mu\nabla p$). The enzymatic breakdown of necrotic tumor tissue is modeled by a local decrease in the pressure that reduces volume (at a constant rate G_N) and slows growth. Cell-to-cell adhesion is modeled as a surface tension (curvature) boundary condition on Σ. The non-cancerous tissue in Ω^c is also assumed to be affected by the tumor-generated pressure, but the cells in Ω^c do not proliferate. We model the pressure by

$$\nabla \cdot \mathbf{u} = -\nabla \cdot (\mu \nabla p) = \begin{cases} 0 & \text{if } \mathbf{x} \in \Omega^c \\ c & \text{if } \mathbf{x} \in \Omega \text{ and } c > c_H \\ 0 & \text{if } \mathbf{x} \in \Omega \text{ and } c_H \geq c > c_N \\ -G_N & \text{if } \mathbf{x} \in \Omega \text{ and } c_N \geq c \end{cases} \tag{5.90}$$

with boundary conditions

$$[p] = \frac{1}{G}\kappa \quad \text{if } \mathbf{x} \in \Sigma \tag{5.91}$$

$$[\mu \nabla p \cdot \mathbf{n}] = 0 \quad \text{if } \mathbf{x} \in \Sigma. \tag{5.92}$$

We model the normal velocity of the tumor boundary by Darcy's law:

$$V = -\mu \nabla p \cdot \mathbf{n} \quad \text{if } \varphi(\mathbf{x}) = 0. \tag{5.93}$$

We choose boundary conditions on p along $\partial\mathcal{D}$ to suit the problem under study. Here, G is a parameter that characterizes the tumor aggressiveness (the rate of proliferation compared to the cell-cell adhesion time scale), G_N is a parameter that governs the rate of tumor cell breakdown in necrotic regions, and μ is the cellular mobility. This tumor growth model is an extension of current models given in Cristini et al. (2003), Macklin (2003), Macklin and Lowengrub (2005), Zheng et al. (2005), and Macklin and Lowengrub (2006, 2007), and will be further extended and investigated in future work (Macklin et al., 2007; Lowengrub and Macklin, 2007).

We simulated this tumor system on a computational domain $\mathcal{D} = [0, 50] \times [0, 50]$ with $\Delta x = \Delta y = 0.10$, with tissue and tumor properties chosen to model the evolution of *glioblastoma* in brain tissue. Because the oxygen diffusional length scale is approximately 200 μm, this corresponds to an approximately 1 cm square of simulated brain tissue. We set $G = 20$, $G_N = 1$, $\lambda_{bulk}^c = 1$, $c_H = 0.3$, $c_N = 0.2$, and used $q(c)$ as given in (5.89). We model growth in a complex, heterogeneous brain tissue as shown in the first frame in Figure 5.10. In the white region, $\mu = 0.0001$, $D = 0.0001$, and $B = 0$, which models a rigid material such as the skull. In the black regions, $\mu = 10$, $D = 1$, and $B = 0$, which models an incompresible fluid (cerebrospinal fluid). The light and dark gray regions model tissues of differing biomechanical properties (white and gray matter). In the light gray regions, $\mu = 1.5$, $D = 1$, and $B = 1$; in the dark gray regions, $\mu = 0.5$, $D = 1$, and $B = 1$. The red region (color images are available online) denotes the initial shape and position of the simulated tumor. We smoothed μ, B, and D using a Gaussian filter with standard deviation $\sigma = 3\Delta x = 0.3$ to satisfy smoothness requirements of the reaction-diffusion equations. We used (linear) extrapolation boundary conditions on the pressure along $x = 0$, $y = 0$, and $y = 50$ to simulate growth into a larger, unshown tissue, and we set $p = 0$ along the rigid boundary at $x = 50$.

We simulated from $t = 0$ to $t = 60$. Using a 3.3 GHz Pentium 4 workstation and a C++ implementation, the 501×501 simulation required under 24 hours to compute. Because our (mitosis) time scale ranges from approximately 18 to 36 hours for this problem, this corresponds to 45 to 90 days of growth. We plot our solution in $t = 5.0$ (approximately 5 days) increments in Figures 5.10 and 5.11. In those plots, red regions correspond to viable tumor tissue (where $c > c_H$), blue regions denote hypoxic tumor tissue ($c_H \geq c > c_N$), and brown regions denote necrotic tumor cells ($c_N \geq c$). (Please see the online version of the article for color figures.) In this simulation, the tumor grows rapidly until the nutrient level drops below $c_H = 0.30$ (see $t = 5.0$), at which time a large portion of the tumor becomes hypoxic. The tumor continues to grow at a slower rate until the interior of the tumor becomes necrotic. (See $t = 10.0$.) This causes non-uniform volume loss within the tumor and contributes to morphological instability. We note that because the biomechanical responsiveness is continuous across the tumor boundary and the microenvironment has a moderate nutrient gradient, this simulation corresponds to the border between the invasive, fingering growth regime and the invasive, fragmenting growth regime that we investigated in Macklin and Lowengrub (2007).

However, additional effects can be seen that were not observed in the aforementioned study. As the tumor grows out of the biomechanically permissive tissue (light gray; $\mu = 1.5$) and into the biomechanically resistant tissue (dark gray; $\mu = 0.5$), its rate of invasion into the tissue slows. (See $t = 15$ to 25.0.) This results in preferential growth into the permissive (light gray) material, a trend which can be clearly seen from $t = 30.0$ onward. When the tumor grows through the resistive tissue (dark gray) and reaches the fluid (black), the tumor experiences a sudden drop in biomechanical resistance to growth. As a result, the tumor grows rapidly and preferentially in the 1/2 mm fluid structures that separate the tissue. Such growth patterns are not observed when simulating homogeneous tissues.

Other observed differences are due to our new treatment of hypoxic (quiescent) tumor cells. Certain regions that we had previously classified as necrotic (in Macklin (2003) and Macklin and Lowengrub (2005, 2006, 2007)) are now treated as quiescent. As a result, tumor volume loss is reduced, and in particular, this may result in large hypoxic regions that have little or no viable rim. Had these regions been treated as necrotic, the invasive fingers would have been thinner, and the tumor may have fragmented. Therefore, the separate treatment of the hypoxic regions can have a significant impact on the details of the invasive morphology of the tumor. We shall investigate this effect in greater detail in future work.

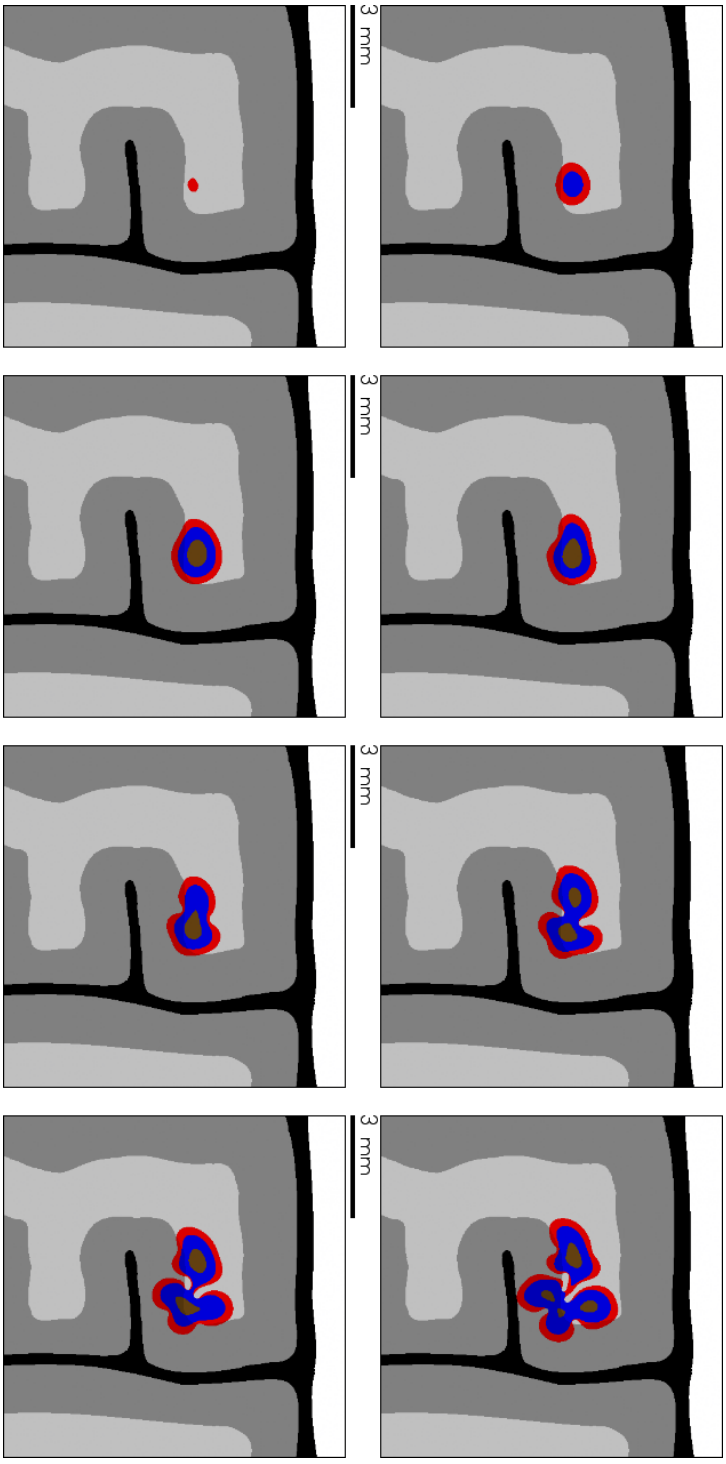

Figure 5.10: Long-time tumor simulation from t = 0.0 days (top left) to t = 35.0 days (bottom right) in 5 day increments. The color version of this figure is available online.

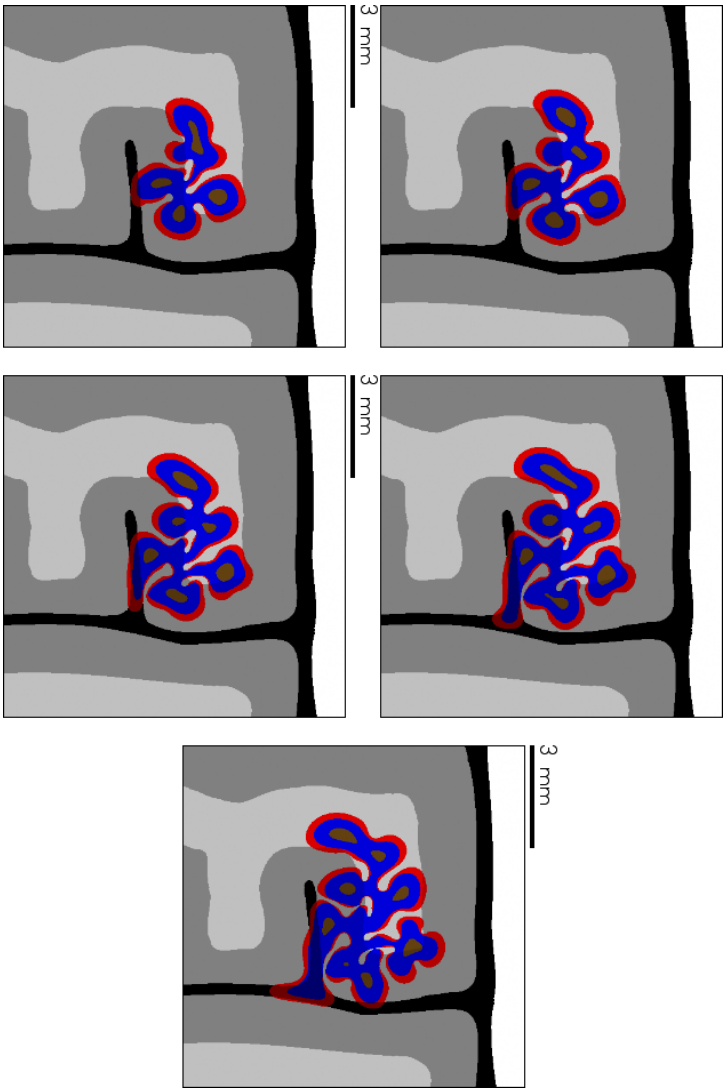

Figure 5.11: Long-time tumor simulation (continued) from t = 40.0 days (top left) to t = 60.0 days (bottom) in 5 day increments. The color version of this figure is available online.

5.6 Conclusions and Future Work

In this paper, we built upon our earlier work from Macklin (2003) and Macklin and Lowengrub (2005, 2006, 2007) to develop an accurate ghost cell/level set technique for evolving interfaces whose normal velocity is given by the normal derivatives of solutions to linear and nonlinear quasi-steady reaction-diffusion equations with curvature-dependent boundary conditions. The technique is capable of describing complex morphologies evolving in heterogeneous domains. The algorithm involved several new developments, including a new ghost cell technique for accurately discretizing jumps in the normal derivative without smearing jumps in the tangential derivative, a new adaptive solver for linear and nonlinear quasi-steady reaction-diffusion problems (NAGSI), an adaptive normal vector discretization for interfaces in close contact, and an accurate discrete approximation to the Heaviside function.

We demonstrated the accuracy, efficiency, and capabilities of the method on a variety examples. For instance, we considered a model of solid tumor growth consisting of a fully nonlinear reaction-diffusion equation for the nutrient and a pressure equation that includes geometric boundary conditions. We solved the tumor system in a heterogeneous environment including complex structures (white and gray matter, cerebrospinal fluid, and bone), much like human brain tissue. We observed growth morphologies that were highly dependent upon the variations in the cellular mobility and the nutrient delivery–an effect observed in real tumor growth. The accuracy of the algorithm is a key step in the development of a new generation of predictive tumor growth models that can eventually lead to clinical applications. In future work, we will conduct a more thorough study of tumor growth in inhomogeneous tissue, investigate models of tumor-microenvironment coupling that include active remodeling of the tissue by the tumor (Lowengrub and Macklin, 2007), and study the effects of coupling tumor growth to complex models of angiogenesis with Alexander Anderson, Mark Chaplain, Steven McDougall, and Vittorio Cristini.

5.7 Acknowledgements

We thank the National Science Foundation Division of Mathematical Sciences and the UCI Department of Mathematics for their financial support. Paul Macklin was partially supported by a U.S. Department of Education GAANN (Graduate Assistance in Areas of

National Need) fellowship.

We thank Alexander "Sandy" Anderson and Mark Chaplain at the University of Dundee, Steven McDougall at Heriot-Watt University, and Vittorio Cristini at the University of Texas Health Science Center in Houston for valuable discussions. We thank the University of Dundee and Heriot-Watt University for their gracious hospitality during numerous visits in 2006 and 2007.

5.8 A Simple Numerical Heaviside Function

Given a discretized domain with grid points $\{x_i\}_{i=0}^m \times \{y_j\}_{j=0}^n$ and a function f defined on those node points, we wish to define a numerical Heaviside function $\widetilde{H}(f) = H_{i,j}(f)$ on the computational node points which approximates the true Heaviside function

$$H(f) = \begin{cases} 0 & \text{if } f < 0 \\ 1 & \text{if } f \geq 0 \end{cases} \tag{5.94}$$

and such that

$$H_{i,j}(f)\Delta x \Delta y \approx \int_{x_i - \frac{1}{2}\Delta x}^{x_i + \frac{1}{2}\Delta x} \int_{y_j - \frac{1}{2}\Delta y}^{y_j + \frac{1}{2}\Delta y} H\left(f(s,t)\right)\, ds\, dt, \tag{5.95}$$

i.e., the numerical Heaviside function approximates the percentage of the computational node centered at (x_i, y_j) that is occupied by the region $\{\mathbf{x} : f(\mathbf{x}) > 0\}$. We accomplish this by examining the value of f at (i, j) and the eight surrounding computational nodes:

$$H_{i,j}(f) = \sum_{s=i-1}^{i+1} \sum_{t=j-1}^{j+1} w_{|s-i|,|t-j|} H(f_{i,j}), \tag{5.96}$$

where the weights are given by the relative areas of the sub-grid sections in Figure 5.12, and can be written as

$$w_{m,n} = \frac{2^{2-m-n}}{16} = \begin{cases} \frac{1}{16} & \text{if } m = 1 \text{ and } n = 1 \\ \frac{1}{8} & \text{if } m = 1 \text{ and } n = 0 \\ \frac{1}{8} & \text{if } m = 0 \text{ and } n = 1 \\ \frac{1}{4} & \text{if } m = 0 \text{ and } n = 0. \end{cases} \tag{5.97}$$

See Figure 5.12. For the function in the figure, $H_{i,j}(f) = \frac{11}{16}$.

To study the accuracy of this numerical Heaviside function, we calculated the order of the convergence for the third ghost cell method example in Section 5.4.1 using our

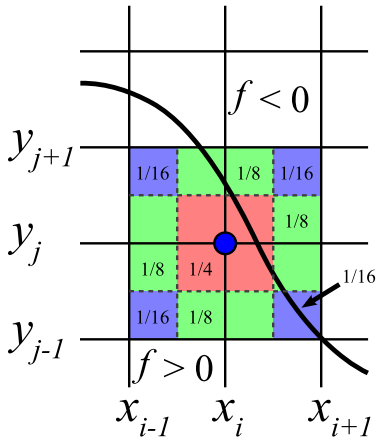

Figure 5.12: The weights w used for computing our numerical Heaviside function at a node (i, j).

discrete Heaviside function. For comparison, we also considered the Heaviside function from Sussman and Fatemi (1999)

$$\widetilde{H}_\delta(f) = \begin{cases} 0 & \text{if} \quad f < -\delta \\ \frac{1}{2}\left[1 + \frac{f}{\delta} + \frac{1}{\pi}\sin\left(\frac{\pi f}{\delta}\right)\right] & \text{if} \quad |f| \le \delta \\ 1 & \text{if} \quad f > \delta \end{cases} \tag{5.98}$$

with $\delta = \Delta x$, and the Heaviside function function in recent work by Engquist et al. (2005):

$$\widetilde{H}_\delta(f) = \begin{cases} 0 & \text{if} \quad f \le -\delta \\ \frac{1}{2}\left(1 + \frac{f}{\delta}\right) & \text{if} \quad |f| < \delta \\ 1 & \text{if} \quad f \ge \delta, \end{cases} \tag{5.99}$$

where we used $\delta = \Delta x$.

The results, given in Table 5.5, demonstrate approximately first-order convergence of the problem using the Sussman and Fatemi Heaviside function (left part of Table 5.5), slightly better than first-order convergence for the Engquist et al. Heaviside function (middle part of Table 5.5), and near-second-order convergence for our discrete Heaviside function (right part of Table 5.5). The key to this problem is the accurate approximation of the source term without smearing the integral of the source outside of the circle $|\mathbf{x}| \le 1$. All three methods approximate the area of the circle to second-order accuracy (not shown), but only the discrete Heaviside approximation was designed to accurately approximate the area of the region locally as well as globally.

Sussman and Fatemi (1999)	
Δx	ℓ_∞ error
0.16	0.0269720
0.08	0.00776372
0.04	0.00671369
order	1.00

Engquist et al. (2005)	
Δx	ℓ_∞ error
0.16	0.0307405
0.08	0.00843434
0.04	0.00598091
order	1.18

discrete Heaviside function	
Δx	ℓ_∞ error
0.16	0.0401866
0.08	0.00830349
0.04	0.00312614
order	1.84

Table 5.5: Convergence of a ghost cell problem using a Heaviside function, computed with the continuous approximation by Sussman and Fatemi (1999) (left), the continuous approxmation by Engquist et al. (2005) (middle), and our discrete Heaviside approximation (right).

Chapter 6

Looking Forward

In the near term, we shall apply the methods developed in this dissertation to model tumor growth in large, centimeter-scale tissues with increasingly detailed structure and biophysics. We are now including the effects of ECM remodeling by tumor cells, and we have introduced a new structure variable S to model the presence ($S = 1$) or absence ($S = 0$) of rigid objects such as bone or foreign objects. To provide a better link between the molecular and macroscopic scales, we are currently reformulating the microphysical parameters (the cellular mobility μ, the genetic parameters G, A, G_N and N, any taxis coefficients, and the various diffusivities and uptake rates) as functional relationships between these and the molecular model variables (the nutrient level, pressure, extracellular matrix density, etc.). For example, the cellular mobility should be a non-monotonic function of ECM density, and it should be nearly zero in rigid structures like bone. On the other hand, hypoxia is known to reduce cell-cell and cell-matrix adhesion in advanced cancer cells, which can be modeled as an increase in the cellular mobility. We shall model the functional cellular mobility as

$$\mu = \mu\left(\mathbf{x}, t, S, E, \sigma\right), \tag{6.1}$$

where E is the ECM density, S is the structure variable, and σ is the oxygen level. We shall model the other microphysical parameters in a similar fashion.

In other ongoing work, we are coupling our tumor growth model with a sophisticated model of angiogenesis (McDougall et al., 2006). In the coupling, hypoxic regions of the tumor secrete pro-angiogenic growth factors that diffuse into the surrounding tissue and recruit endothelial cells to grow toward the tumor and create a new vascular network. We couple with the dynamic adaptive tumor-induced angiogenesis (DATIA) model of McDougall et al.

(2006), which includes such effects as blood flow, blood rheology (with haematocrit), wall shear stress-induced vessel branching, and blood flow-induced vascular network remodeling. In our coupling, only blood vessels with active flow supply oxygen to the tumor, which subsequently affects hypoxia in the tumor and the spatial distribution of angiogenic growth factors. This, in turn, further affects the vascular network topology, oxygen delivery, and future tumor growth. Furthermore, proliferation-induced pressure can squeeze closed the new blood vessels, which further affects both the network topology and the tumor's growth and morphology. We shall explore these and other aspects in coming work (Macklin et al., 2007).

In the longer term, we are working toward the goal of predictive *computational oncology*: the use of computer simulations to study cancer in real human beings and make clinically-relevant predictions. Along the path toward that goal, we will continue to expand the sophistication of the tumor and tissue models, couple them to improved angiogenesis models, and introduce pharmacokinetic models for the study of drug-tumor-patient interactions. As we further develop our computational expertise, we shall simulate cancer in larger 2D and 3D tissues and eventually in virtual patients. If we succeed in these goals, the potential implications are vast. A validated virtual tissue simulator could provide a valuable testbed for understanding both healthy and diseased human tissue beyond the context of cancer. Coupled with a sophisticated cancer model, our simulator could provide a virtual laboratory to reduce or eliminate animal testing, efficiently explore broad combinations of treatments, select promising new treatments more quickly, and reduce the financial risk and time to market for new cancer drugs. In the educational context, medical students and doctors could use an advanced tumor-patient simulator to explore treatment protocols and gain experience in a risk-free, interactive environment.

However, several mathematical, scientific, computational, data processing, and clinico-medical challenges must be surmounted if we are to attain these long-term goals. The mathematical model must include a better treatment of tissue stress and residual strain, and the motion of many tissue components (e.g., water, collagen, various cell types, cellular debris, etc.) must be accounted for; mixture models with well-founded conservation and interaction laws may provide a means for addressing these difficulties. The effect of the host immune system must be included, both for modeling immunotherapy and understanding the role of the immune system in both preventing and promoting the spread of cancer. The motion of individual and clumps of metastatic tumor cells must be incorporated into the

model if metastasis and invasion are to be properly understood. These issues may possibly be addressed by the use of hybrid models that combine a continuum treatment of the tissue-scale phenomena with agent-based models of the immune system (e.g., white blood cells, haematopoietic stem cells, etc.) and metastatic cells. The functional relationships between the microphysical parameters and the simulated physical variables must be better understood. We are investigating the idea of *integrative modeling* to address this problem, where coordinated biological experiments are used to inform the modeling process at every step of the way.

Once these modeling issues have been addressed, a key scientific challenge remains: current modeling approaches to date have been phenomenological in nature, limiting the value of model predictions. (Prediction results are not necessarily unique because the same prediction may obtained with several combinations of parameters.) Future models must be more tightly constrained to identify the parameters as uniquely as possible. Our recent move to reformulate the microphysical parameters is one approach to addressing this issue, because the parameters will be determined by (experimentally-validated) functions of physical quantities and genetic characteristics of the tumor cells, rather than unconstrained and free. This approach could be combined with hybrid models and upscaling to further incorporate molecular data and uniquely determine the model parameters. Such an approach would help the transition from phenomenological to physical, where the model can be uniquely initialized from physically measurable quantities.

From a computational point of view, simulating increasingly complex, coupled systems in 3D on large domains will be challenging. The efficiency of existing numerical methods must be improved, such as by implementing adaptive meshes and combining NAGSI with nonlinear multigrid approaches. Ultimately, these computations will likely require parallel computing, and so numerical methods should be formulated with parallel architectures in mind. Indeed, new computer workstations are increasingly parallel, with 2, 4 or more computational cores on a single chip, and new high-end graphics cards can be used as programmable, highly-parallel vector processing machines (Owens et al., 2007). Making use of this newfound computational power on commodity hardware should allow high-performance computing with consumer hardware, but will require careful algorithm design and an openness to new computer architectures and technologies.

Assuming that realistic models are formulated, validated, and efficiently implemented, additional challenges remain. Patient data, consisting of collections of MRI, PET scan,

X-ray, ultrasound, and other image data, handwritten doctor's notes, biopsies, and genetic testing must be integrated to initiate any patient-tailored simulator. This will involve computational challenges, such as segmentation of medical imagery into separate tissue types and structure, classification of those tissues, and the assignment of tissue properties, perhaps from large databases of known tissue characteristics for various tissue types. Biopsies and other tumor data must be translated into model biophysical parameters. It is most likely that these goals must be attained with incomplete patient datasets, especially in cases where patients are weak or testing is deemed too invasive or expensive.

Lastly, medical and clinical challenges must be overcome. Any simulator must be powerful enough to accurately model the tumor-patient interaction and progression, yet simple enough for a non-Ph.D. doctor or technician to initialize and run. The data must be presented in a format that is informative, easy to understand, and trustworthy. A virtual cancer patient will likely require FDA approval for clinical use and must therefore have a proven reliability. Significant outreach and education will be required in the medical community if a virtual cancer simulator is to be seriously regarded as a clinical tool for planning a patient's treatment, with proven reliability an essential first step. For instance, our current models predict that over-aggressive anti-angiogenic therapy that completely shuts down nutrient supply to the tumor may increase tumor invasiveness and could potentially increase metastasis, and that normalizing nutrient delivery may stabilize tumor morphologies. However, in a clinical context, it could be very difficult to convince a patient and his/her physician that "feeding a tumor is better than starving it as quickly as possible." Indeed, many current oncologists define the success of a treatment by how quickly and by what amount tumor volume is decreased, even while our current models predict that this may worsen the patient's long-term prognosis by increasing the chance of metastasis and recurrence. Such institutional wisdom has been developed over several decades of clinical experimentation, and only a thoroughly-developed, highly-accurate, and well-validated model with a proven track record will be seriously considered, and only with sustained public outreach beyond the mathematical community.

In spite of these challenges, now is a promising time for computational oncology. Tumor models have progressed rapidly from their simple state just a few years ago to include many important biological aspects of cancer progression. Emerging models of tissue structure and tumor-tissue interaction are showing a hint of things to come, with increasing realism and the potential for integrating the vast mountain of biological data into the functional

relationships that govern and couple the microphysical parameters and variables. The biomathematics community has begun to acquire the vocabulary and background necessary to communicate with biologists, and it has begun to seek expertise within the biomedical community. At the same time, there is increasing awareness in the biomedical community that cancer *systems* are far too complex to study without a modeling framework. The time is ripe for increasing dialog between the mathematical and biological communities, and mathematical-biomedical collaborations are already springing up across the country (e.g., at the Tufts University/Caritas St. Elizabeth's Medical Center in Boston and at the University of Texas Health Science Center in Houston) and around the world (for instance, between the University of Dundee and the Vanderbilt Medical Center). Now is truly an exciting time to be involved in biomathematics and computational oncology!

Bibliography

R. G. Abbott, S. Forrest, and K. J. Pienta. Simulating the Hallmarks of Cancer. *Artif. Life*, 12(4):617–34, 2006. doi: 10.1162/artl.2006.12.4.617.

D. Adalsteinsson and J. A. Sethian. The Fast Construction of Extension Velocities in Level Set Methods. *J. Comput. Phys.*, 148(1):2–22, 1999. doi: 10.1006/jcph.1998.6090.

J. Adam. General aspects of modeling tumor growth and the immune response. In J. Adam and N. Bellomo, editors, *A survey of models on tumor immune systems dynamics*, pages 15–87. Birkhauser, Boston, MA, 1996.

T. Alarcón, H. M. Byrne, and P. K. Maini. A cellular automaton model for tumour growth in inhomogeneous environment. *J. Theor. Biol.*, 225(2):257–274, 2003. doi: 10.1016/S0022-5193(03)00244-3.

T. Alarcón, H. M. Byrne, and P. K. Maini. Towards whole-organ modelling of tumour growth. *Progress Biophys. Mol. Biol.*, 85(2-3):451–472, 2004. doi: 10.1016/j.pbiomolbio.2004.02.004.

J. W. Allen, S. R. Khetani, R. S. Johnson, and S. Bhatia. *In Vitro* Liver Tissue Model Established from Transgenic Mice: Role of HIF-1alpha on Hypoxic Gene Expression. *Tissue Engineering*, 12(11):3135–47, 2006. doi: 10.1089/ten.2006.12.3135.

D. Ambrosi and F. Guana. Stress-modulated growth. *Math. Mech. Solids*, 2006. doi: 10.1177/1081286505059739. (in press).

D. Ambrosi and F. Mollica. On the mechanics of a growing tumor. *Int. J. Eng. Sci.*, 40 (12):1297–1316, 2002. doi: 10.1016/S0020-7225(02)00014-9.

D. Ambrosi and F. Mollica. The role of stress in the growth of a multicell spheroid. *J. Math. Biol.*, 48(5):477–499, 2004. doi: 10.1007/s00285-003-0238-2.

D. Ambrosi and L. Preziosi. On the closure of mass balance models for tumor growth. *Math. Mod. Meth. Appl. Sci.*, 12(5):737–754, 2002. doi: 10.1142/S0218202502001878.

A. R. A. Anderson. A Hybrid Mathematical Model of Solid Tumour Invasion: The Importance of Cell Adhesion. *IMA Math. App. Med. Biol.*, 22(2):163–186, 2005. doi: 10.1093/imammb/dqi005.

A. R. A. Anderson and M. A. J. Chaplain. Continuous and discrete mathematical models of tumor-induced angiogenesis. *Bull. Math. Biol.*, 60(5):857–900, 1998. doi: 10.1006/bulm.1998.0042.

A. R. A. Anderson, A. M. Weaver, P. T. Cummings, and V. Quaranta. Tumor Morphology and Phenotypic Evolution Driven by Selective Pressure from the Microenvironment. *Cell*, 127(5):905–915, 2006. doi: 10.1016/j.cell.2006.09.042.

R. P. Araujo and D. L. S. McElwain. A mixture theory for the genesis of residual stresses in growing tissues II: Solutions to the biphasic equations for a multicell spheroid. *SIAM J. Appl. Math.*, 66(2):447–467, 2005. doi: 10.1137/040607125.

R. P. Araujo and D. L. S. McElwain. A history of the study of solid tumor growth: The contribution of mathematical modeling. *Bull. Math. Biol.*, 66(5):1039–1091, 2004a. doi: 10.1016/j.bulm.2003.11.002.

R. P. Araujo and D. L. S. McElwain. A linear-elastic model of anisotropic tumour growth. *Euro. J. Appl. Math.*, 15(3):365–384, 2004b. doi: 10.1017/S0956792504005406.

R. Arvind, C. Wang, and S. L. Schreiber. Perturbational profiling of a cell-line model of tumorigenesis by using metabolic measurements. *PNAS*, 102(17):5992–7, 2005. doi: 10.1073/pnas.0502267102.

D. H. Ausprunk and J. Folkman. Migration and proliferation of endothelial cells in preformed and newly formed blood vessels during tumour angiogenesis. *Microvasc. Res.*, 14 (1):53–65, 1977. doi: 10.1016/0026-2862(77)90141-8.

A. Bardelli, M. L. Basile, E. Audero, S. Giordano, S. Wennström, S. Ménard, P. M. Comoglio, and C. Ponzetto. Concomitant activation of pathways downstream of Grb2 and PI 3-kinase is required for MET-mediated metastasis. *Oncogene*, 18(5):1139–46, 1999.

P. A. Beachy, S. S. Karhadkar, and D. M. Berman. Tissue repair and stem cell renewal in carcinogenesis. *Nature*, 432(7015):324–331, 2004. doi: 10.1038/nature03100.

L. Bello, V. Lucini, F. Costa, M. Pluderi, C. Giussani, F. Acerbi, G. Carrabba, D. Pannacci, Marilou Caronzolo, S. Grosso, S. Chinkaruk, F. Colleoni, X. Canron, G. Tomei, G. Deleris, and A. Bikfalvi. Combinatorial administration of molecules that simultaneously inhibit angiogenesis and invasion leads to increased therapeutic efficacy in mouse models of malignant glioma. *Clin. Cancer Res.*, 10(13):4527–37, 2004.

N. Bellomo, E. de Angelis, and L. Preziosi. Multiscale modelling and mathematical problems related to tumor evolution and medical therapy. *J. Theor. Med.*, 5(2):111–136, 2003. doi: 10.1080/1027336042000288633.

J. R. Berenson, L. Rajdev, and M. Broder. Pathophysiology of Bone Metastases. *Cancer Biol. Ther.*, 5(9):1078–1081, 2006.

M. V. Blagosklonny and A. B. Pardee. The restriction point of the cell cycle. *Cell Cycle*, 1 (2):103–110, 2002.

C. Blanpain and E. Fuchs. Epidermal Stem Cells of the Skin. *Annu. Rev. Cell Dev. Biol.*, 22:339–73, 2006. doi: 10.1146/annurev.cellbio.22.010305.104357.

C. Boccaccio, M. Andò, L. Tamagnone, A. Bardelli, P. Michieli, C. Battistini, and P. M. Comoglio. Induction of epithelial tubules by growth factor HGF depends on the STAT pathway. *Nature*, 391(6664):285–8, 1998. doi: 10.1038/34657.

A. A. Brandes. Adding temozolomide to radiotherapy prolongs survival in people with glioblastoma. *Cancer Treat Rev.*, 31(7):577–581, 2005. doi: 10.1016/j.ctrv.2005.08.004.

A. Bredel-Geissler, U. Karbach, S. Walenta, L. Vollrath, and W. Mueller-Kleiser. Proliferation associated oxygen consumption and morphology of tumor cells in monolayer and spheroid culture. *J. Cell. Phys.*, 153(1):44–52, 1992. doi: 10.1002/jcp.1041530108.

D. M. Brizel, S. P. Scully, J. M. Harrelson, L. Layfield, J. M. Bean, L. R. Prosnitz, and M. W. Dewhirst. Tumor oxygenation predicts for the likelihood of distant metastases in human soft tissue sarcoma. *Cancer Res.*, 56(5):941–3, 1996.

H. Byrne and L. Preziosi. Modelling solid tumour growth using the theory of mixtures. *Math. Med. Biol.*, 20(4):341–366, 2003. doi: 10.1093/imammb/20.4.341.

H. M. Byrne and M. A. J. Chaplain. Modelling the role of cell-cell adhesion in the growth and development of carcinomas. *Math. Comput. Model.*, 24(12):1–17, 1996a. doi: 10.1016/S0895-7177(96)00174-4.

H. M. Byrne and M. A. J. Chaplain. Growth of necrotic tumors in the presence and absence of inhibitors. *Math. Biosci.*, 135(2):187–216, 1996b. doi: 10.1016/0025-5564(96)00023-5.

H. M. Byrne and P. Matthews. Asymmetric growth of models of avascular solid tumors: exploiting symmetries. *IMA J. Math. Appl. Med. Biol.*, 19(1):1–29, 2002. doi: 10.1093/imammb/19.1.1.

H. M. Byrne, T. Alarcón, M. R. Owen, S. D. Webb, and P. K. Maini. Modeling aspects of cancer dynamics: A review. *Phil. Trans. R. Soc. A*, 364(1843):1563–1578, 2006. doi: 10.1098/rsta.2006.1786.

R. A. Cairns, T. Kalliomaki, and R. P. Hill. Acute (cyclic) hypoxia enhances spontaneous metastasis of KHT murine tumors:. *Cancer Res.*, 61(24):8903–8, 2001.

D. Q. Calcagno, M. F. Leal, A. D. Seabra, A. S. Khayat, E. S. Chen, S. Demachki, P. P. Assumpcao, M. H. G. Faria, S. H. B. Rabenhorst, M. V. P. Ferreira, M. D. C. Smith, and R. R. Burbano. Interrelationship between chromosome 8 aneuploidy, C-MYC amplification and increased expression in individuals from northern Brazil with gastric adenocarcinoma. *World J. Gastroenterol.*, 12(38):6027–6211, 2006.

P. Carmellet and R. K. Jain. Angiogenesis in cancer and other diseases. *Nature*, 407: 249–257, 2000. doi: 10.1038/35025220.

P. Castro, P. Soares, L. Gusmo, R. Seruca, and M. Sobrinho-Simes. H-*RAS* 81 polymorphism is significantly associated with aneuploidy in follicular tumors of the thyroid. *Oncogene*, 25:4620–4627, 2006. doi: 10.1038/sj.onc.1209491.

M. A. J. Chaplain. Pattern Formation in Cancer. In M. A. J. Chaplain, G. D. Singh, and J. C. MacLachlan, editors, *On growth and Form: Spatio-temporal pattern formation in Biology*, pages 47–70. Wiley Series in Mathematical and Computational Biology, New York, NY, 2000. ISBN 0-471-98451-5.

M. A. J. Chaplain, M. Ganesh, and I. G. Graham. Spatio-temporal pattern formation on spherical surfaces: numerical simulation and application to solid tumour growth. *J. Math. Biol.*, 42(5):387–423, 2001. doi: 10.1007/s002850000067.

M. A. J. Chaplain, L. Graziano, and L. Preziosi. Mathematical modelling of the loss of tissue compression responsiveness and its role in solid tumour development. *Math. Med. Biol.*, 23(3):192–229, 2006. doi: 10.1093/imammb/dql009.

C. Chatterjee and E. K. P. Chong. Efficient Algorithms for Finding the Centers of Conics and Quadrics in Noisy Data. *Patt. Recog.*, 30(5):673–684, 1997. doi: 10.1016/S0031-3203(96)00122-7.

S. Chen, B. Merriman, S. Osher, and P. Smereka. A Simple Level Set Method for Solving Stefan Problems. *J. Comput. Phys.*, 135(1):8–29, 1997. doi: 10.1006/jcph.1997.5721.

J.-T. Chi, Z. Wang, D. S. A. Nuyten, E. H. Rodriguez, M. E. Schaner, A. Salim, Y. Wang, G. B. Kristensen, Å. Helland, A.-L. Børresen-Dale, A. Giaccia, M. T. Longaker, T. Hastie, G. P. Yang, M. J. van de Vijver, and P. O. Brown. Gene expression programs in response to hypoxia: Cell type specificity and prognostic significance in human cancers. *PLoS Med.*, 3(3):e47, 2006. doi: 10.1371/journal.pmed.0030047.

M. Classon and E. Harlow. The retinoblastoma tumour suppressor in development and cancer. *Nat. Rev. Cancer*, 2(12):910–917, 2002. doi: 10.1038/nrc950.

R. G. Clyde, J. L. Brown, T. R. Hupp, N. Zhelev, and J. W. Crawford. The role of modelling in identifying drug targets for diseases of the cell cycle. *J. R. Soc. Interface*, 3 (10):617–627, 2006. doi: 10.1098/rsif.2006.0146.

V. Cristini, J. S. Lowengrub, and Q. Nie. Nonlinear simulation of tumor growth. *J. Math. Biol.*, 46:191–224, 2003. doi: 10.1007/s00285-002-0174-6.

V. Cristini, H. B. Frieboes, R. Gatenby, S. Caserta, M. Ferrari, and J. Sinek. Morphological instability and cancer invasion. *Clin. Cancer Res.*, 11(19):6772–6779, 2005.

K. Date, K. Matsumoto, K. Kuba, H. Shimura, M. Tanaka, and T. Nakamura. Inhibition of tumor growth and invasion by a four-kringle antagonist (HGF/NK4) for hepatocyte growth factor. *Oncogene*, 17(23):3045–54, 1998.

C. de Boor. *A Practical Guide to Splines*. Springer-Verlag, New York, NY, 1978.

L. G. de Pillis, W. Gu, and A. E. Radunskaya. Mixed immunotherapy and chemotherapy of tumors: modeling, applications, and biological interpretations. *J. Theor. Biol.*, 238(4): 841–862, 2006. doi: 10.1016/j.jtbi.2005.06.037.

K. DeJaeger, M.-C. Kavanagh, and R. P. Hill. Relationship of hypoxia to metastatic ability in rodent tumors. *Br. J. Cancer*, 84(9):1280–1285, 2001. doi: 10.1054/bjc.2001.1743.

H. D. Dell. Milestone 1 (1889) Seed and soil hypothesis: Observations from a ploughman. *Nat. Rev. Cancer*, 6:S7, 1989. doi: 10.1038/nrc1843. http://www.nature.com/milestones/milecancer/index.html.

J. Dobson. Percivall Pott. *Ann. R. Coll. Surg. Eng.*, 50(1):54–65, 1972.

T. Douki, A. Reynaud-Angelin, J. Cadet, and E. Sage. Bipyrimidine photoproducts rather than oxidative lesions are the main type of DNA damage involved in the genotoxic effect of solar UVA radiation. *Biochemistry*, 42(30):9221–6, 2003. doi: 10.1021/bi034593c.

M. Ducasse and M. A. Brown. Epigenetic aberrations and cancer. *Mol. Cancer*, 5:60, 2006. doi: 10.1186/1476-4598-5-60.

L. S. Duff, D. C. Sorensen, H. A. van der Vorst, and J. J. Dongarra. *Numerical Linear Algebra for High-Performance Computers*. Society for Industrial and Applied Math, Philadelphia, PA, 1998. ISBN 0-89871-428-1 (paperback).

T. Eguchi, T. Takaki, H. Itadani, and H. Kotani. Rb silencing compromises the DNA damage-induced G2/M checkpoint and causes deregulated expression of ECT2 oncogene. *Oncogene*, 26(4):509–520, 2007. doi: 10.1038/sj.onc.1209810.

M. Elshaikh, M. Ljungman, R. T. Haken, and A. S. Lichter. Advances in Radiation Oncology. *Ann. Rev. Med.*, 57:19–31, 2006. doi: 10.1146/annurev.med.57.121304.131431.

Y. I. Elshimali and W. W. Grody. The Clinical Significance of Circulating Tumor Cells in the Peripheral Blood. *Diagn. Mol. Pathol.*, 15(4):187–194, 2006.

S. A. Enam, M. L. Rosenblum, and K. Edvardsen. Role of extracellular matrix in tumor invasion: migration of glioma cells along fibronectin-positive mesenchymal cell processes. *Neurosurgery*, 42(3):599–608, 1998.

B. Engquist, A.-K. Tornbergb, and R. Tsai. Discretization of Dirac delta functions in level set methods. *J. Comput. Phys.*, 207(1):28–51, 2005. doi: 10.1016/j.jcp.2004.09.018.

R. M. Enmon Jr., K. C. O'Connor, D. J. Lacks, D. K. Schwartz, and R. S. Dotson. Dynamics of spheroid self-assembly in liquid overlay culture of DU 145 human prostate cancer cells. *Biotech. Bioeng.*, 72(6):579–591, 2001. doi: 10.1002/1097-0290(20010320)72:6<579::AID-BIT1023>3.0.CO;2-L.

J. T. Erler, K. L. Bennewith, M. Nicolau, N. Dornhöfer, C. Kong, Q.-T. Le, J.-T. A. Chi, S. S. Jeffrey, and A. J. Giaccia. Lysyl oxidase is essential for hypoxia-induced metastasis. *Nature*, 440(27):1222–1226, 2006. doi: 10.1038/nature04695.

M. A. Esteban and P. H. Maxwell. HIF, a missing link between metabolism and cancer. *Nat. Med.*, 11(10):1047–8, 2005. doi: 10.1038/nm1005-1047.

P. Farrell. Mechanisms of viral carcinogenesis. In Knowles and Selby (2005), chapter 13, pages 229–241. ISBN 0-19-852563-X.

R. P. Fedkiw, T. Aslam, B. Merriman, and S. Osher. A Non-Oscillatory Eulerian Approach to Interfaces in Multimaterial Flows (the Ghost Fluid Method). *J. Comput. Phys.*, 152 (2):457–492, 1999. doi: 10.1006/jcph.1999.6236.

N. Festjens, T. Vanden Berghe, and P. Vandenabeele. Necrosis, a well-orchestrated form of cell demise: Signalling cascades, important mediators and concomitant immune response. *Biochim. Biophys. Acta*, 1757(9-10):1371–1387, 2006. doi: 10.1016/j.bbabio.2006.06.014.

I. Fischer, J.-p. Gagner, M. Law, E. W. Newcomb, and D. Zagzag. Angiogenesis in Gliomas: Biology and Molecular Pathophysiology. *Brain Pathol.*, 15(4):297–310, 2005. doi: 10.1111/j.1750-3639.2005.tb00115.x.

A. B. Fisher, S. Chien, A. I. Barakat, and R. M. Nerem. Endothelial cellular response to altered shear stress. *Am. J. Physiol. Heart Circ. Physiol.*, 281(3):L529L533, 2001.

G. B. Fogarty, N. M. Conus, J. Chu, and G. McArthur. Characterization of the expression and activation of the epidermal growth factor receptor in squamous cell carcinoma of the skin. *Brit. J. Derm.*, 156(1):92–98, 2007. doi: 10.1111/j.1365-2133.2006.07603.x.

J. Folkman. Angiogenesis in cancer, vascular, rheumatoid and other disease. *Nat. Med.*, 1: 27–30, 1995. doi: 10.1038/nm0195-27.

L. M. Franks and M. A. Knowles. What is Cancer? In Knowles and Selby (2005), chapter 1, pages 1–24. ISBN 0-19-852563-X.

J. P. Freyer. Role of necrosis in regulating the growth saturation of multicellular spheroids. *Cancer Res.*, 48(9):2432–9, 1988.

H. B. Frieboes, S. M. Wise, J. S. Lowengrub, and V. Cristini. Three-dimensional Diffuse-Interface Simulation of Multispecies Tumor Growth-II: Investigation of Tumor Invasion. *Bull. Math. Biol.*, 2006a. (in review).

H. B. Frieboes, X. Zheng, C.-H. Sun, B. Tromberg, R. Gatenby, and V. Cristini. An integrated computational/experimental model of tumor invasion. *Canc. Res.*, 66(3):1597–1604, 2006b.

H. B. Frieboes, J. S. Lowengrub, S. Wise, X. Zheng, P. Macklin, and V. Cristini. Computer simulations of glioma growth and morphology. *NeuroImage*, 2007. doi: 10.1016/j.neuroimage.2007.03.008. (in press).

P. Friedl and K. Wolf. Tumour-Cell Invasion and Migration: Diversity and Escape Mechanisms. *Nat. Rev. Cancer*, 3:362–374, 2003. doi: 10.1038/nrc1075.

S. H. Friend, R. Bernards, S. Rogelj, R. A. Weinberg, J. M. Rapaport, D. M. Albert, and T. P. Dryja. A human DNA segment with properties of the gene that predisposes to retinoblastoma and osteosarcoma. *Nature*, 323:643–6, 1986. doi: 10.1038/323643a0.

D. Galaris, A. Barbouti, and P. Korantzopoulos. Oxidative Stress in Hepatic Ischemia-Reperfusion Injury: The Role of Antioxidants and Iron Chelating Compounds. *Current Pharma. Design*, 12(23):2875–2890, 2006. doi: 10.2174/138161206777947614.

K. Garber. Energy Boost: The Warburg effect returns in a new theory of cancer. *JNCI*, 96 (24):1805–6, 2004. doi: 10.1093/jnci/96.24.1805.

R. A. Gatenby and E. T. Gawlinski. The Glycolytic Phenotype in Carcinogenesis and Tumor Invasion: Insights through Mathematical Models. *Cancer Res.*, 63(14):3847–3854, 2003.

R. A. Gatenby and E. T. Gawlinski. A reaction-diffusion model of cancer invasion. *Cancer Res.*, 56(24):5745–5753, 1996.

F. Gibou and R. Fedkiw. A Fourth Order Accurate Discretization for the Laplace and Heat Equations on Arbitrary Domains, with Applications to the Stefan Problem. *J. Comput. Phys.*, 202(2):577–601, 2005. doi: 10.1016/j.jcp.2004.07.018.

F. Gibou, R. Fedkiw, L.-T. Cheng, and M. Kang. A Second Order Accurate Symmetric Discretization of the Poisson Equation on Irregular Domains. *J. Comput. Phys.*, 176(1): 205–227, 2002. doi: 10.1006/jcph.2001.6977.

F. Gibou, R. Fedkiw, R. Caflisch, and S. Osher. A Level Set Approach for the Numerical Simulation of Dendritic Growth. *J. Sci. Comput.*, 19(1-3):183–199, 2003. doi: 10.1023/A:1025399807998.

M. A. Gimbrone, R. S. Cotran, S. B. Leapman, and J. Folkman. Tumor growth and neovascularization: an experimental model using the rabbit cornea. *J. Natl. Cancer Inst.*, 52(2):413–427, 1974.

J. Glimm, D. Marchesin, and O. McBryan. A Numerical-Method for 2 Phase Flow with an Unstable Interface. *J. Comput. Phys.*, 39:179–200, 1981. doi: 10.1016/0021-9991(81)90144-3.

R. Godde and H. Kurz. Structural and biophysical simulation of angiogenesis and vascular remodeling. *Dev. Dyn.*, 220(4):387401, 2001. doi: 10.1002/dvdy.1118.

R. Gonzalez and R. Woods. *Digital Image Processing*. Addison-Wesley Publishing Company, 2nd edition, 1992. ISBN 0-201-18075-8.

S. Gottlieb and C.-W. Shu. Total Variation Diminishing Runge-Kutta Schemes. *Math. Comp.*, 67(221):73–85, 1997. doi: 10.1090/S0025-5718-98-00913-2.

S. Gottlieb, C.-W. Shu, and E. Tadmor. Strong Stability-Preserving High-Order Time Discretization Methods. *SIAM Review*, 43(1):89–112, 2001. doi: 10.1137/S003614450036757X.

H. P. Greenspan. On the Growth and Stability of Cell Cultures and Solid Tumors. *J. Theor. Biol.*, 56(1):229–242, 1976. doi: 10.1016/S0022-5193(76)80054-9.

A. V. Gudkov and E. A. Komarova. The role of P53 in determining sensitivity to radiotherapy. *Nat. Rev. Cancer*, 3(2):117–129, 2003. doi: 10.1038/nrc992.

G. P. Gupta and J. Massagu. Cancer Metastasis: Building a Framework. *Cell*, 127(4): 679–695, 2006. doi: 10.1016/j.cell.2006.11.001.

A. H. Hallett, Y. Ma, and Y. P. Yin. Hybrid algorithms with automatic switching for solving nonlinear equation systems. *J. Econ. Dynam. Control*, 20(6):1051–1071, 1996. doi: 10.1016/0165-1889(95)00889-6.

D. Hanahan and R. A. Weinberg. The hallmarks of cancer. *Cell*, 100(1):57–70, 2000. doi: 10.1016/S0092-8674(00)81683-9.

Z. Haroon, K. G. Peters, C. S. Greenberg, and M. W. Dewhirst. Angiogenesis and Blood Flow in Solid Tumors. In B. Teicher, editor, *Antiangiogenic Agents in Cancer Therapy*, chapter 1, pages 3–21. Humana Press, Totowa, NJ, 1999. ISBN 0-896-03641-3.

A. L. Harris. Hypoxia-a key regulatory factor in tumour growth. *Nat. Rev. Cancer*, 2(1): 38–47, 2002. doi: 10.1038/nrc704.

I. Hart. The Spread of Tumours. In Knowles and Selby (2005), chapter 16, pages 278–288. ISBN 0-19-852563-X.

H. Hashizume, P. Baluk, S. Morikawa, G. McLean, S. Roberge, R. K. Jain, and D. M. McDonald. Openings between defective endothelial cells explain tumor vessel leakiness. *Am. J. Pathol.*, 156:1363–80, 2000.

T. E. Hedlund, R. C. Duke, and G. J. Miller. Three dimensional spheroid cultures of human prostate cancer cell lines. *Prostate*, 41(3):154–165, 1999. doi: 10.1002/(SICI)1097-0045(19991101)41:3<154::AID-PROS2>3.0.CO;2-M.

S. Hiratsuka, K. Nakamura, S. Iwai, M. Murakami, T. Itoh, H. Kijima, J. M. Shipley, R. M. Senior, and M. Shibuya. MMP9 induction by vascular endothelial growth factor receptor-1 is involved in lung-specific metastasis. *Cancer Cell*, 2(4):289–300, 2002. doi: 10.1016/S1535-6108(02)00153-8.

M. Höckel and P. Vaupel. Tumor hypoxia: definitions and current clinical, biologic, and molecular aspects. *J. Natl. Cancer Inst.*, 93(4):266–276, 2001. doi: 10.1093/jnci/93.4.266.

M. Höckel, K. Schlenger, B. Aral, M. Mitze, U. Schäffer, and P. Vaupel. Association between tumor hypoxia and malignant progression in advanced cancer of the uterine cervix. *Canc. Res.*, 56(19):4509–4515, 1996.

C. S. Hogea, B. T. Murray, and J. A. Sethian. Simulating complex tumor dynamics from avascular to vascular growth using a general level-set method. *J. Math. Biol.*, 53(1): 86–134, 2006. doi: 10.1007/s00285-006-0378-2.

J. M. Horowitz, D. W. Yandell, S.-H. Park, S. Canning, P. Whyte, K. Buchkovich, E. Harlow, R. A. Weinberg, and T. P. Dryja. Point mutational inactivation of the retinoblastoma antioncogene. *Science*, 243(4893):937–940, 1989. doi: 10.1126/science.2521957.

K. B. Hotary, E. D. Allen, P. C. Brooks, N. S. Datta, M. W. Long, and S. J. Weiss. Membrane type 1 matrix metalloproteinase usurps tumour growth control imposed by the three-dimensional extracellular matrix. *Cell*, 114(1):33–45, 2003. doi: 10.1016/S0092-8674(03)00513-0.

M. Hu, J. Yao, L. Cai, K. E. Bachman, F. van den Brle, V. Velculescu, and K. Polyak. Distinct epigenetic changes in the stromal cells of breast cancers. *Nat. Genet.*, 37(8): 899–905, 2005. doi: 10.1038/ngl1596.

F. Iovino, L. Lentini, A. Amato, and A. Di Leonardo. RB acute loss induces centrosome amplification and aneuploidy in murine primary fibroblasts. *Mol. Cancer*, 5:38, 2006. doi: 10.1186/1476-4598-5-38.

T. Ishii, J. Murakami, K. Notohara, H. M. Cullings, H. Sasamoto, T. Kambara, Y. Shirakawa, Y. Naomoto, M. Ouchida, K. Shimizu, N. Tanaka, J. R. Jass, and N. Matsubara. Oeophageal squamous cell carcinoma may develop within a background of accumulating DNA methylation in normal and dysplastic mucosa. *Gut*, 56(1):13–19, 2007. doi: 10.1136/gut.2005.089813.

R. K. Jain. Physiological Barriers to Delivery of Monoclonal Antibodies and Other Macromolecules in Tumors. *Cancer Res. (Suppl.)*, 50(3 Suppl.):814s–819s, 1990.

R. K. Jain. Normalizing tumor vasculature with anti-angiogenic therapy: A new paradigm for combination therapy. *Nat. Med.*, 7(9):987989, 2001. doi: 10.1038/nm0901-987.

G.-S. Jiang and D. Peng. Weighted ENO Schemes for Hamilton-Jacobi Equations. *SIAM J. Sci. Comput.*, 21(6):2126–2143, 2000. doi: 10.1137/S106482759732455X.

G.-S. Jiang and C.-W. Shu. Efficient Implementation of Weighted ENO Schemes. *J. Comput. Phys.*, 126(2):202–228, 1996. doi: 10.1006/jcph.1996.0130.

Y. Jiang, J. Pjesivac-Grbovic, C. Cantrell, and J. P. Freyer. A Multiscale Model for Avascular Tumor Growth. *Biophys. J.*, 89(6):3884–3894, 2005. doi: 10.1529/biophysj.105.060640.

A. F. Jones, H. M. Byrne, J. S. Gibson, and J. W. Dold. A mathematical model of the stress induced during avascular tumor growth. *J. Math. Biol.*, 40(6):473–499, 2000. doi: 10.1007/s002850000033.

P. A. Jones and S. B. Baylin. The fundamental role of epigenetic events in cancer. *Nat. Rev. Genet*, 3(6):415–28, 2002. doi: 10.1038/nrg816.

P. A. Jones and P. W. Laird. Cancer epigenetics comes of age. *Nat. Genet.*, 21(2):163–7, 1999. doi: 10.1038/5947.

A. A. Kansal, S. Torquato, G. R. Harsh IV, E. A. Chiocca, and T. S. Deisboeck. Simulated brain tumor growth dynamics using 3-D cellular automaton. *J. Theor. Biol.*, 203(4): 367–382, 2000. doi: 10.1006/jtbi.2000.2000.

R. N. Kaplan, S. Rafii, and D. Lyden. Preparing the "Soil": The Premetastatic Niche. *Cancer Res.*, 66(23):11089–93, 2006. doi: 10.1158/0008-5472.CAN-06-2407.

B. Kaur, F. W. Khwaja, E. A. Severson, S. L. Matheny, D. J. Brat, and E. G. Van Meir. Hypoxia and the hypoxia-inducible-factor pathway in glioma growth and angiogenesis. *Neuro-oncol.*, 7(2):134–153, 2005. doi: 10.1215/S1152851704001115.

A. Kiltie. Radiotherapy and molecular radiotherapy. In Knowles and Selby (2005), chapter 25, pages 414–427. ISBN 0-19-852563-X.

R. A. Kloner and R. B. Jennings. Consequences of brief ischemia: stunning, preconditioning, and their clinical implications: part 1. *Circulation*, 104(24):2981–2989, 2001.

M. A. Knewitz and J. C. M. Mombach. Computer simulation of the influence of cellular adhesion on the morphology of the interface between tissues of proliferating and quiescent cells. *Comp. Biol. Med.*, 36(1):59–69, 2006. doi: 10.1016/j.compbiomed.2004.08.002.

M. Knowles and P. Selby, editors. *Introduction to the Cellular and Molecular Biology of Cancer*. Oxford University Press, Oxford, UK, fourth edition, 2005. ISBN 0-19-852563-X.

A. G. Knudson. Two genetic hits (more or less) to cancer. *Nat. Rev. Cancer*, 1(2):157–62, 2001. doi: 10.1038/35101031.

A. G. Knudson. Mutation and cancer: statistical study of retinoblastoma. *Proc. Natl. Acad. Sci. USA*, 68(4):820–3, 1971.

B. Köberle, J. P. Wittschieben, and R. D. Wood. DNA repair and cancer. In Knowles and Selby (2005), chapter 4, pages 61–77. ISBN 0-19-852563-X.

N. L. Komarova. Cancer, aging and the optimal tissue design. *Sem. Cancer Biol.*, 15(6): 494–505, 2005. doi: 10.1016/j.semcancer.2005.07.003.

N. L. Komarova and P. Cheng. Epithelial tissue architecture protects against cancer. *Math. Biosci.*, 200(1):90–117, 2006. doi: 10.1016/j.mbs.2005.12.001.

N. L. Komarova and L. Wang. Initiation of Colorectal Cancer: Where do the Two Hits Hit? *Cell Cycle*, 3(12):1558–1565, 2004.

M. Konopleva, S.-R. Zhao, W. Hu, S.-W. Jiang, V. Snell, D. Weidner, C. E. Jackson, X. Zhang, R. Champlin, E. Estey, J. C. Reed, and M. Andreeff. The anti-apoptotic genes Bcl-X-L and Bcl-2 are over- expressed and contribute to chemoresistance of non-proliferating leukaemic CD34(+) cells. *Brit. J. Haematology*, 118(2):521–534, 2002. doi: 10.1046/j.1365-2141.2002.03637.x.

R. Küppers and Dalla-Favera. Mechanisms of chromosomal translocations in B cell lymphomas. *Oncogene*, 20(40):5580–94, 2001.

K. Lamszus, P. Kunkel, and M. Westphal. Invasion as limitation to anti-angiogenic glioma therapy. *Acta Neurochir. Suppl.*, 88:169–177, 2003.

A. R. Lehmann. The xeroderma pigmentosum group D (XPD) gene: one gene, two functions, three diseases. *Genes Dev.*, 15(1):15–23, 2001. doi: 10.1101/gad.859501.

S. Lehoux and A. Tedgui. Signal transduction of mechanical stresses in the vascular wall. *Hypertension*, 32(2):338345, 1998.

R. D. Lester, M. Jo, W. M. Campana, and S. L. Gonias. Erythropoietin promotes MCF-7 breast cancer cell migration by an ERK/mitogen-activated protein kinase-dependent pathway and is primarily responsible for the increase in migration observed in hypoxia. *J. Biol. Chem.*, 280(47):39273–39277, 2005. doi: 10.1074/jbc.M509446200.

R. J. LeVeque and Z. Li. The Immersed Interface Method for Elliptic Equations with Discontinuous Coefficients and Singular Sources. *SIAM J. Numer. Anal.*, 31(4):1019–1044, 1994. doi: 10.1137/0731054.

W. Li, S. Xu, G. Zhao, and L. P. Goh. Adaptive knot placement in B-spline curve approximation. *Comput. Aided Des.*, 37(8):791–797, 2005. doi: 10.1016/j.cad.2004.09.008.

X. Li, V. Cristini, Q. Nie, and J. S. Lowengrub. Nonlinear three-dimensional simulation of solid tumor growth. *Disc. and Cont. Dyn. Sys., Series B*, 2006. (in review).

A. Lipton. Pathophysiology of Bone Metastases: How This Knowledge May Lead to Therapeutic Intervention. *J. Support. Oncol.*, 2(3):205–220, 2004.

X.-D. Liu, R. Fedkiw, and M. Kang. A Boundary Condition Capturing Method for Poisson's Equation on Irregular Domains. *J. Comput. Phys.*, 160(1):151–178, 2000. doi: 10.1006/jcph.2000.6444.

J. Lotem and L. Sachs. Epigenetics and the plasticity of differentiation in normal and cancer stem cells. *Oncogene*, 25(59):7663–7672, 2006. doi: 10.1038/sj.onc.1209816.

R. M. B. Loureiro and P. A. D'Amore. Transcriptional regulation of vascular endothelial growth factor in cancer. *Cytokine Growth Factor Rev.*, 16(1):77–89, 2005. doi: 10.1016/j.cytogfr.2005.01.005.

J. S. Lowengrub and P. Macklin. A Centimeter-Scale Nonlinear Model of Tumor Growth in Complex, Heterogeneous Tissues. *J. Math. Biol.*, 2007. (in preparation).

H. T. Lynch, A. J. Krush, H. M. Lemon, A. R. Kaplan, P. T. Condit, and R. H. Bottomley. Tumor variation in families with breast cancer. *J. Am. Med. Assoc.*, 222(13):1631–5, 1972.

P. Macklin. Numerical Simulation of Tumor Growth and Chemotherapy. M.S. thesis, University of Minnesota School of Mathematics, September 2003.

P. Macklin. *Toward Computational Oncology: Nonlinear Simulation of Centimeter-Scale Tumor Growth in Complex, Heterogeneous Tissues.* Ph.D. dissertation, University of California, Irvine Department of Mathematics, June 2007.

P. Macklin and J. S. Lowengrub. An improved geometry-aware curvature discretization for level set methods: application to tumor growth. *J. Comput. Phys.*, 215(2):392–401, 2006. doi: 10.1016/j.jcp.2005.11.016.

P. Macklin and J. S. Lowengrub. Evolving interfaces via gradients of geometry-dependent interior Poisson problems: application to tumor growth. *J. Comput. Phys.*, 203(1):191–220, 2005. doi: 10.1016/j.jcp.2004.08.010.

P. Macklin and J. S. Lowengrub. Nonlinear simulation of the effect of microenvironment on tumor growth. *J. Theor. Biol.*, 245(4):677–704, 2007. doi: 10.1016/j.jtbi.2006.12.004.

P. Macklin, S. R. McDougall, A. R. A. Anderson, M. A. J. Chaplain, V. Cristini, and J. S. Lowengrub. Nonlinear Simulation of Tumour Invasion and Angiogenesis. *Bull. Math. Biol.*, 2007. (in preparation).

E. A. Maher, F. B. Furnari, R. M. Bachoo, D. H. Rowitch, D. N. Louis, C. W. K, and R. A. DePinho. Malignant glioma: genetics and biology of a grave matter. *Genes and Development*, 15(11):1311–1333, 2001. doi: 10.1101/gad.891601.

R. Malladi, J. A. Sethian, and B. C. Vemuri. Shape Modeling with Front Propagation: A Level Set Approach. *IEEE Trans. Pattern Anal. Mach. Intell.*, 17(2), 1995. doi: 10.1109/34.368173.

R. Malladi, J. A. Sethian, and B. C. Vemuri. A fast level set based algorithm for topology-independent shape modeling. *J. Math. Imaging Vision*, 6(2-3):269–289, 1996. doi: 10.1007/BF00119843.

D. G. Mallett and L. G. de Pillis. A Cellular Automata Model of Tumor-immune System Interactions. *J. Theor. Biol.*, 239(3):334–350, 2006. doi: 10.1016/j.jtbi.2005.08.002.

M. Malumbres and M. Barbacis. RAS oncogenes: the first 30 years. *Nat. Rev. Cancer*, 3 (6):459–465, 2001. doi: 10.1038/nrc1097.

Y. Mansury, M. Kimura, J. Lobo, and T. S. Deisboeck. Emerging Patterns in Tumor Systems: Simulating the Dynamics of Multicellular Clusters with an Agent-based Spatial Agglomeration Model. *J. Theor. Biol.*, 219(3):343–370, 2002. doi: 10.1006/jtbi.2002.3131.

K. Matsumoto and T. Nakamura. Hepatocyte growth factor and the Met system as a mediator of tumor-stromal interactions. *Int. J. Cancer*, 119(3):477–483, 2006. doi: 10.1002/ijc.21808.

Y. Matsumura and H. N. Ananthaswamy. Toxic effects of ultraviolet radiation on the skin. *Tox. Appl. Pharm.*, 195(3):298–308, 2004. doi: 10.1016/j.taap.2003.08.019.

S. R. McDougall, A. R. A. Anderson, and M. A. J. Chaplain. Mathematical modelling of dynamic adaptive tumour-induced angiogenesis: Clinical implications and therapeutic targeting strategies. *J. Theor. Biol.*, 241(3):564–589, 2006. doi: 10.1016/j.jtbi.2005.12.022.

D. L. S. McElwain and L. E. Morris. Apoptosis as a Volume Loss Mechanism in Mathematical Models of Solid Tumor Growth. *Mathematical Biosciences*, 39:147–157, 1978.

P. Michieli, C. Basilico, S. Pennacchietti, A. Maffè, L. Tamagnone, S. Giordano, A. Bardelli, and P. Comoglio. Mutant Met-mediated transformation is ligand-dependent and can be inhibited by HGF antagonists. *Oncogene*, 18(37):5221–31, 1999.

Y. Miki, J. Swensen, D. Shattuck-Eidens, P. A. Futreal, K. Harshman, S. Tavtigian, Q. Liu, C. Cochran, L. M. Bennett, W. Ding, et al. A strong candidate for the breast and ovarian cancer susceptibility gene BRCA1. *Science*, 266:66–71, 1994. doi: 10.1126/science.7545954.

A. Morotti, S. Mila, P. Accornero, E. Tagliabue, and C. Ponzetto. K252a inhibits the oncogenic properties of Met, the HGF receptor. *Oncogene*, 21(32):4885–93, 2002. doi: 10.1038/sj.onc.1205622.

W. Mueller-Kleiser. Three dimensional cell cultures: from molecular mechanisms to clinical applications. *Am. J. Physiol.*, 273(4):C1109–C1123, 1997.

G. R. Mundy. Metastasis to bone: causes, consequences and therapeutic opportunities. *Nat. Rev. Cancer*, 2(8):584–93, 2002. doi: 10.1038/nrc867.

V. R. Muthukkaruppan, L. Kubai, and R. Auerbach. Tumor-induced neovascularization in the mouse eye. *J. Natl. Cancer Inst.*, 69(3):699705, 1982.

K. Nabeshima, T. Moriyama, Y. Asada, N. Komada, T. Inoue, H. Kataoka, A. Sumiyoshi, and M. Koono. Ultrastructural study of TPA-induced cell motility: human well-differentiated rectal adenocarcinoma cells move as coherent sheets via localized modulation of cell-cell adhesion. *Clin. Exp. Med.*, 13(6):499508, 1995. doi: 10.1007/BF00118189.

M. N. Nakatsu, R. C. A. Sainson, J. N. Aoto, K. L. Taylor, M. Aitkenhead, S. Prez-del Pulgard, P. M. Carpenter, and C. C. W. Hughes. Angiogenic sprouting and capillary lumen formation modeled by human umbilical vein endothelial cells (HUVEC) in fibrin gels: the role of fibroblasts and Angiopoietin-1. *Microvasc. Res.*, 66:102–112, 2003. doi: 10.1016/S0026-2862(03)00045-1.

C. M. Nelson and M. J. Bissell. Of Extracellular Matrix, Scaffolds, and Signaling: Tissue Architecture Regulates Development, Homeostasis, and Cancer. *Ann. Rev. Cell Dev. Biol.*, 22(1):287–309, 2006. doi: 10.1146/annurev.cellbio.22.010305.104315.

M. A. Nowak, N. L. Komarova, A. Sengupta, J. V. Prasad, I.-M. Shih, B. Vogelstein, and C. Lengauer. The role of chromosomal instability in tumor initiation. *Proc. Natl. Acad. Sci. USA*, 99(25):16226–16231, 2002. doi: 10.1073/pnas.202617399.

S. Osher and R. Fedkiw. Level Set Methods: An Overview and Some Recent Results. *J. Comput. Phys.*, 169(2):463–502, 2001. doi: 10.1006/jcph.2000.6636.

S. Osher and R. Fedkiw. *Level Set Methods and Dynamic Implicit Surfaces*. Springer, New York, NY, 2002. ISBN 0-387-95482-1.

S. Osher and J. A. Sethian. Fronts propagating with curvature-dependent speed: algorithms based on Hamilton-Jacobi formulations. *J. Comput. Phys.*, 79(1):12–49, 1988. doi: 10.1016/0021-9991(88)90002-2.

M. R. Owen, H. M. Byrne, and C. E. Lewis. Mathematical modelling of the use of macrophages as vehicles for drug-delivery to hypoxic tumour sites. *J. Theor. Biol.*, 226 (4):377–391, 2004. doi: 10.1016/j.jtbi.2003.09.004.

J. D. Owens, D. Luebke, N. Govindaraju, M. Harris, J. Krueger, A. E. Lefohn, and T. J. Purcell. A survey of general-purpose computation on graphics hardware. *Comput. Graphics Forum*, 26(1):80–113, 2007. doi: 10.1111/j.1467-8659.2007.01012.x.

S. Paget. The distribution of secondary growths in cancer of the breast. *Lancet*, 133(3421): 571–573, 1889. doi: 10.1016/S0140-6736(00)49915-0.

D. Palmieri, C. E. Horak, J.-H. Lee, D. O. Halverson, and P. S. Steeg. Translational approaches using metastasis suppressor genes. *J. Bioenerg. Biomembr.*, 38(3-4):151–161, 2006. doi: 10.1007/s10863-006-9039-9.

D. Peng, B. Merriman, S. Osher, H. Zhao, and M. Kang. A PDE-Based fast local level set method. *J. Comput. Phys.*, 155(2):410–438, 1999. doi: 10.1006/jcph.1999.6345.

S. Pennacchietti, P. Michieli, M. Galluzzo, M. Mazzone, S. Giordano, and P. M. Comoglio. Hypoxia promotes invasive growth by transcriptional activation of the *met* protooncogene. *Cancer Cell*, 3(4):347–361, 2003. doi: 10.1016/S1535-6108(03)00085-0.

B. Piccoli and F. Castiglione. Optimal vaccine scheduling in cancer immunotherapy. *Physica A: Stat. Theor. Phys.*, 370(2):672–680, 2006. doi: 10.1016/j.physa.2006.03.011.

L.-M. Postovit, M. A. Adams, G. E. Lash, J. P. Heaton, and C. H. Graham. Oxygen-mediated regulation of tumor cell invasiveness. Involvement of a nitric oxide signaling pathway. *J. Biol. Chem.*, 277(38):35730–7, 2002. doi: 10.1074/jbc.M204529200.

P. Pott. *Chirurgical observations relative to the cataract, the polypus of the nose, cancer of the scrotum, different kinds of ruptures, and the mortification of the toes and feet.* Hawes, London, 1775.

J. Pouysségur, F. Dayan, and N. M. Mazure. Hypoxia signalling in cancer and approaches to enforce tumour regression. *Nature*, 441(25):437–443, 2006. doi: 10.1038/nature04871.

F. Prall. Tumour budding in colorectal carcinoma. *Histopathology*, 50(1):151–162, 2007. doi: 10.1111/j.1365-2559.2006.02551.x.

W. H. Press, B. P. Flannery, S. A. Teukolsky, and W. T. Vetterling. *Numerical Recipes in C: The Art of Scientific Computing.* Cambridge University Press, 2nd edition, 1992. ISBN 0-521-43108-5.

L. Preziosi, editor. *Cancer Modeling and Simulation.* CRC, Boca Raton, LA, 2003. ISBN 1-58488-361-8.

V. Quaranta, A. M. Weaver, P. T. Cummings, and A. R. A. Anderson. Mathematical Modeling of Cancer: The future of prognosis and treatment. *Clinica Chimica Acta*, 357 (2):173–9, 2005. doi: 10.1016/j.cccn.2005.03.023.

C. M. Quick, W. L. Young, E. F. Leonard, S. Joshi, E. Gao, and T. Hashimoto. Model of structural and functional adaptation of small conductance vessels to arterial hypotension. *Am. J. Physiol. Heart Circ. Physiol.*, 279(4):H1645H1653, 2000.

K. C. Quon and A. Berns. Haplo-insufficiency? Let me count the ways. *Genes Dev.*, 15 (22):2917–21, 2001. doi: 10.1101/gad.949001.

F. Ravandi and Z. Estrov. Eradication of leukemia stem cells as a new goal of therapy in leukemia. *Clin. Cancer Res.*, 12(2):340–344, 2006.

W. Reik and J. Walter. Genomic imprinting: paternal influence on the genome. *Nat. Rev. Genet.*, 2(1):21–32, 2001. doi: 10.1038/35047554.

B. I. Rini and E. J. Small. Biology and Clinical Development of Vascular Endothelial Growth Factor-Targeted Therapy in Renal Cell Carcinoma. *J. Clin. Oncology*, 23(5), 2005. doi: 10.1200/JCO.2005.01.186.

E. K. Rofstad and E. F. Halso. Hypoxia-associated spontaneous pulmonary metastasis in human melanoma xenographs: involvement of microvascular hotspots induced in hypoxic foci by interleukin. *Br. J. Cancer*, 86(8):301–308, 2002. doi: 10.1038/sj/bjc/6600052.

E. K. Rofstad, H. Rasmussen, K. Galappathi, B. Mathiesen, K. Nilsen, and B. A. Graff. Hypoxia promotes lymph node metastasis in human melanoma xenografts by up-regulating the urokinase-type plasminogen activator receptor. *Cancer Res.*, 62(6):1847–53, 2002.

T. Roose, P. A. Netti, L. L. Munn, Y. Boucher, and R. Jain. Solid stress generated by spheroid growth estimated using a linear poroelasticity model. *Microvasc. Res.*, 66(3): 204–212, 2003. doi: 10.1016/S0026-2862(03)00057-8.

P. Rous. A transmissible avian neoplasm. (Sarcoma of the common fowl). *J. Exp. Med.*, 12 (5):696–U46, 1910.

J. L. Rubinstein, J. Kim, O. Tomoko, M. Zhang, M. Westphal, D. F. Deen, and M. A. Shuman. Anti-VEGF antibody treatment of glioblastoma prolongs survival but results in increased vascular cooption. *Neoplasia*, 2(4):306–314, 2000.

B. Sadikovic and D. I. Rodenhiser. Benzopyrene exposure disrupts DNA methylation and growth dynamics in breast cancer cells. *Tox. Appl. Pharm.*, 216(3):458–468, 2006. doi: 10.1016/j.taap.2006.06.012.

G. Sakamoto. Infiltrating carcinoma: major histological types. In D. L. Page and T. J. Anderson, editors, *Diagnostic Histopathology of the Breast*, pages 219–222. Churchill-Livingstone, London, United Kingdom, 1987.

S. Sanga, J. P. Sinek, H. B. Frieboes, J. P. Fruehauf, and V. Cristini. Mathematical modeling of cancer progression and response to chemotherapy. *Expert. Rev. Anticancer Ther.*, 6 (10):1361–76, 2006. doi: 10.1586/14737140.6.10.1361.

B. C. Sansone, P. P. Delsanto, M. Magnano, and M. Scalerandi. Effects of anatomical constraints on tumor growth. *Phys. Rev. E*, 64(2):21903ff, 2002. doi: 10.1103/PhysRevE.64.021903.

K. L. Schmeichel, V. M. Weaver, and M. J. Bissel. Structural cues from the tissue microenvironment are essential determinants of the human mammary epithelial cell phenotype. *J. Mammary Gland Biol. and Neoplasia*, 3(2):201–213, 1998. doi: 10.1023/A:1018751124382.

P. Sdek, Z. Y. Zhang, J. Cao, H. Y. Pan, W. T. Chen, and J. W. Zheng. Alteration of cell-cycle regulatory proteins in human oral epithelial cells immortalized by HPV16 E6 and E7. *Int. J. Oral Maxillofac. Surg.*, 35(7):653–657, 2006. doi: 10.1016/j.ijom.2006.01.017.

E. A. Seftor, P. S. Meltzer, D. A. Kirshmann, et al. Molecular determinants of human uveal melanoma invasion and metastasis. *Clin. Exp. Metastasis*, 19:233–246, 2002. doi: 10.1023/A:1015591624171.

A. E. Segall and M. J. Sipics. The influence of interpolation errors on finite-element calculations involving stress-curvature proportionalities. *Finite Elem. Anal. Des.*, 40(13-14): 1873–1884, 2004. doi: 10.1016/j.finel.2003.11.006.

J. A. Sethian. *Level Set Methods and Fast Marching Methods*. Cambridge University Press, New York, NY, 1999. ISBN 0-521-64557-3.

J. A. Sethian and P. Smereka. Level set methods for fluid interfaces. *Ann. Rev. of Fluid Mech.*, 35(1):341–372, 2003. doi: 10.1146/annurev.fluid.35.101101.161105.

N. Sharifi, B. T. Kawasaki, E. M. Hurt, and W. L. Farrar. Stem Cells in Prostate Cancer: Resolving the Castrate-Resistant Conundrum and Implications for Hormonal Therapy. *Cancer Biol. Ther.*, 5(8):910–906, 2006.

C. J. Sherr. Cancer Cell Cycles. *Science*, 274(5293):1672–1677, 1996. doi: 10.1126/science.274.5293.1672.

I. Shuryak, R. K. Sachs, L. Hlatky, M. P. Little, P. Hahnfeldt, and D. Brenner. Radiation-Induced Leukemia at Doses Relevant to Radiation Therapy: Modeling Mechanisms and Estimating Risks. *J. Natl. Cancer Inst.*, 98(24):1794–1806, 2006. doi: 10.1093/jnci/djj497.

J. Sinek, H. Frieboes, X. Zheng, and V. Cristini. Two-dimensional Chemotherapy Simulations Demonstrate Fundamental Transport and Tumor Response Limitations Involving Nanoparticles. *Biomed. Microdev.*, 6(4):197–309, 2004. doi: 10.1023/B:BMMD.0000048562.29657.64.

G. L. G. Sleijpen, H. A. van der Vorst, and D. R. Fokkema. bicgstab(ℓ) and other hybrid Bi-CG methods. *Numer. Algorithms*, 1(7):75109, 1994. doi: 10.1007/BF02141261.

V. I. F. Slettenaar and J. L. Wilson. The chemokine network: A target in cancer biology? *Adv. Drug Deliv. Rev.*, 58(8):962–974, 2006. doi: 10.1016/j.addr.2006.03.012.

X.-F. Sun and H. Zhang. Clinicopathological significance of stromal variables: angiogenesis, lymphangiogenesis, inflammatory infiltration, MMP and PINCH in colorectal carcinomas. *Mol. Cancer*, 5:43, 2006. doi: 10.1186/1476-4598-5-43.

M. Sussman and E. Fatemi. An Efficient, Interface Preserving Level Set Re-Distancing Algorithm and its Application to Interfacial Incompressible Fluid Flow. *SIAM J. Sci. Comput.*, 20(4):1165–1191, 1999. doi: 10.1137/S1064827596298245.

M. Sussman, P. Smereka, and S. Osher. A level set approach for computing solutions to incompressible two-phase flow. *J. Comput. Phys.*, 114(1):146–159, 1994. doi: 10.1006/jcph.1994.1155.

M. Sussman, E. Fatemi, P. Smereka, and S. Osher. An Improved Level Set Method for Incompressible Two-Phase Flows. *Comput. Fluids*, 27(5-6):663–680, 1998. doi: 10.1016/S0045-7930(97)00053-4.

L. A. Taber. An optimization principle for vascular radius including the effects of smooth muscle tone. *Biophys. J.*, 74(1):109114, 1998.

H. A. van der Vorst. BI-CGSTAB: A fast and smoothly converging variant of BI-CG for the solution of nonsymmetric linear systems. *SIAM J. Sci. Stat. Comput.*, 13(2):631–644, 1992. doi: 10.1137/0913035.

V. V. Vasko and M. Saji. Molecular mechanisms involved in differentiated thyroid cancer invasion and metastasis. *Curr. Opin. Oncol.*, 19(1):11–17, 2007.

P. Vaupel, F. Kallinowski, and P. Okunieff. Blood flow, oxygen and nutrient supply, and metabolic microenvironment of human tumours: a review. *Cancer Res.*, 49(23):6449–6465, 1989.

M. N. Vrahatis, G. D. Magoulas, and V. P. Plagianakos. From linear to nonlinear iterative methods. *Appl. Num. Math.*, 45(1):59–77, 2003. doi: 10.1016/S0168-9274(02)00235-0.

S. M. Wise, J. S. Lowengrub, H. B. Frieboes, and V. Cristini. Three-dimensional Diffuse-Interface Simulation of Multispecies Tumor Growth-I: Numerical Method. *Bull. Math. Biol.*, 2006. (in review).

D. Wodarz and N. L. Komarova. *Computational Biology of Cancer*. World Scientific, Hackensack, NJ, 2005. ISBN 9812560270.

R. I. Yarden, S. Pardo-Reoyo, M. Sgagias, K. H. Cowan, and L. C. Brody. BRCA1 regulates the G2/M checkpoint by activating Chk1 kinase upon DNA damage. *Nat. Genet.*, 30: 285–9, 2002. doi: 10.1038/ng837.

H.-S. Yu, W.-T. Liao, and C.-Y. Chai. Arsenic carcinogenesis in the skin. *J. Biomed. Sci.*, 13(5):657–666, 2006. doi: 10.1007/s11373-006-9092-8.

S. Yu, Y. Zhou, and G. W. Wei. Matched interface and boundary (MIB) method for elliptic problems with sharp-edged interfaces. *J. Comput. Phys.*, 224(2), 2007. doi: 10.1016/j.jcp.2006.10.030.

A. Zagorska and J. Dulak. HIF-1: the knowns and unknowns of hypoxia sensing. *Acta Biochimica Polonica*, 51(3):563–585, 2004.

A. Zetterberg, O. Larsson, and K. G. Wilman. What is the restriction point? *Curr. Opin. Cell Biol.*, 7(6):835–842, 1995. doi: 10.1016/0955-0674(95)80067-0.

L. Zhang, C. A. Athale, and T. S. Deisboeck. Development of a three-dimensional multiscale agent-based tumor model: Simulating gene-protein interaction profiles, cell phenotypes and multicellular interaction patterns in brain cancer. *J. Theor. Biol.*, 244(1):96–107, 2007. doi: 10.1016/j.jtbi.2006.06.034.

H.-K. Zhao, T. Chan, B. Merriman, and S. Osher. A variational level set approach to multiphase motion. *J. Comput. Phys.*, 127(1):179–195, 1996. doi: 10.1006/jcph.1996.0167.

X. Zheng, S. M. Wise, and V. Cristini. Nonlinear simulation of tumor necrosis, neovascularization and tissue invasion via an adaptive finite-element/level set method. *Bull. Math. Biol.*, 67(2):211–259, 2005. doi: 10.1016/j.bulm.2004.08.001.

Y. C. Zhou and G. W. Wei. On the ficticious-domain and interpolation formulations of the matched interface and boundary (MIB) method. *J. Comput. Phys.*, 219(1):228–246, 2006. doi: 10.1016/j.jcp.2006.03.027.

Y. C. Zhou, S. Zhao, M. Feig, and G. W. Wei. High order matched interface and boundary method for elliptic equations with discontinuous coefficients and singular sources. *J. Comput. Phys.*, 213(1):1–30, 2006. doi: 10.1016/j.jcp.2005.07.022.

D. Zipori. The mesenchyme in cancer therapy as a target tumor component, effector cell modality and cytokine expression vehicle. *Cancer Metastasis Rev.*, 25(3):459–467, 2006. doi: 10.1007/s10555-006-9012-4.